An experimental study of a turbulent jet in cross-flow by using LDA

Özcan, Oktay; Larsen, Poul Scheel

Publication date:
2001

Document Version
Publisher's PDF, also known as Version of record

MEK-FM 2001-02 June 2001
FLUID MECHANICS
ISBN 87-7475-247-2

DTU

AN EXPERIMENTAL STUDY OF A TURBULENT JET IN CROSS-FLOW BY USING LDA

Oktay Özcan
Poul S. Larsen

TECHNICAL UNIVERSITY OF DENMARK
DEPARTMENT OF MECHANICAL ENGINEERING

Preface

This study was conducted while the first author was on sabbatical leave from the Technical University of Istanbul, Turkey. He acknowledges the receipt of a grant in scope of the NATO Science Fellowship Programme by the Scientific and Technical Research Council of Turkey in 1999. The first author was also supported financially by DTU, Department of Energy Engineering and Department of Mechanical Engineering during his sabbatical stay. He expresses his gratitude to Prof. Poul S. Larsen for giving him the privilige to participate in this study. He also thanks Ruth Svane Vestergard, Hanne Bondorff and Birthe Ringtved for their assistance in solving numerous non-technical problems. Thanks are also due to Knud Erik Meyer, Erik Tobiesen, Benny Edelsten, K.B.Jensen, Ulrik Ullum, Nicholas Pedersen, Simon Matlok, Mads Reck and Dan Nortoft Sorensen for their generous help and support in the course of this study.

Abstract

A turbulent jet in a crossflow was studied by making detailed LDA measurements in three mutually perpendicular planes of the flow field near the jet exit. The data presented include three components of the mean velocity and six components of the Reynolds stress tensor for jet-to-crossflow velocity ratios of 1.3 and 3.3. The experiments were carried out in a wind tunnel with test section dimensions of 300 by 600 mm. The Reynolds number based on the free stream velocity (U_∞=1.5 m/s) and the jet diameter (D=24 mm) was nominally 2400. The jet issued normal to a flat plate raised from the side wall of the tunnel. The length of the pipe employed to produce the jet flow was sufficiently large so that fully developed pipe flow approached the jet exit. The boundary layer on the flat plate approaching the jet was also turbulent. A two-component, four-beam, fiber-optic based LDA system was used in three different configurations to measure all components of the mean velocity and turbulent stresses. Special consideration was given to establish and document the fully-developed incoming flow conditions on the flat plate and in the pipe. Static pressure measurements were made along the jet pipe in order to verify the existence of fully-developed conditions. Thanks to a thick boundary-layer developing on the flat plate (three jet diameters thick upstream of the jet exit), skin-friction could be determined from velocity measurements close to the wall. This report documents all the raw LDA data taken during the study with minimal amount of discussion. It also serves as a guide to a database. Further analysis and discussion of results will be made in future publications.

Table of Contents

Chapter 1

Introduction

A jet in crossflow is an important practical problem encountered in gas turbines, fuel injection, V/STOL aircraft, in chemical unit operations and boilers, and waste disposal into water bodies or the atmosphere. Some natural flows such as volcanic plumes and atmospheric updrafts in cross wind are also examples of a jet in crossflow as reported by Moussa et al. (1977). Experiments by Fric and Roshko (1994), Kelso et al. (1996) and Haven and Kurosaka (1997) show that there exists a complex vortical flow structure in the near field of a jet in a crossflow. In addition to the horse-shoe vortex (HSV), ring-like vortices (RLV) (jet shear–layer vortices) and counter rotating bound vortex pair (CVP), Fric and Roshko (1994) observed up-right wake vortices (URV) which extend vertically from the wall to the jet. A schematic description of the vortical structures near the jet exit is shown in Fig.1.1. There is a scarcity of turbulence data for the near flow field of a transverse jet. The majority of existing experimental data were obtained with hot–wire anemometry which is insensitive to flow direction and can give large errors in regions of high turbulence kinetic energy which may be larger than the mean kinetic energy of the cross flow. The present report presents detailed LDA measurements in three mutually perpendicular planes of the flow field near the jet exit. The data include three components of the mean velocity and six components of the Reynolds stress tensor for jet-to-crossflow velocity ratios of 3.3 and 1.3.

Previous experimental studies of a round jet in crossflow have been reported by Patrick (1967), Andreoupoulos (1985), Andreoupoulos and Rodi (1984), Crabb et al. (1981), Moussa et al. (1977), Sherif and Pletcher (1989), Andresen et al. (1993), Kavsaoglu and Schetz (1989), Fric and Roshko(1994), Haven and Kurosaka (1997), Kelso et al.(1993,1996), Kim et al. (1999), Meyer et al. (2000), Gustaffson (2000) and Ozcan et al. (2001). The primary governing parameters of the flow are the jet-to-crossflow velocity ratio R, the crossflow Reynolds number Re_c, the jet flow Reynolds number Re_j, and the normalized momentum thicknesses of the incoming crossflow and jet flow. In the case of fully developed flows, the normalized momentum thicknesses of the incoming crossflow and jet flow are determined by Re_c and Re_j, respectively. As reported by Andreopoulos and Rodi (1984), at high velocity ratios the near field of the jet is controlled by inviscid dynamics, whereas for low values of R the flow field is dominated by turbulence. Fric and Roshko (1994) and Kelso et al. (1997) report that the wake structure is most orderly for velocity ratios near the value of 4. Kelso et al. (1993) report that, depending on the Reynolds number, the wake vortices may have either a von Karman vortex street pattern or a mushroom–like pattern.

Computational studies of a round jet in crossflow have been reported by Patankar et al. (1977), Jones and McGuirk (1980), Kim and Benson (1993) Yuan and Street (1998) and Yuan et al. (1999). The Navier–Stokes solutions obtained by Ince and Leschziner (1993) and Alvarez et al. (1993) show that the

Reynolds stress modeling produces slightly better agreement with experimental data than the k–ϵ modeling. Reviews of experimental and computational studies are reported by Schetz (1990) and Margason (1993).

In the present study, both the mean velocity components and the turbulent stresses were measured in the near field of an incompressible round jet by using LDA. The experiments were carried out in a wind tunnel with test section dimensions of 300 by 600 mm. The Reynolds number based on the free stream velocity (U_∞=1.5 m/s) and the jet diameter (D=24 mm) was nominally 2400. A low Reynolds number was chosen partly for comparison of the data with computational solutions which become more difficult with increasing Reynolds number. The jet issued normal to a flat plate raised from the side wall of the tunnel. The length of the pipe employed to produce the jet flow was sufficiently large so that fully developed pipe flow approached the jet exit. The boundary layer on the flat plate approaching the jet was also turbulent. This was important because previous computational studies of the flow reported that solutions were fairly sensitive to the state of turbulence at the jet discharge plane. The pipe was made of glass so that LDA data could be obtained for the turbulent pipe flow approaching the jet exit. The jet issued from a flat plate raised from the side wall. Some manipulation of the flat plate boundary layer was necessary in order to produce a fully developed turbulent boundary layer approaching the jet. The state of the incoming boundary layer on the flat plate was determined in sufficient detail. Thus, well defined boundary conditions of the flow were documented.

A two-component, four-beam, fiber-optic based LDA system was used in three different configurations to measure all components of the mean velocity and turbulent stresses. At each point, 2000 statistically independent samples were used to calculate residence-time-averaged moments of the instantaneous velocities. Static pressure measurements were made along the jet pipe in order to verify the existence of fully-developed conditions. Thanks to a thick boundary-layer developing on the flat plate (three jet diameters thick upstream of the jet exit), skin-friction could be determined from velocity measurements close to the wall. Surface flow visulization was made to determine the topology of the skin–friction line patterns on the flat plate. Laser light sheet tomography was also employed for flow visualization.

The experimental setup and conditions are described in Chapter 2 which also gives an assessment of the measurement uncertainties in measured and derived quantities. The experimental results for the incoming flow on the flat plate and the jet pipe are presented in Chapter 3 . Chapter 4 discusses the results for the mean velocities, turbulent stresses, vorticity, skin-friction coefficient and the jet trajectories. A summary of preliminary results are given in Chapter 5. All figures appear at the end of the report.

All the data presented in this report can be made available upon request. The data base includes the MATLAB files which are used to make the plots presented in the report. An explanation of how to access the data base is given in Appendix A.

Chapter 2

Experimental methodology

2.1 Experimental setup and test conditions

The experiments were carried out in a low speed wind tunnel with test section dimensions of 300 by 600 mm. The test section of the tunnel was optically accessible through glass walls on the sides, top and bottom. A flat plate which had a length of 1950 mm, a width of 598 mm and a thickness of 10 mm was placed in the tunnel. The plate was made of plexiglass and it was raised from one side wall of the tunnel by using 26 mm thick spacers. Fig.2.1 presents a schematic drawing of the flat plate assembly in the wind tunnel. The jet axis was located 1350 mm downstream of the leading edge of the plate. In order to make use of a lens with a small focal length in LDA measurements, the jet axis was slightly offset from the centerlines of the flat plate and the tunnel. The leading and trailing edges of the flat plate were machined by 9 degrees to produce an edge thickness of 2 mm.

In order to enhance turbulence in the low Reynolds number incoming boundary layer flow, a vortex generator and a step both having thicknesses of 12 mm were placed near the leading edge of the flat plate as shown in Fig. 2.2. The vortex generator was made of half delta wings inclined at 15 degrees with respect to the flow direction. The vortex generator is produced by LM Glasfiber of Denmark for use on wind turbine blades.

Shop air was used to produce the jet flow. A two meter long hose pipe followed by a 2.5 m long plexiglass pipe was used to feed the jet air into the tunnel. The inside diameter of the circular pipe (i.e. the jet diameter) was D=24 mm. Fig.2.3 presents a schematic drawing of the pipe flow assembly which includes a flow straightener and a venturi tube. A schematic drawing of the venturi tube is shown in Fig. 2.4.a. For convenience in the production of the pipe and execution of experiments, the pipe was made of three sections (pipes A,B and C) which had ends suitable for quick disconnection (Fig.2.4.b). Pipe B was instrumented with 4 pressure taps spaced 400 mm apart.

The experiments were conducted at a nominal free stream velocity (crossflow velocity) of U_∞=1.50. Two different values for the jet bulk velocity (W_j) were employed to produce jet to free stream velocity ratios (R =W_j/U_∞) of 1.3 and 3.3, nominally. Air temperature was kept at 22 $\pm$ 2 degrees in the course of the experiments. The Reynolds number based on the jet diameter (D=24mm) and the free stream velocity U_∞ was Re_c= 2370 $\pm$ 40. Table 1 gives the values of the free stream velocity U_∞, jet bulk velocity W_j and the Reynolds number based on D and W_j (Re_j= Re_D) for the two velocity ratios (R) used in the study. The relavant parameters of the turbulent pipe flow approaching the flat plate and the state of the turbulent flat plate boundary layer approaching the jet are discussed in Sections 3.1 and 3.2, respectively.

R	U_∞(m/s)	W_j(m/s)	Re_j
1.33 ± 0.02	1.50 ± 0.02	2.00 ± 0.02	3200 ± 50
3.33 ± 0.07	1.48 ± 0.02	4.95 ± 0.03	7920 ± 130

TABLE 1 . Test parameters R,U_∞, W_j and Re_j

2.2 Experimental techniques

A two-component, four beam, fiber optic based LDA system (DANTEC55X, 310 mm and 1100 mm front lens) was used to obtain the velocity data . The green and blue lines of a 5 watt Argon-Ion laser were utilized. Determination of the flow direction was made possible through application of a 40 Mhz frequency shift to one of the green and blue beams. The light scattered from the particles passing through the measuring volume was collected in the backscatter mode. LDA signals were processed by a DANTEC 58N20 Flow Velocity Analyzer. In order to avoid high velocity biasing, residence time averaging was used to obtain the first and second moments of the instantaneous velocities.

Data were obtained in three different configurations of the LDA optics which are shown schematically in Fig.2.5. The right- handed Cartesian coordinate system (x,y,z) used in the discussion of results is also shown in Fig.2.5. The instantaneous velocity components in the x,y and z directions (U_i, V_i, W_i), mean velocity components (U,V,W) and second moments (U^2_{rms}, V^2_{rms}, W^2_{rms}, uv, uw, vw) measured by each LDA configuration are also indicated. The LDA fiber optics probe is located on top of the wind tunnel in Configurations 1 and 3, and on the side of the tunnel in Configuration 2. A 100 mm diameter mirror is placed in the section downstream of the flat plate in order to direct the laser beams along the x direction in Configuration 3. The focal length of the front lens was 310 mm for Configurations 1 and 2, and 1200 mm for configuration 3. The effective measuring volume had a diameter of 0.08 mm an a length of 0.7mm for the 310 mm focal length lens. For the 1200 mm focal length lens (Configuration 3), the diameter and length of the measuring volume were 0.3 mm and 9.8mm, respectively. Due to the rather long measuring volume, Configuration 3 was used only in a limited flow region (x/D=2.4 plane) where the streamwise flow gradients were small. In order to make measurements close to the surface of the flat plate, the laser beams were tilted by 7 degrees with respect to the y axis when using Configuration 1. Tilting of the laser beams do not affect U_i but introduces a systematic error in W_i. Appendix 1 discusses these errors and presents algebraic relations for correction of data. However, since the errors are shown to be smaller than the estimated uncertainties, no corrections were applied to the data presented in this report.

LDA data were obtained in the coincident mode so that processing of the data produced not only the mean and rms velocities but also the turbulent stress components of the Reynolds stress tensor. An exception to this applied to LDA measurements in the pipe where the curvature of the pipe surface prevented

the green and blue beam pairs from crossing at the same point. Therefore, turbulent shear stresses could not be measured in pipe flow. Moments of velocity U, U^2_{rms} and uv were calculated from N statistically independent samples by using the formulae given below:

$$U = \frac{\sum U_i \Delta t_i}{\Delta t_i} \tag{2.2.1}$$

$$U^2_{rms} = \frac{\sum (U_i - U)^2 \Delta t_i}{\Delta t_i} \tag{2.2.2}$$

$$uv = \frac{\sum (U_i - U)(V_i - V) \Delta t_i}{\Delta t_i} \tag{2.2.3}$$

where Δt_i is the residence time corresponding to a concident pair of U_i and V_i. Expressions similar to Eqns. 1,2 and 3 were used for the mean velocity components V and W, turbulent normal stresses V^2_{rms} and W^2_{rms} and turbulent shear stresses uw and vw, respectively.

A Laskin type seed generator utilizing shop air and a glycerol/water mixture was used to generate seed particles which had a mean diameter of 2 to 4 microns. Separate seed generators were used in seeding the tunnel flow and the jet flow.

An orifice plate located downstream of the tunnel test section was used to monitor the tunnel velocity. A Furness Control micromanometer (Model MDC-FC001) was employed in measuring the pressure difference from the two sides of the orifice plate. The same micrometer was also employed in measuring the pressure drop along the pipe in preliminary tests. A Betz micromanometer was used in measuring the pressure difference from the venturi tube mounted in the jet pipe assembly.

A Collins chain compensated gasometer was used to calculate the mass flow coefficient of the venturi tube used for measuring the jet flow rate. The flow coefficient α is defined as the ratio of the real mass flow to the ideal mass flow of an inviscid fluid. Use of Bernoulli's equation gives the ideal mass flow rate through a venturi tube once the pressure difference between the maximum and minimum cross sections is measured. The calibration of the venturi tube involved partial filling of a 120 liter tank with air and measuring the filling time of the gasometer with a stopwatch.

2.3 Experimental accuracy

Uncertainties in the moments measured by LDA can be estimated by using analytical expressions given by Benedict and Gould(1996). When Gaussian distributions are assumed, the uncertainties in U, U^2_{rms} and uv (with a confidence level of 95 percent) are given by

$$S(U) = \pm 1.96 \frac{\sigma_u}{\sqrt{N}} \tag{2.3.1}$$

$$S(U_{rms}^2) = \pm 1.96\sqrt{\frac{2}{N}}\sigma_u^2 \tag{2.3.2}$$

$$S(uv) = \pm 1.96\sqrt{\frac{1+R_{uv}^2}{N}}\sigma_u\sigma_v \tag{2.3.3}$$

where σ_u and σ_v are standart deviations of the U_i and V_i distributions, N is ensemble size and R_{uv} is the correlation coefficient given by

$$R_{uv} = \frac{uv}{U_{rms}V_{rms}} \tag{2.3.4}$$

Assuming a Gaussian distribution, the uncertainties in U_{rms} and R_{uv} can be calculated from the following relations:

$$S(U_{rms}) = \pm 1.96\sqrt{\frac{1}{2N}}\sigma_u \tag{2.3.5}$$

$$S(R_{uv}) = \pm 1.96\sqrt{\frac{1}{N}}(1 - R_{uv}^2) \tag{2.3.6}$$

It is interesting to note that the uncertainty in the correlation coefficient decreases with increasing R_{uv}. This trend is opposite to that of other turbulence quantities.

Since uncertainties depend on standart deviations, it is not proper to prescribe a single uncertainty value which is valid in the whole flow field. For practical purposes, however, we may state the relative uncertainty which is defined as uncertainty normalized by maximum measured value. The relative uncertainties for mean velocity components (U,V,W), normal stresses ($U_{rms}^2, V_{rms}^2, W_{rms}^2$) and shear stresses ($uv, uw, vw$) are estimated to be 4, 6 and 15 percent, respectively.

The uncertainties in derived quantities such as eddy viscosity or skin friction coefficient can be calculated by using the error propagation formula of Kline and McClintock (1953). This formula relates the uncertainty in a quantity $A(x_1, x_2, ...x_n)$ to the uncertainties in $x_1, x_2, ...x_n$ by

$$S(A) = \pm\sqrt{[\frac{\partial A}{\partial x_1}S_{x1}]^2 + [\frac{\partial A}{\partial x_2}S_{x2}]^2 + ...[\frac{\partial A}{\partial x_n}S_{xn}]^2} \tag{2.3.7}$$

where $S(A), S_{x1}, S_{x2}...S_{xn}$ are the uncertainties in A, $x_1, x_2, ...x_n$, respectively.

Chapter 3

Flow Conditions

3.1 Incoming Pipe Flow

3.1.1 Static pressure measurements

Fig. 3.1 presents the variation of the static pressure drop Δp across the pipe length Δz for the pipe bulk velocities (jet velocities) of W_j= 2.00, 3.00, 4.00 and 4.93 m/s. Δp and Δz are referenced to the upstream pressure tap T1 as shown in Fig 2.3 (z=0 is the plane of the flat plate). The fact that the pressure gradient $\partial p/\partial z$ is constant along the pipe is a definite indication that the pipe flow is fully developed. The following relation exists between the pressure gradient $\partial p/\partial z$ and the surface shear stress τ_{wj} in fully developed pipe flow:

$$\tau_{wj} = -\frac{\partial p}{\partial z}\frac{a}{2} \tag{3.1}$$

where a is the internal pipe radius (a=D/2). Eq. 3.1 can be used to evaluate the pipe skin friction coefficient C_{fj} which is defined by

$$C_{fj} = \frac{\tau_{wj}}{0.5\rho W_j^2} \tag{3.2}$$

where ρ is the density of air.

W_j(m/s)	R	w_τ (m/s)	C_{fj}	C_{fB}	α
2.00 $\pm$ 0.02	1.33 $\pm$ 0.02	0.141 $\pm$ 0.004	0.0100	0.0105	0.920
3.00 $\pm$ 0.02	2.01 $\pm$ 0.04	0.205 $\pm$ 0.006	0.0093	0.0095	0.930
4.00 $\pm$ 0.03	2.68 $\pm$ 0.06	0.264 $\pm$ 0.008	0.0087	0.0088	0.940
4.95 $\pm$ 0.03	3.33 $\pm$ 0.07	0.318 $\pm$ 0.009	0.0083	0.0084	0.945

TABLE 2 . Parameters of pipe flow $W_j, R, w_\tau, C_{fj}, C_{fB}$ and α

The values of C_{fj} evaluated by using the measured pressure gradients are presented in Table 2 along with the skin friction coefficient C_{fB} values predicted by the Blasius relation which is given as

$$C_{fB} = 0.079 Re_D^{-0.25} \tag{3.3}$$

where Re_D=Re_j is the Reynolds number based on D and W_j. There is a close agreement between the measurement and prediction of Eq.3.3. Table 2

also presents the flow coefficient of the venturi tube, the velocity ratio R, the Reynolds number Re_j and the friction velocity in the pipe (w_τ) given by

$$w_\tau = \sqrt{\tau_{wj}/\rho} = W_j\sqrt{0.5C_{fj}} \tag{3.4}$$

for the four jet velocities indicated in Fig. 3.1. Flow coefficients α at W_j=3 and 4 m/s were calculated by interpolation between the measured values of α for W_j=2 and 4.93 m/s. Uncertainties in C_{fj} and α are $\pm$ 0.0005 and $\pm$ 0.01, respectively.

3.1.2 Flow rate measurements

The flow rate in the pipe was measured by using a venturi tube which was calibrated against a gasometer as described in Section 2. Table 2 gives the values of the the flow coefficients of the venturi tube (α) for the two velocity ratios (R) used in the study. alpha was also measured by using the pipe flow velocity profiles measured by LDA The two methods gave the same results within the specified accuracy of the alpha measurement. Ref. 2 presents empirical data for the variation of α with Reynolds number (Re_j) which indicates that as Re_j decreases from 150,000 to 40,000 α decreases from 0.995 to 0.970. This trend is consistent with the measurements of the present study.

3.1.3 LDA measurements

It would be highly desirable to make LDA measurements in the pipe near the jet exit. However, due to optical inaccessibility of this region, measurements could be made for Z<-80 mm. Fig.3.2 presents the variation of the normalized axial velocity W/W_j with the normalized radial distance r/a in pipe flow at z=-120 mm(z/D=-5). W_j is the jet bulk velocity(or pipe bulk velocity) and a is the internal radius of the pipe (a=D/2=12mm). Direct numerical simulation results of Eggels et al.(1994), experimental data of Patel and Head (1969) and a 1/7 power law approximation are also presented for fully developed pipe flow in the absence of a cross flow. The following two results can be deduced from the good agreement between the measurements of the present study and the data of fully developed pipe flow : a) The incoming flow of the present study is fully developed b) The flow at z/D=-5 is not affected significantly by the cross flow. It is interesting to note that power law approximation is not satisfactory for a low Reynolds number Re_j which was 7260 and 5400 for the data of Patel (1969) and Eggels et al.(1994), respectively.

Fig.3.3 presents the variation of the axial mean velocity in the pipe in wall coordinates ($y^+ = w_\tau y/\nu$, $W^+ = W/w_\tau$) at z/D=-5. y is the distance normal to the wall (y=r-a), ν is the kinematic viscosity of air. w_τ values are calculated by using Eqns. 3.3 and 3.4. The well known logarithmic law of the wall given by

$$W^+ = 2.5lny^+ + 5.5 \tag{3.5}$$

and the laminar sublayer relation

$$W^+ = y^+ \tag{3.6}$$

are also plotted in Fig.2.8. As noted by Patel and Head (1969) and Eggels et al.(1994), the mean pipe flow velocity fails to conform with Eq.3.5 whose constants are established for high Reynolds number flows.

Fig.3.4 shows the variation of the axial rms velocity in the pipe in wall coordinates ($y^+ = w_\tau y/\nu, W^+_{rms} = W_{rms}/w_\tau$) at z/D=-5. There is a reasonably good agreement with the data of the present study and the computations. Discrepancies are largest near the axis of symmetry where turbulence intensity goes through a minimum.

Study	Re_j	δ_j^*/D	θ_j/D	H_j
Present (R=1.3)	3200	0.075	0.033	2.23
Eggels et al. (1994)	5300	0.064	0.034	1.86
Present (R=3.3)	8400	0.057	0.033	1.75

TABLE 3 Integral parameters of the pipe flow Re_j, $\delta_j{}^*$/D, θ_j/D and H_j=$\delta_j{}^*/\theta_j$ at z/D=-5

Eggels et al. (1994) define a displacement thickness δ_j^* and a momentum thickness θ_j by calculating the real mass flow defect and momentum defect in a pipe and setting these quantities equal to the mass defect and momentum defect of imaginary layers (near the pipe wall with thicknesses of δ_j^* and θ_j in which velocity is zero. In other words, the following two equations which give the mass and momentum defect,respectively, define the displacement thickness δ_j^* and momentum thickness θ_j implicitly:

$$\int (W_o - W) 2\pi r dr = W_o[\pi a^2 - \pi(a - \delta_j^*)^2] \tag{3.7}$$

$$\int (W_o - W) W 2\pi r dr = W_o[\pi a^2 - \pi(a - \theta_j)^2] \tag{3.8}$$

where W_o is the mean velocity on the pipe centerline. Integral limits are from zero to pipe radius a. Solution of δ_j^* and θ_j from the above equations produce the following explicit relations:

$$\frac{\delta_j^*}{a} = 1 - \sqrt{1 - \int (1 - \frac{W}{W_o}) 2\frac{r}{a} d(\frac{r}{a})} \tag{3.9}$$

$$\frac{\theta_j}{a} = 1 - \sqrt{1 - \int (1 - \frac{W}{W_o}) \frac{W}{W_o} 2\frac{r}{a} d(\frac{r}{a})} \tag{3.10}$$

Table 3 gives the values of Re_j, δ_j^*/D, θ_j/D and shape factor H_j=δ_j^*/θ_j for the flow of the present study at z/D=-5 and of Eggels et al.(1994). An inspection of Table 3 shows that θ_j/D is insensitive to changes in Re_j. On the other hand

δ_j^*/D and H_j decrease monotonically with increasing Re_j. It is believed that these integral parameters define the incoming pipe flow adequately.

3.2 Incoming boundary layer flow on the flat plate

The Reynolds number based on the free stream velocity and the distance from the leading edge of the flat plate to the jet axis (L= 1350 mm.) was nominally $Re_L = 1.35\text{x}10^5$. As mentioned earlier, a vortex generator and a boundary layer tripping step were mounted near the leading edge of the flat plate in order to enhance turbulence in the incoming boundary layer. Several steps were tested. The locations of the steps and the vortex generated were varied such that the boundary layer approaching the jet axis had properties similar to the fully developed turbulent boundary layers reported in the literature. The geometry shown in Fig.2.2 produced the best results for this purpose.

The incoming velocity profile was measured at x=-90 mm (x/D=-3.8). The undisturbed boundary layer thickness at this location was δ_c= 70 mm. The displacement and momentum thicknesses were δ_c^*=10.8 mm and θ_c=7.7 mm, respectively (δ_c^*/D=0.45, θ_c/D=0.32). It must be noted that δ_c^*/D and θ_c/D values are roughly an order of magnitude smaller than the δ_j^*/D and θ_j/D values of the incoming pipe flow given in Table 3. Fig. 3.5 shows that the streamwise velocity profile close to the wall. The exact position of the wall from the LDA measuring volume and the skin friction on the flat plate (τ_{wc}) could be determined by fitting a linear curve to the data. Such a determination was possible because the boundary layer was much thicker than the diameter of the measuring volume. The friction velocity on the flat plate u_τ is defined by

$$u_\tau = \sqrt{\tau_{wc}/\rho} = U_\infty \sqrt{0.5 C_{fc}} \tag{3.11}$$

where ρ is air density, τ_{wc} is the wall shear stress on the flat plate for incoming boundary layer and C_{fc} is the skin friction coefficient defined by

$$C_{fc} = \frac{\tau_{wc}}{0.5\rho U_\infty^2} \tag{3.12}$$

u_τ was equal to 0.07 m/s which produced a z^+ value of 4.7 mm at z=1 mm. The Rotta thickness defined by

$$\Delta_R = \delta_c^* U_\infty / u_\tau \tag{3.13}$$

was equal to 230. Fig.3.6 gives the variation of the normalized velocity defect $(U - U_\infty)/u_\tau$ with the normalized distance z/Δ_R. The computational data of Spalart (1988) obtained by DNS for a fully developed turbulent boundary layer flow is also shown. The velocity data is plotted in wall coordinates U^+ vs z^+ in Fig. 3.7 which shows a good agreement with the logarithmic law of the wall given by

$$U^+ = 2.5 ln z^+ + 5.5 \tag{3.14}$$

Table 4 presents some dimensionless parameters for the incoming crossflow boundary layer of the present study and Spalart's computational data. $Re_{c\delta^*}$ is the Reynolds number based on the crossflow velocity U_∞ and the displacement thickness δ_c^*. $Re_{c\theta}$ is the Reynolds number based on U_∞ and the momentum thickness θ_c. H_c=$\delta_c{}^*/\theta_c$ is the crossflow shape factor which is the ratio of displacement and momentum thicknesses. Re_{c+} is the Reynolds number based on the friction velocity u_τ and the boundary layer thickness δ_c. The approximate equivalence of these dimensionless numbers indicate that Spalart's data set was suitable for comparison with the incoming boundary layer data of the present study.

Study	$Re_{c\delta^*}$	$Re_{c\theta}$	H_c	C_{fc}	U_∞/u_τ	Re_{c+}	δ_c/δ_c^*
Present	1080	770	1.40	0.0043	21.29	327	6.46
Spalart (1988)	1000	670	1.50	0.0048	20.34	325	6.60

TABLE 4 Integral parameters of the crossflow boundary layer $Re_{c\delta^*}$ $Re_{c\theta}$, H_c=δ_c^*/θ_c, C_{fc}, , U_∞/u_τ $Re_{\tau\delta^*}$ and δ_c/δ_c^*

Figs. 3.8, 3.9, 3.10 and 3.11 present variations of the normalized turbulent stresses U_{rms}/u_τ, V_{rms}/u_τ, W_{rms}/u_τ and uw/u_τ, respectively, with normalized distance z/Δ_R. The agreement between the present measurements and Spalart's computations suggest that the incoming turbulent boundary layer can be considered as fully developed . This is an important simplification in the boundary conditions of a potential computation of this flow.

3.3 Inviscid cross flow

Fig.3.12 gives the variation of the streamwise velocity component (normalized with the nominal value of the free stream velocity which is 1.5 m/s) in the inviscid outer flow at z/D=7.5 and z/D=5.4 for the respective R values of 3.3 and 1.3. The free stream velocity is formally defined as the inviscid tunnel velocity near the jet exit (x=0) when the jet velocity is zero. Data for R=0 which corresponds to zero jet velocity are also shown in Fig. 3.10. Since room air could be sucked into the test section during tunnel runs, a plug was fitted to the upstream end of the pipe to ensure zero jet velocity. R=0 data shows that inviscid streamwise velocity increases slightly along the streamwise direction. This is due to thickening of the boundary layers on the side walls and the flat plate. At R=3.3, the jet flow creates an obstruction to the crossflow which decelerates as it approaches the jet exit. Inviscid flow accelerates downstream of the jet exit. This acceleration is basically due to additional mass flow brought into the test section by the jet. Interestingly, the data for R=1.3 indicates a barely noticable flow deceleration upstream of the jet.

Assuming a flow coefficient of 0.96, the volumetric flow rate of the cross flow between the flat plate and the side walls is approximately Q_c=230 liter/second

for a free stream velocity of 1.50 m/s. Table 5 gives the ratio of the cross flow rate and the jet flow rate Q_c/Q_j which varies from 103 to 252 as the velocity ratio is decreased from 3.3 to 1.3. Thus, for large x/D values the tunnel bulk velocity would increase by percentages of 1/103 and 1/252 for R=3.3 and 1.3, respectively, due to conservation of mass in this incompressible flow.

W_j(m/s)	R	Q_c/Q_j
2.00 ± 0.02	1.33 ± 0.02	103 ± 2
3.00 ± 0.02	2.01 ± 0.04	126 ± 2
4.00 ± 0.03	2.68 ± 0.06	170 ± 3
4.95 ± 0.03	3.33 ± 0.07	252 ± 4

TABLE 5 . Ratio of cross flow rate and jet flow rate Q_t/Q_j

3.4 Repeatibility of LDA data

Time correlation measurements were made in various regions of the flow field in order to estimate the time scale of the flow. Largest values of time scales were observed in the vicinity of the jet between -24<x(mm)<48. These maximum values were approximately 40 ms and 20 ms for R=3.3 and 1.3 flows, respectively. In order to make statistically independent moments of velocity, Dead times of 80 ms and 40 ms were employed in LDA measurements for R=3.3 and 1.3, respectively, in the region of -24<x(mm)<48. Outside this range, dead times of 40 ms and 20 ms were employed for R=3.3 and 1.3, respectively. An ensemble size of N=2000 was chosen for a great majority of the data. N=500 samples were used very close to the flat plate (y<1 mm) due to very low data rates. A typical data acqusition time for a velocity profile consisting of 40 data points was one to two hours.

Fig. 3.13 presents the variations of the normalized streamwise velocity U/U_∞ with z/D in the y=0 plane for x/D=-3.75, -0.66, 0 and 1.83 at R=3.3. Data are shown for experiments which were repeated two or three times. Repeatibility of measurements is very good considering the fact that some of the data were taken with different LDA configurations (X/D=-3.75). The discrepancies between the different runs is probably due to errors in setting the jet and crossflow velocities.

Chapter 4

Results and discussion

Global features of the flow such as mean velocity vector maps, sectional streamlines, jet trajectories will be discussed in section 4.1 together with the vorticity and divergence fields and the skin friction distribution on the centerline of the flat plate. The mean flow and turbulent stress fields will be presented in Sections 4.2, 4.3 and 4.4 for describing the flow in constant y, z and x planes, respectively.

4.1 Global flow features

4.1.1 Mean velocity vector maps and sectional streamlines

Figs. 4.1.1 and 4.1.2 show the mean velocity (U,W) vector maps and sectional streamlines in the y=0 plane (centerplane, plane of symmetry) of the flow field for R=3.3 and 1.3, respectively. Assuming that the mean velocity normal to the y=0 plane is zero, the sectional streamlines and streamlines are identical. Figs. 4.1.3 and 4.1.4 give closeup views of the streamline patterns near the jet exit for R=3.3 and 1.3, respectively. The jet flow at the pipe exit for R=1.3 is more slanted and less symmetric (with respect to the z axis) than the flow for R=3.3. For both velocity ratios, we observe a deflection of the streamlines towards the plate surface upstream of the jet. This is due to attachment of the crossflow following the boundary layer separation which genarates the horseshoe vortex. For both velocity ratios, there appears to exist a nodal point of singularity in the flow field downstream of the jet exit.

Fig. 4.1.5 shows the streamline pattern in the y=0 plane upstream of the jet exit for R=3.3. The horseshoe vortex and a singular focus point around x^*=x/D=-0.7 and z^*=Z/D=0.05 is clearly visible. Another focus can be observed in the streamline pattern presented in Fig.4.1.6 around (x^*=-0.5, z^*=0.23). As shown in the schematic streamline pattern given by Fig.4.1.7, one can hypothesize the existence of a saddle point S above the focus shown in Fig.4.1.6. However, detailed measurements did not extend to region above z/D=0.25 for verification of the saddle point S shown in Fig.4.1.7. The streamline patterns given in Figs. 4.1.8 and 4.1.9 fail to pinpoint the exact location of the nodal singular point downstream of the jet exit. One can only speculate that flow attachment on the plate occurs around x/D=3.2 and the nodal point is located around (x^*= 2.0 , z^*=0.3). The hypothesized streamline pattern shown in Fig. 4.1.7 indicate a focus point of singularity in the pipe. This focus, which is reported by Kelso et al.(1996), is due to a vortex genarated by separation of the pipe flow approaching the jet exit.

Fig. 4.1.10 show the sectional streamlines together with the inplane (U,V) mean velocity vectors in the z/D=0.17 plane for R=3.3 and 1.3. The size of the reverse flow region is larger for R=3.3 than for R=1.3. A saddlepoint of

singularity S , which marks the downstream boundary of the reverse flow region approximately, is located around x^*=x/D=2.5 and y^*=y/D=1.5 for R=3.3 and 1.3, respectively. Acceleration of the crossflow by the jet in this plane is readily apparent from the large magnitude of the velocity vectors near the jet exit.

Figs. 4.1.11 and 4.1.12 present sectional streamlines together with the inplane mean velocity (U,V) vector map in a closeup view of the flow in the z/D=0.17 plane for R=3.3 and 1.3, respectively. The magnitude of the reverse flow (U<0) is much larger for R=3.3 than for R=1.3. There appears to exist one focus for R=1.3 and two foci for R=3.3. As shown in the hypothesized streamline pattern given by Fig. 4.1.11a, these foci must be connected by a sectional streamline which passes through a saddle point of singularity. This requires the presence of two clockwise rotating vortices.

Figs. 4.1.13 and 4.1.14 present sectional streamlines for R=3.3 at z/D=3.0 and for R=1.3 at z/D=1.3, respectively. The flow is deflected severely in the y direction away from the centerline and decelarated in the x direction near the centerline. However, there is no evidence of reverse flow for x/D values up to 2.

Figs. 4.1.15 and 4.1.16 give the sectional streamlines together with the inplane mean velocity vector map (V,W) in the x/D=2.4 plane for R=3.3 and 1.3, respectively. In order to relate the sectional streamlines to the schematic drawing given in Fig.1.1, one must note that in Figs.4.1.15 and 4.1.16, we look at the flow field from upstream of the jet exit in the positive x direction. The center of the kidney vortex is located around (y^*=1.4, z^*=2.3) for R=3.3 and around (y^*=0.6, z^*=1.3) for R=1.3.

Figs. 4.1.17 and 4.1.18 give the sectional streamlines together with the inplane mean velocity vector map (V,W) in a closeup view near y=z=0 in the x/D=2.4 plane for R=3.3 and 1.3, respectively. In both cases, one can observe a weak vortex which has a sense of rotation opposite to that of the CVP. This weak vortex is believed to be one leg of the horseshoe vortex which originates upstream of the jet exit. For positive y, the leg of the CVP has counterclockwise rotation whereas the leg of the horseshoe vortex has clockwise rotation. Both vortices induce a negative spanwise velocity towards the centerplane y=0 where there is a saddle point of singularity around z/D=0.4 and 0.3 for R=3.3 and 1.3, respectively. This indicates that the horseshoe vortex is slightly larger for the larger velocity ratio of 3.3.

4.1.2 Jet trajectory

There exist several methods in the literature for defining the jet trajectory on the centerplane. The jet trajectory can be defined as the locus of points for which a) the magnitude of the velocity vector (speed) or b) the scalar concentration or c) the scalar temperature is a maximum. These trajectories are called speed maximum, concentration maximum and temperature maximum, respectively. For nonbouyant(unheated, isothermal) flow of a single species, the speed maximum is the relavant definition. Yuan (1997) introduces a new method for defining the jet trajectory which is called streamline trajectory:

It can be reasonably assumed that the jet trajectory coincides with the mean streamline originating from the center of the jet at the level of the flat plate.

Figs. 4.1.19 and 4.1.20 present the streamline and maximum speed trajectories for velocity ratios of R=3.3 and 1.3, respectively. The streamline and maximum speed trajectories calculated by Yuan for R=3.3 is also shown in Fig.4.1.19. The discrepancy between the trajectories is probably due to differences in the state of the incoming flat plate boundary layer which is laminar in the computation and turbulent in the experiment. Close to the jet exit, the speed distribution have multiple local maximal and hence the trajectory becomes difficult to define. Yuan and Street(1981) report that the speed maximum trajectory rises slightly above the streamline trajectory sufficiently away from the jet axis. They explain this by the acceleration of the crossflow over the jet and conclude that for the purpose of marking the actual position of the jet, the streamline trajectory is superior to other trajectories.

It must be noted that there is a basic difference between the flows of the present study at R=3.3 and 1.3. For R=3.3, the jet penetrates through the incoming boundary layer into the inviscid flow region. On the other hand, for R=1.3 the jet remains embedded in the incoming boundary layer. Fig. 4.1.20 shows that the streamline trajectory is significantly closer to to plate than the maximum speed trajectory which essentially marks the edge of the boundary layer. It is believed that the streamline trajectory is the best indicator of the actual jet position in this case too.

For the trajectory of a nonbouyant jet Yuan (1997) presents the following theoretical expression which is based on some self-similarity concepts.

$$\frac{z}{RD} = A(\frac{x}{RD})^b \tag{4.1}$$

where A is a constant and b is 1/3. Pratte and Bains (1967) report that A=2.05 and b=0.28 are suitable parameters for 5<R<35. Margason (1993) provides a comprehensive review of previous studies on jet trajectories and proposes the following correlation

$$\frac{x}{D} = F(\frac{1}{R})^n(\frac{z}{D})^m \tag{4.2}$$

where F,n and m are empirical constants. Table 5 presents the values of F, n and m (taken from Margason(1993)) which fit the data of the indicated studies.

Figs. 4.1.21 and 4.1.22 present the streamline trajectories for velocity ratios of R=3.3 and 1.3, respectively, together with the trajectories defined by Eq.4.2. There exist significant discrepancies between the jet trajectories. Use of different criteria in defining the trajectory may be responsible for some of the observed discrepancies. However, it is more likely that the discrepancies are due to the effect of some parameters (other than R) governing the flow. As reported by Foss (1980), the primary governing parameters of the nonbouyant jet in a crossflow are R=W_j/U_∞, Re_c, θ_c/D and θ_j/D where Re_c is the Reynolds number based on U_∞ and D, θ_c and θ_j are momentum thicknesses of the incoming crossflow and jet flow, respectively. In addition to these parameters, the

free-stream turbulence level of the crossflow and tunnel dimensions can also affect the constants in Eq.4.2. R=W_j/U_∞ and Re_c appear in the dimensionless Navier-Stokes equation (Yuan (1997)), whereas θ_c/D and θ_j/D are introduced by the boundary conditions. In addition to these parameters, the states of the incoming crossflow and jet flow (i.e. whether they are laminar or turbulent) must be specified. It appears that in the literature there exist no empirical correlations which incorporate the effect of Re_c, θ_c/D and θ_j/D on the jet trajectory. Correlations given by Eqns.4.1 and 4.2 can be accurate only for large values of Re_c and small values of θ_c/D and θ_j/D.

Study	F	n	m
Wooler (1969)	2.645	2.50	2.50
Storm (1965)	0.195	2.00	3.00
Fearn (1974)	1.07	3.18	2.99
Bratte and Baines (1967)	0.077	2.57	3.57
Kamotani and Geber (1972)	1.21	1.64	1.58
Ivanov (1963)	1.00	2.60	3.00
Schetz and Billig (1961)	1.00	2.00	2.30
Jordinson (1956)	2.30	3.00	3.00

TABLE 5 . Values of the empirical constants F, n and m appearing in Eq.4.2 (taken from Margason)

4.1.3 Vorticity field

Components of the nondimensional vorticity vector are given by

$$\zeta_x^* = \frac{\partial W^*}{\partial y^*} - \frac{\partial V^*}{\partial z^*} \tag{4.3}$$

$$\zeta_y^* = \frac{\partial U^*}{\partial z^*} - \frac{\partial W^*}{\partial x^*} \tag{4.4}$$

$$\zeta_z* = \frac{\partial V^*}{\partial x^*} - \frac{\partial U^*}{\partial y^*} \tag{4.5}$$

where U^*, V^* and W^* are mean velocities normalized by U_∞ and x^*, y^* and z^* are space variables normalized by D. In this section the vorticity components ζ_x^*, ζ_y^* and ζ_z^* will be presented for constant x, y and z planes of the flow.

Figs. 4.1.23 and 4.1.24 show the contour plots of ζ_y^* in the centerplane of the flow (y=0) for R=3.3 and 1.3, respectively. The streamline jet trajectory and the ζ_x^*=0 line are indicated by dashed and dotted lines, respectively. ζ_x^*=0 line is almost coincident with the streamline jet trajectory for R=3.3. The ζ_y^*=0 line is displaced slighly to downstream of the jet trajectory for R=1.3.

Figs. 4.1.25 and 4.1.26 give the contour plots of ζ_z^* in the z^*=z/D=0.17 plane for R=3.3 and 1.3, respectively. The jet exit is indicated by a dashed line. Except for a small region around (x^*=0.4, y^*=0.2), ζ_z^* is mostly negative for both velocity ratios. The location of vorticity minimum is near the edge of the jet around (x^*=0, y^*=0.5) for R=3.3 and downstream of the jet around (x^*=0.5, y^*=0.4) for R=1.3.

Figs. 4.1.27 and 4.1.28 present the contour plots of ζ_x^* in the x^*=x/D=2.4 plane for R=3.3 and 1.3, respectively. The z^* location of the jet trajectory and the center of one leg of the CVP (counter rotating vortex pair) in the x^*=2.4 plane are denoted by diamond-cross and circle-cross symbols, respectively. The location of minimum vorticity does not coincide with focus F (the center of CVP).

4.1.4 Skin-friction distribution on the axis of symmetry

Surface shear stress τ_{wc} on the flat plate in the centerplane was determined from velocity measurements close to the surface. The laminar sublayer was sufficiently thick over a large portion of the flow field to allow such measurements. Figs. 4.1.29 and 4.1.30 present the vertical variation of the streamwise velocity U near the flat plate at x^*=x/D locations where τ_{wc} was measured for R=3.3 and 1.3, respectively. z_u is the uncorrected value of the vertical distance from the wall. There were 3 to 9 data points in the linear velocity region where a vertical spacing of 0.1 mm was employed in taking the LDA data. A linear curve fit to the data produced the value of the velocity gradient on the wall $(\partial U/\partial z)_w$ and also the z_u value where velocity is zero (z_o). z_o was assumed to be the real position of the wall and was employed to correct the z_u values by using

$$z = z_u - z_o \tag{4.10}$$

where z is the correct vertical position. The shear stress on the flat plate was determined from

$$\tau_{wc} = \mu(\frac{\partial U}{\partial z})_w \tag{4.11}$$

where μ is the absolute viscosity of air. It may be noted that there exist two components of the surface shear stress in this three-dimensional flow. However, the shear stress component in the y direction vanishes on the plane of symmetry. The skin friction coefficient was calculated from Eq. 3.12. Fig. 4.1.31 gives the variation of the skin friction coefficient C_{fc} on the flat plate along the x axis for R 3.3 and 1.3. Data were not obtained for x/D<-1 for R=1.3. C_{fc} is not defined for -0.5<x/D<0.5. It is interesting to note that in the reverse flow region, the absolute values of C_{fc} are roughly 5 times larger

the values of the incoming boundary layer. The dip in C_{fc} is larger for the larger velocity ratio of 3.3 which indicates a higher scavenging action of the horse-shoe vortex for larger R. For velocity ratio 1.3, downstream values of C_{fc} are larger than the values of the incoming boundary layer. This is probably due to the energizing effect of CVP which is closer to the surface for R=1.3.

4.2 Flow in the y=0 plane

4.2.1 Nearly-complete data sets (Line plots) for R=3.3 and R=1.3

Figs. 4.2.1 to 4.2.10 present line plots of the mean velocity and turbulence data for velocity ratios of 3.3 and 1.3 at x^* locations of -0.67, 0, 0.67, 1.83 and 3.67. The data sets include the normalized velocities U^*=U/U_∞, V^*=V/U_∞, W^*=W/U_∞, the normalized turbulent stresses $uu^*=(U_{rms}/U_\infty)^2$, $vv^*=(V_{rms}/U_\infty)^2$, $ww^*=(W_{rms}/U_\infty)^2$, $uv^*=(uv/U_\infty)^2$ and $uw^*=(uw/U_\infty)^2$. Q^* and k^* are the normalized magnitude of the mean velocity vector (speed) and the normalized turbulent kinetic energy given by

$$Q^* = \sqrt{U^2 + V^2 + W^2}/U_\infty \tag{4.12}$$

$$k^* = (U_{rms}^2 + V_{rms}^2 + W_{rms}^2)/2U_\infty^2 \tag{4.13}$$

The data set can be considered as complete with the exception of vw^* which could not be measured. In Figs. 4.2.1 to 4.2.10, the position of the streamline trajectory is indicated by dashed and dotted lines for R=3.3 and 1.3, respectively.

Fig. 4.2.1 presents the variations of the normalized mean velocities U^*=U/U_∞, V^*=V/U_∞, W^*=W/U_∞ and Q^* with z^* at x^*=x/D=-0.67 for R=3.3 and 1.3. The effect of the jet is felt further upstream with increasing R as indicated with the inflection points in the U^* and Q^* profiles. V^* values are rather small and close to the theoretical value of zero. Values of W^* are also small and have the same trend for both R at this upstream x^* location. The flow is towards the wall at small z^* where larger W^* values are observed for larger R. This indicates a stronger HSV for the larger R flow. W^* increases with increasing z^* up to z^*=4 and 1.5 for R=3.3 and 1.3, respectively and decreases for larger z^* values. Fig. 4.2.2 gives the variations of the normalized turbulent stresses $uu^*=(U_{rms}/U_\infty)^2$, $vv^*=(V_{rms}/U_\infty)^2$, $ww^*=(W_{rms}/U_\infty)^2$, $uv^*=(uv/U_\infty)^2$, $uw^*=(uw/U_\infty)^2$ and the turbulent kinetic energy k^* at x^*=x/D=-0.67 for R=3.3 and 1.3. Larger turbulent streses are measured for the larger velocity ratio. This effect is more pronounced in ww^* and uw^* distributions.

Fig. 4.2.3 presents the variations of the normalized mean velocities U^*, V^*, W^* and Q^* with z^* at x^*=0 for R=3.3 and 1.3. The values of $\partial U^*/\partial z^*$ and $\partial Q^*/\partial z^*$ at the wall are zero for R=3.3 and negative for R=1.3. This indicates that the pipe flow approaching the jet exit is much more significantly decelerated for the smaller R case. The jet induces a severe deceleration of the flat plate boundary layer as indicated by the U^* and Q^* profiles which have dips around z^*=2.5

and 1.0 for R=3.3 and 1.3, respectively. For z^* positions smaller than these dip locations, U^* first increases and then decreases whereas Q^* increases to a maximum as the wall is approached. It is interesting to note that computations of Yuan et al.(1999) for R=3.3 do not reveal a velocity dip around z^*=2.5. It appears that this velocity defect (undershoot) of the U^* and Q^* profiles near the boundary-layer edge is due to the rather large δ_c^*/D ratio of the flow in the present study. Fig. 4.2.4 presents the variations of the normalized turbulent stresses uu^*, vv^*, ww^*, uv^*, uw^* and the turbulent kinetic energy k^* at x^*=0 for R=3.3 and 1.3. The strong anisotropy of the flow is evident from a comparison of the normal stresses whose maximium values are located around z^*=1.8 and 0.8 for R=3.3 and 1.3, respectively. The maximum values of ww^* are roughly twice and thrice larger than the maximum values of uu^* and vv^*, respectively for both R. Similar to the normal stresses, the shear stresses increase significantly with increasing velocity ratio. uw^* levels are an order of magnitude larger than the uv^* levels. uv^* changes sign along the z direction whereas uw^* is generally negative.

Fig. 4.2.5 presents the variations of the normalized mean velocities U^*, V^*, W^* and Q^* with z^* at x^*=0.67 for R=3.3 and 1.3. U^*, W^* and Q^* have multiple maximum values in the z direction. Locations of maximum U^*, W^* and Q^* maximum coincide roughly at this streamwise location. As also reported by Yuan (1997), the maximum speed location is slightly lower than the streamline trajectory. Fig. 4.2.6 shows the variations of the normalized turbulent stresses uu^*, vv^*, ww^*, uv^*, uw^* and the turbulent kinetic energy k^* at x^*=0.67 for R=3.3 and 1.3. The location of maximum uu^* is slightly below the jet trajectory whereas the locations of vv^* and ww^* are very close to the jet trajectory.

Fig. 4.2.7 shows the variations of the normalized mean velocities U^*, V^*, W^* and Q^* with z^* at x^*=1.83 for R=3.3 and 1.3. U^* changes sign three times in the z^* direction. This indicates that the reverse flow regions is divided by a positive streamwise velocity region. The maximal values of U^*, W^* and Q^* are near the jet trajectory for R=3.3 but above the jet trajectory for R=1.3. Fig. 4.2.8 presents the variations of the normalized turbulent stresses uu^*, vv^*, ww^*, uv^*, uw^* and the normalized turbulent kinetic energy k^* at x^*=1.83 for R=3.3 and 1.3. The extreme values of the Reynolds stresses are generally observed slightly below the jet trajectory.

Fig. 4.2.9 gives the variations of the normalized mean velocities U^*, V^*, W^* and Q^* with z^* at x^*=3.67 for R=3.3 and 1.3. The overshoot in U^* and Q^* (values larger than one) disappears for R=1.3 but still exists for R=3.3. Fig. 4.2.10 shows the variations of the normalized turbulent stresses uu^*, vv^*, ww^*, uv^*, uw^* and the normalized turbulent kinetic energy k^* at x^*=3.67 for R=3.3 and 1.3. The number of times uw^* changes sign is 4 and 2 for R=3.3 and 1.3, respectively. Above the jet trajectory, uw^* is positive and negative for R=3.3 and 1.3, respectively.

4.2.2 Downstream development of flow in the y=0 plane for R=3.3 and 1.3

Fig. 4.2.11 and 4.2.12 present the variations of the normalized streamwise mean velocity U^* with z^* at various x^* locations in the y^*=0 plane for R=3.3 and 1.3, respectively. For R=3.3, the overshoot in U^* first appears at x^*=0.5 and persists as far downstream as x^*=5. The division of the separated flow region by a positive U region is visible between 0.83< x^* <3.0. The division of the separated flow region by a positive U region can be observed for x^*=1.17 and 1.50 at R=1.3. Except for a very weak overshoot region between 0.83< x^* <1.5, U^* remains smaller than one for R=1.3.

Fig. 4.2.13 and 4.2.14 show the variation of the normalized vertical mean velocity W^* with z^* at various x^* locations in the y^*=0 plane for R=3.3 and 1.3, respectively. Negative W^* region upstream of the jet is much larger in size for R=3.3 than for R=1.3. This indicates existence of a stronger horseshoe vortex for the larger velocity ratio case. For R=1.3, the value of the derivative $\partial W^*/\partial z^*$ at z^*=0 is very small for x^*=0.17, but in contrast to the R=3.3 case, it is quite large for x^*=-0.17. For R=3.3, a certain trend in W^* is observed: The vertical velocity increases and decreases twice in the z^* direction so that the profile appears as an rotated ω. For R=1.3, this rotated ω profile can be observed only in a limited region between 1.17< x^* <2.17.

Fig. 4.2.15 and 4.2.16 give the variation of the normalized total mean velocity (speed) Q^* with z^* at various x^* locations in the y^*=0 plane for R=3.3 and 1.3, respectively. For R=3.3, Q^* is almost zero around x^*=-0.5 and z^*=0.5. This is consistent with the hypothesized streamline pattern given in Fig.4.1.7 which involves two singular points (a saddle and a focus) around x^*=-0.5. For R=1.3, the overshoot in Q^* disappears for x^* >1.50.

Fig. 4.2.17 and 4.2.18 give the variation of the normalized turbulent stress uu^* with z^* at various x^* locations in the y^*=0 plane for R=3.3 and 1.3, respectively. For both velocity ratios, the maximal value of uu^* first increases up to x^*=0.83 and then decreases with increasing x^*.

Fig. 4.2.19 and 4.2.20 show the variation of the normalized turbulent stress ww^* with z^* at various x^* locations in the y^*=0 plane for R=3.3 and 1.3, respectively. For both velocity ratios, the maximal value of ww^* first increases up to x^*=0.17 and then decreases with increasing x^*.

Fig. 4.2.21 and 4.2.22 present the variation of the normalized turbulent shear stress uw^* with z^* at various x^* locations in the y^*=0 plane for R=3.3 and 1.3, respectively. The variation is rather complex and a certain trend is observable only for x^* >3: uw^* assumes negative values near the wall and with increasing $z*$, it changes sign twice to reach negative values near the jet trajectory for R=1.3. In contrast, the number of sign changes is four and uw^* is positive near the jet trajectory for R=3.3.

4.2.3 Contour plots in the y=0 plane for R=3.3 and 1.3

Fig. 4.2.23 and 4.2.24 are contour plots of the normalized streamwise mean velocity U^* in the y^*=0 plane for R=3.3 and 1.3, respectively. The reverse flow region, which is indicated by dashed contour lines, has a thumb-like shape with a wide base and a narrow throat around z^*=0.5 and 0.3 for R=3.3 and 1.3, respectively. This gives rise to the divided reverse flow region mentioned previously. Since the jet trajectory remains buried in the incoming flat plate boundary layer for R=1.3, U^* values are generally smaller than one in Fig.4.2.4.

Fig. 4.2.25 and 4.2.26 give contour plots of the normalized vertical mean velocity W^* in the y^*=0 plane for R=3.3 and 1.3, respectively. At the jet exit, the maximal value of W^* is 4 and 1.65 for R=3.3 and 1.3, respectively. These values agree well with the respective jet bulk velocities of 5 m/s and 2 m/s and the assumption that the maximum pipe velocity is approximately 20 percent larger than the pipe bulk velocity.

Figs. 4.2.27 and 4.2.28 show contour plots of the normalized total mean velocity (speed) Q^* in the y^*=0 plane for R=3.3 and 1.3, respectively. Near the jet exit, contours of W^* and Q^* are almost perpendicular to the wall for R=3.3, whereas they are inclined in the downstream direction for R=1.3.

Figs. 4.2.29 and 4.2.30 present contour plots of the normalized turbulent stress uu^* in the y^*=0 plane for R=3.3 and 1.3, respectively. Maximal uu^* values are significantly larger for the larger R case. Near the jet exit, there exist a jet core with much lower uu^* levels than its surroundings.

Figs. 4.2.31 and 4.2.32 show contour plots of the normalized turbulent stress ww^* in the y^*=0 plane for R=3.3 and 1.3, respectively. For both velocity ratios, the maximal values of uu^* and ww^* are located upstream and downstream of the jet trajectory, respectively.

Figs. 4.2.33 and 4.2.34 give contour plots of the normalized turbulent shear stress uw^* in the y^*=0 plane for R=3.3 and 1.3, respectively. For R=3.3, uw^* is always negative and generally positive upstream and downstream of the jet trajectory, respectively. This may be explained by reasoning that a positive fluctuation in W_i causes deceleration and acceleration of the streamwise velocity U_i upstream and downstream of the jet trajectory, respectively. However, this argument fails to explain the negative uw^* values observed downstream of the jet rajectory for R=1.3 case. It appears that effects of the flat plate wall on turbulence structure is much stronger for the lower R case.

4.3 Flow in the constant z planes

4.3.1 Contour plots in the z/D=0.17 plane for R=3.3 and 1.3

Figs. 4.3.1 and 4.3.2 present contour plots of the normalized mean velocities U^*, V^* and ${Q_z}^*$ in the z^*=0.17 plane for R=3.3 and 1.3, respectively. The jet exit is indicated by a dashed line. Very close to the flat plate, contour plots for R=3.3 and 1.3 are rather similar in appearance and comparable in magnitudes of U^*, ${Q_z}^*$. However, the size of the reverse flow region and extreme values of V^* are larger for R=3.3 than for R=1.3.

Figs. 4.3.3 and 4.3.4 show contour plots of the normalized turbulent stresses uu^*, vv^* and uv^* in the z^*=0.17 plane for R=3.3 and 1.3, respectively. Extreme values of turbulent stresses are larger for R=3.3 than for R=1.3. As the velocity ratio changes from 3.3 to 1.3, the region of maximum turbulent activity moves from (x^*=y^*=0) to (x^*=0.9, y^*=0.3).

4.3.2 Nearly-complete data sets near the jet exit in the z/D=0.17 plane for R=3.3 and 1.3

Figs. 4.3.5 and 4.3.6 present contour plots of the normalized streamwise and spanwise mean velocities U^* and V^* in the z^*=0.17 plane near the jet exit for R=3.3 and 1.3, respectively. U^* is severely reduced by the jet over the jet exit. This deceleration and the size of the reverse flow region is larger for the larger velocity ratio case. There exists a significant acceleration of streamwise flow near the edge of the jet exit around y^*=0.6. The maximal value of U^* is 1.5 and 1.2 for R=3.3 and 1.3, respectively. The maximal value of V^* is 0.5 which is located around x^*=0.3 and y^*=0.4 for both velocity ratios.

Figs. 4.3.7 and 4.3.8 give contour plots of the normalized vertical and total mean velocities W^* and Q^* in the z^*=0.17 plane near the jet exit for R=3.3 and 1.3, respectively. For R=3.3, the W^* and Q^* contours are approximately circular and concentric with the pipe axis over the jet exit with maximal values located at x^*=y^*=0. For R=1.3, the W^* and Q^* contours become elliptical in shape and the maximal value locations move to (x^*=0.2, y^*=0). There exists a negative W^* region near the outer and upstream edge of the jet exit.

Figs. 4.3.9 and 4.3.10 show contour plots of the normalized turbulent stresses uu^* and vv^* in the z^*=0.17 plane near the jet exit for R=3.3 and 1.3, respectively. Similar to the mean velocity contours, uu^* and vv^* contours are roughly circular over the jet exit for R=3.3. In contrast, this approximate cylindrical symmetry over the jet exit is not observed for R=1.3.

Figs. 4.3.11 and 4.3.12 give contour plots of the normalized turbulent stress ww^* and the normalized turbulent kinetic energy k^* in the z^*=0.17 plane near the jet exit for R=3.3 and 1.3, respectively. A series of ww^* maximals are located near the edge of the jet exit for R=3.3. In contrast, the maximal of turbulent kinetic energy k^* is observed outside of the jet exit.

Figs. 4.3.13 and 4.3.14 show contour plots of the normalized turbulent shear stresses uv^* and uw^* in the z^*=0.17 plane near the jet exit for R=3.3 and 1.3, respectively. uv^* is almost always negative. In contrast, uw^* is generally negative for x^* <0 and positive for x^* >0.

4.3.3 Nearly-complete data sets in the z/D=3.00 plane for R=3.3

Fig. 4.3.15 and 4.3.16 present contour plots of the normalized velocities U^*, V^*, W^* and Q^* in the z^*=3.00 plane for R=3.3. Contours of U^*, W^* and Q^* are rather similar with maximal values observed around (x^*=0.75, y^*=0) which coincides with the jet trajectory location. The maximal of V^* is located off the centerplane at the same x^* location of the jet trajectory.

Fig. 4.3.17 and 4.3.18 present contour plots of the normalized turbulent stresses uu^*, vv^*, ww^* and the turbulent kinetic energy k^*in the z^*=3.00 plane for R=3.3. The maximal value of uu^* is located on the centerplane whereas the maximal values of uu^*, vv^* and ww^* are observed off the centerplane.

Fig. 4.3.19 presents contour plots of the normalized turbulent shear stresses uv^* and uw^* in the z^*=3.00 plane for R=3.3. uv^* is generally negative wheras uw^* has a large region with positive values. The maximal value of uw^* is larger than that of uv^*.

4.3.4 Nearly-complete data sets in the z/D=1.3 plane for R=1.3

Fig. 4.3.20 and 4.3.21 present contour plots of the normalized velocities U^*, V^*, W^* and Q^* in the z^*=1.3 plane for R=1.3. Contours of U^*, W^* and Q^* are rather similar with maximal values observed around (x^*=0.65, y^*=0) which coincides with the jet trajectory location. Similar to the flow in the z^*=3.0 plane, the maximal value of V^* is located off the centerplane at the same x^* location of the jet trajectory.

Fig. 4.3.22 and 4.3.23 present contour plots of the normalized turbulent stresses uu^*, vv^*, ww^* and the turbulent kinetic energy k^*in the z^*=1.3 plane for R=1.3. The maximal values of uu^* and ww^* are observed on the plane of symmetry at x^*=1 and 0.6, respectively. On the other hand, the maximal values of ww^* and k^* are located off the centerplane.

Fig. 4.3.24 gives contour plots of the normalized turbulent shear stresses uv^* and uw^* in the z^*=1.3 plane for R=1.3. Both contours involve two negative value regions separated by a positive value region. As in the case of z^*=3.0 plane, the maximal value of uw^* is larger than that of uv^*.

4.4 Flow in the x/D=2.4 plane

4.4.1 Nearly-complete data sets in the x/D=2.4 plane for R=3.3 and 1.3

In Figs.4.4.1 to 4.4.10, the z^* location of the jet trajectory and the center of one leg of the CVP (counter rotating vortex pair) in the x^*=2.4 plane are denoted by diamond-cross and circle-cross symbols, respectively. The center of CVP is defined as the singular focus point where V=W=0. The jet trajectory is located at z^*= 4.47 and 2.12 for R=3.3 and 1.3, respectively. The center of CVP is positioned at (z^*=2.57, y^*=1.45) and (z^*=1.20, y^*=0.59) for R=3.3 and 1.3, respectively.

Figs. 4.4.1 and 4.4.2 give contour plots of the normalized streamwise and spanwise mean velocities U^* and V^* in the x^*=2.40 plane for R=3.3 and R=1.3, respectively. The locations of the jet trajectory and the maximal U are very close for R=3.3. In contrast, U velocity is not maximal at the jet trajectory for R=1.3. The value of U^* at the center of CVP is 1.1 and 0.4 for R=3.3 and 1.3, respectively. In other words, the center of CVP is located in a much higher streamwise momentum region for the higher R case. The maximal value of V^* is observed around the same z^* location as that of the jet trajectory for both velocity ratios.

Fig. 4.4.3 and 4.4.4 present contour plots of the normalized vertical and total mean velocities W^* and Q^* in the x^*=2.40 plane for R=3.3 and R=1.3, respectively. W^* has two maximals along the z^* direction on the plane of symmetry (y^*=0). Location of the jet trajectory is close to the outer maximal which is smaller than the inner one. The inner maximal of W^* is located around the same z^* value as that of the jet trajectory for both R.

Figs. 4.4.5 and 4.4.6 give contour plots of the normalized turbulent stresses uu^* and vv^* in the z^*=3.00 plane near the jet exit for R=3.3 and R=1.3, respectively. For both velocity ratios, the maximal values of uu^* and vv^* are located at z^* values larger and smaller than that of the CVP center, respectively. uu^* maximals are larger than vv^* maximals. z^* locations of the maximals are smaller that that of the jet trajectories.

Figs. 4.4.7 and 4.4.8 show contour plots of the normalized turbulent stress ww^* and the normalized turbulent kinetic energy k^* in the x^*=2.40 plane for R=3.3 and R=1.3, respectively. ww^* maximals are smaller that the maximals of uu^* and vv^* for both velocity ratios.

Fig. 4.4.9 and 4.4.10 give contour plots of the normalized turbulent shear stresses uv^* and uw^* in the x^*=2.40 plane for R=3.3 and R=1.3, respectively. The center of CVP is located away from the locations of shear stress maximals. uv^* contours are similar for the two velocity ratios whereas uw^* contours appear quite dissimilar: For R=1.3, the negative uw^* region is so large that it divides the positive uw^* region into two parts.

4.4.2 Contour plots near the flat plate in the x/D=2.4 plane for R=3.3 and 1.3

Figs. 4.4.11 and 4.4.12 give contour plots of the normalized spanwise mean velocity V^* and the vertical velocity W^*, respectively, in the x^*=2.40 plane near the flat plate for R=3.3 and 1.3. Positive V^* and negative W^* regions for small z^* are due to the horseshoe vortex. As stated in the discussion of Figs.4.1.17 and 4.1.18, the horseshoe vortex is slightly larger for the larger velocity ratio of 3.3. Figs.4.1.7 and 4.1.8 indicate that the horseshoe vortex is located below z^*=0.4 and 0.3 for R=3.3 and 1.3, respectively.

Figs. 4.4.13, 4.4.14 and 4.4.15 present contour plots of the normalized turbulent stresses vv^*, ww^* and vw^*, respectively, in the x^*=2.40 plane near the flat plate for R=3.3 and 1.3. It is readily observed that turbulent stresses are reduced by the dampening action of the wall.

Chapter 5

Conclusions

A turbulent jet in a crossflow was studied by making detailed LDA measurements in three mutually perpendicular planes of the flow field near the jet exit. Special consideration was given to establish and document the fully-developed incoming flow conditions on the flat plate and in the pipe. Static pressure measurements verified the existence of fully-developed conditions. Thanks to a thick boundary-layer developing on the flat plate (three jet diameters thick upstream of the jet exit), skin-friction could be determined from velocity measurements close to the wall. An assessment of the measurement uncertainties in measured and derived quantities was made.

This report documents all the raw LDA data taken during the study with minimal amount of discussion. It also serves as a guide to a database. Further analysis and discussion of results will be made in future publications. Some preliminary results of the study can be listed as follows:

a) The mean velocity and turbulent stress distributions in the incoming pipe and boundary-layer flows are in good agreement with existing data for turbulent and fully-developed pipe and flat-plate flows.

b) The skin friction values C_{fc} in the reverse flow region on the center plane are roughly five times larger in absolute value than that of the incoming boundary layer for R=3.3. The extreme value of C_{fc} is slightly lower for the lower velocity ratio of R=1.3.

c) Mean velocity data on the center plane (y=0) reveal a couple of singular points which are in agreement with a hypothesized streamline pattern. Singular points are also observed in the sectional streamline patterns in constant x and z planes.

d) The reverse streamwise flow region on the center plane has a thumb-like shape with a wide base and a narrow throat around z^*=0.5 and 0.3 for R=3.3 and 1.3, respectively.

e) The negative W^* region upstream of the jet on the center plane is much larger in size for R=3.3 than for R=1.3. This indicates existence of a stronger horseshoe vortex upstream of the jet for the larger velocity ratio case.

f) Near the jet exit on center plane, contours of W^* and Q^* are almost perpendicular to the wall for R=3.3, whereas they are inclined in the downstream direction for R=1.3.

g) In the center plane, the jet trajectory coincides with the zero y-vorticity line (ζ_y^*=0) for R=3.3. In contrast, the jet trajectory is located slighly downstream of the ζ_y^*=0 line for R=1.3. ζ_y^* is counter clockwise on the upstream side of the trajectory and generally clockwise on the downstream side. The extreme values of dimensionless vorticity ζ_y^* is -10 and 6 for R=3.3 and 1.3, respectively.

h) In the center plane, the maximal values of the turbulent normal stresses are roughly equal to U_∞^2 and $0.3U_\infty^2$ for R=3.3 and 1.3, respectively. The maximal absolute value of uw is $0.2U_\infty^2$ and $0.1U_\infty^2$ in the center plane for R=3.3 and 1.3, respectively.

i) In the z/D=0.17 plane , the dimensionless z-vorticity (ζ_z^*) is as large as 8.5 and 7 in absolute value for R=3.3 and 1.3, respectively. ζ_z^* values decrease significantly with increasing z.

j) Large values of uv (around $0.2U_\infty^2$ and $0.1U_\infty^2$ for R=3.3 and 1.3, respectively) are measured in the z/D= 0.17 plane. The maximal absolute value of uv in the z/D=3 plane is $0.06U_\infty^2$ for R=3.3.

k) In the z/D=0.17 plane, W^*, Q^*, uu^* and vv^* contours are roughly circular over the jet exit for R=3.3. In contrast, this approximate cylindrical symmetry over the jet exit is not observed for R=1.3.

l) In the x/D=2.4 plane, the center of CVP is located at (z^*=2.57, y^*=1.45) and (z^*=1.20, y^*=0.59) for R=3.3 and 1.3, respectively. The maximal dimensionless x-vorticity (ζ_x^*=-1) is observed at z^* and y^* locations smaller than that of the center of CVP.

m) Mean velocity data in the x/D=2.4 plane give evidence of the horseshoe vortex which is slightly larger for the larger velocity ratio of 3.3.

n) In the x/D=2.4 plane , the locations of the jet trajectory and the maximal U are very close for R=3.3. In contrast, U velocity is not maximal at the jet trajectory for R=1.3.

o) In the x/D=2.4 plane, the maximal value of U_{rms}^2 is $0.4U_\infty^2$ which is roughly 30 percent larger than the maximal values of V_{rms}^2 and W_{rms}^2 for R=3.3. The maximal absolute values of uv and uw in this plane are 0.08 $U_\infty^2$and $0.05U_\infty^2$, respectively for R=3.3. Smaller turbulent stresses are observed for the smaller velocity ratio of 1.3. The center of CVP is located away from the locations of maximal turbulent stresses.

List of symbols

A	Constant (in Eq.4.1)
C_{fB}	Skin friction coefficient predicted by the Blasius relation $C_{fB} = 0.079Re_D^{-0.25}$
C_{fc}	Skin friction coefficient on flat plate $C_{fc} = \tau_{wc}/0.5\rho U_\infty^2$
C_{fj}	Skin friction coefficient in pipe $C_{fj} = \tau_{wj}/0.5\rho W_j^2$
D	Jet and pipe diameter
F	Constant (in Eq.4.2)
H_c	Shape factor for crossflow H_c=δ_c^*/θ_c
H_j	Shape factor for pipe flow H_j=δ_j^*/θ_j
L	Distance from leading edge of flat plate to jet axis
N	Sample size of LDA measurements
Q	Speed Q=$\sqrt{U^2+V^2+W^2}$
Q_c	Volumetric flow rate of cross flow
Q_j	Volumetric flow rate of jet flow
Q_{rms}	Total rms velocity of velocity fluctuations $Q_{rms} = \sqrt{U_{rms}^2 + V_{rms}^2 + W_{rms}^2}$
Q^*	Normalized speed $Q^* = \sqrt{U^2+V^2+W^2}/U_\infty$
R	Velocity ratio R=W_j/U_∞
R_{uv}	Correlation coefficient $R_{uv} = uv/U_{rms}V_{rms}$
Re_j	Reynolds number based on bulk jet velocity W_j and jet diameter D $Re_j = W_jD/\nu$
Re_D	Reynolds number based on bulk jet velocity W_j and jet diameter D $Re_D = Re_j = W_jD/\nu$
$Re_{c\delta^*}$	Reynolds number based on crossflow velocity U_∞ and displacement thickness δ_c^* $Re_{c\delta^*} = U_\infty\delta_c^*/\nu$
$Re_{c\theta^*}$	Reynolds number based on crossflow velocity U_∞ and momentum thickness θ_c^* $Re_{c\delta^*} = U_\infty\theta_c^*/\nu$
Re_{c+}	Reynolds number based on friction velocity u_τ and boundary thickness δ_c $Re_{c+} = U_\tau\delta_c/\nu$
Re_L	Reynolds number based on free stream velocity U_∞ and length L $Re_L = U_\infty L/\nu$
S(x)	Uncertainty in x
U	Mean velocity in the x direction
U_∞	Free stream (crossflow) velocity
U_i	Instantaneous streamwise velocity
U_{rms}	Root-mean-square of streamwise velocity fluctuations
U^*	Normalized streamwise velocity $U^* = U/U_\infty$
U^+	Normalized streamwise velocity in wall coordinates $U^+ = U/u_\tau$
V	Mean velocity in the y direction
V_i	Instantaneous spanwise velocity
V_{rms}	Root-mean-square of spanwise velocity fluctuations
V^*	Normalized spanwise velocity $V^* = V/U_\infty$
W	Mean velocity in the z direction
W_i	Instantaneous vertical velocity

W_j	Bulk velocity of jet
W_o	Mean velocity on pipe centerline
W_{rms}	Root-mean-square of vertical velocity fluctuations
W^+	Normalized velocity in wall coordinates $W^+ = W/w_\tau$
W^*	Normalized vertical velocity $W^* = W/U_\infty$
a	Jet radius (a=D/2)
b	Constant (in Eq.4.1)
k^*	Normalized turbulent kinetic energy $k^* = (U_{rms}^2 + V_{rms}^2 + W_{rms}^2)/2U_\infty^2$
m	Constant (in Eq.4.2)
n	Constant (in Eq.4.2)
p	Pressure
r	Radial distance measured from pipe axis
u_τ	Friction velocity on flat plate $u_\tau = \sqrt{\tau_{wc}/\rho} = U_\infty\sqrt{0.5C_{fc}}$
uu^*	Normalized turbulent stress $uu^*=(U_{rms}/U_\infty)^2$
uv^*	Normalized turbulent stress $uv^*=(uv/U_\infty)^2$
uw^*	Normalized turbulent stress $uw^*=(uw/U_\infty)^2$
vv^*	Normalized turbulent stress $vv^*=(V_{rms}/U_\infty)^2$
vw^*	Normalized turbulent stress $vw^*=(vw/U_\infty)^2$
w_τ	Friction velocity on pipe wall $w_\tau = \sqrt{\tau_{wj}/\rho} = W_j\sqrt{0.5C_{fj}}$
ww^*	Normalized turbulent stress $ww^*=(W_{rms}/U_\infty)^2$
(x,y,z)	Cartesian coordinate system defined in Fig.1.1
y^+	Normalized distance perpendicular to pipe in wall coordinates $y^+ = w_\tau y/\nu$
z_o	Correction to z values
z_u	Uncorrected z values
α	Flow coefficient of venturi tube
δ_c	Boundary layer thickness on flat plate
δ_c^*	Displacement thickness on flat plate
δ_j^*	Displacement thickness on pipe wall
Δ_c	Contour spacing
Δ_R	Rotta thickness $\Delta_R = \delta_c^* U_\infty/u_\tau$
Δt_i	Residence time
μ	Absolute viscosity of air
ν	Kinematic viscosity of air
ϕ	Tilt angle of laser beams
ρ	Density of air
θ_c	Momentum thickness on flat plate
θ_j	Momentum thickness on pipe wall
σ_u	Standart deviation of U_i distribution
σ_v	Standart deviation of V_i distribution
τ_{wc}	Surface shear stress on flat plate $\tau_{wc} = \mu(\partial U/\partial z)_w$
τ_{wj}	Surface shear stress on pipe wall
ζ_x^*	Normalized vorticity in the x direction $\zeta_x^* = \partial W^*/\partial y^* - \partial V^*/\partial z^*$
ζ_y^*	Normalized vorticity in the y direction $\zeta_x^* = \partial U^*/\partial z^* - \partial W^*/\partial x^*$
ζ_z^*	Normalized vorticity in the z direction $\zeta_x^* = \partial V^*/\partial x^* - \partial U^*/\partial y^*$

Bibliography

Alvarez,J., Jones W.P. and Seoud, R., "Predictions of momentum and scalar fields in a jet in crossflow using first and second order turbulence closures," AGARD CP–534, Paper No.24, 1993.

Andresen, E., Larsen, P.S. and Dam-Johansen, K. "Jets in a cross flow: Mixing studies by light sheet visualization," ASME FED, Vol.172, Experimental and Numerical Flow Visualization, pp.293-300, 1993.

Andreopoulos, J, Rodi, W., "An experimental investigation of jets in a crossflow," Journal of Fluid Mechanics, Vol. 138, pp.93-127, 1984.

Andreopoulos, J, "On the structure of jets in a crossflow," Journal of Fluid Mechanics, Vol. 157, pp. 163-197, 1985.

Andreopoulos, J., "Measurements in a jet-pipe flow issuing perpendicular into a cross stream," Journal of Fluids Engineering, Vol. 104, pp. 493-499, 1982

Benedict, L.H. and Gould, R.D., "Towards better uncertainty estimates for turbulence statistics," Experiments in Fluids, Vol. 22, pp.129-136, 1996.

Camussi, R., Guj, G. and Leone, A. "Experimental analysis of jets in crossflow at low and moderate Reynolds number", 8th International Symposium on Flow Visualization, Sorrento, Italy, September 1-4, 1998.

Cenedese, A. and De Angelis , G. "Near field analysis of a jet in cross-flow by means of LIF and PTV", 8th International Symposium on Flow Visualization, Sorrento, Italy, September 1-4, 1998.

Coelho, S.L.V. and Hunt, J.C.R., "The dynamics of the near field of strong jets in crossflows," Journal of Fluid Mechanics, Vol.200, pp.95-120, 1989.

Crabb, D., Durao, D.F.G. and Whitelaw, J.H. , "A Round jet normal to a crossflow," Journal of Fluids Engineering, Vol. 103, pp.142-153, 1981.

Eggels, J.G.M., Unger, F., Weiss, M.H. Westerweel, J. Adrian, R.J., Friedrich, R. and Nieustadt, F.T.M., "Fully developed turbulent pipe flow: A comparison between direct numerical simulation and experiment," Journal of Fluid Mechanics, Vol. 268, pp.175-209, 1994.

Fearn R. and Weston, P., "Vorticity associated with a jet in a cross flow," AIAA Journal, Vol. 12, No.12, pp.1666-1671, 1974.

Findlay, M.J., Salcudean, M. and Gartshore, I.S., "Jets in a crossflow: Effects of geometry and blowing ratio," Journal of Fluids Engineering, Vol.121, pp.373-378, 1999.

Foss, J.F., "Interaction region phenomena for the jet in a cross flow problem," Rep. SFB 80/E/161, University of Karlsruhe, 1980.

Fric,T.F. and Roshko,A., "Vortical structure in the wake of a transverse jet, Journal of Fluid Mechanics, Vol.279, pp.1-47,1994.

Gustaffson, K.M.B., "LDA measurements of jets in crossflow for effusion cooling applications," 10th International Symposium on " Applications of Laser Techniques to Fluid Mechanics," Lisbon, Portuqal, July 10-13, 2000.

Haven, B.A. and Kurosaka, M., "Kidney and anti-kidney vortices in crossflow jets," Journal of Fluid Mechanics, Vol.352, pp.27-64, 1997.

Ince, N.Z. and Leschziner,M.A., "Calculation of single and multiple jets in crossflow with and witout impingement using Reynolds stress transport closure," AGARD CP–534, Paper No.23, 1993.

ISO Standard Handbook 15, Measurement of fluid Flow in Closed Circuits, International Organization for Standardization, Geneve, Switzerland, ISBN 9267-100769, 1983.

Ivanov, Y.V. "Shape of the centerline of an axisymmetric fan type jet in a cross flow," Izv. VUZ Aviotsionnaya Teknika, No.4, April 1963.

Jones, W.P. and McGuirk, J.J. "Computation of a round turbulent jet discharging into a confined cross flow," in Turbulent Shear Flows 2, Edited by Bradbury et al., pp.233-245, Springer, 1980.

Jordinson, R. "Flow in a jet directed normal to the wind," R.M. No.3074, British A.R.C., Oct. 1956.

Kamotani, Y. and Greber, I. "Experiments on a turbulent jet in a cross flow," AIAA Journal, Vol.10, No.11, pp.1425-1429,1972.

Kavsaoglu,M.S. and Schetz, J.A. "Effects of swirl and high turbulence on a jet in crossflow," Journal of Aircraft, Vol.26, No.6, 1989.

Kavsaoglu, M.S., Akmandor, I.S., Ciray, S. and Fujii, K., "Navier-Stokes simulation of two and three dimensional jets in crossflow, Effects of grid and boundary conditions," AGARD CP-534, Paper No.25,1993.

Keffer, J.F. and Baines W.D., "The round turbulent jet in a cross-wind, Journal of Fluid Mechanics, Vol.15, pp.481-496, 1963.

Kelso, R.M., Lim, T.T. and Perry, A.E., "An experimental study of round jets in cross flow, Journal of Fluid Mechanics, Vol.306, pp.111-144, 1996.

Kelso, R.M., Delo, C. and Smits, A.J., "Unsteady wake structures in transverse jets," AGARD CP–534, Paper No.4, 1993.

Kim, S.W. and Benson, T.J., "Fluid flow of a row of jets in crossflow: A numerical study," AIAA Journal, Vol.31, No.5, 1993.

Kim, K.C., Kim, S.K. and Yoon, S.Y., "PIV measurements of the flow and turbulent characteristics of a round jet in crossflow," Third international Workshop on Paricle Image Velocimetry, Santa Barbara, CA, USA, Sep.16-18, 1999.

Kline S.J. and McClintock F.A. , "Describing uncertainties in single sample experiments," Mechanical Engineering, Vol.75, pp.3-8, 1953.

Larsen, P.S., Böhme, L and Andresen, E., "Laser sheet tomography of jet flows," Proceedings of the Seventh International Symposium on Applications of Laser Techniques to Fluid Mechanics, 11-14 July, Lisbon, Portugal, 1994.

Margason, R.J., "Fifty years of jet in cross flow research," AGARD CP 534, pp. 1-1 to 1-33, 1993.

Meyer, K.E., Özcan, O., Larsen, P.S., Gjelstrup, P. and Westergaard, C.H., "Point and planar LIF for velocity-concentration correlations in a jet in cross-flow," 10th International Symposium on " Applications of Laser Techniques to Fluid Mechanics," Lisbon, Portuqal, July 10-13, 2000.

Moussa, Z.M., Trichka, J.W. and Eskinazi, S., "The near field in the mixing of a round jet with a cross-stream," Journal of Fluid Mechanics, Vol. 80,pp.49-80, 1977.

Özcan, O., Meyer, K.E., Larsen, P.S. and Westergaard, C.H., "Simultaneous measurement of velocity and concentration in a jet in channel-crossflow," FEDSM2001-18220, ASME Fluids Engineering Division Summer Meeting, New Orleans, Lousiana, USA, May 29- June 1, 2001.

Patankar, S.V., Basu, D.K. and Alpay, S.A., "Prediction of the three-dimensional velocity field of a deflected turbulent jet," Journal of Fluids Engineering, Vol.99, pp.758-762, 1977.

Patel,V.C. and Head, M.R., "Some observations on skin friction and velocity profiles in fully developed pipe and channel flows," Journal of Fluid Mechanics, Vol. 38, pp.181-201, 1969.

Patrick, M.A., "Experimental investigation of the mixing and penetration of a round turbulent jet injected perpendicularly into a transverse stream," Trans. Instn. Chem. Engns., Vol.45, pp.16-31, 1967.

Pratte, B.D. and Baines W.D., "Profiles of the round turbulent jet in a cross flow," J. Hydronaut. Div. Proc. ASCE, Vol.92, pp.53-64, 1967.

Schetz, J.A. and Billig, F.S., "Penetration of Gaseous Jets injected into a supersonic stream," J. of Spacecraft and Rockets, Vol.11, pp.21-32, 1961.

Schetz, J.A., *Injection and mixing in turbulent flows*, Progress in Astronautics and Aeronautics, Vol.68, AIAA, New York, 1980.

Schmidt, J. J. , "Experimental and numerical investigation of separated flows," Ph.D. Thesis, Technical University of Denmark, 1997.

Sherif, S.A. and Pletcher, R.H., "Measurements of the flow and turbulence characteristics of round jets in crossflow," Journal of Fluids Engineering, Vol.111, pp.165-171, 1989.

Spalart, P.R., "Direct simulation of a turbulent boundary layer up to R_θ=1410," Journal of Fluid Mechanics, Vol.187, pp. 61-98, 1998.

Storms K.R., "Low-Speed wind tunnel investigation of a jet directed normal to the wind," Report 885, Aeronaut. Lab., Univ. Of Washington, Nov. 1965.

Ullum, U., "Imaging techniques for planar velocity and concentration measurements," Ph.D. Thesis, Department of Energy Engineering, Technical University of Denmark, 1999.

Wooler, P.T., "Flow of a circular jet into a cross flow," J. of Aircraft, May-June 1969, pp. 283-284.

Yuan, L.L., "Large eddy simulations of a jet in crossflow," Ph.D. Thesis, Department of Mechanical Engineering, Stanford University, 1997.

Yuan, L.L. and Street, R.L., "Trajectory and entrainment of a round jet in crossflow," Physics of Fluids, Vol.10, No. 9, 1998.

Yuan, L.L, Street, R.L and Ferziger, J.H., "Large-eddy simulations of a round jet in crossflow," Journal of Fluid Mechanics, Vol.379, pp.71-104, 1999.

Appendix A

Data base

MATLAB software was used to make the plots presented in this report. The MATLAB files, data files and postscript files for all figures are accessible from a CD-ROM which may be made available upon request. MATLAB files and postscript files have the same name as the figures in the report. Entry into the database of our study can be explained by the following example:

Fig. 4.2.6 shows the variations of the normalized turbulent stresses uu^*, vv^*, ww^*, uv^*, uw^* and the turbulent kinetic energy k^* at x^*=0.67 for R=3.3 and 1.3. The MATLAB file Fig4d2d6.m is used to generate Fig. 4.2.6 which is given in postscript format by file Fig4d2d6.ps. The MATLAB file shows that the relevant data files are d3c16.dat and sd3x16.dat for R=3.3 and 1.3, respectively. It also indicates that z, U_{rms}, V_{rms}, W_{rms}, uv and uw values are given as the 1st, 3rd, 5th, 7th, 8th and 9th columns of the data files.

Appendix B

Systematic errors due to tilting of laser beams

Fig. B.1.a shows the tilting of the axis of the LDA optics by tilt angle ϕ in the y-z plane in order to make measurements close to the flat plate. Tilting of the laser beams do not affect U_i but introduces a systematic error in W_i. Appendix B discusses these errors and presents algebraic relations for correction of data. However, since the errors are shown to be smaller than the estimated uncertainties, no corrections are applied to the data presented in this report.

Let us rotate the (x,y,z) coordinate system around x axis by tilt angle ϕ as shown in Fig. B.1.b. The two coordinate systems are related to each other by

$$x = x_t \tag{B.1}$$

$$y = cos\phi\ y_t\ -\ sin\phi\ z_t \tag{B.2}$$

$$z = cos\phi\ z_t\ +\ sin\phi\ y_t \tag{B.3}$$

The mean velocities (U_i) and Reynolds stresses ($u_i u_j$) in the (x,y,z) coordinate system are transformed according to

$$U_i = \frac{\partial x_i}{\partial x_{tk}} U_{tk} \tag{B.4}$$

$$u_i u_j = \frac{\partial x_i}{\partial x_{tk}} \frac{\partial x_j}{\partial x_{tl}} u_{tk} u_{tl} \tag{B.5}$$

where (U_{tk}) and ($u_{tk}u_{tl}$) denote the mean velocity and Reynolds stresses (divided by density), respectively, in the (x_t, y_t, z_t) coordinate system. Note that i and j are free indices whereas k and l are dummy(repeated) indeces in the index notation (t is neither a free nor a dummy index). Equations (B.4) and (B.5) give

$$U = U_t \tag{B.6}$$

$$V = cos\phi\ V_t\ -\ sin\phi\ W_t \tag{B.7}$$

$$W = cos\phi\ W_t\ +\ sin\phi\ V_t \tag{B.8}$$

$$U^2_{rms} = U^2_{trms} \tag{B.9}$$

$$V^2_{rms} = V^2_{trms}\ cos^2\phi\ +\ W^2_{trms}\ sin^2\phi\ -\ sin2\phi\ v_t w_t \tag{A.10}$$

$$W_{rms}^2 = W_{trms}^2\, cos^2\phi \;+\; V_{trms}^2\, sin^2\phi \;+\; sin2\phi\; v_t w_t \qquad (A.11)$$

$$uv = u_t v_t\, cos\phi \;-\; u_t w_t\, sin\phi \qquad (A.12)$$

$$uw = u_t w_t\, cos\phi \;+\; u_t v_t\, sin\phi \qquad (A.13)$$

$$vw = 0.5\; sin2\phi\; V_{trms}^2 \;-\; 0.5\; sin2\phi\; W_{trms}^2 \;+\; cos2\phi\; v_t w_t \qquad (A.14)$$

where (U_t, V_t, W_t) are the mean velocity components, and $(U_{trms}^2, V_{trms}^2, W_{trms}^2, u_t v_t, u_t w_t, v_t w_t)$ are the Reynolds stresses in the (x_t, y_t, z_t) coordinate system.

The mean velocity components (U, W_t) and Reynolds stresses $(U_{rms}^2, W_{trms}^2$ and $u_t w_t)$ are measured if LDA Configuration 1 is employed with tilted beams. Therefore, systematic errors appear only in W, W_{rms}^2 and uw, which are given by Eqns. B.8, B.11 and B.13, respectively. The terms $V_t, V_{trms}^2, u_t v_t$ and $v_t w_t$ appearing in those equations are not measured. However, they are related to measured quantities V, V_{rms}^2, uv and vw by Eqns. B.7, B.10, B.12 and B.14. Thus, Eqns. B.8, B.11 and B.13 reduce to

$$W = cos\phi\; W_t \;+\; tan\phi\; (V \;+\; sin\phi\; W_t) \qquad (B.15)$$

$$W_{rms}^2 = W_{trms}^2\, cos^2\phi \;+\; tan^2\phi\; (\; V_{rms}^2 \;-\; W_{trms}^2\, sin^2\phi) \;+$$

$$tan2\phi\; [vw \;+\; 0.5 sin2\phi (W_{trms}^2 \;-\; V_{trms}^2)] \qquad (B.16)$$

$$uw = u_t w_t\, cos\phi \;+\; tan\phi\; (\; uv \;+\; u_t w_t\, sin\phi) \qquad (B.17)$$

Eqns. B.15, B.16 and B.17 can be used to correct W_t, W_{trms}^2 and $u_t w_t$ provided that data obtained by Configurations 2 and 3 are available. Figs.(B.2) and (B.3) show a comparison of the corrected and uncorrected data at two different locations for two velocity ratios. Since vw was not measured, it was neglected in Eq.(B.16). This causes a negligible error in the correction of W_{rms}^2 because vw is smaller than W_{rms}^2 and U_{rms}^2. Figs. (B.2) and (B.3) show that corrections are smaller than the overall measurement uncertainties. Therefore, data are presented without corrections in this report.

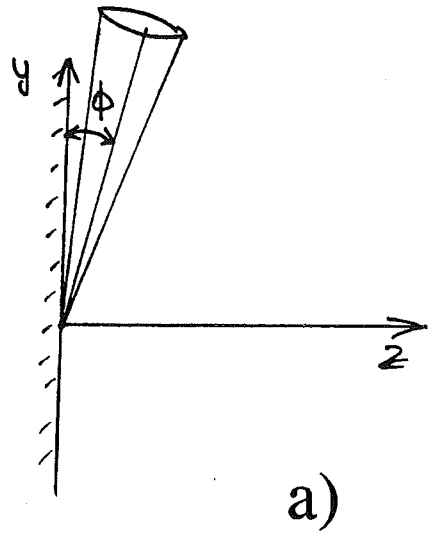

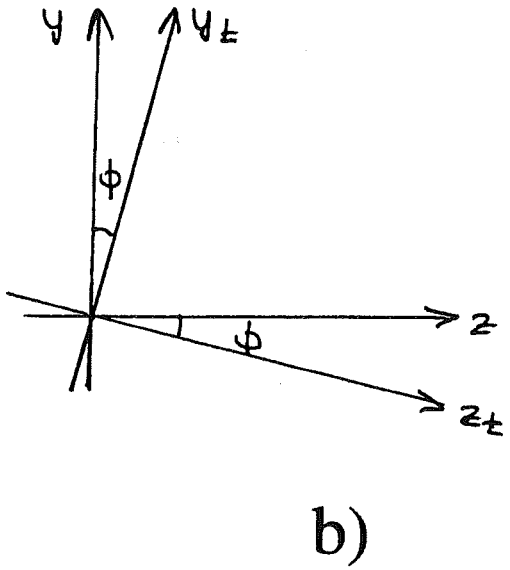

Fig.B.1 A schematic description of the tilte angle ϕ and the (x_t, y_t, z_t) coordinate system

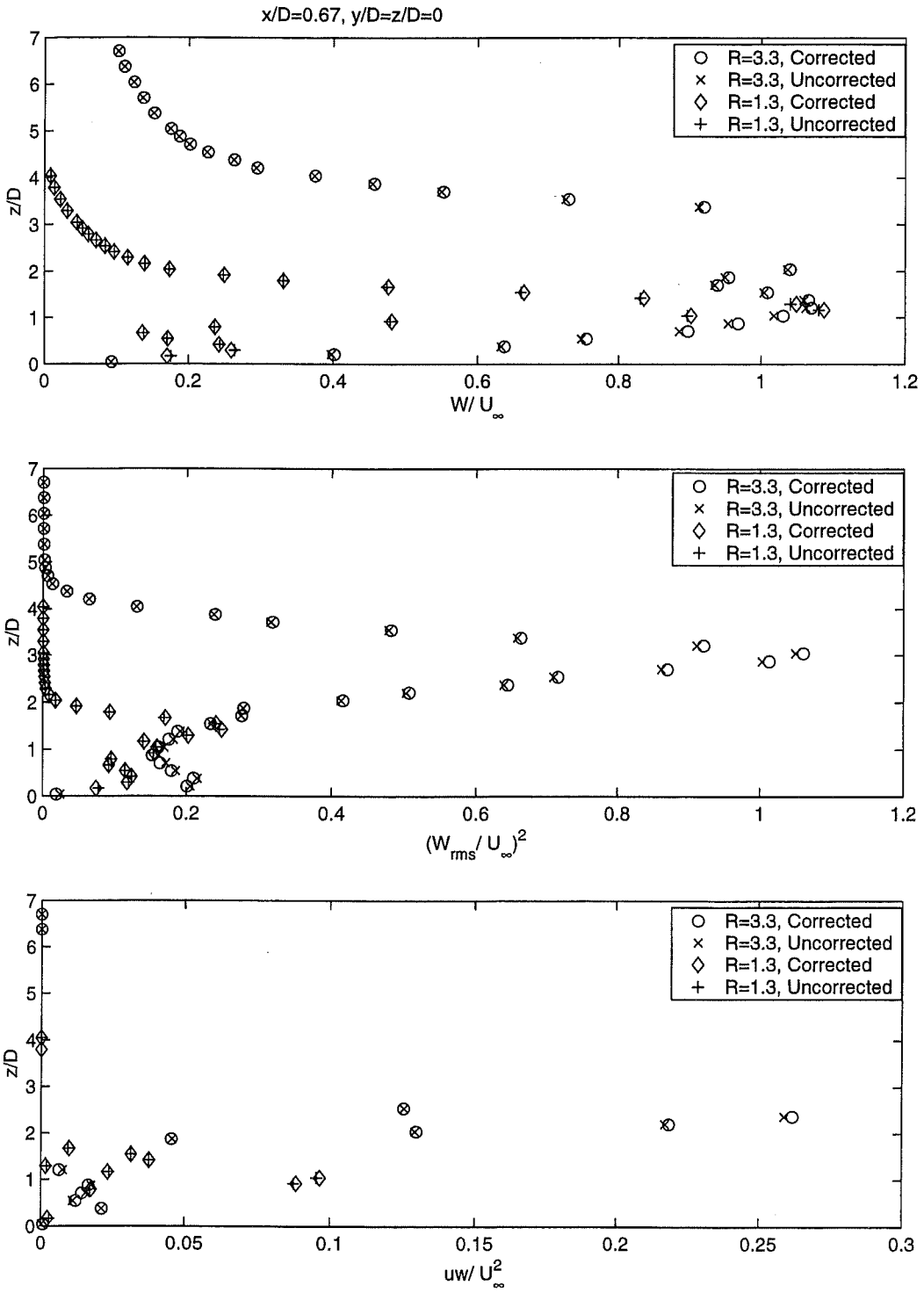

Fig.B.2 A comparison of the corrected and uncorrected data at x/D=0.67, y/D=z/D=0 for R=3.3 and 1.3

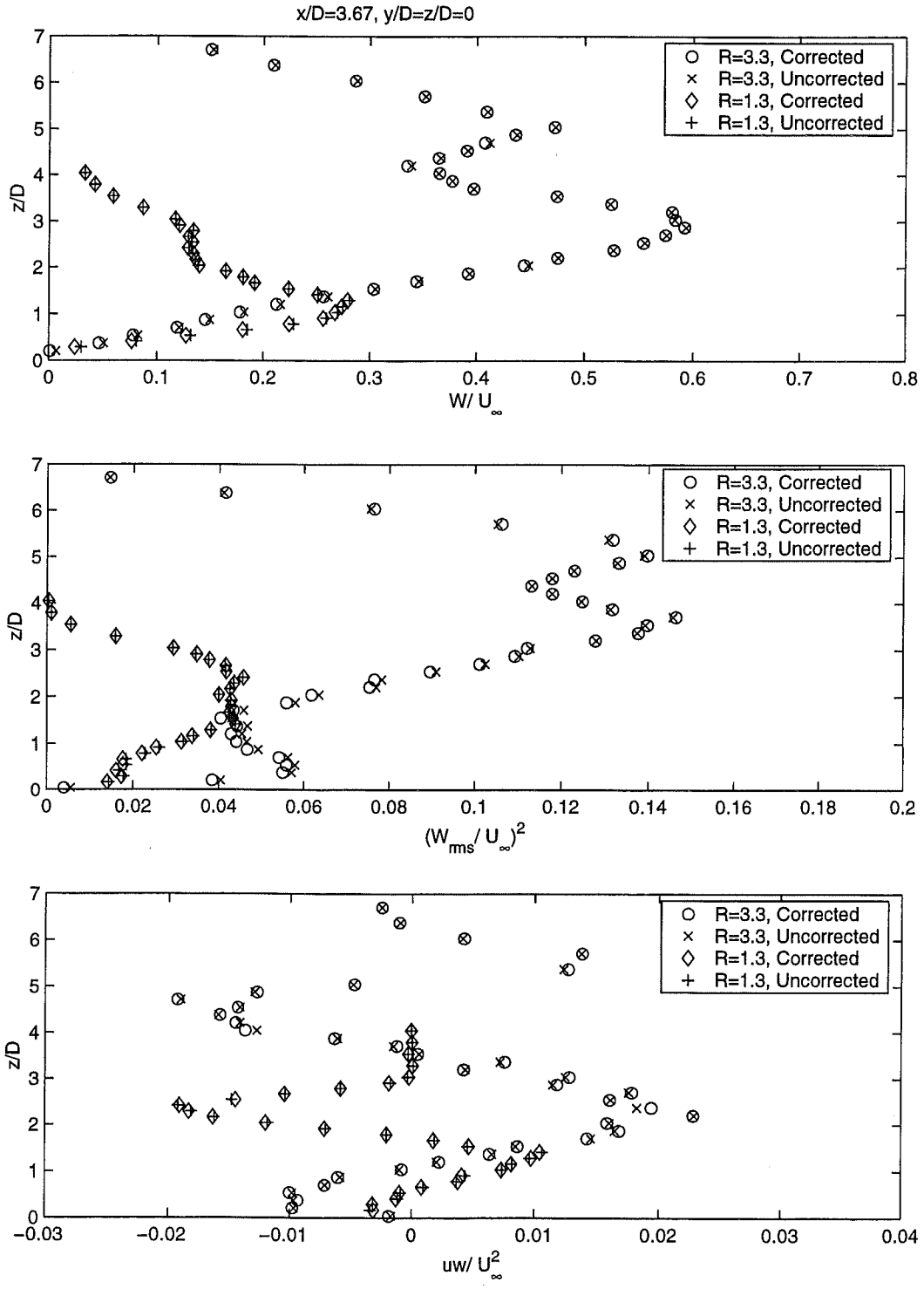

Fig.B.3 A comparison of the corrected and uncorrected data at x/D=3.67, y/D=z/D=0 for R=3.3 and 1.3

Figures

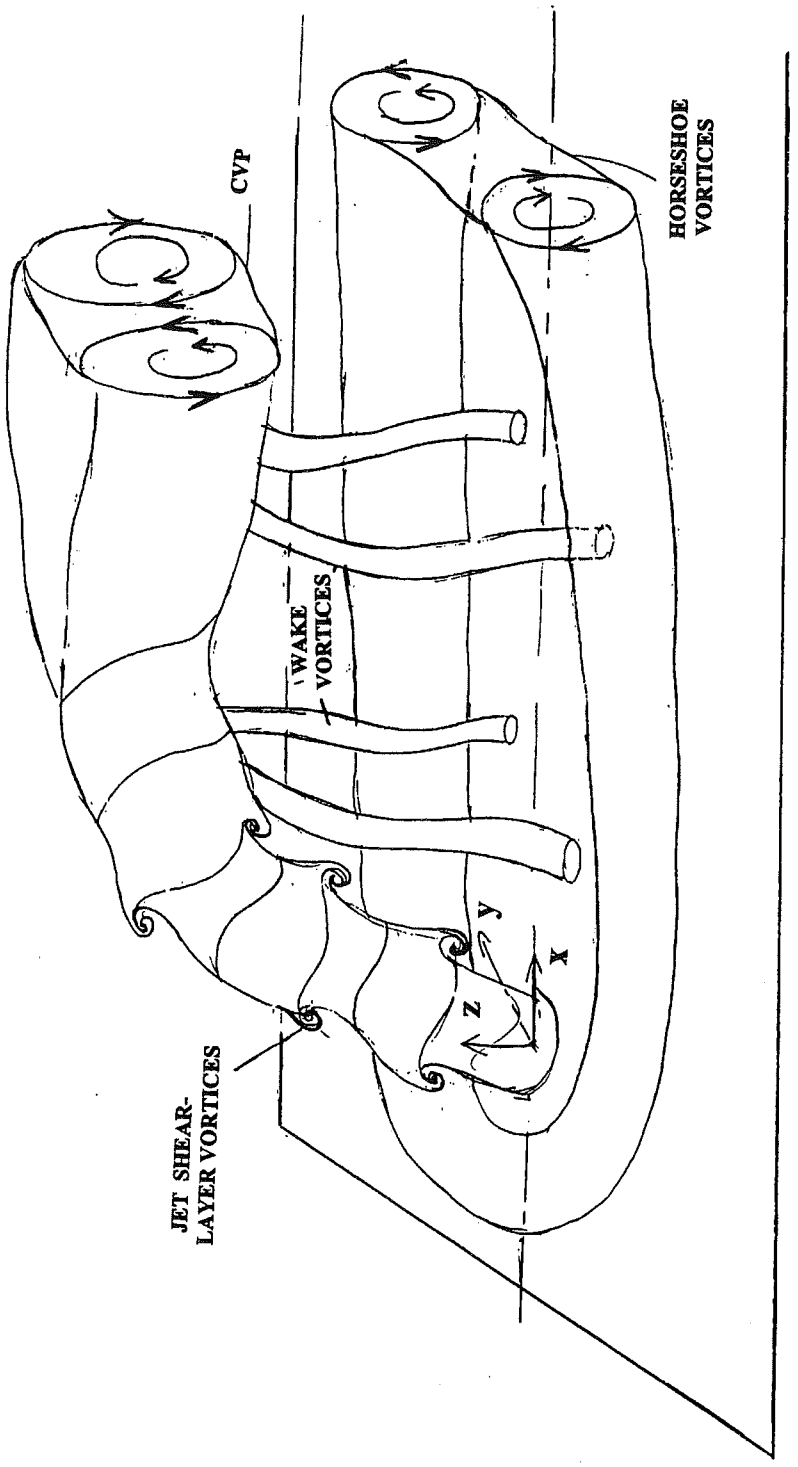

Fig.1.1 A schematic description of the vortical structures near the jet exit

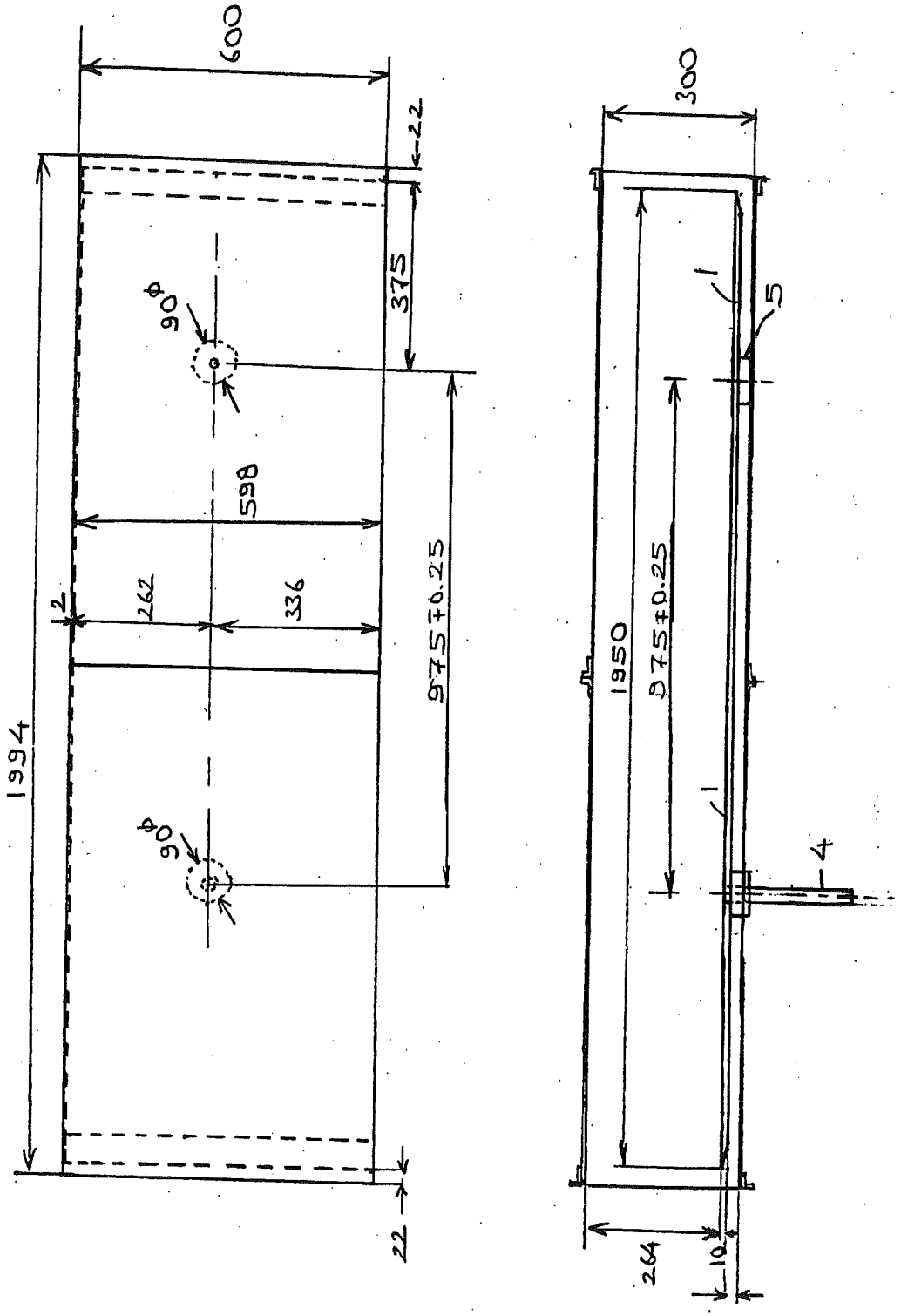

Fig.2.1 A schematic drawing of the flat plate assembly placed in the test section of the wind tunnel

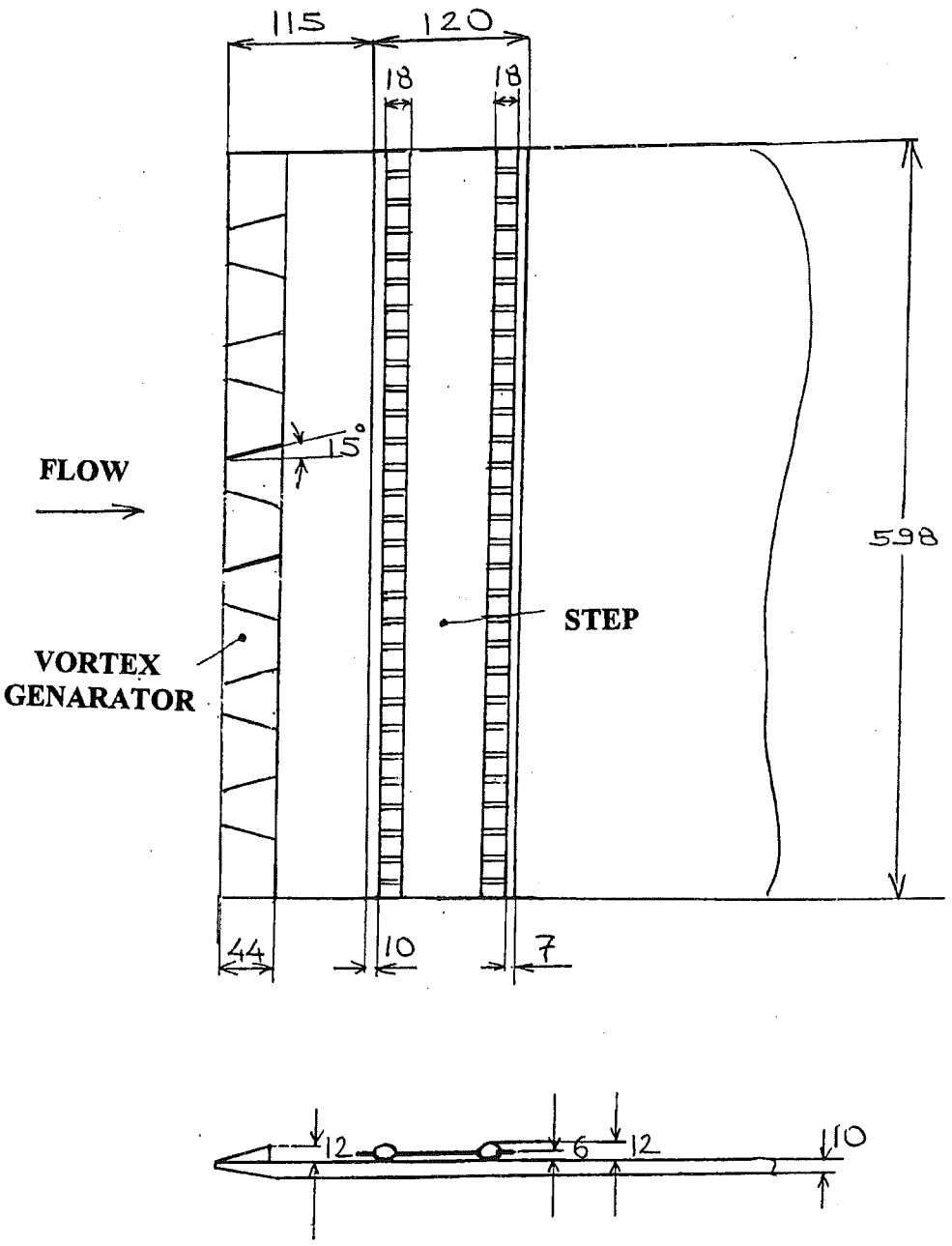

Fig.2.2 A schematic drawing of the vortex generator and step mounted on the flat plate

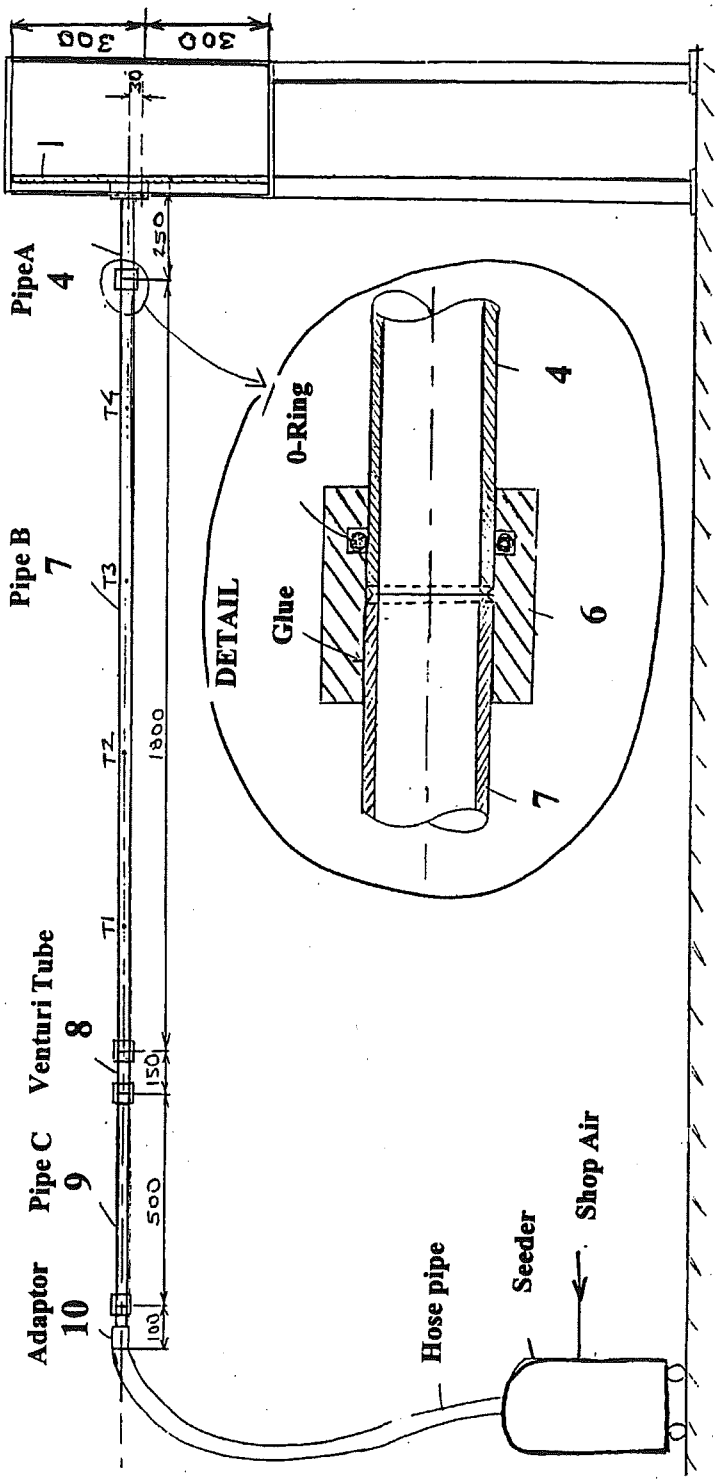

Fig.2.3 A schematic drawing of the pipe flow assembly

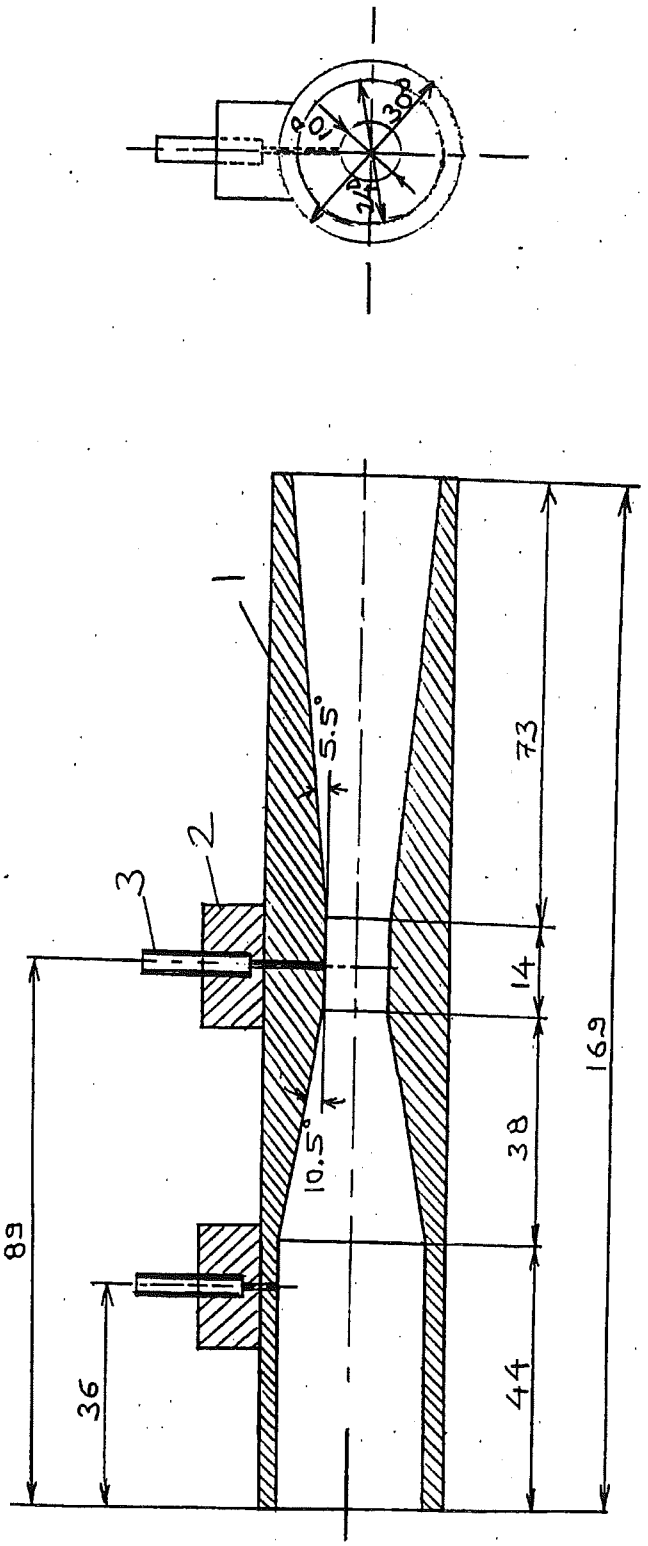

Fig.2.4 A schematic drawing of the venturi tube

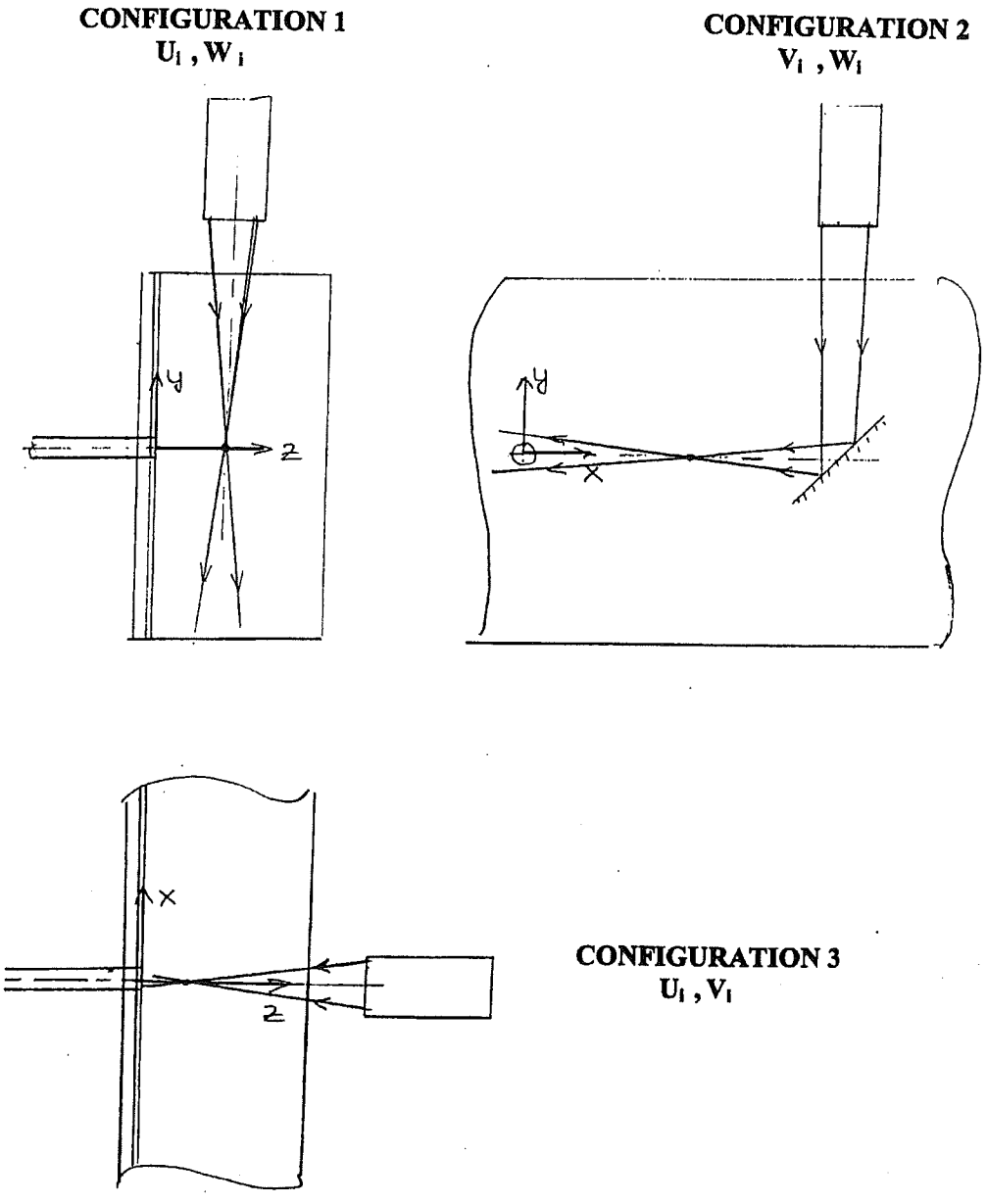

Fig.2.5 A schematic description of the LDA configurations employed in the study

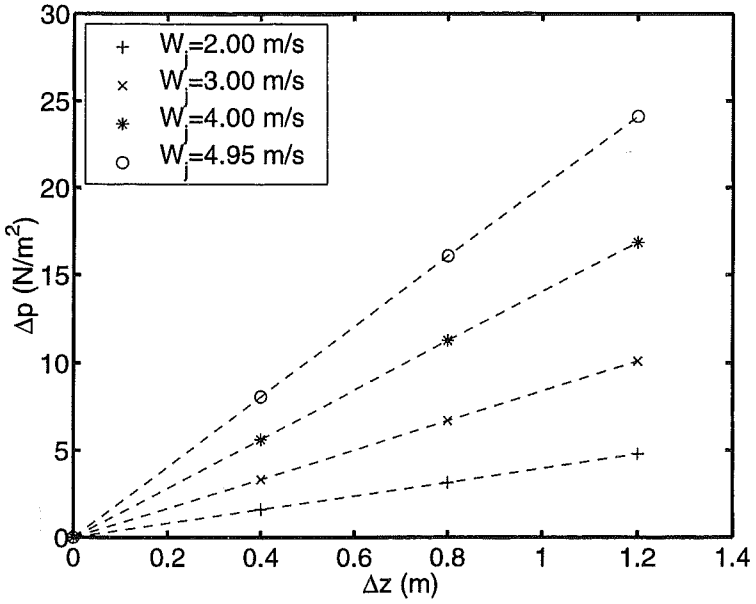

Fig.3.1 Variation of the static pressure drop Δp across the pipe length Δz for the jet bulk velocities of W_j= 2.00, 3.00, 4.00 and 4.95 m/s.

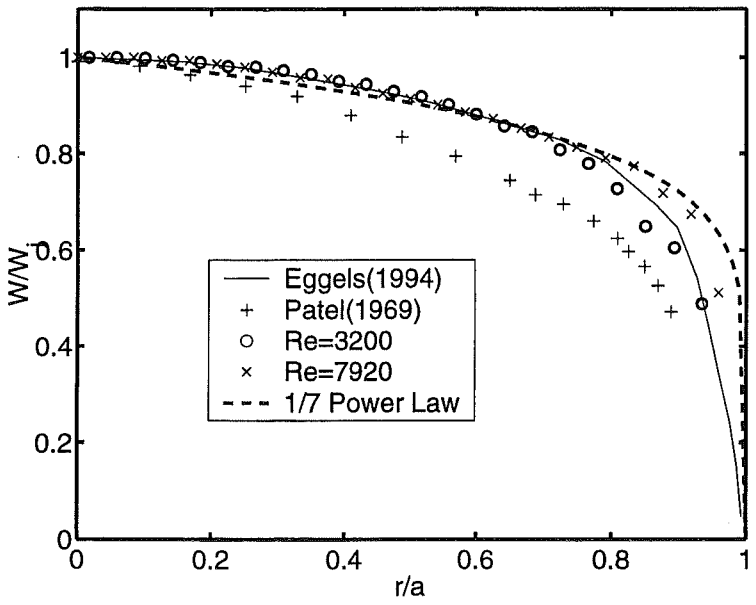

Fig.3.2 Variation of the normalized axial velocity W/W_j with the normalized radial distance r/a in pipe flow at z=-120 mm(z/D=-5).

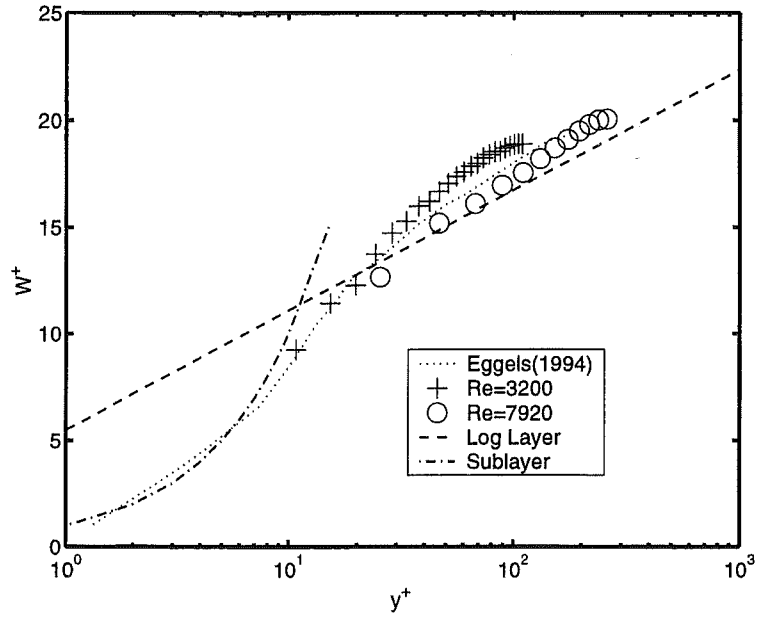

Fig.3.3 Variation of the axial mean velocity in the pipe in wall coordinates ($y^+ = w_\tau y/\nu$, $W^+ = W/w_\tau$) at z/D=-5.

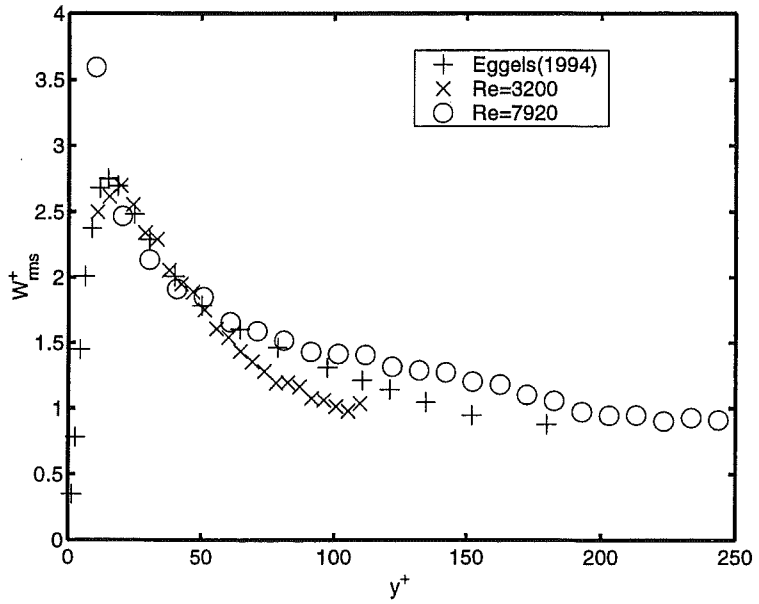

Fig.3.4 Variation of the axial rms velocity in the pipe in wall coordinates ($y^+ = w_\tau y/\nu, W^+_{rms} = W_{rms}/w_\tau$) at z/D=-5.

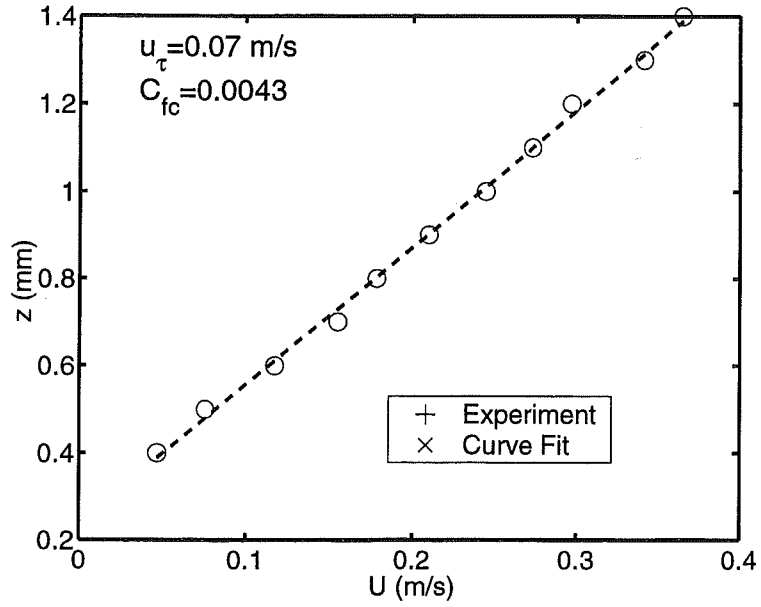

Fig 3.5 Variation of the streamwise velocity profile close to the flat plate at x/D=-3.8

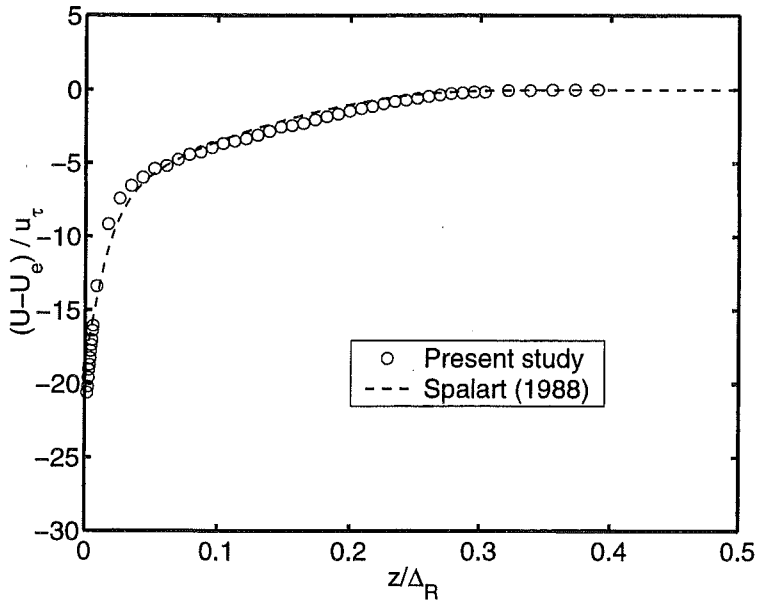

Fig.3.6 Variation of the normalized velocity defect $(U - U_\infty)/u_\tau$ with the normalized distance z/Δ_R at x/D=-3.8

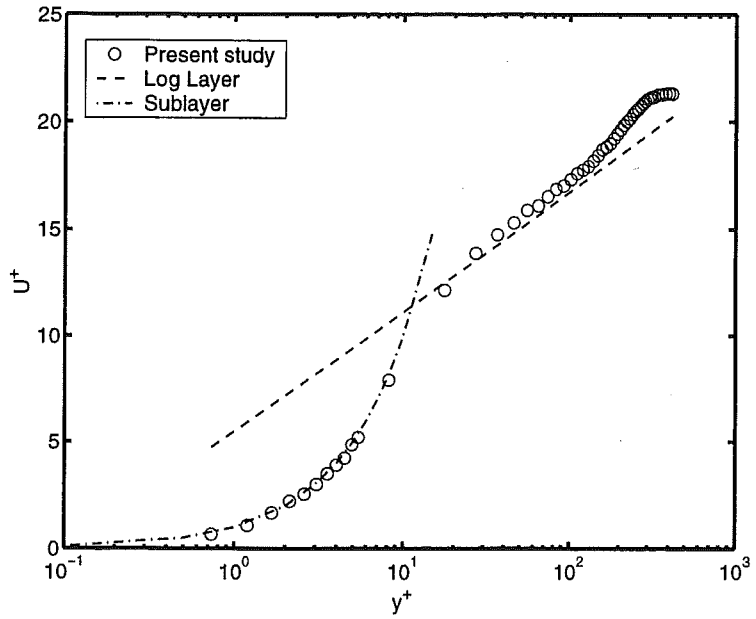

Fig 3.7 Variation of the streamwise velocity profile in wall coordinates U^+ vs z^+ at x/D=-3.8

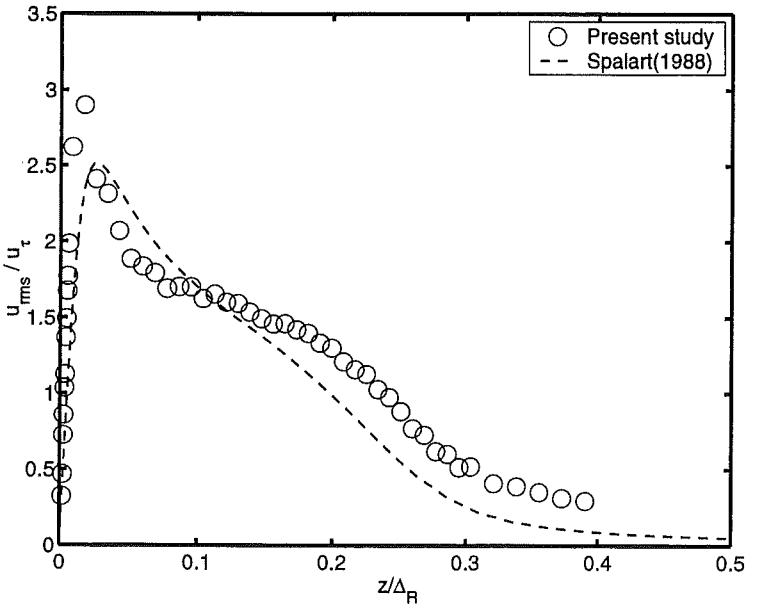

Fig. 3.8 Variation of the normalized turbulent stresses U_{rms}/u_τ with normalized distance z/Δ_R at x/D=-3.8

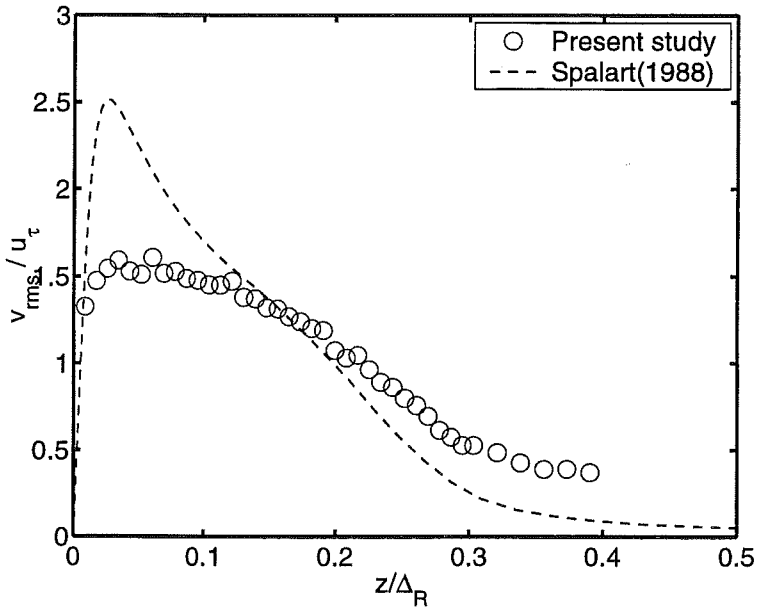

Fig. 3.9 Variation of the normalized turbulent stress V_{rms}/u_τ with normalized distance z/Δ_R at x/D=-3.8

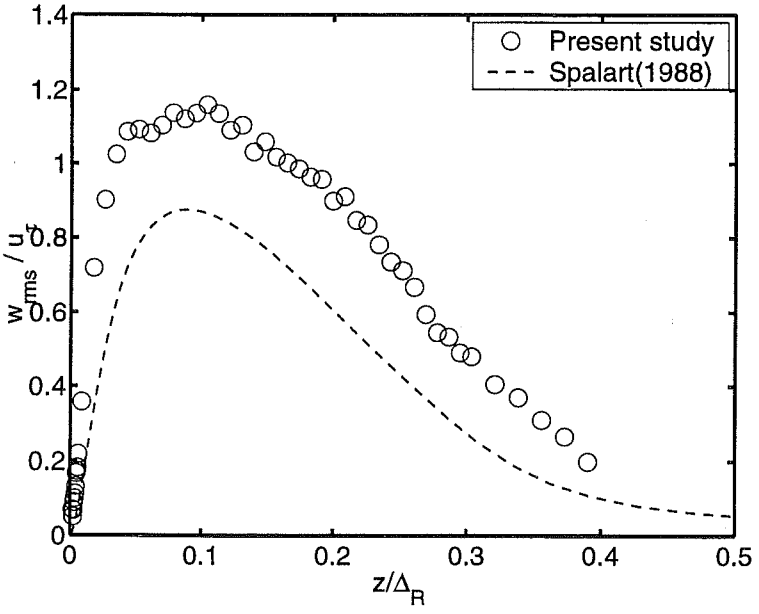

Fig. 3.10 Variation of the normalized turbulent stress W_{rms}/u_τ with normalized distance z/Δ_R at x/D=-3.8

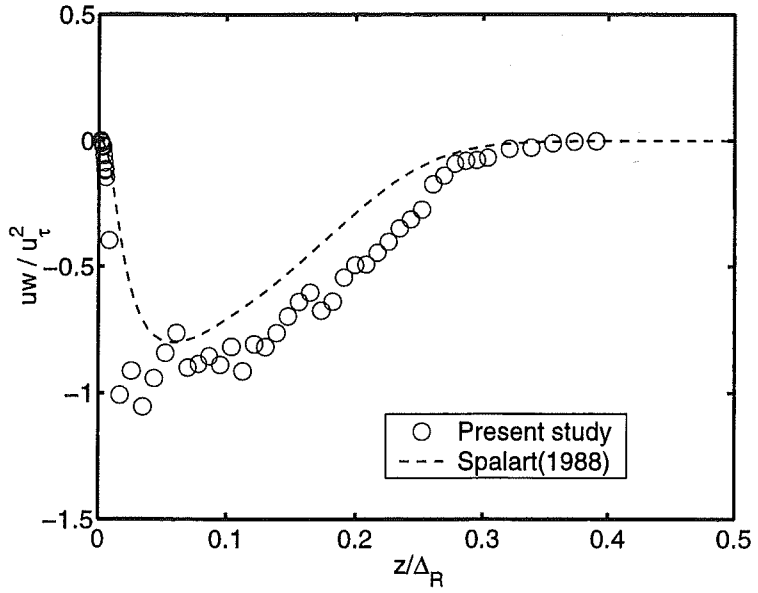

Fig. 3.11 Variation of the normalized turbulent shear stress uw/u_τ with normalized distance z/Δ_R at x/D=-3.8

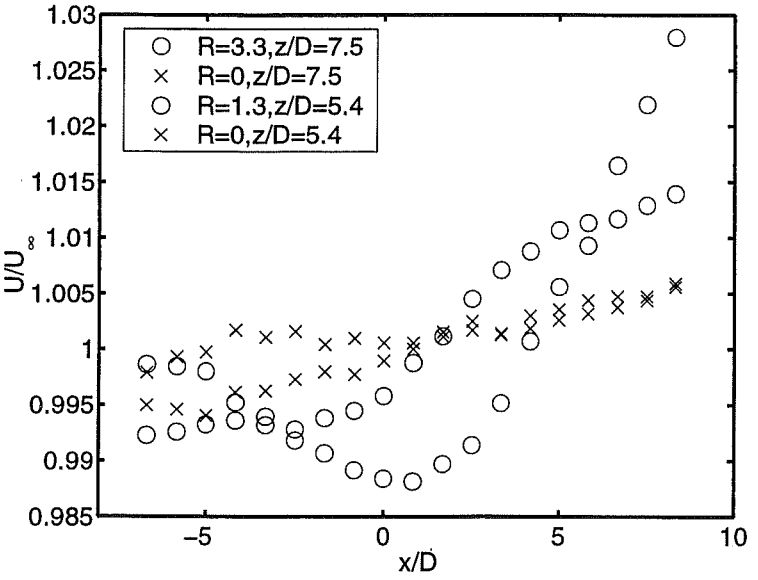

Fig. 3.12 Variations of the streamwise velocity component in the inviscid outer flow at z/D=7.5 and z/D=5.4 for R=3.3 and 1.3

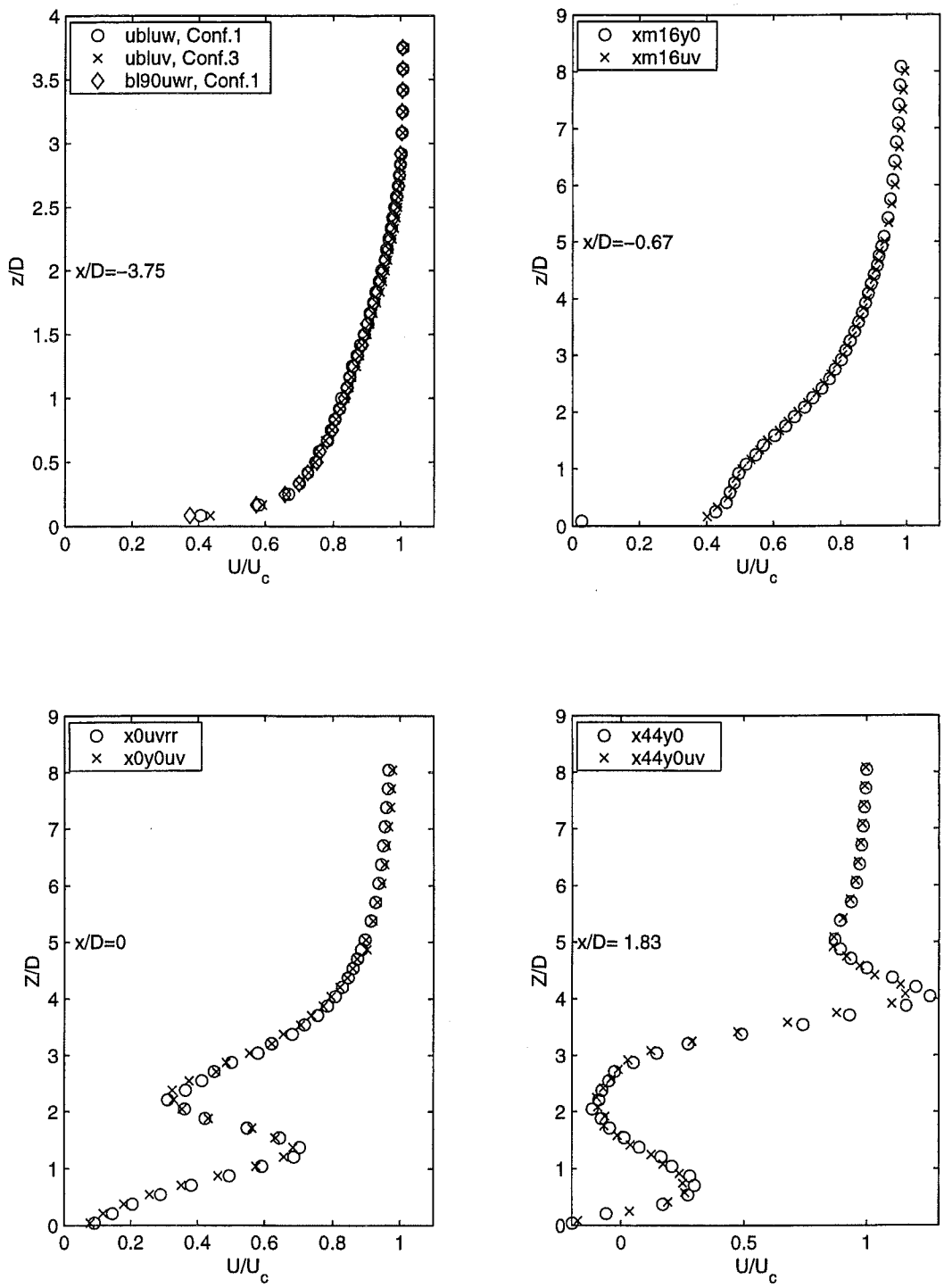

Fig. 3.13 Variations of the normalized streamwise velocity U/U_∞ with z/D in the y=0 plane for x/D=-3.75, -0.66, 0 and 1.83 at R=3.3.

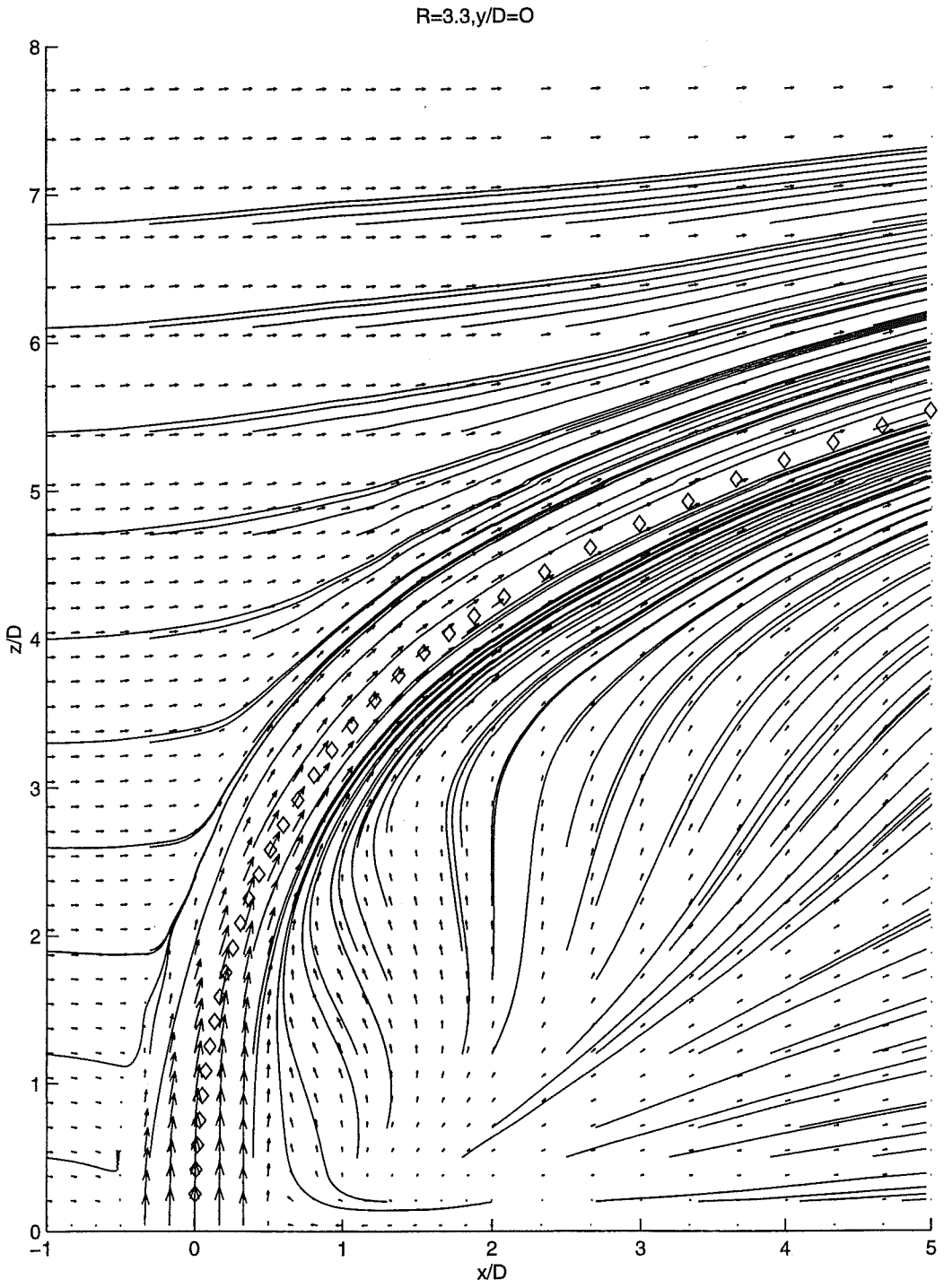

Fig. 4.1.1 Mean velocity (U,W) vector maps and sectional streamlines in the y=0 plane (centerplane, plane of symmetry) of the flow field for R=3.3

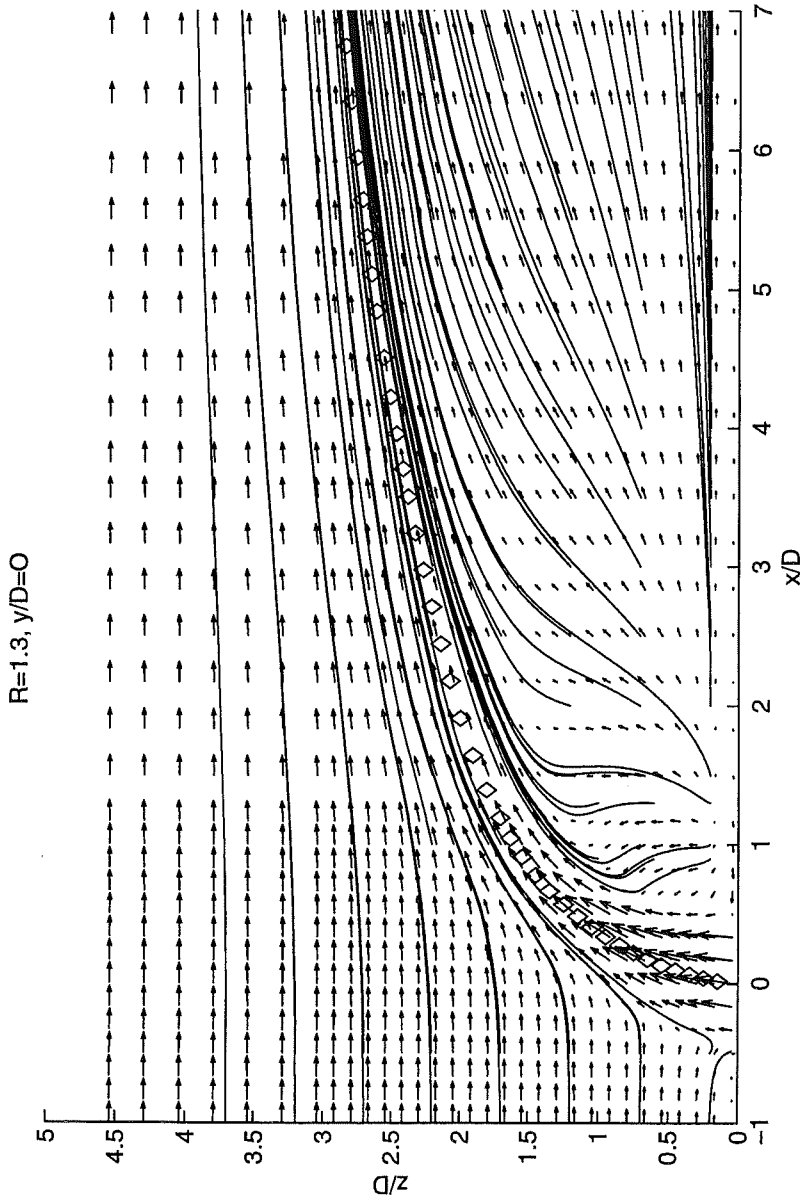

Fig. 4.1.2 Mean velocity (U,W) vector maps and sectional streamlines in the y=0 plane (centerplane, plane of symmetry) of the flow field for R=1.3

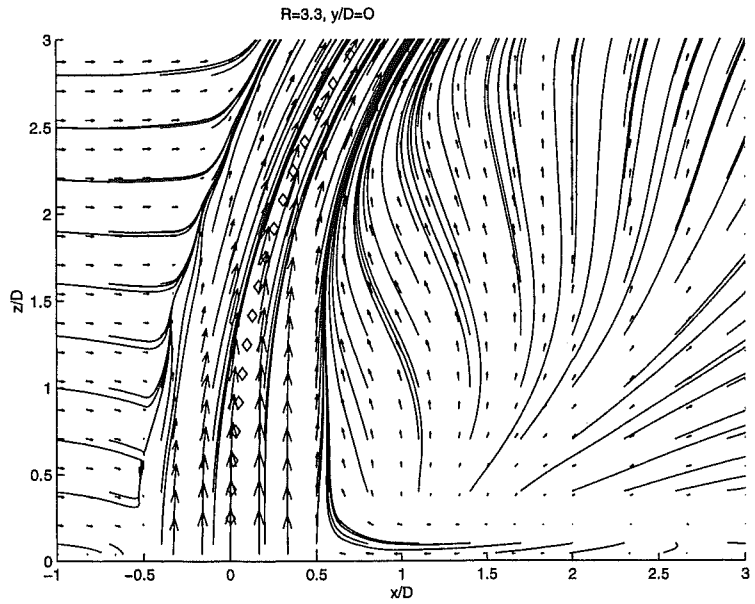

Fig. 4.1.3 Closeup view of the mean velocity (U,W) vector maps and sectional streamlines in the y=0 plane for R=3.3

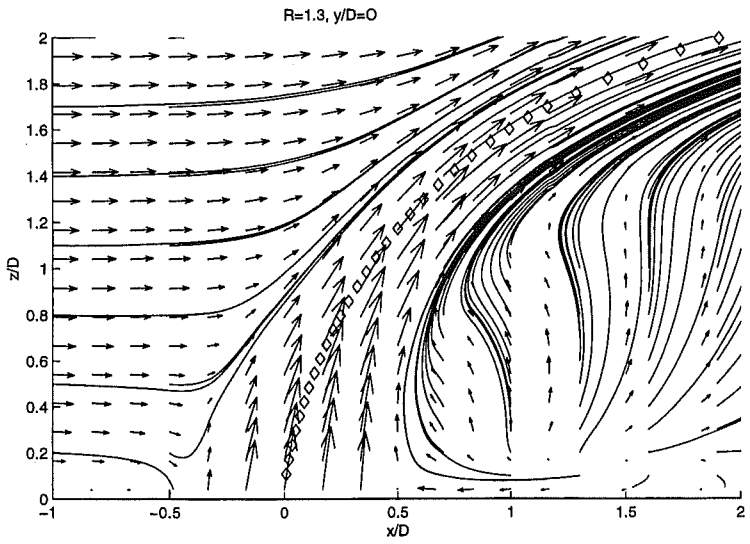

Fig. 4.1.4 Closeup view of the mean velocity (U,W) vector maps and sectional streamlines in the y=0 plane for R=1.3

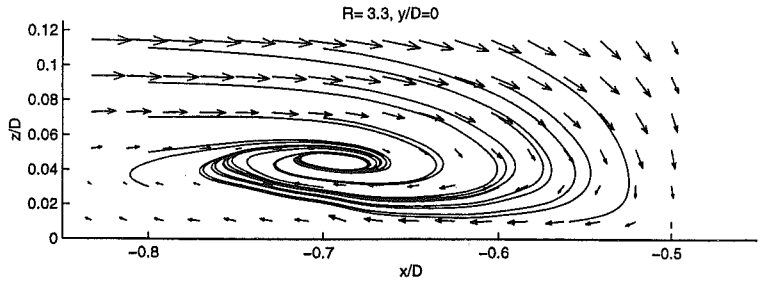

Fig. 4.1.5 Mean velocity (U,W) vector maps and sectional streamlines in the y=0 plane showing the horseshoe vortex for R=3.3.

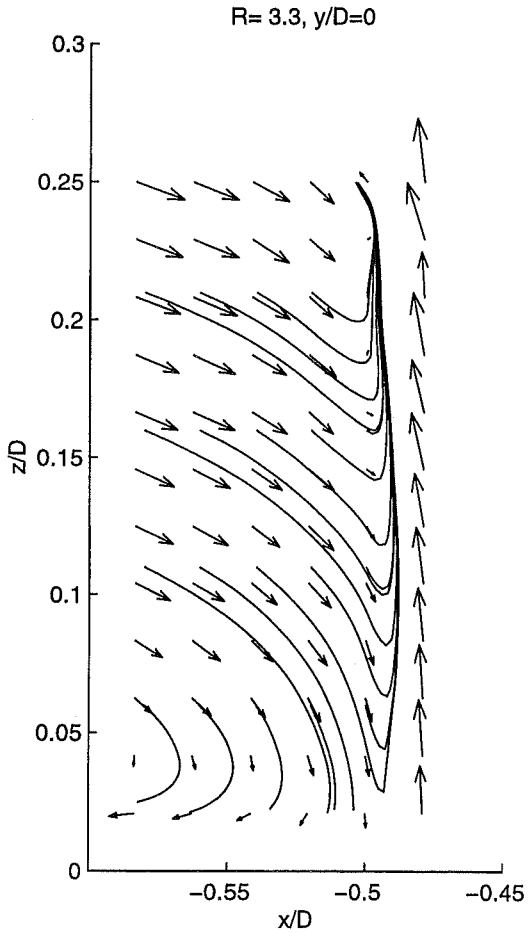

Fig.4.1.6 Mean velocity (U,W) vector maps and sectional streamlines in the y=0 plane around (x^*=-0.5, z^*=0.23) for R=3.3

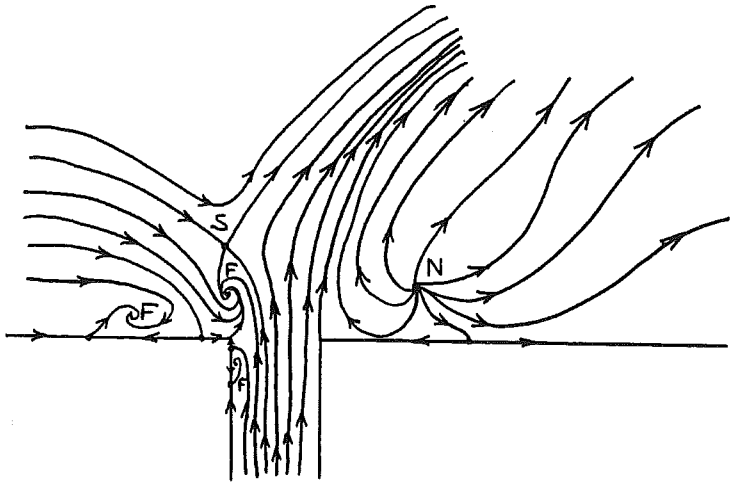

Fig.4.1.7 Hypothesized mean streamline pattern in the y=0 plane for R=3.3

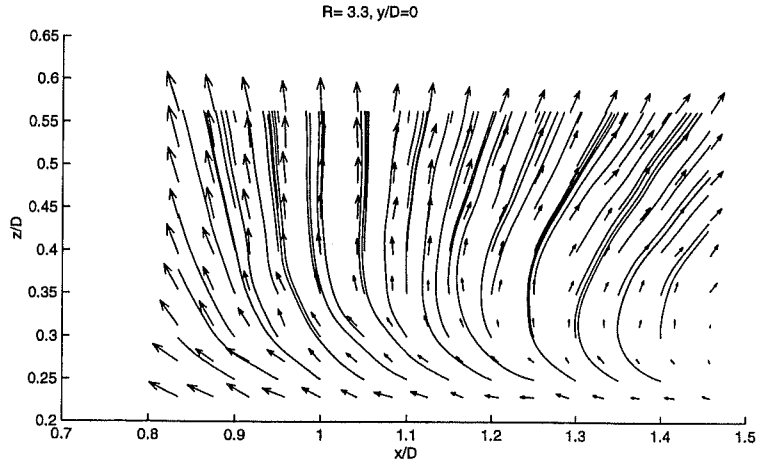

Fig.4.1.8 Mean streamline pattern in the y=0 plane downstream of the jet exit for R=3.3

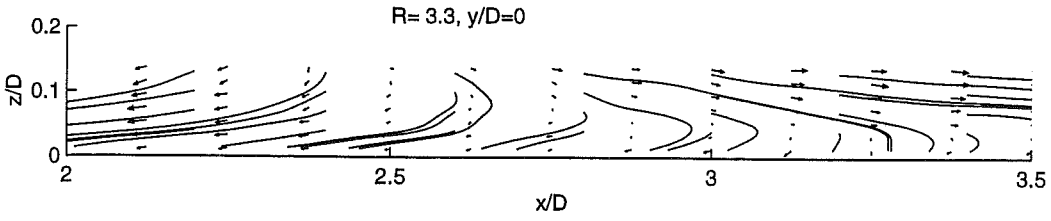

Fig. 4.1.9 Sectional streamlines together with the inplane (U,V) mean velocity vectors in the z/D=0.17 plane for R=3.3

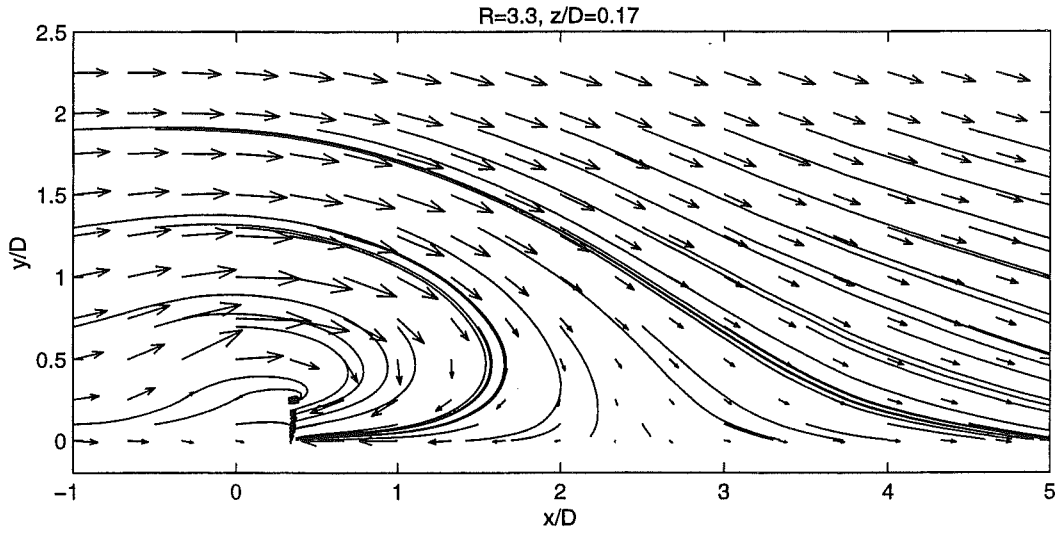

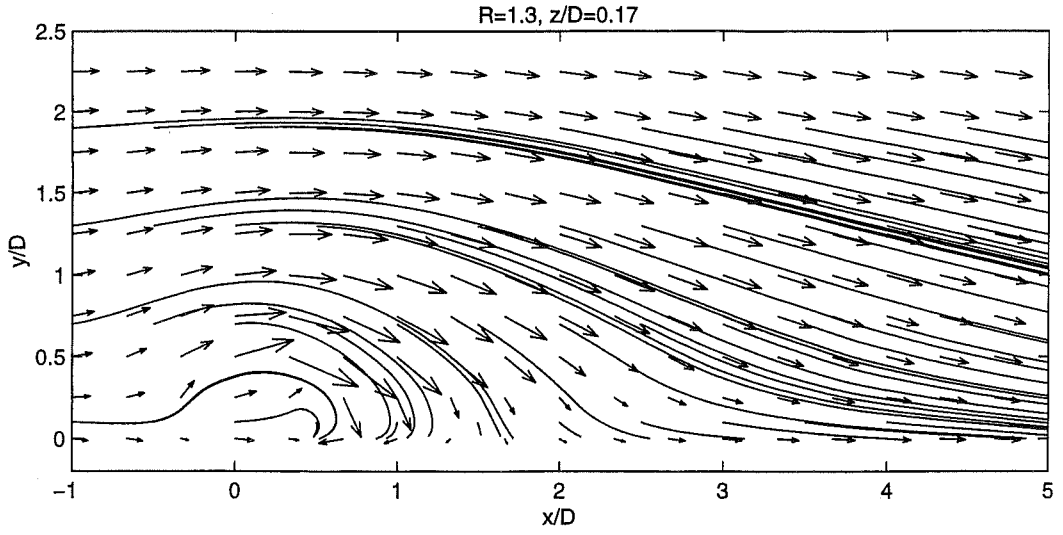

Fig. 4.1.10 Sectional streamlines together with the inplane (U,V) mean velocity vectors in the z/D=0.17 plane for R=1.3

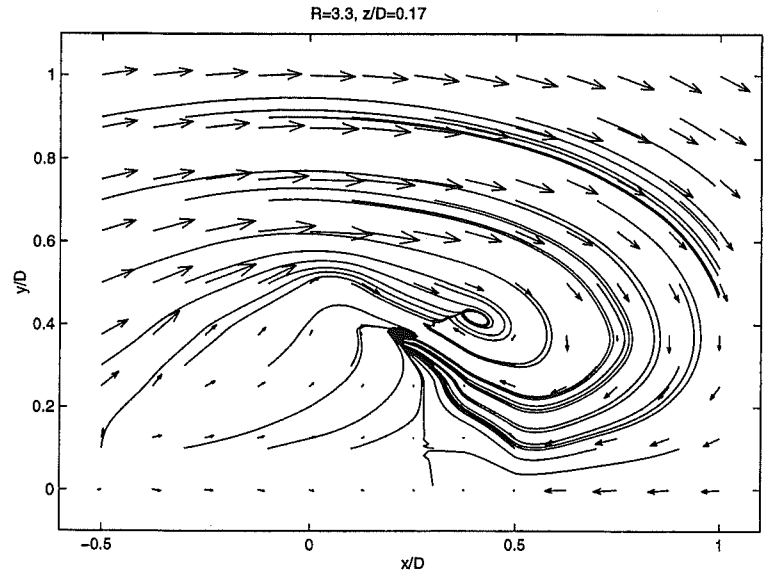

Fig. 4.1.11 Sectional streamlines together with the inplane mean velocity (U,V) vector map near the jet exit in the z/D=0.17 plane for R=3.3

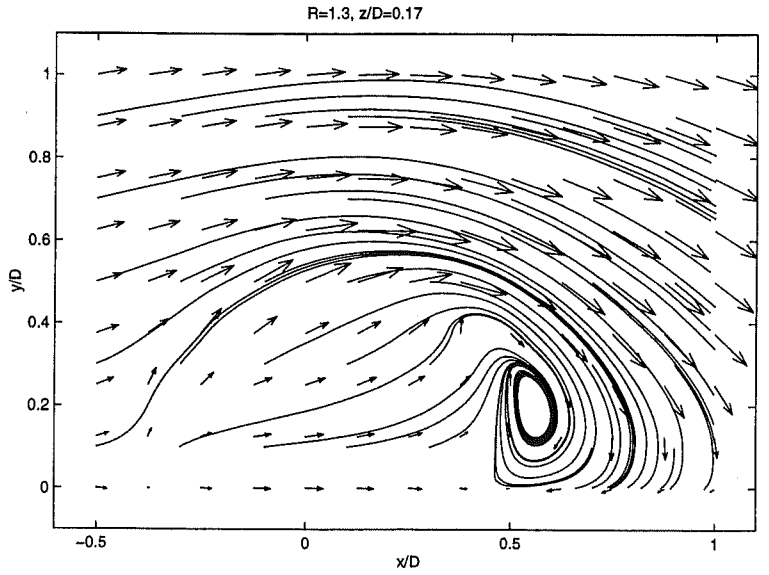

Fig. 4.1.12 Sectional streamlines together with the inplane mean velocity (U,V) vector map near the jet exit in the z/D=0.17 plane for R=1.3

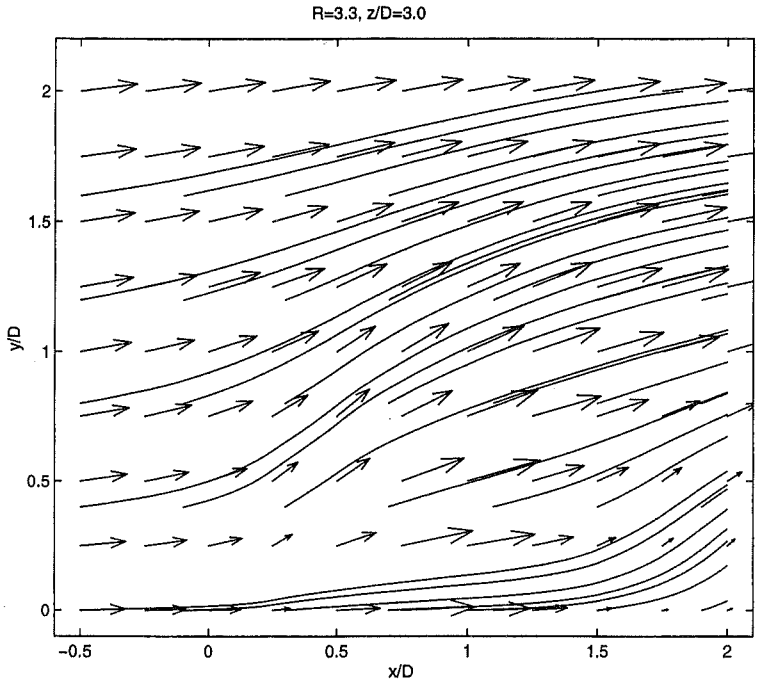

Fig. 4.1.13 Sectional streamlines in the z/D=3.0 plane for R=3.3

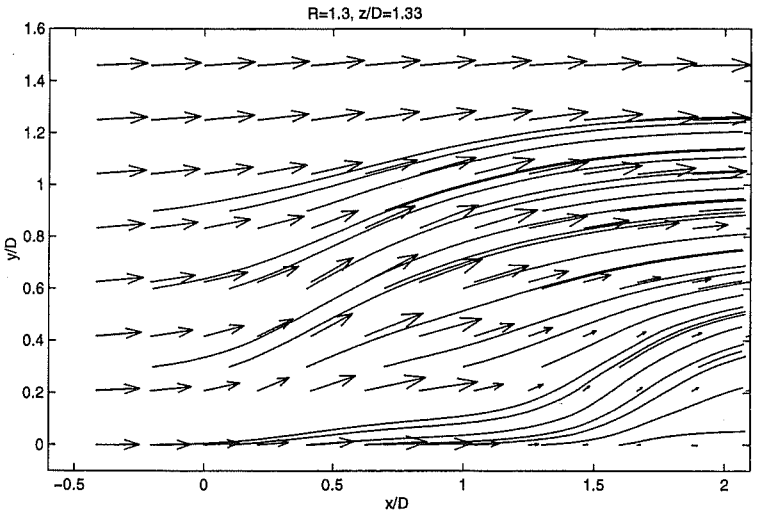

Fig. 4.1.14 Sectional streamlines in the z/D=1.3 plane for R=1.3

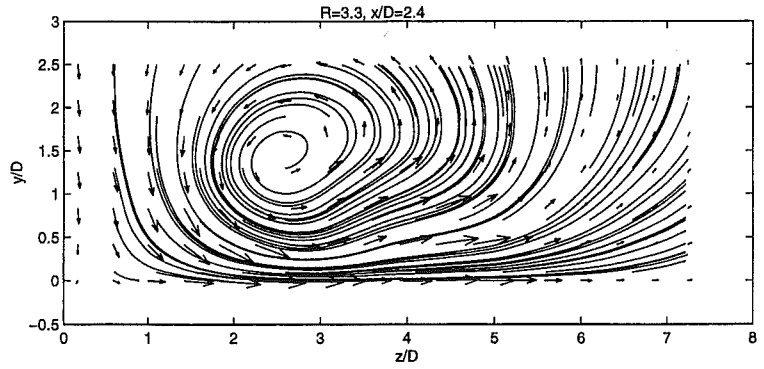

Fig. 4.1.15 Sectional streamlines together with the inplane mean velocity vector map (V,W) in the x/D=2.4 plane for R=3.3

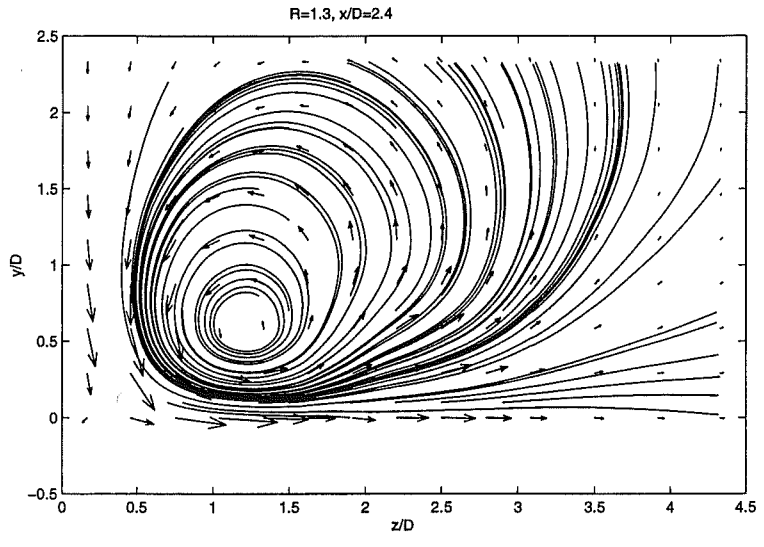

Fig. 4.1.16 Sectional streamlines together with the inplane mean velocity vector map (V,W) in the x/D=2.4 plane for R=1.3

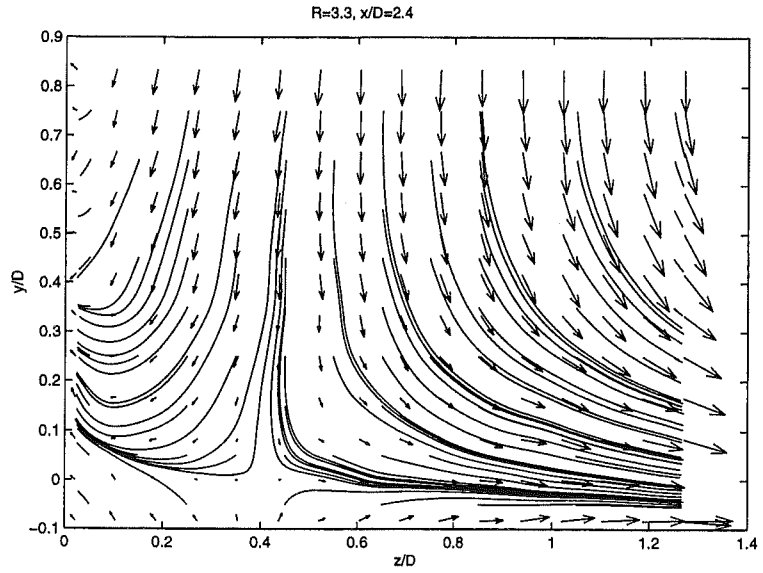

Fig. 4.1.17 Sectional streamlines together with the inplane mean velocity vector map (V,W) near the flat plate in the x/D=2.4 plane for R=3.3

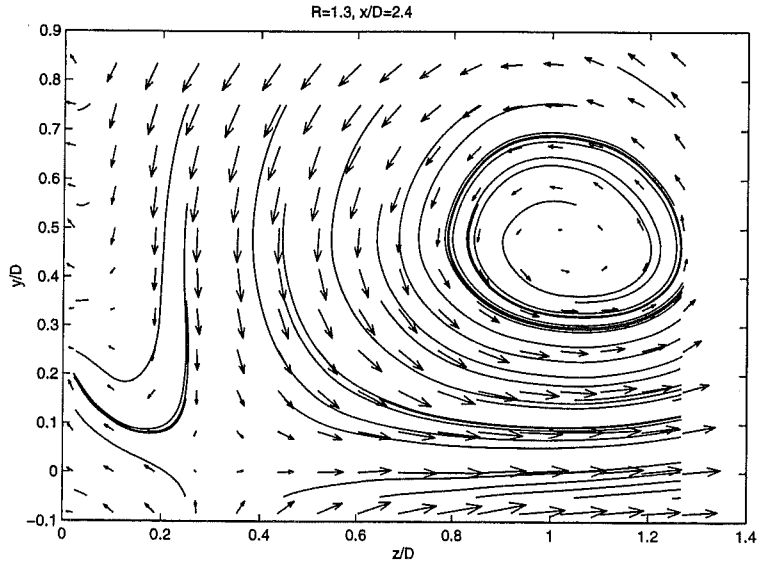

Fig. 4.1.18 Sectional streamlines together with the inplane mean velocity vector map (V,W) near the flat plate in the x/D=2.4 plane for R=1.3

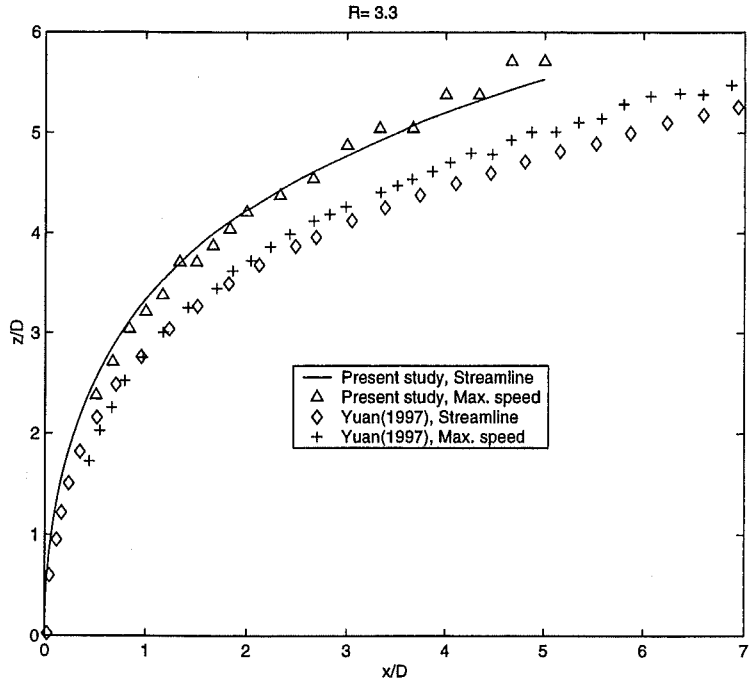

Fig. 4.1.19 Streamline and maximum speed trajectories for velocity ratio of R=3.3

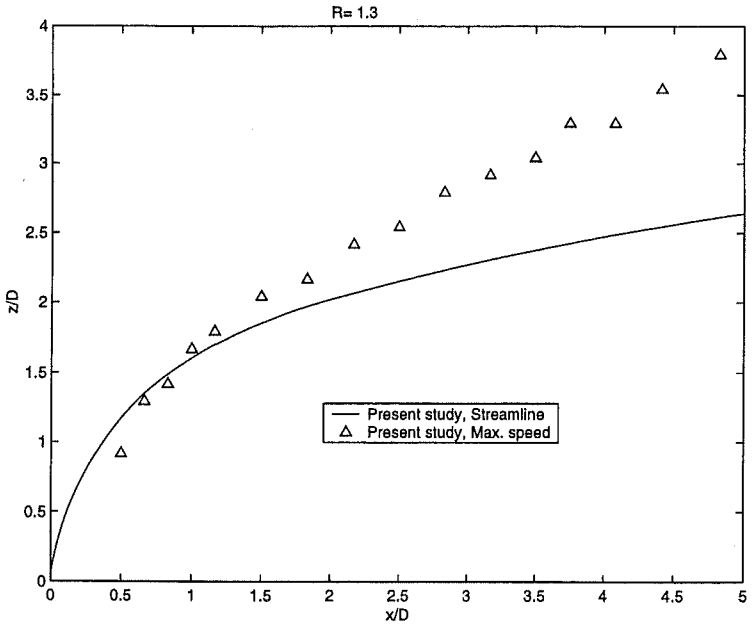

Fig. 4.1.20 Streamline and maximum speed trajectories for velocity ratio of R=1.3

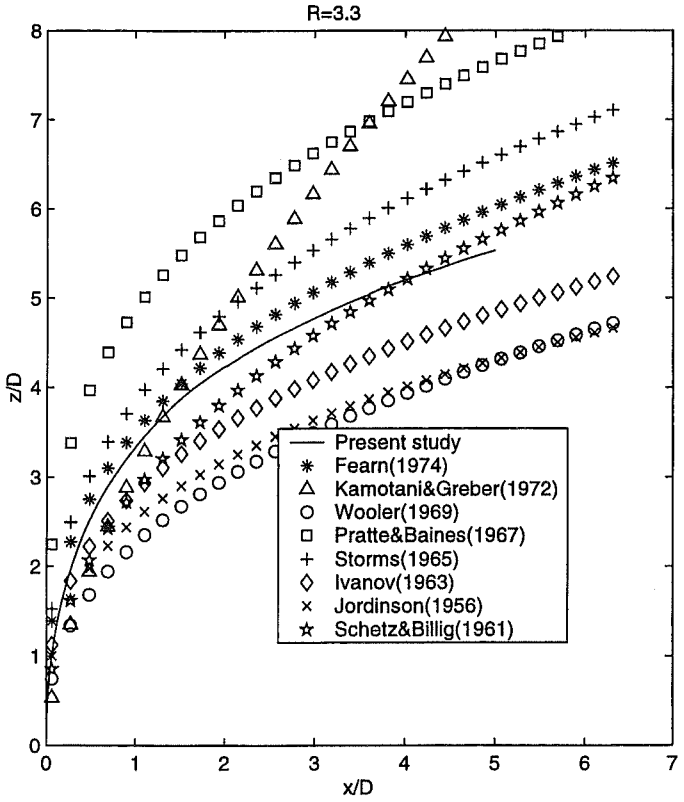

Fig. 4.1.21 Jet trajectories for velocity ratio of R=3.3

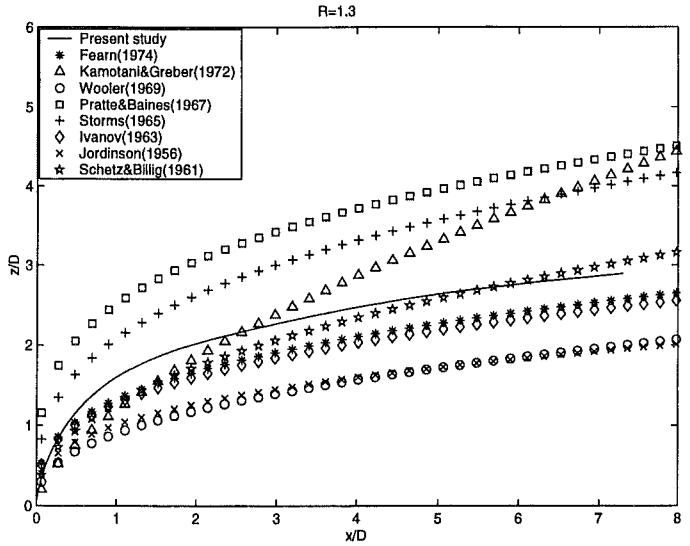

Fig. 4.1.22 Jet trajectories for velocity ratio of R=1.3

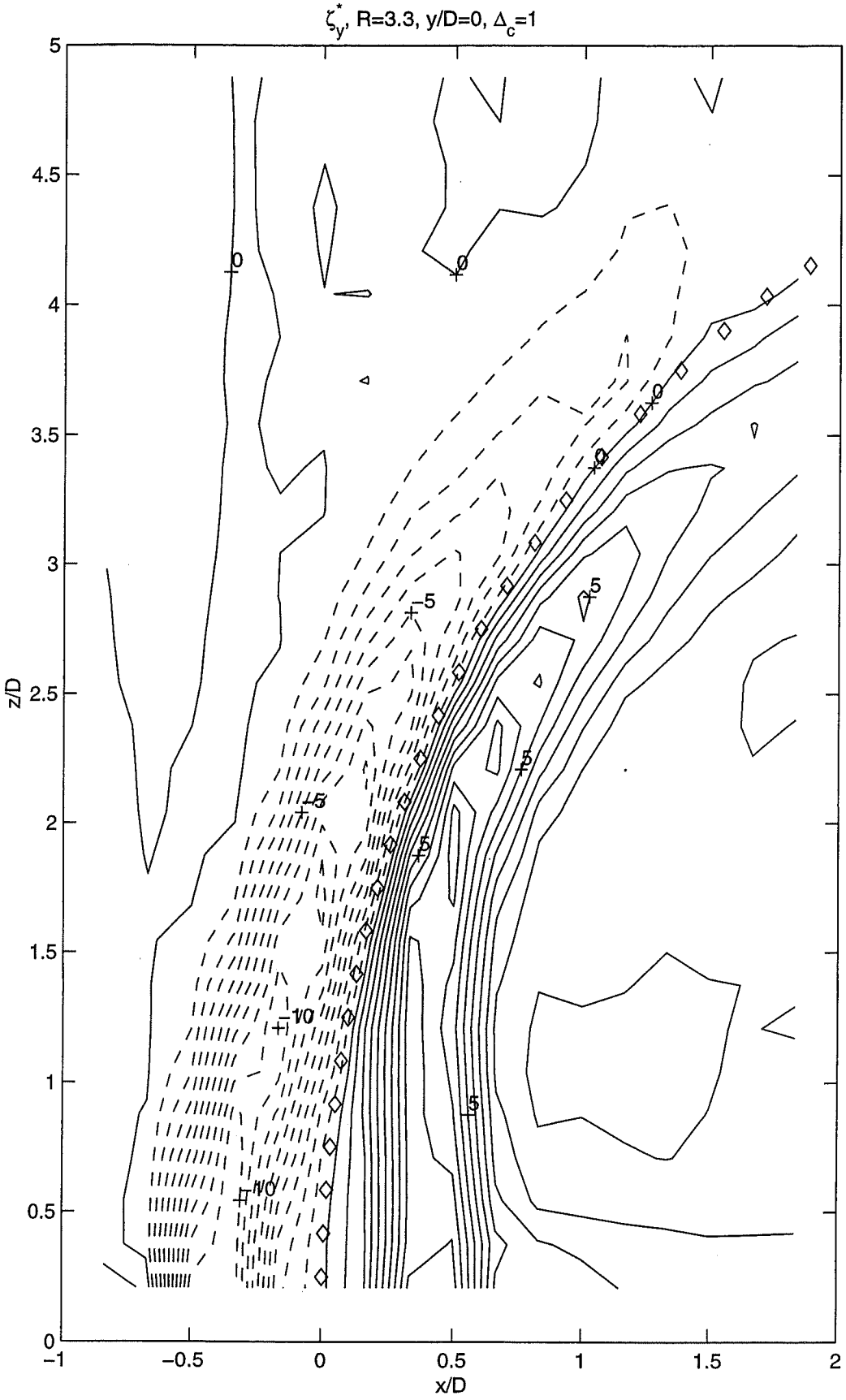

Fig. 4.1.23 Contour plot of ζ_y^* in the y/D=0 plane for R=3.3

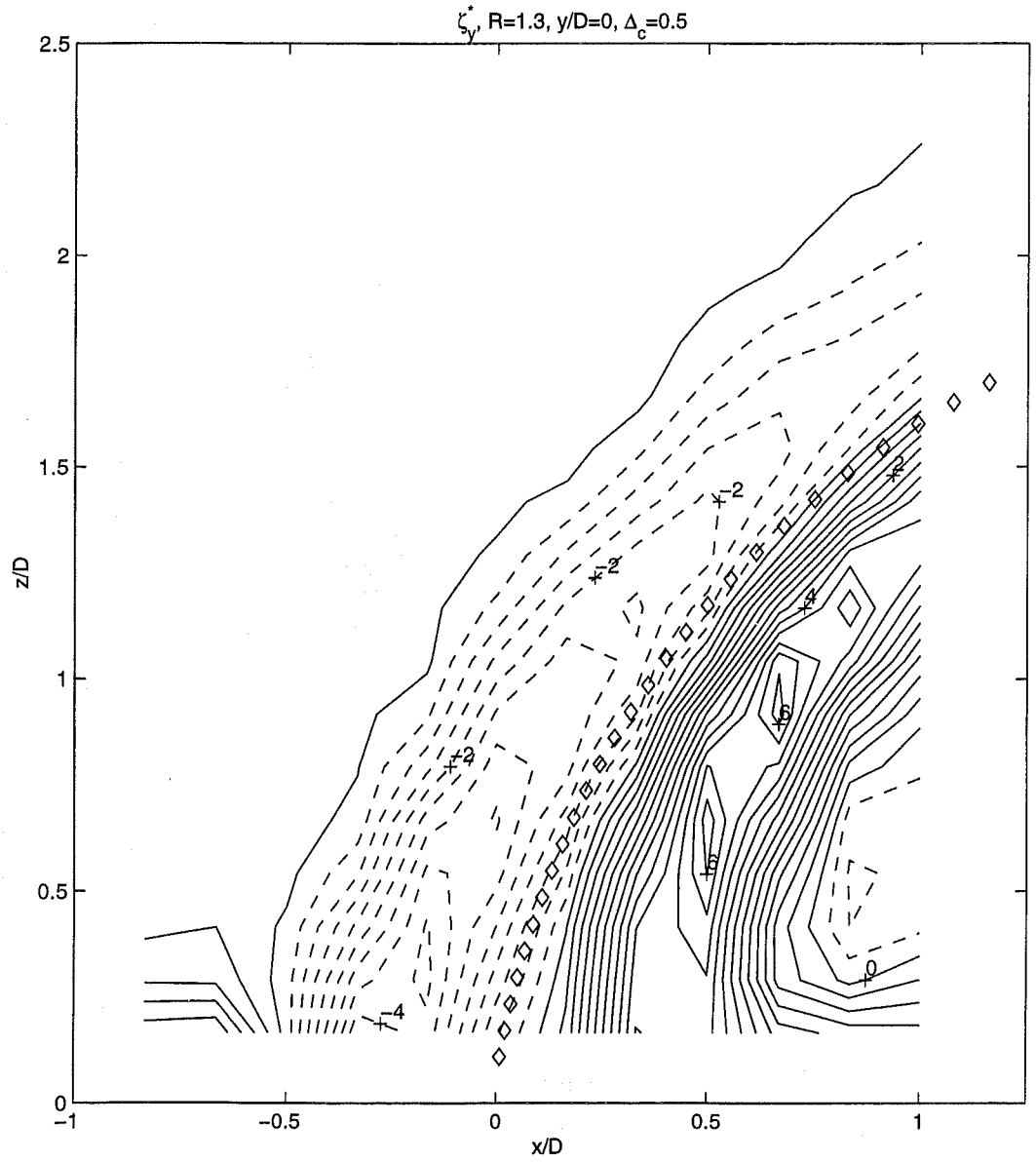

Fig. 4.1.24 Contour plot of ζ_y^* in the y/D=0 plane for R=3.3

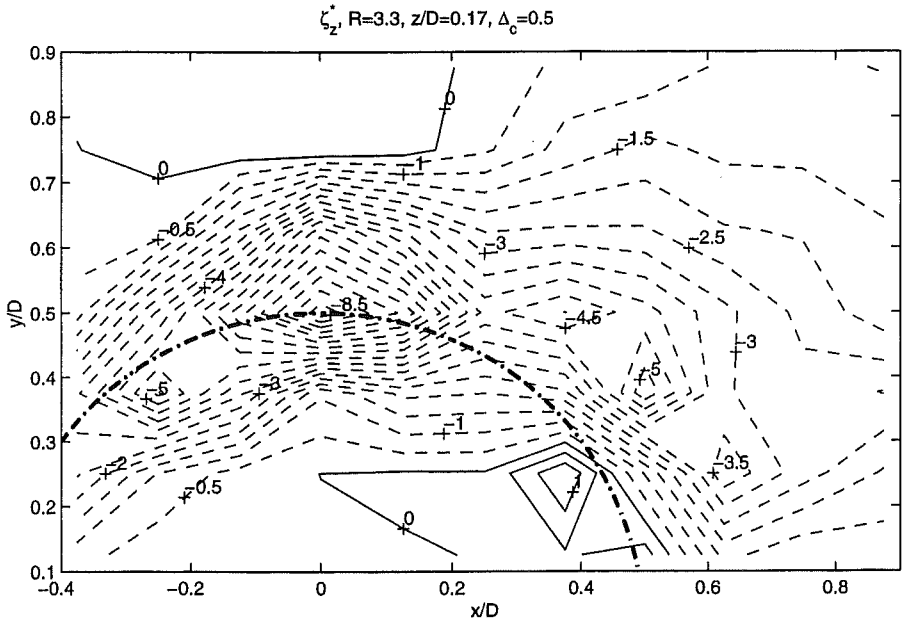

Fig. 4.1.25 Contour plot of ζ_z^* in the z^*=z/D=0.17 plane for R=3.3

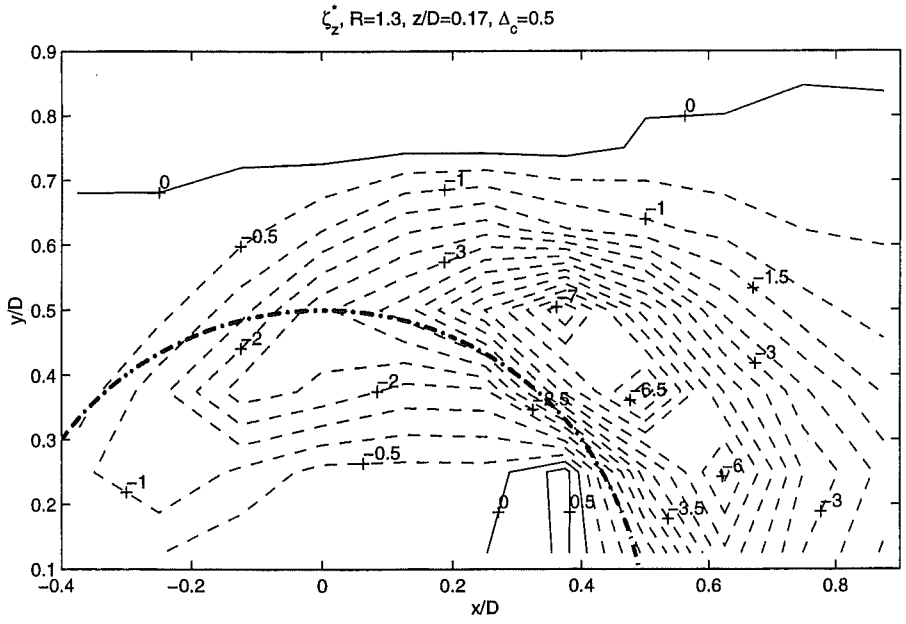

Fig. 4.1.26 Contour plot of ζ_z^* in the z^*=z/D=0.17 plane for R=1.3

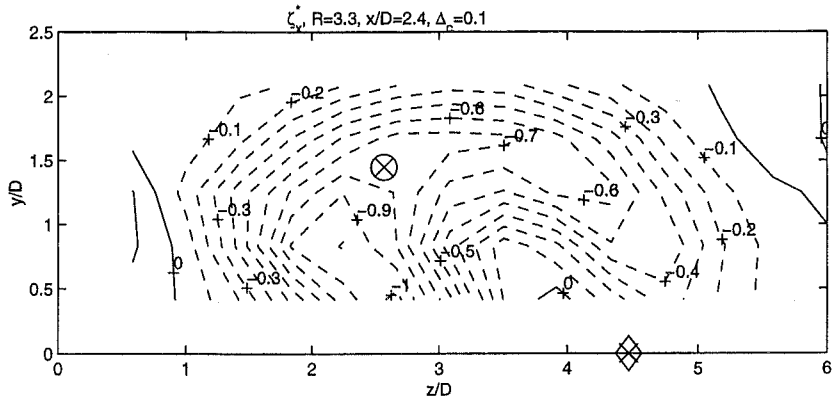

Fig. 4.1.27 Contour plot of ζ_x^* in the x^*=x/D=2.4 plane for R=3.3

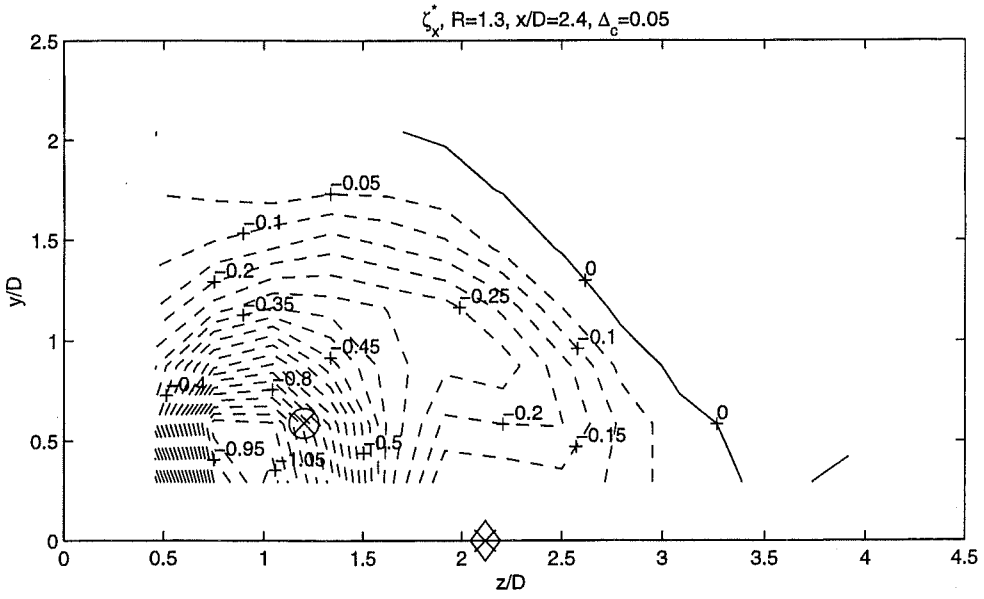

Fig. 4.1.28 Contour plot of ζ_x^* in the x^*=x/D=2.4 plane for R=1.3

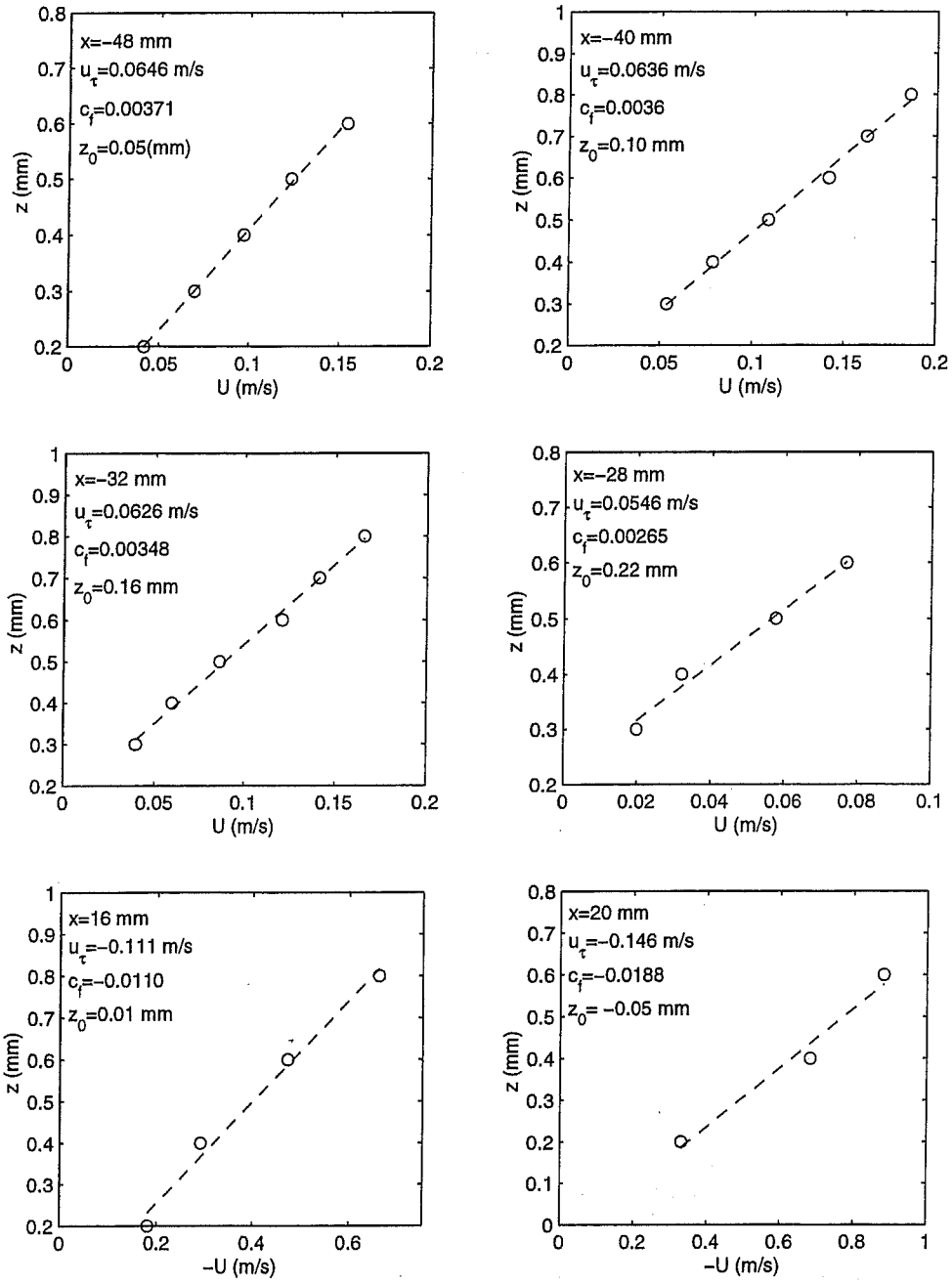

Fig. 4.1.29a Variation of the streamwise velocity U with z near the flat plate at x^*=x/D locations where τ_{wc} was measured for R=3.3

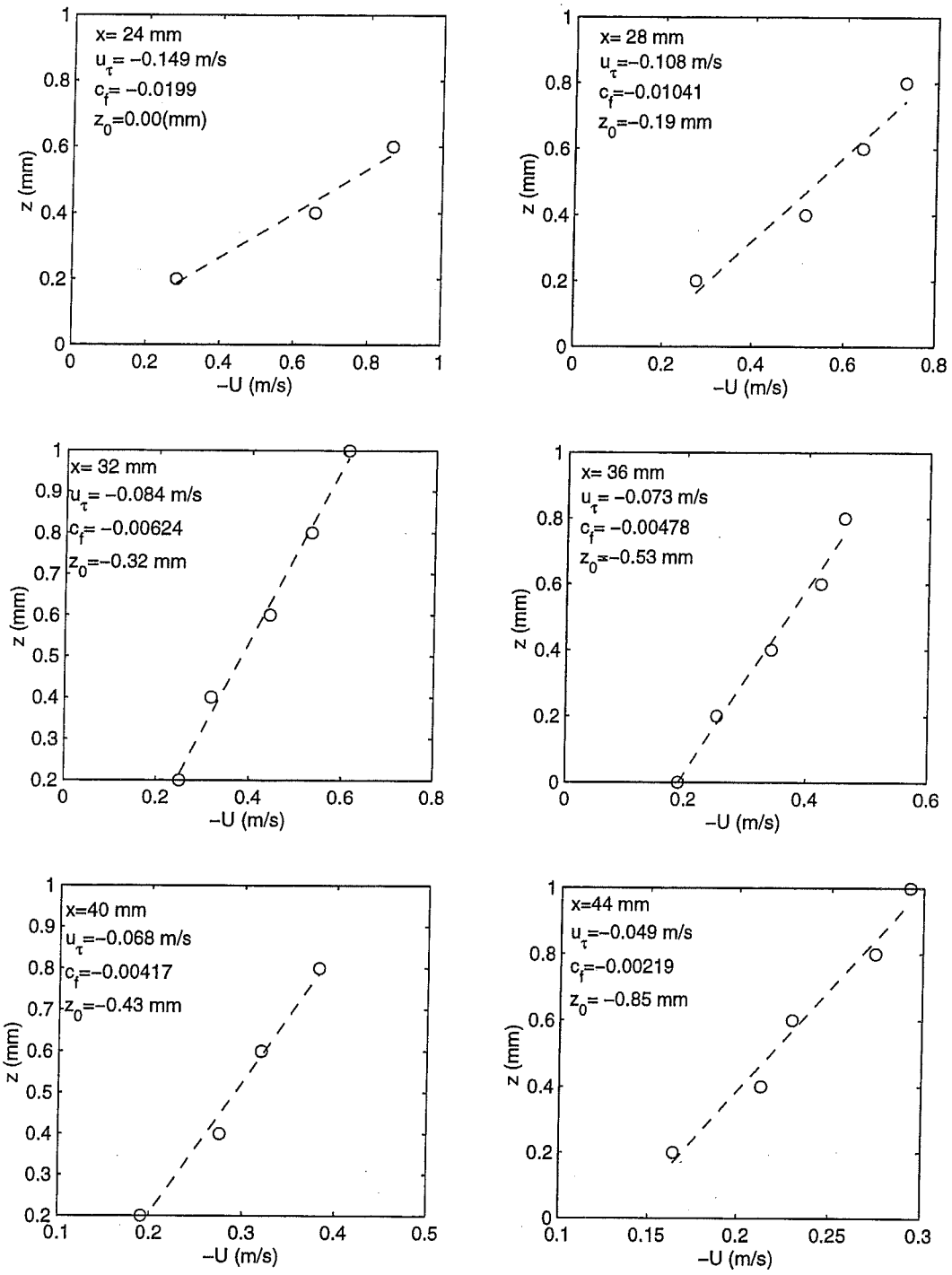

Fig. 4.1.29b Variation of the streamwise velocity U with z near the flat plate at x^*=x/D locations where τ_{wc} was measured for R=3.3

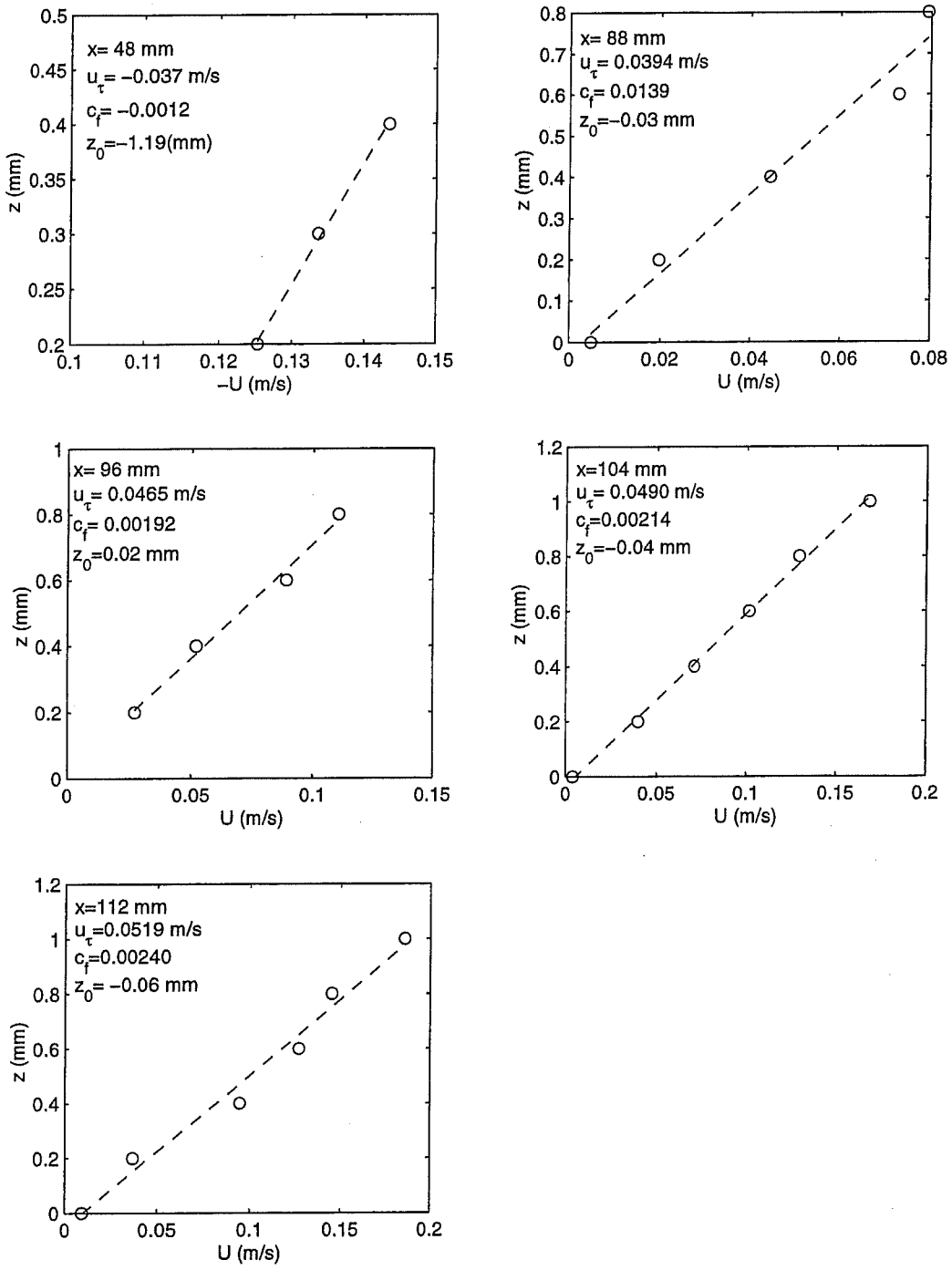

Fig. 4.1.29c Variation of the streamwise velocity U with z near the flat plate at x^*=x/D locations where τ_{wc} was measured for R=3.3

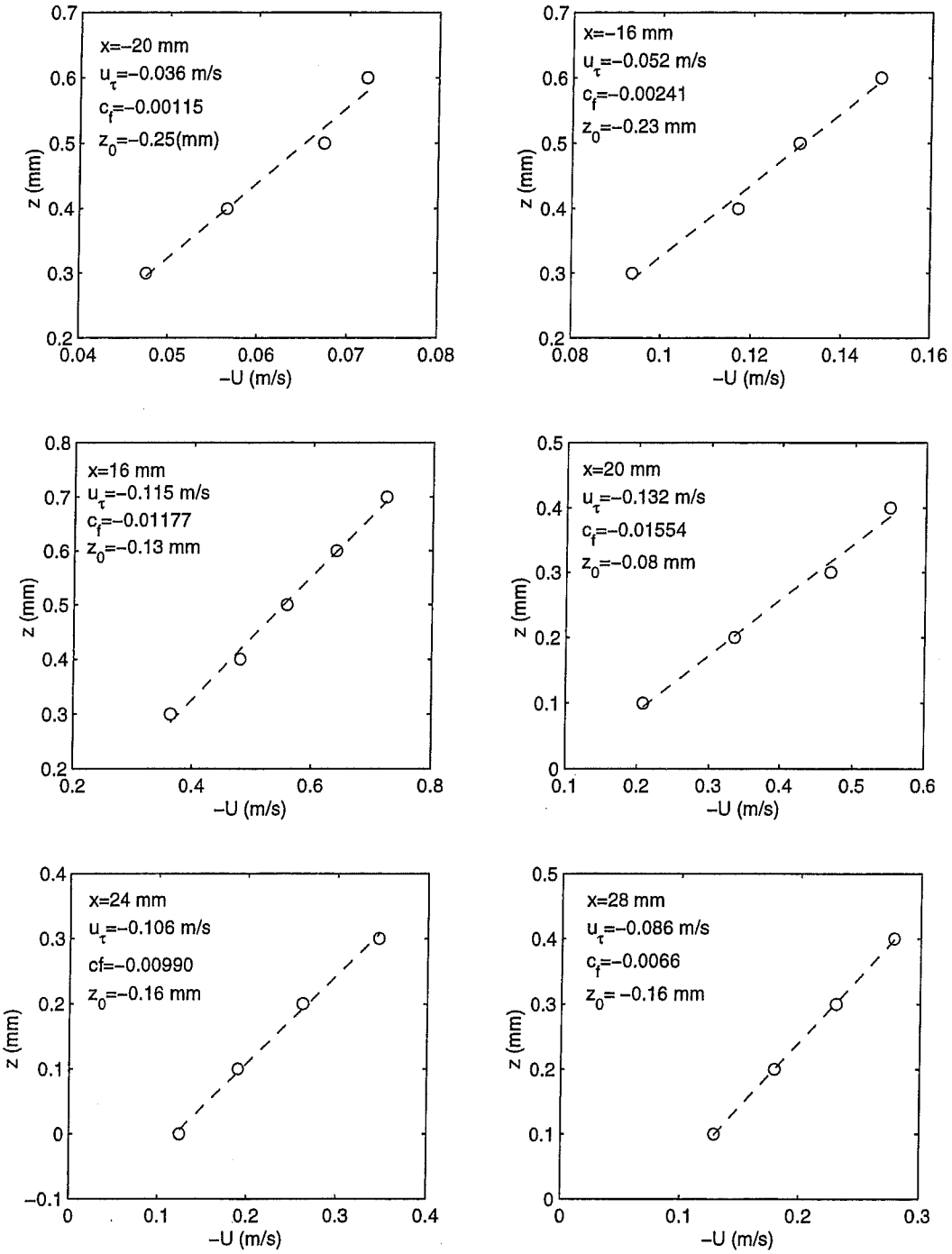

Fig. 4.1.30a Variation of the streamwise velocity U with z near the flat plate at x^*=x/D locations where τ_{wc} was measured for R=1.3

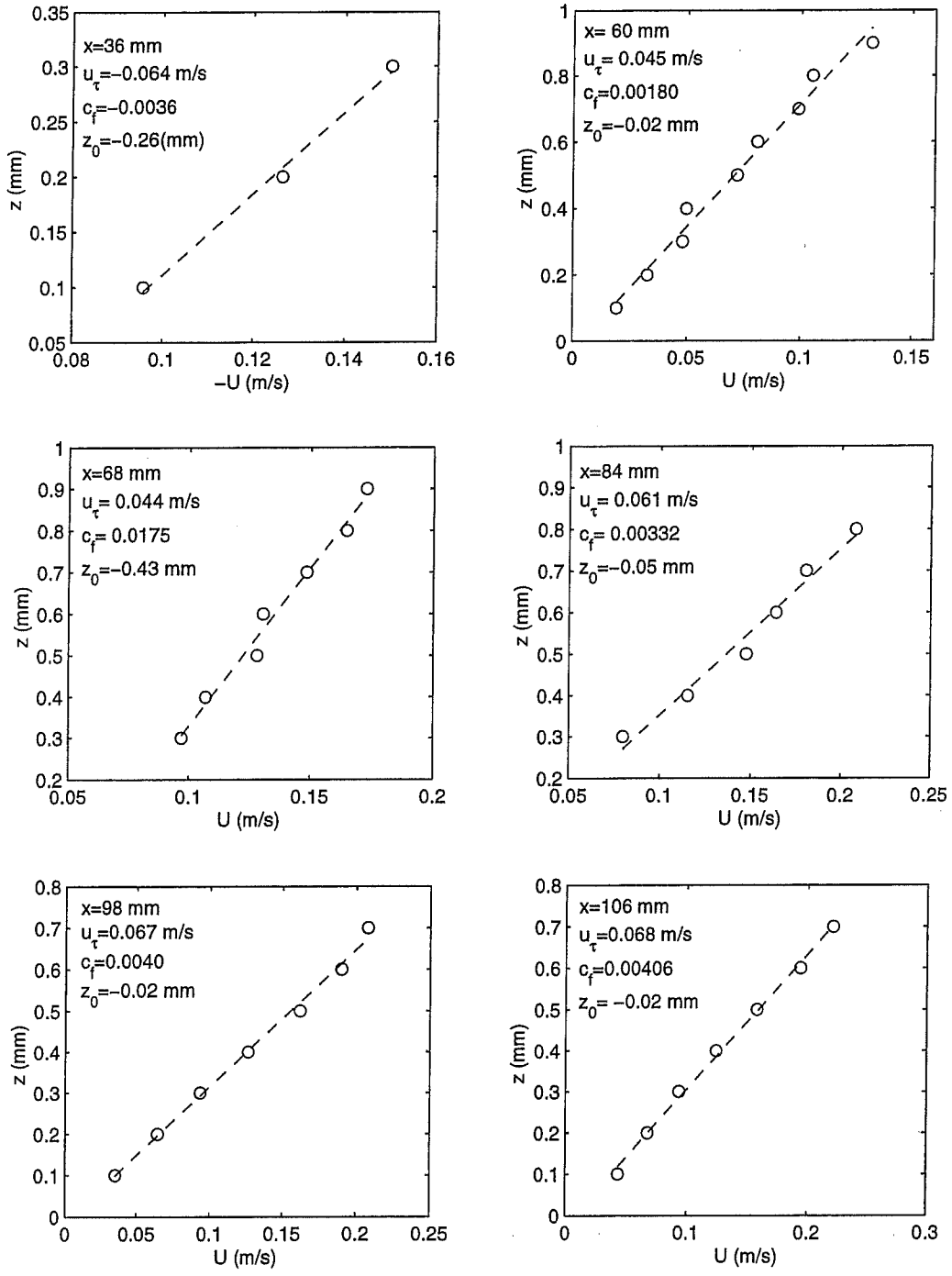

Fig. 4.1.30b Variation of the streamwise velocity U with z near the flat plate at x^*=x/D locations where τ_{wc} was measured for R=1.3

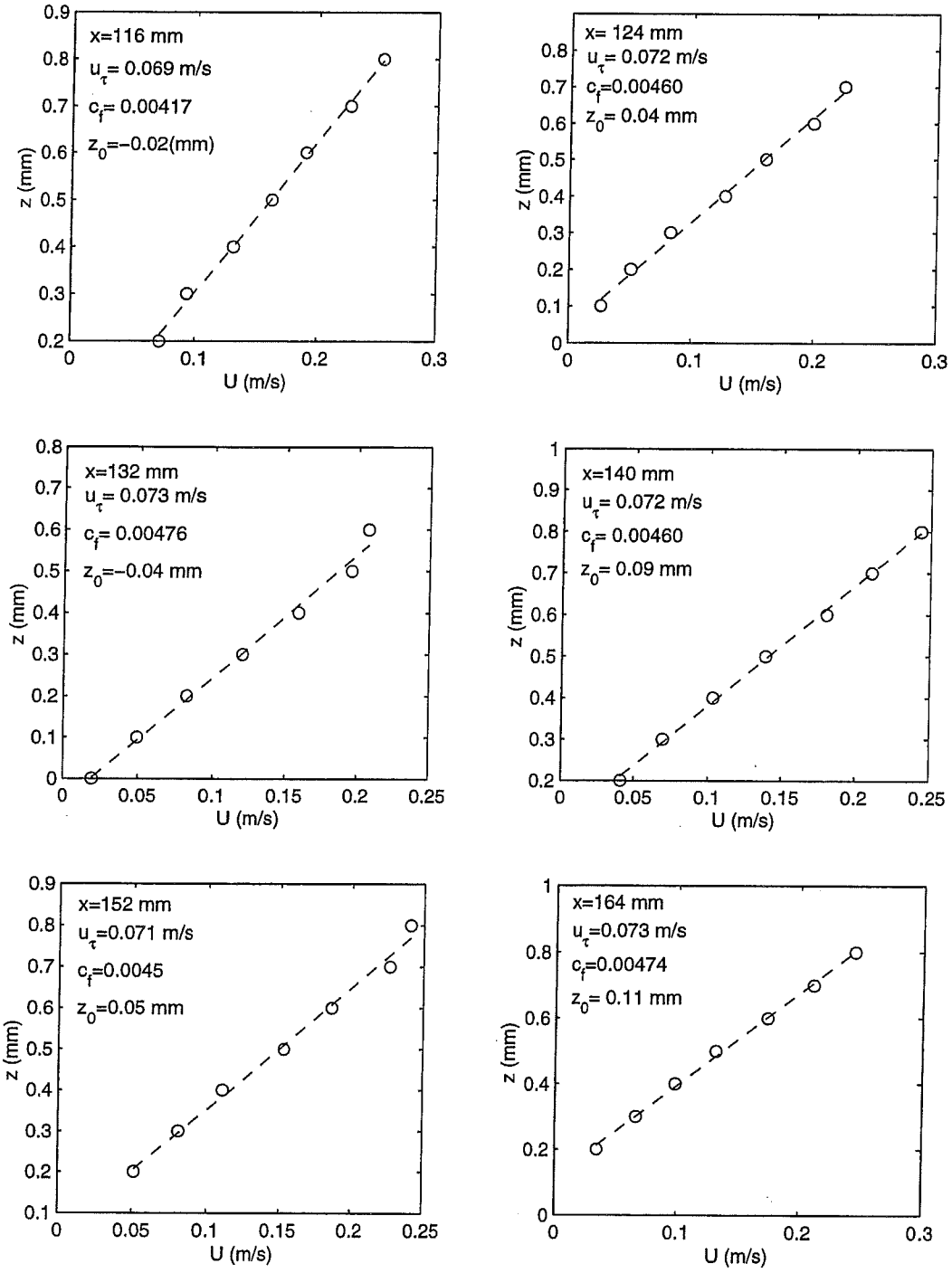

Fig. 4.1.30c Variation of the streamwise velocity U with z near the flat plate at x^*=x/D locations where τ_{wc} was measured for R=1.3

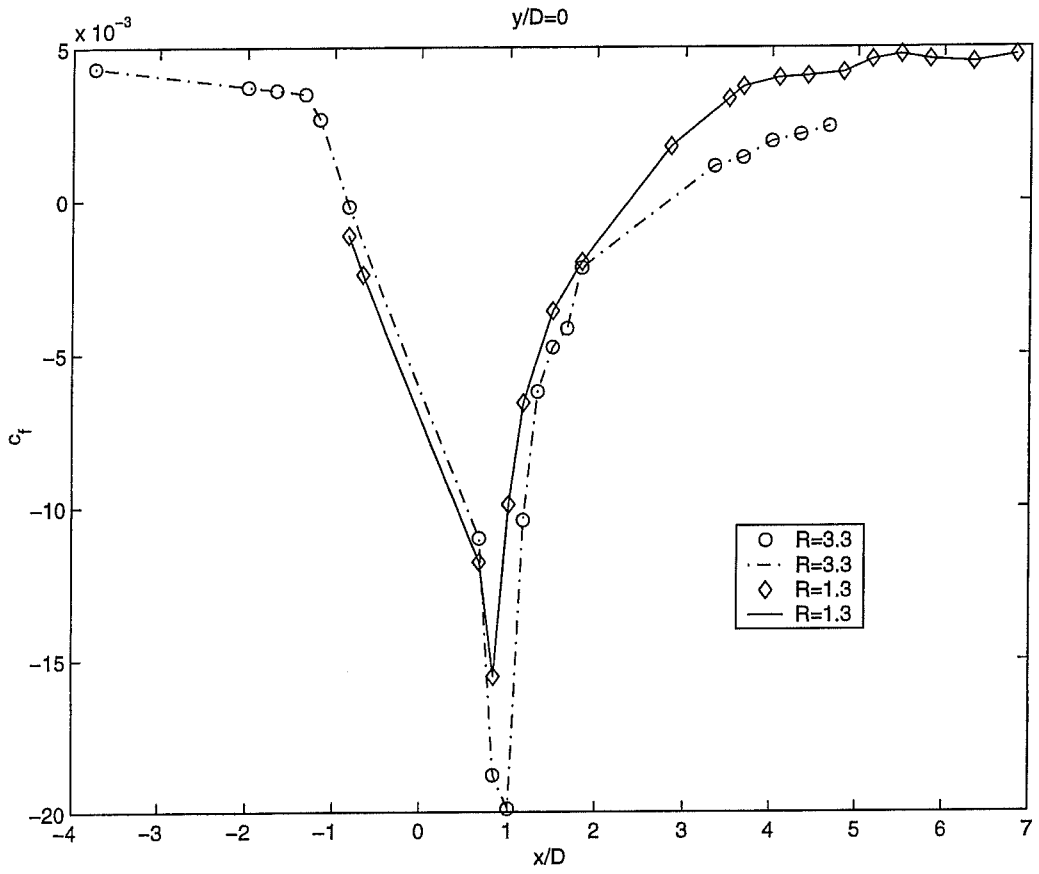

Fig. 4.1.31 Variation of the skin friction coefficient C_{fc} on the flat plate along the x axis for R=3.3 and 1.3

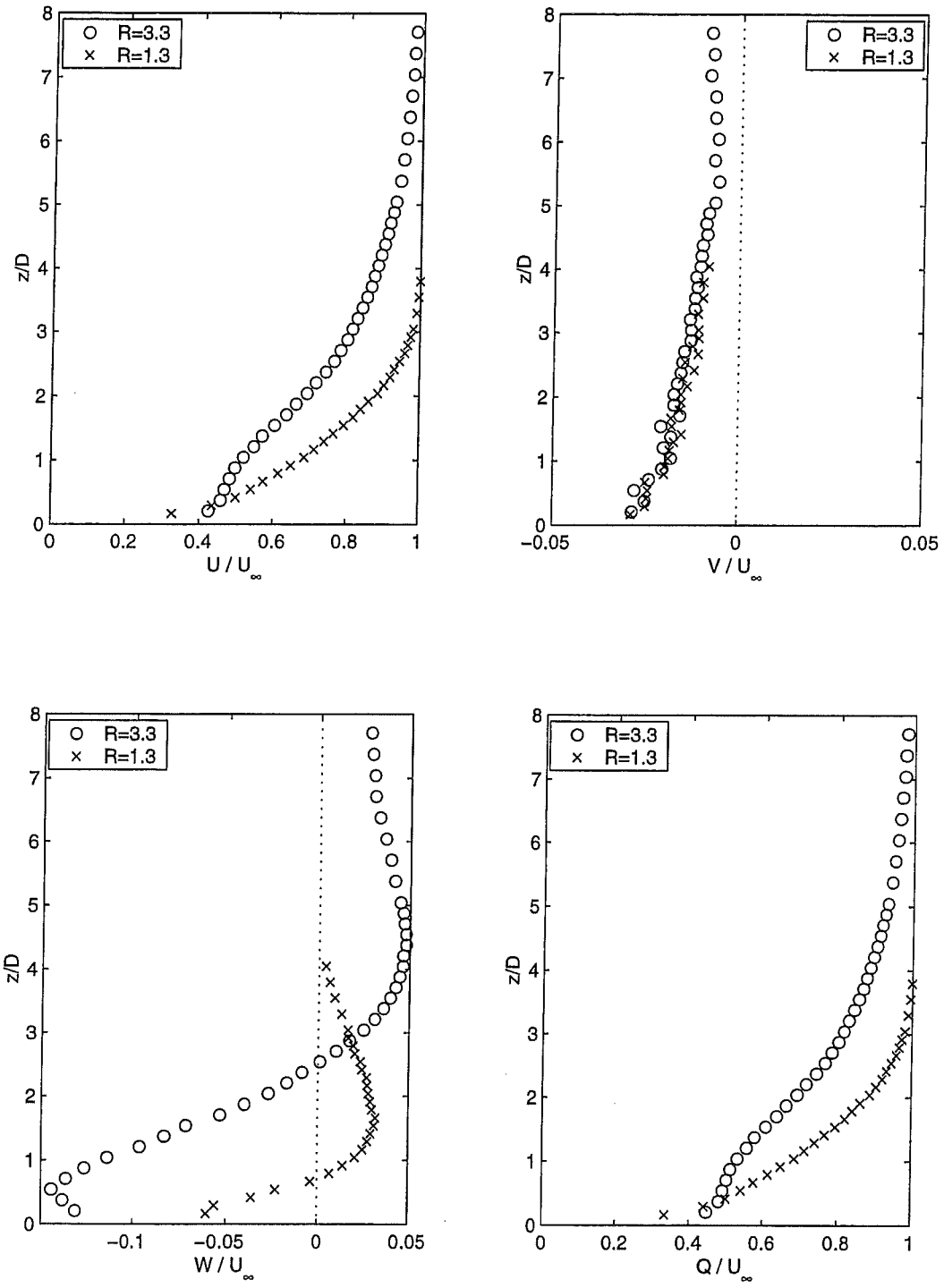

Fig. 4.2.1 Variations of the normalized mean velocities U^*, V^*, W^* and Q^* with z^* at x^*=-0.67 for R=3.3 and 1.3

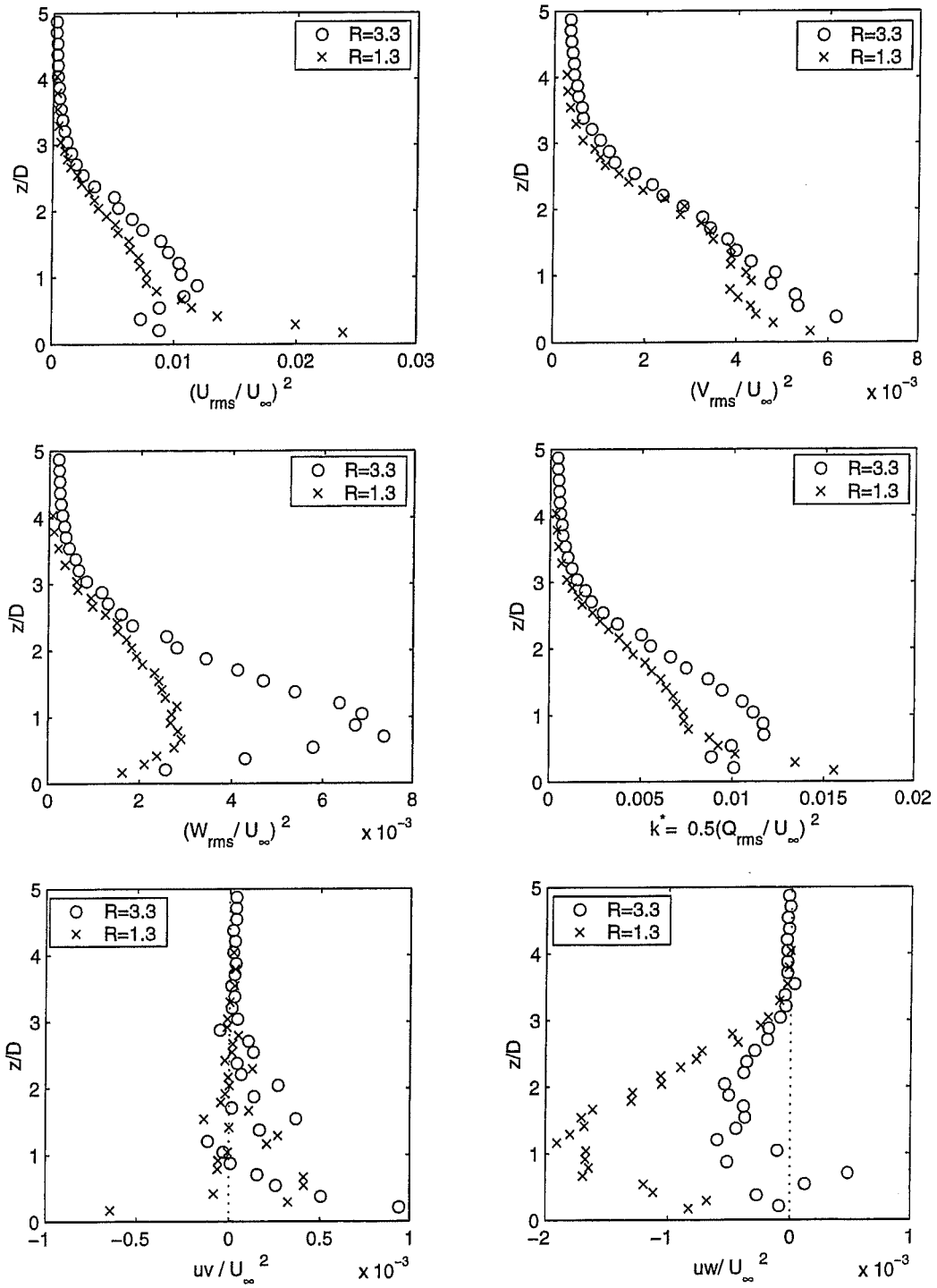

Fig. 4.2.2 Variations of the normalized turbulent stresses uu^*, vv^*, ww^*, uv^*, uw^* and the normalized turbulent kinetic energy k^* at x^*=-0.67 for R=3.3 and 1.3

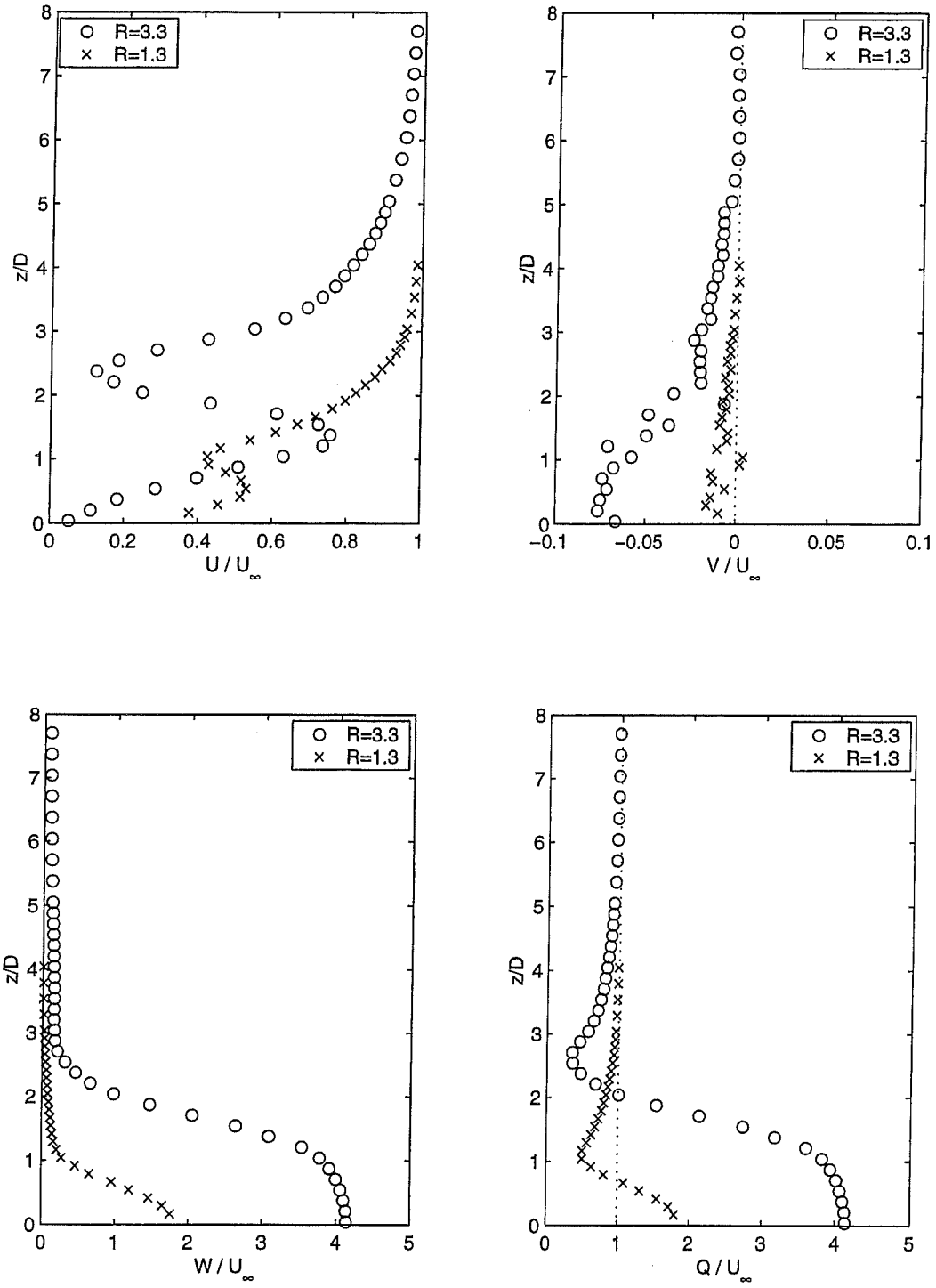

Fig. 4.2.3 Variations of the normalized mean velocities U^*, V^*, W^* and Q^* with z^* at x^*=0 for R=3.3 and 1.3

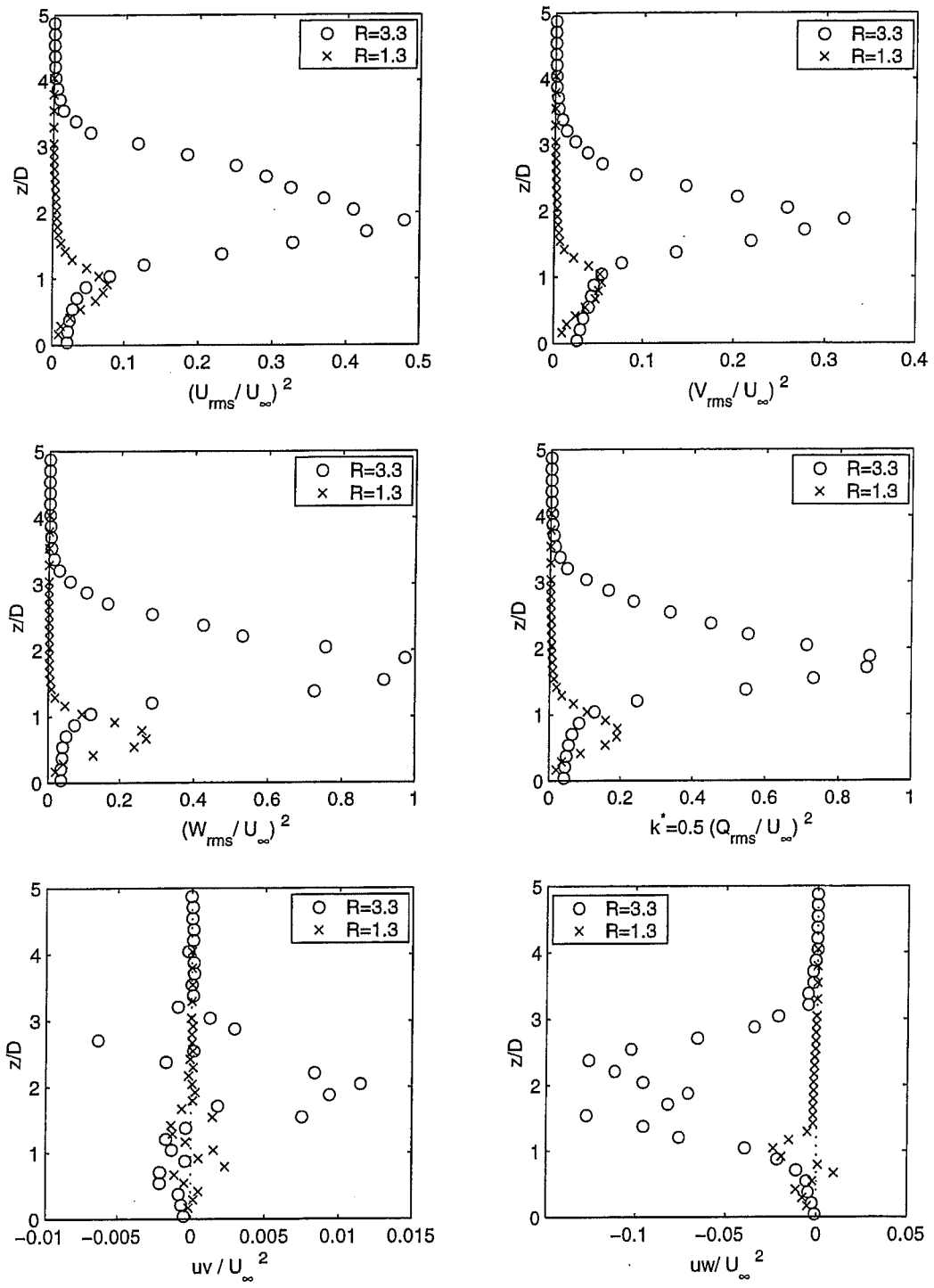

Fig. 4.2.4 Variations of the normalized turbulent stresses uu^*, vv^*, ww^*, uv^*, uw^* and the normalized turbulent kinetic energy k^* at x^*=0 for R=3.3 and 1.3

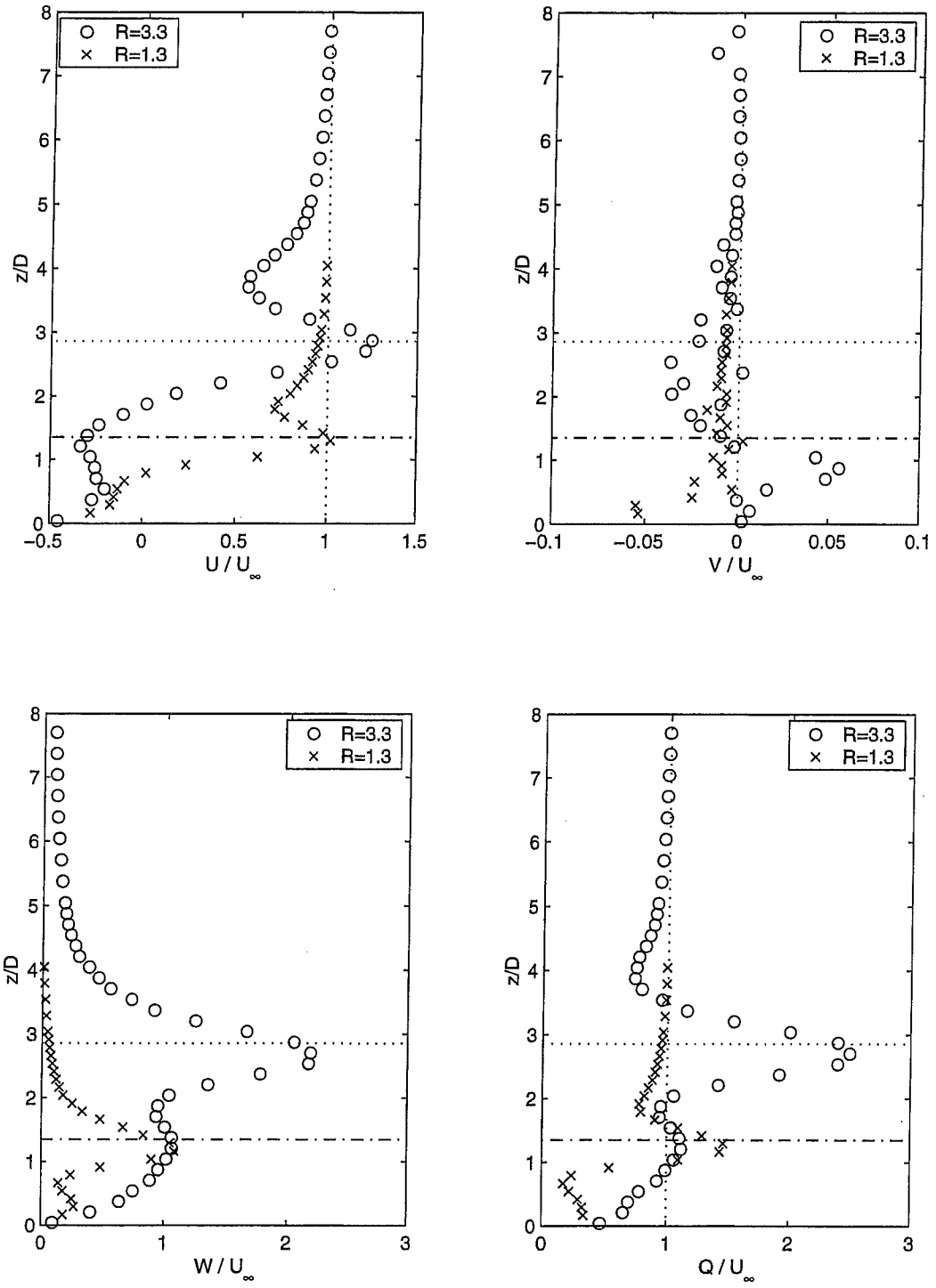

Fig. 4.2.5 Variations of the normalized mean velocities U^*, V^*, W^* and Q^* with z^* at x^*=0.67 for R=3.3 and 1.3

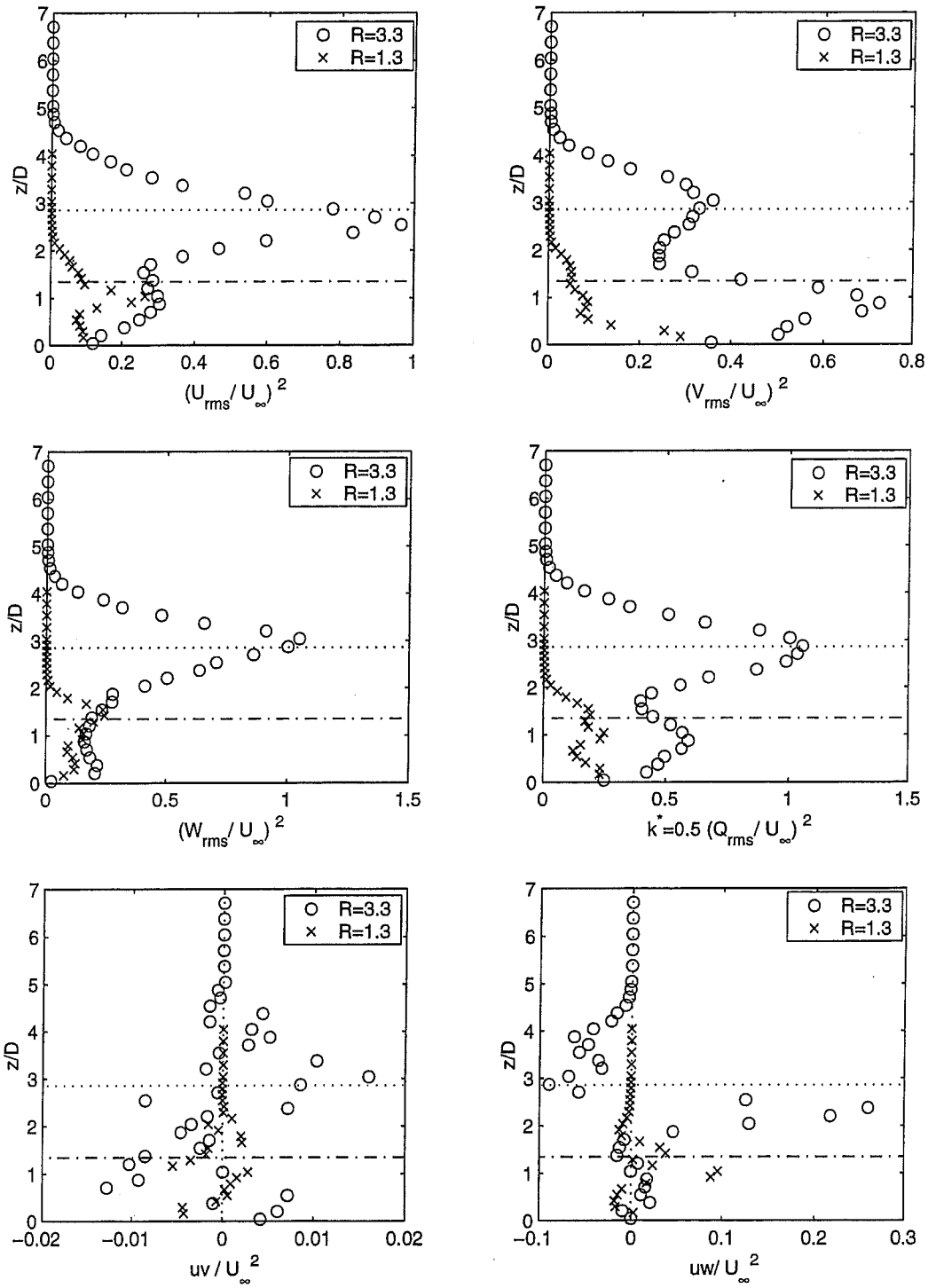

Fig. 4.2.6 Variations of the normalized turbulent stresses uu^*, vv^*, ww^*, uv^*, uw^* and the normalized turbulent kinetic energy k^* at x^*=0.67 for R=3.3 and 1.3

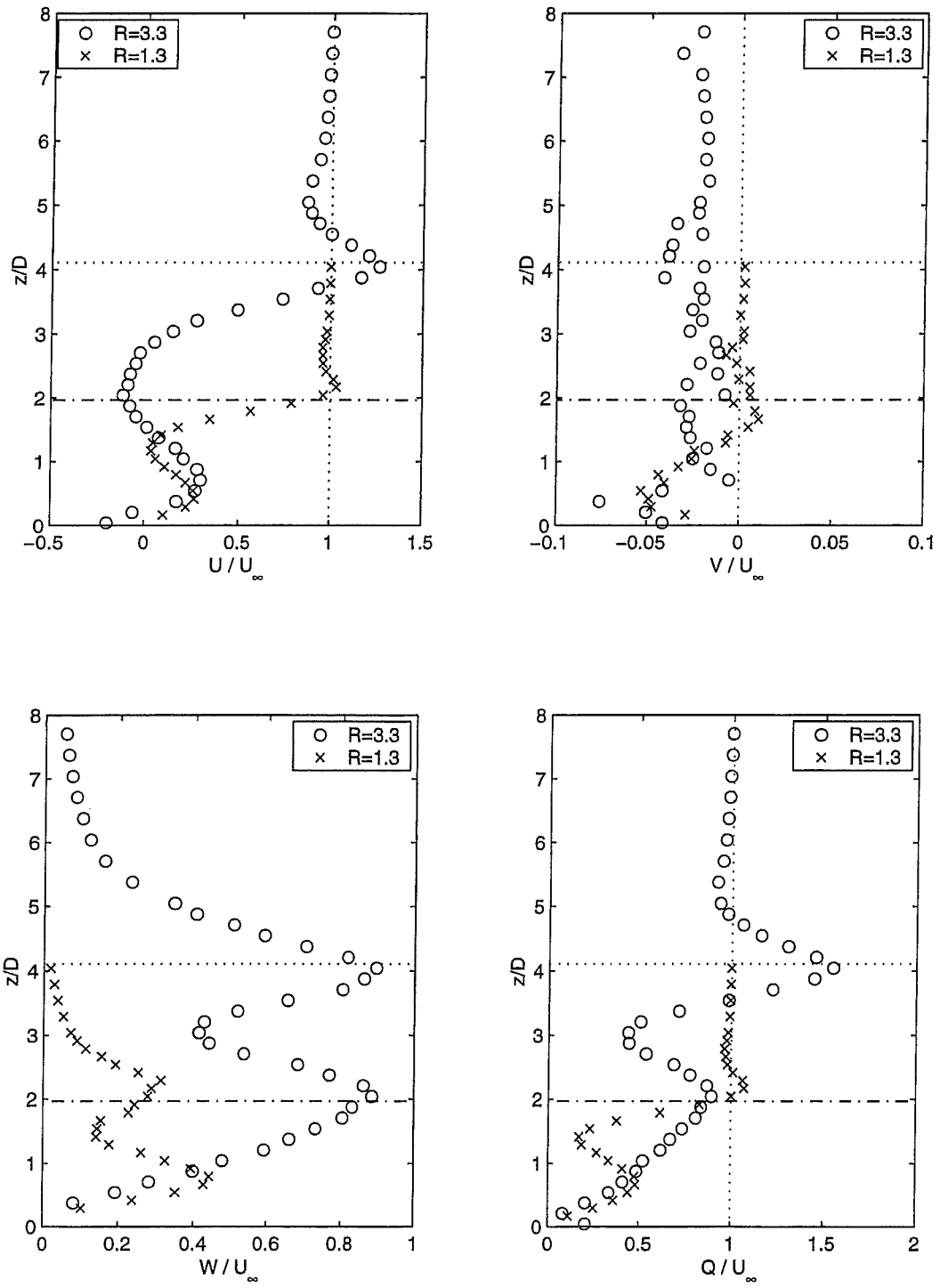

Fig. 4.2.7 Variations of the normalized mean velocities U^*, V^*, W^* and Q^* with z^* at x^*=1.83 for R=3.3 and 1.3

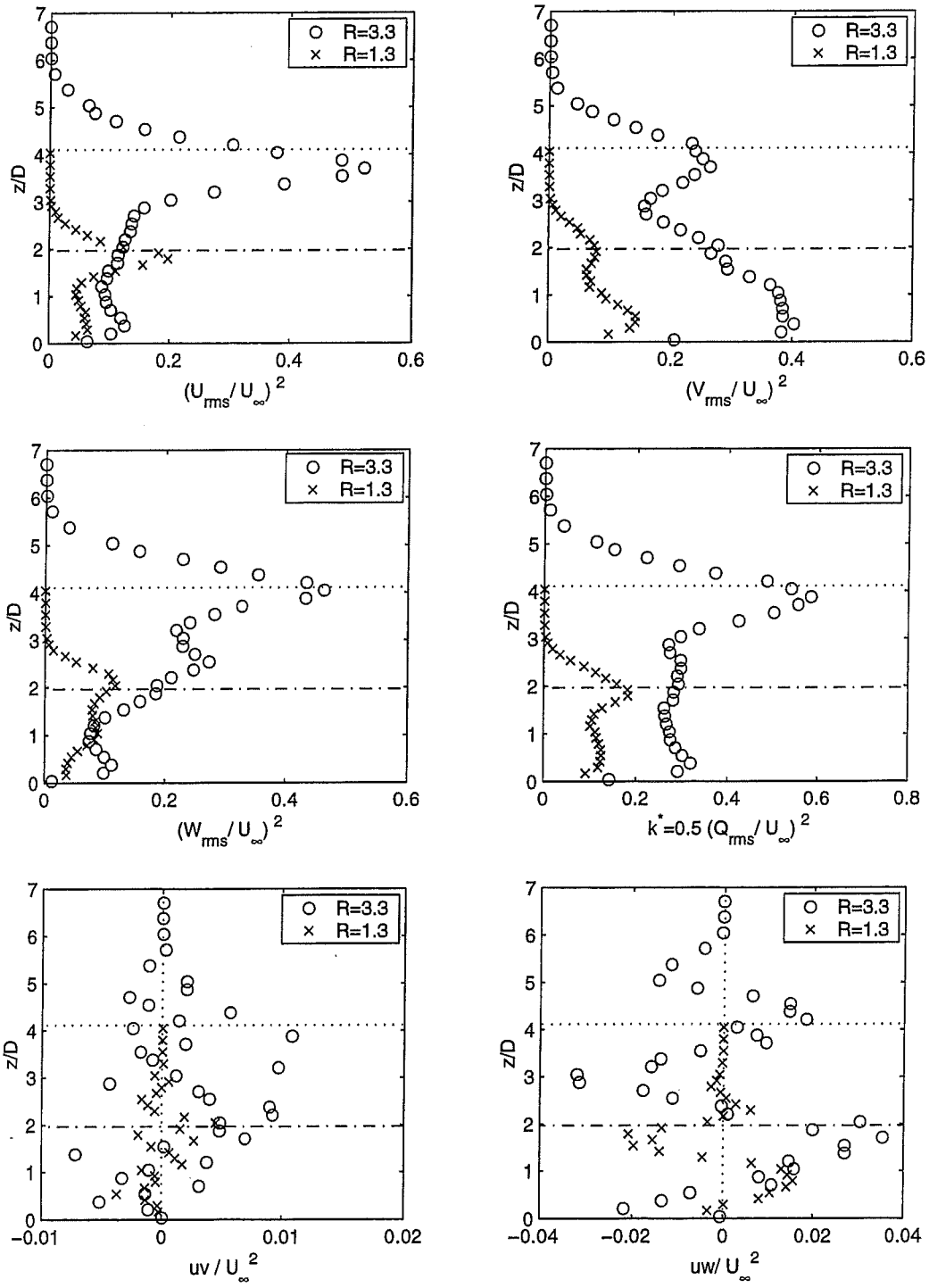

Fig. 4.2.8 Variations of the normalized turbulent stresses uu^*, vv^*, ww^*, uv^*, uw^* and the normalized turbulent kinetic energy k^* at x^*=1.83 for R=3.3 and 1.3

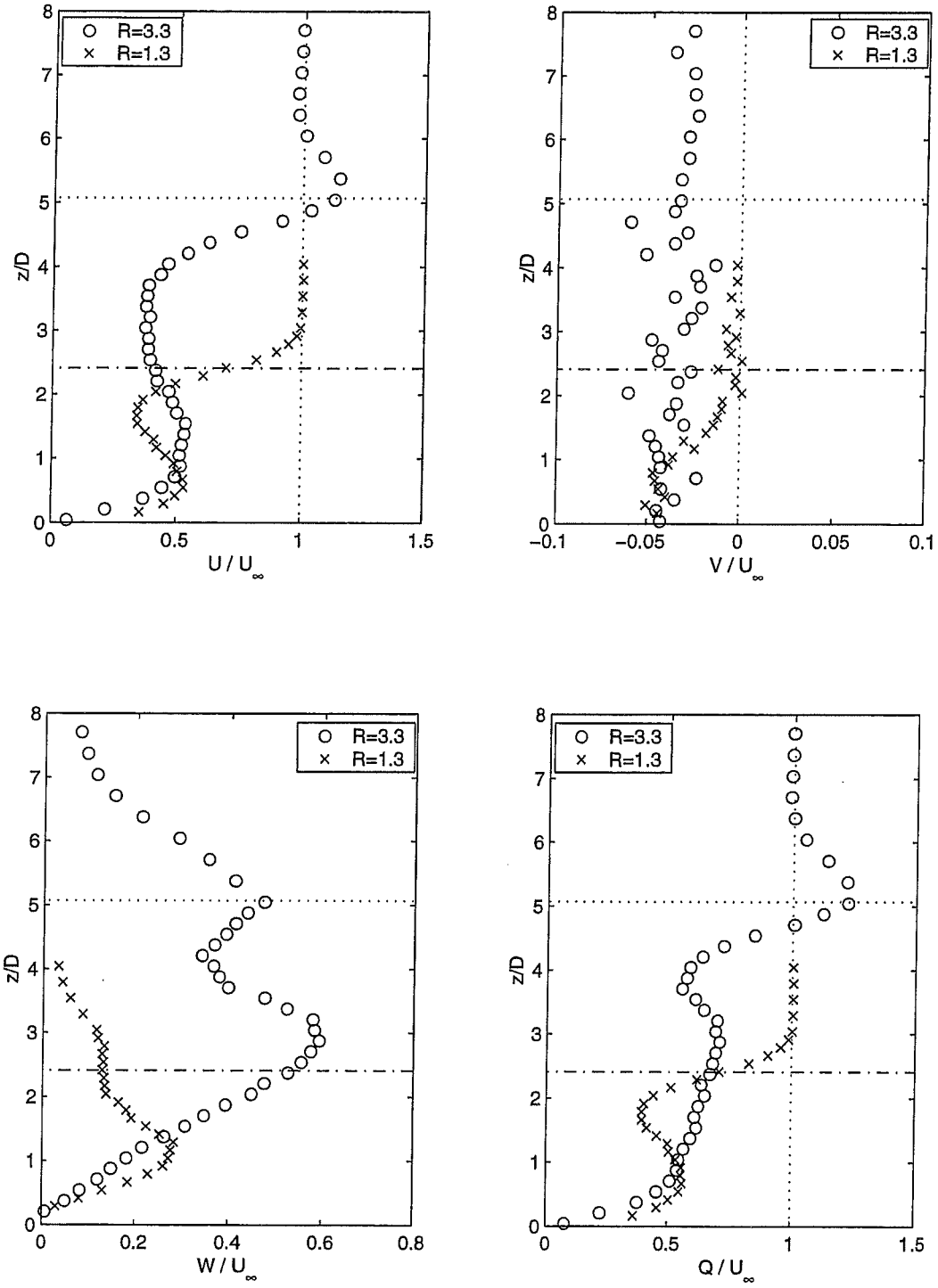

Fig. 4.2.9 Variations of the normalized mean velocities U^*, V^*, W^* and Q^* with z^* at x^*=3.67 for R=3.3 and 1.3

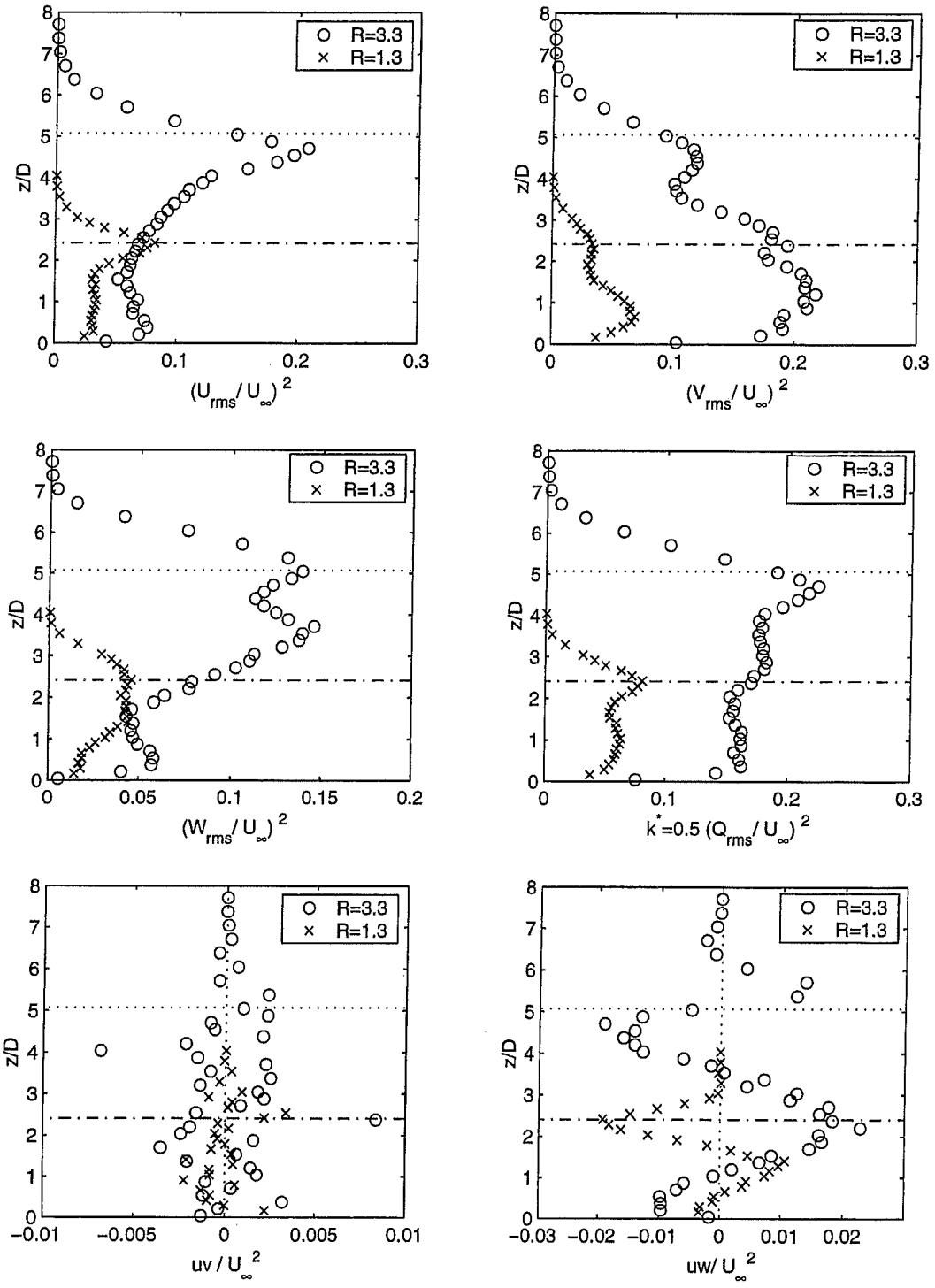

Fig. 4.2.10 Variations of the normalized turbulent stresses uu^*, vv^*, ww^*, uv^*, uw^* and the normalized turbulent kinetic energy k^* at x^*=3.67 for R=3.3 and 1.3

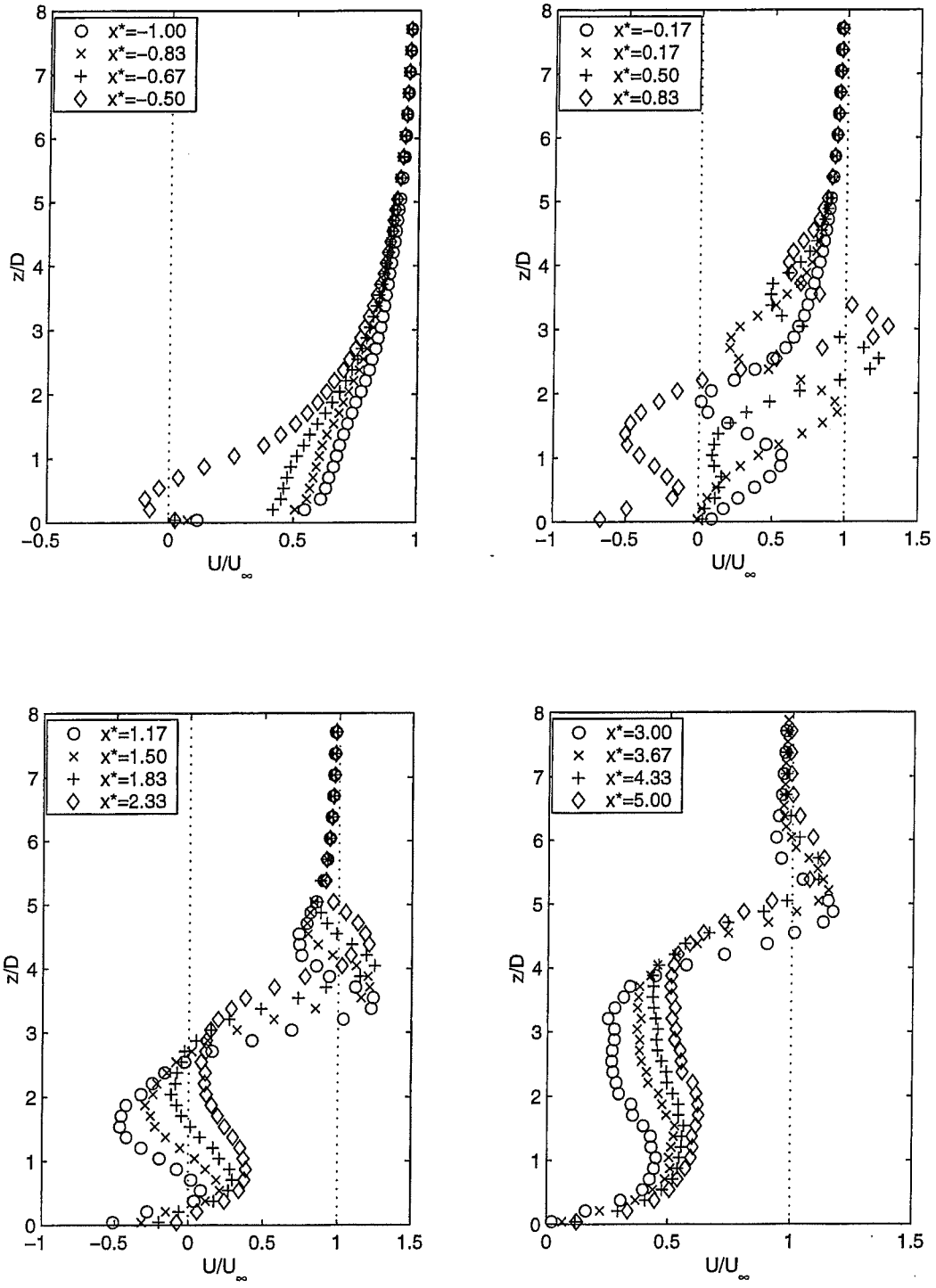

Fig. 4.2.11 Variation of the normalized streamwise mean velocity U^* with z^* at various x^* locations in the y^*=0 plane for R=3.3

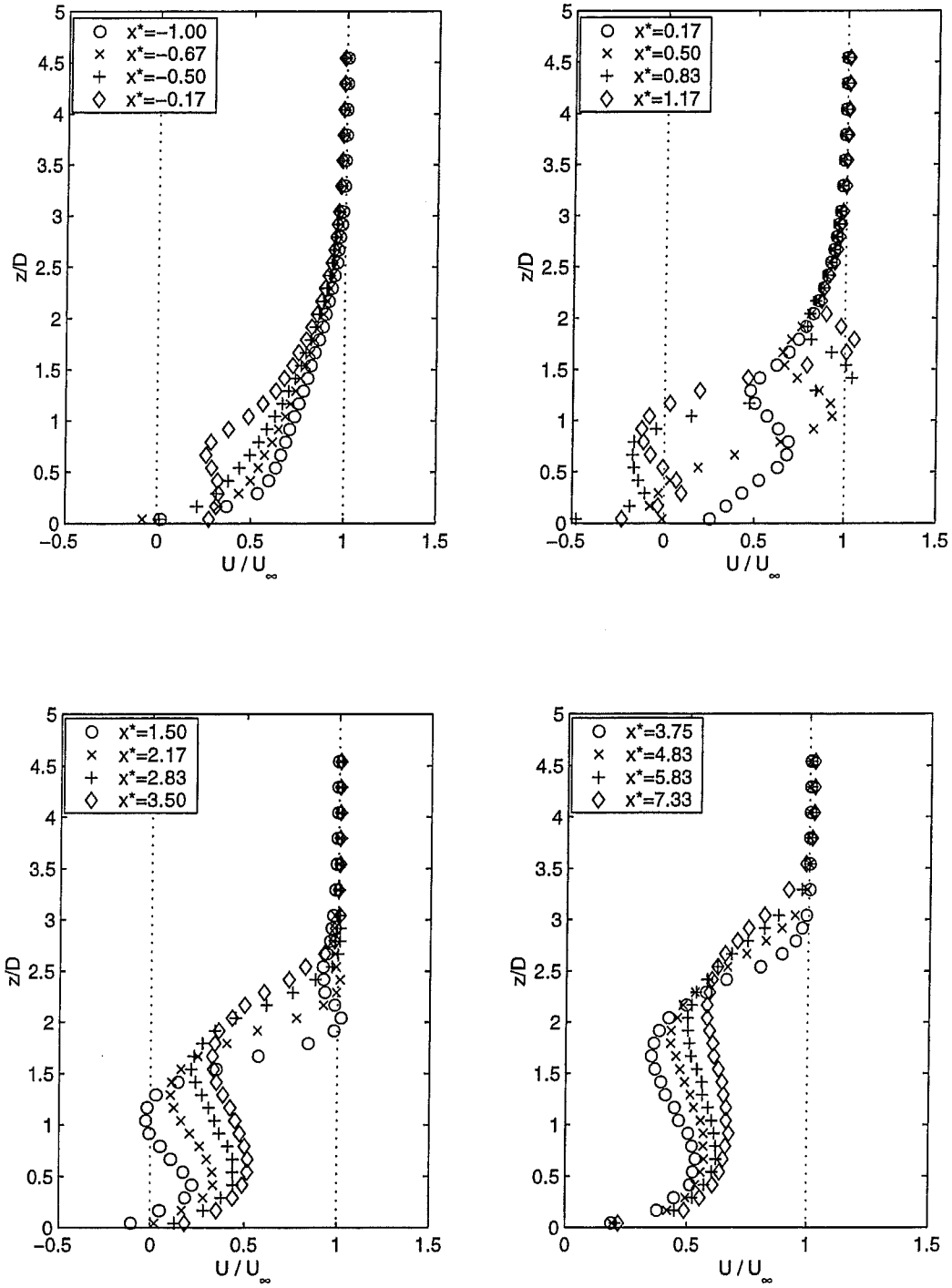

Fig. 4.2.12 Variation of the normalized streamwise mean velocity U^* with z^* at various x^* locations in the y^*=0 plane for R=1.3

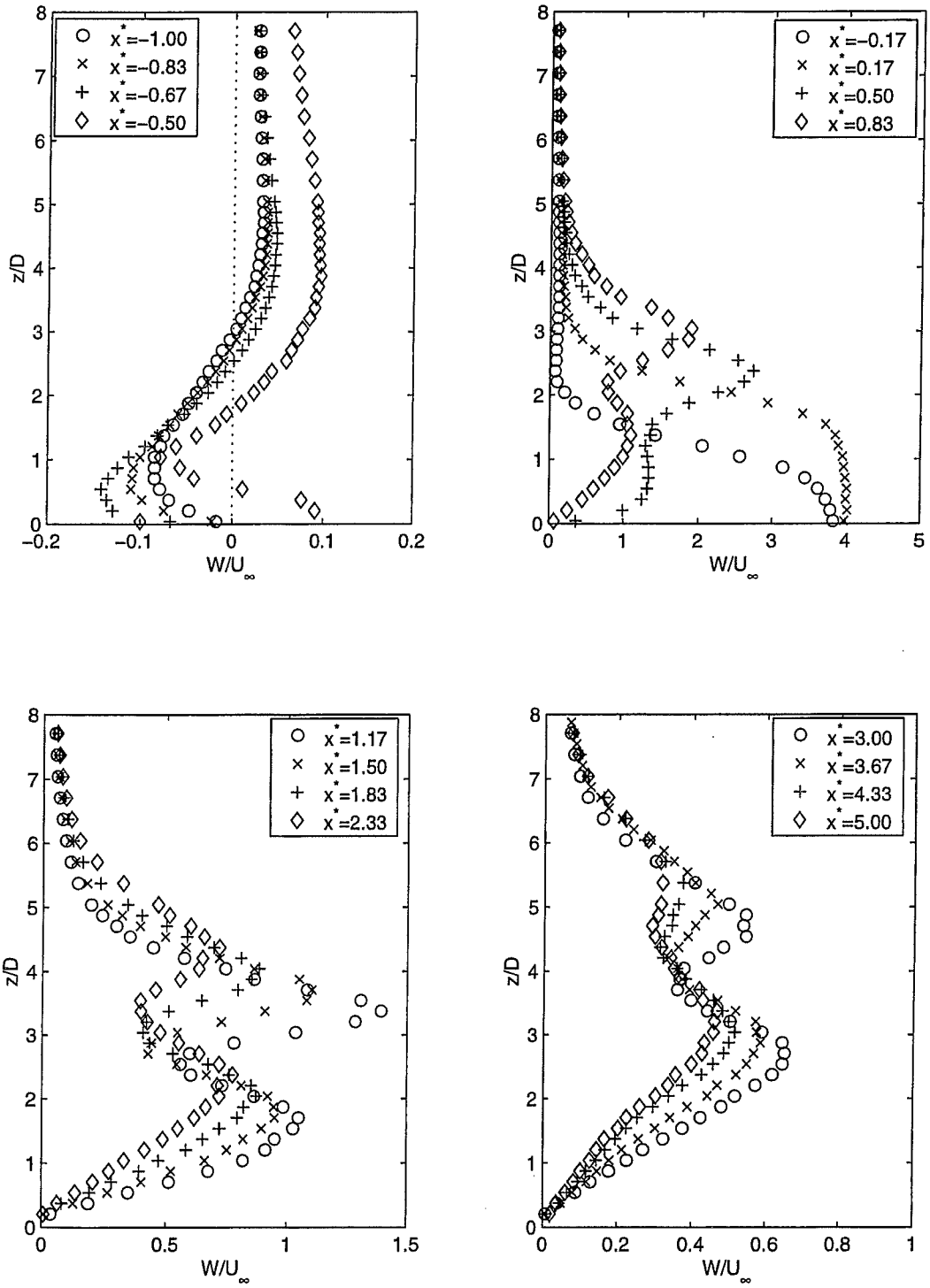

Fig. 4.2.13 Variation of the normalized vertical mean velocity W^* with z^* at various x^* locations in the y^*=0 plane for R=3.3

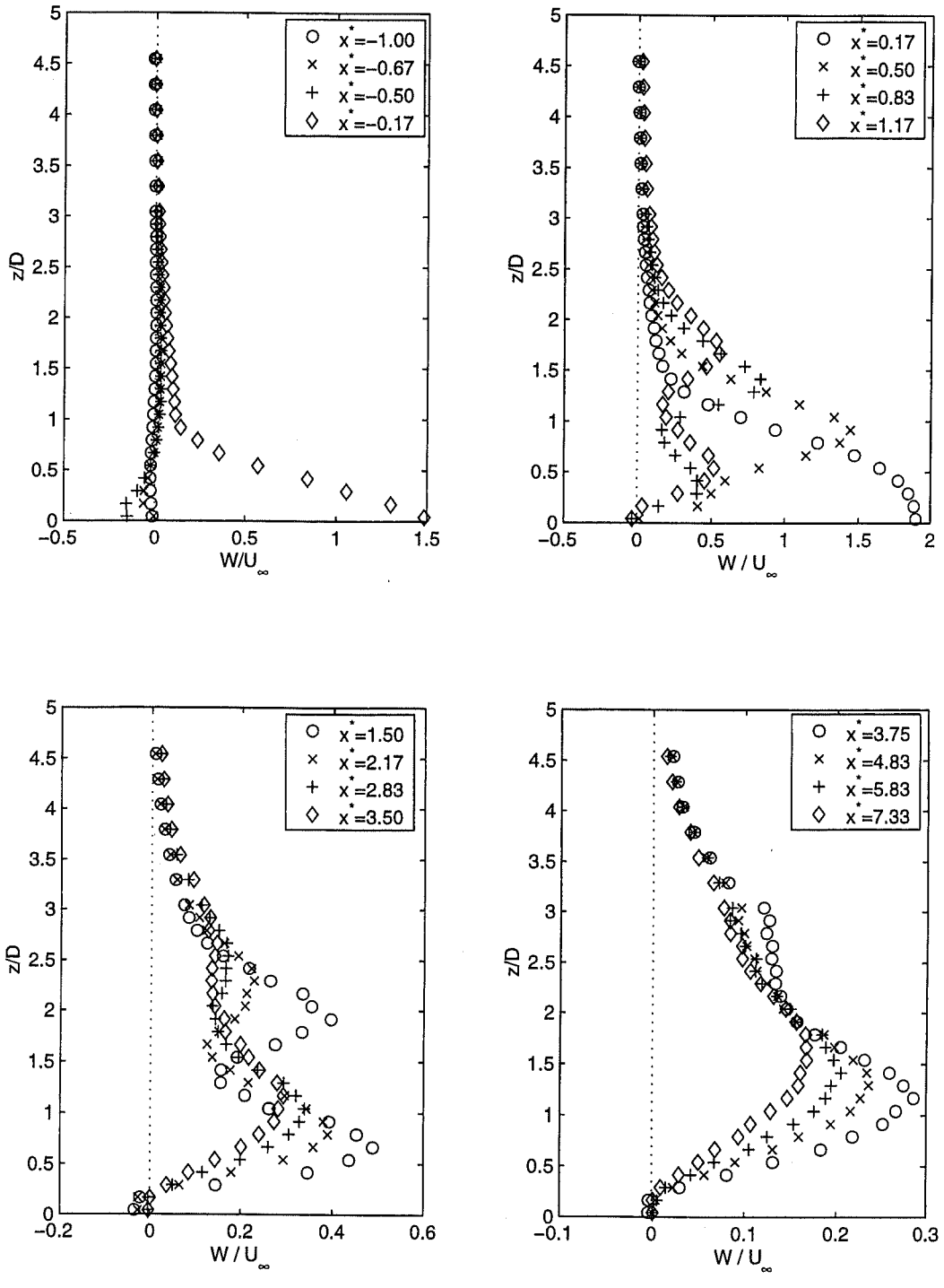

Fig. 4.2.14 Variation of the normalized vertical mean velocity W^* with z^* at various x^* locations in the y^*=0 plane for R=1.3

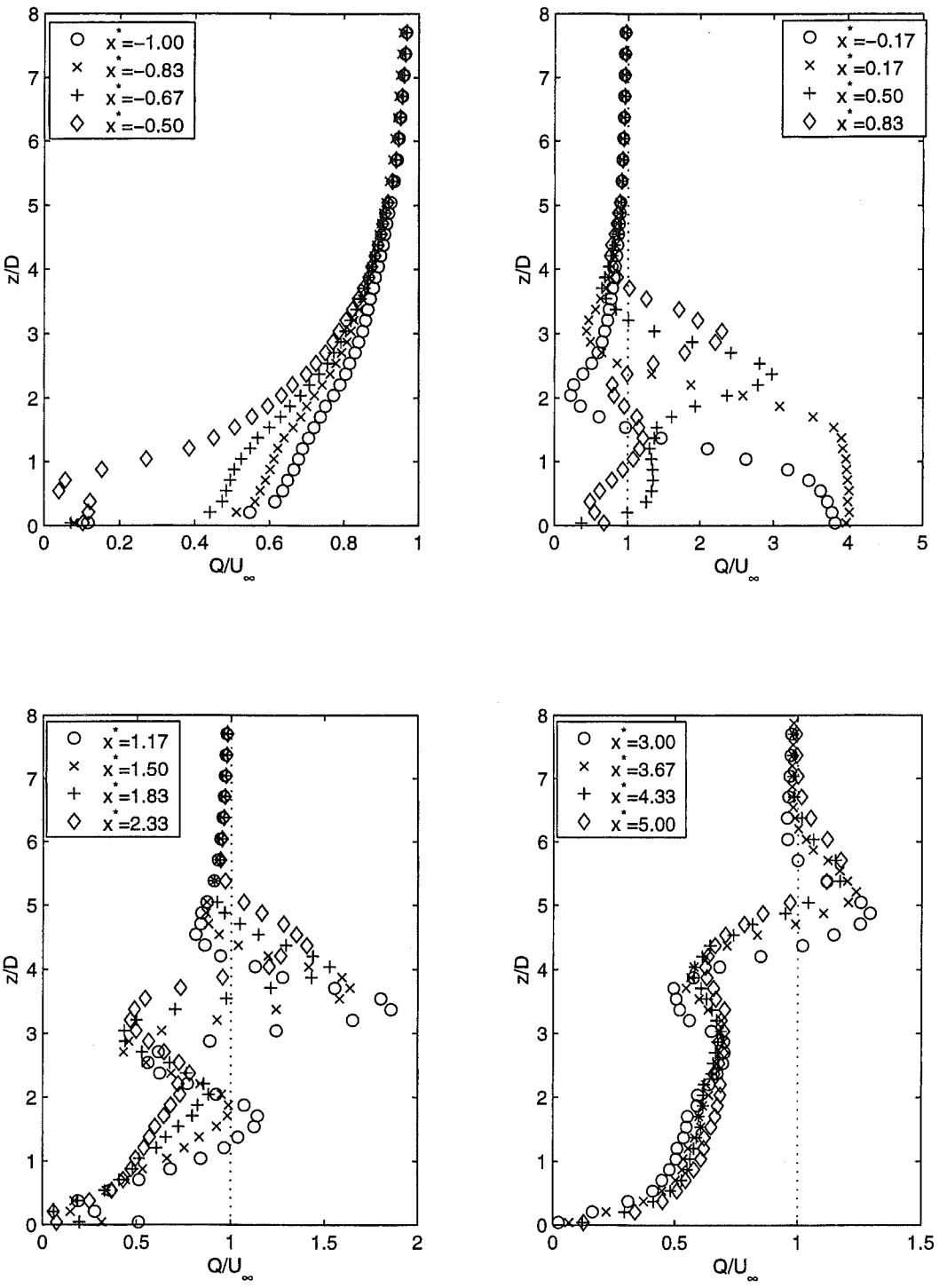

Fig. 4.2.15 Variation of the normalized total mean velocity (speed) Q^* with z^* at various x^* locations in the y^*=0 plane for R=3.3

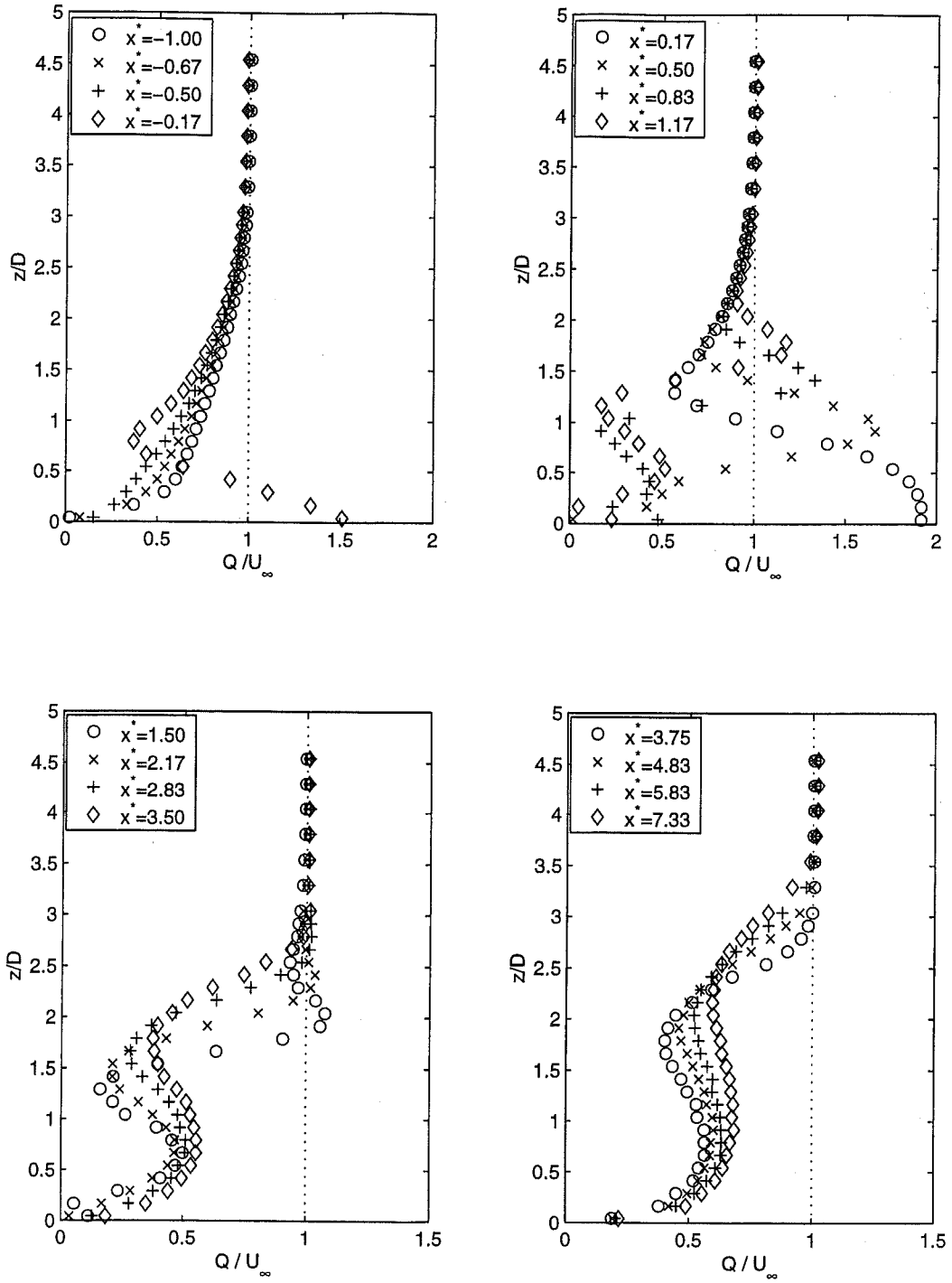

Fig. 4.2.16 Variation of the normalized total mean velocity (speed) Q^* with z^* at various x^* locations in the y^*=0 plane for R=1.3

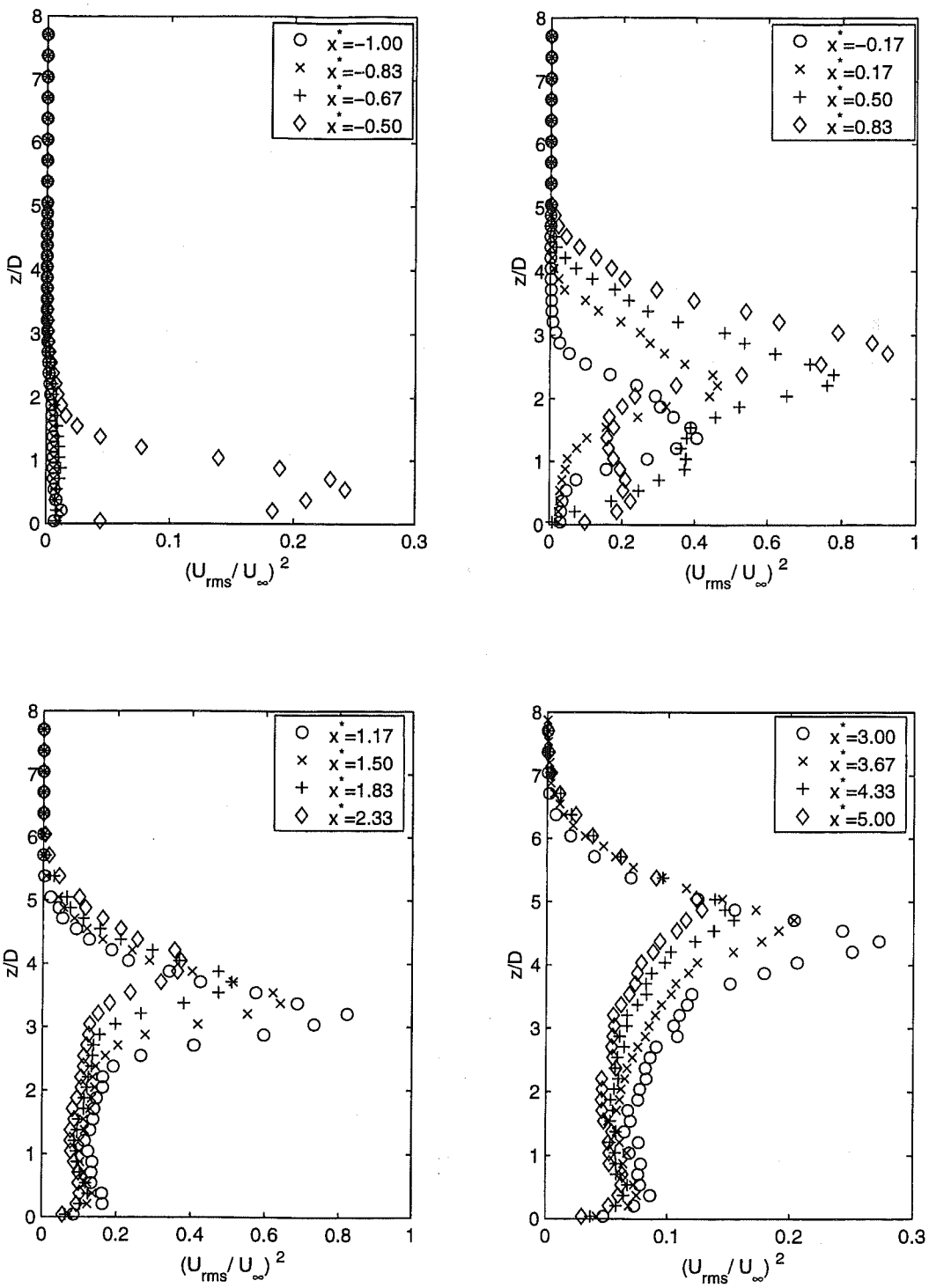

Fig. 4.2.17 Variation of the normalized turbulent stress uu^* with z^* at various x^* locations in the y^*=0 plane for R=3.3

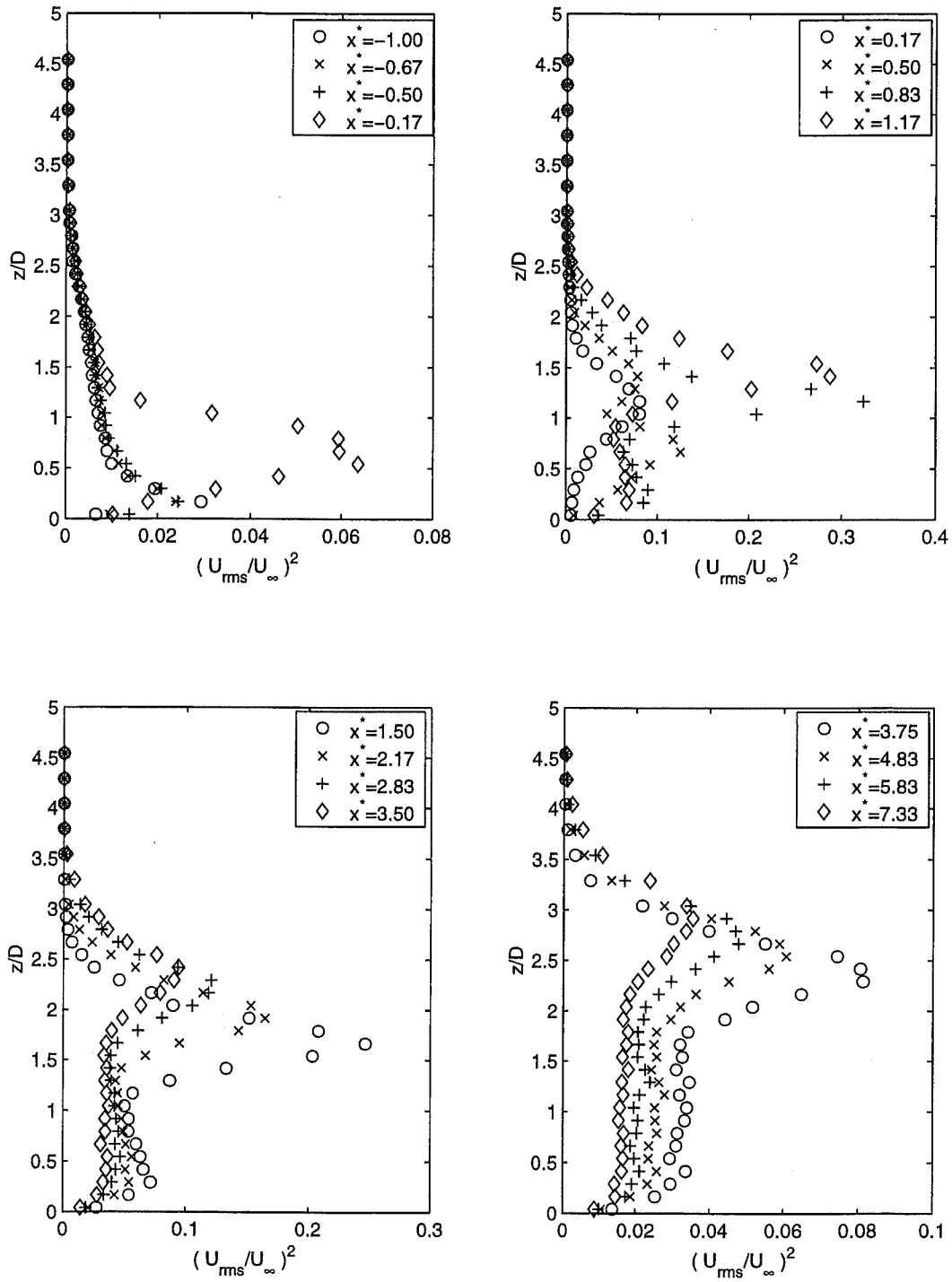

Fig. 4.2.18 Variation of the normalized turbulent stress uu^* with z^* at various x^* locations in the y^*=0 plane for R=1.3

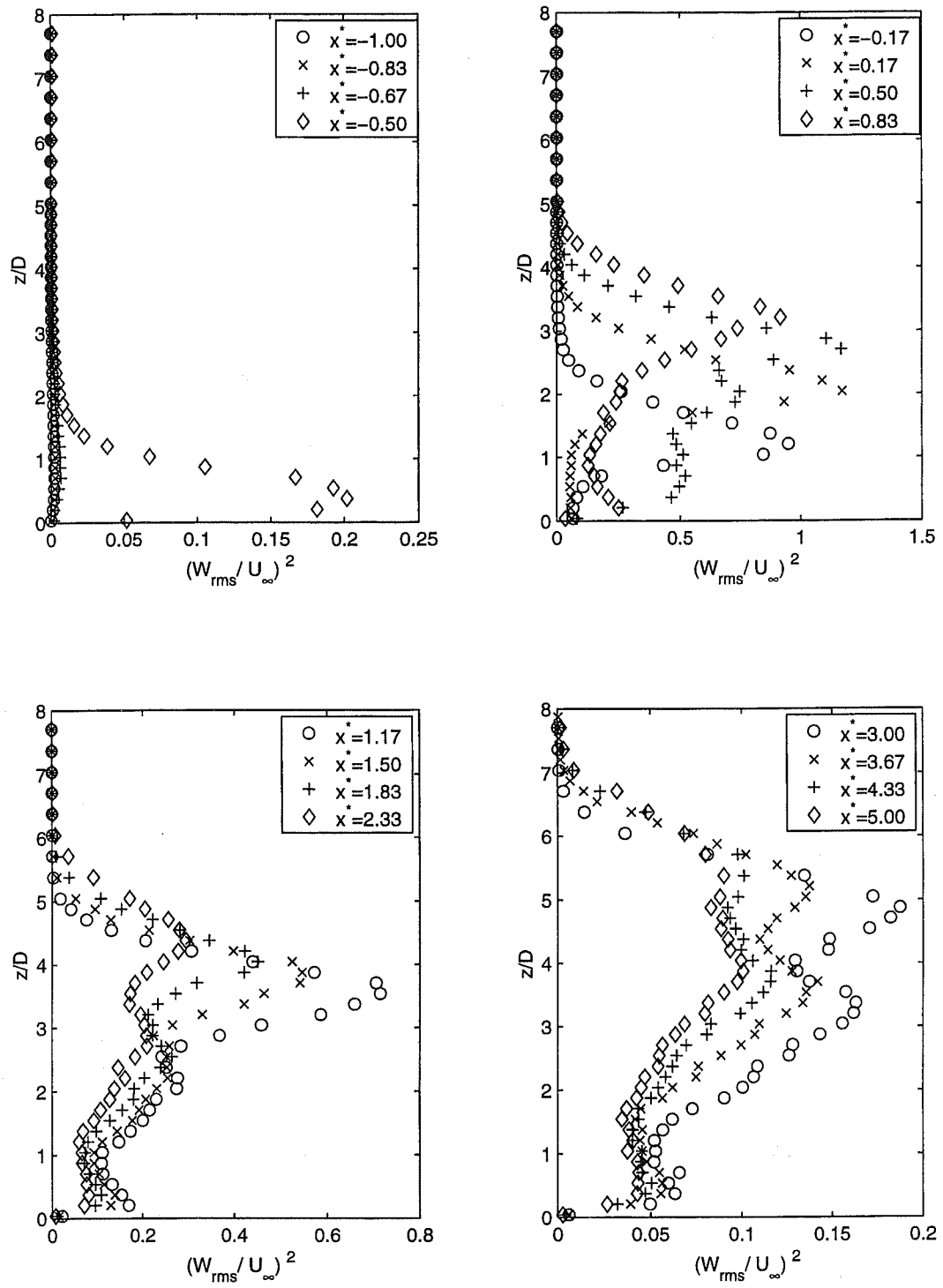

Fig. 4.2.19 Variation of the normalized turbulent stress ww^* with z^* at various x^* locations in the y^*=0 plane for R=3.3

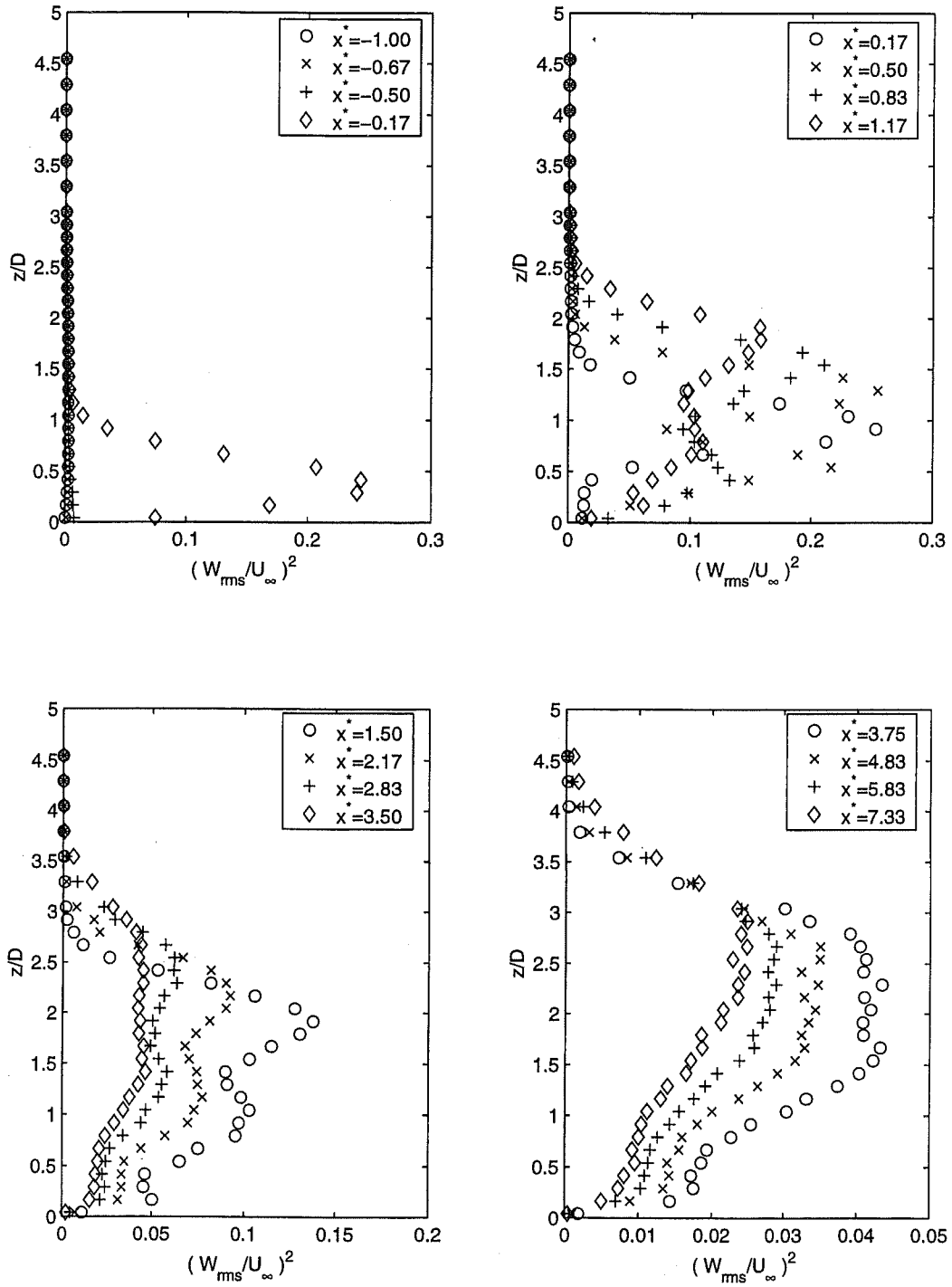

Fig. 4.2.20 Variation of the normalized turbulent stress ww^* with z^* at various x^* locations in the y^*=0 plane for R=1.3

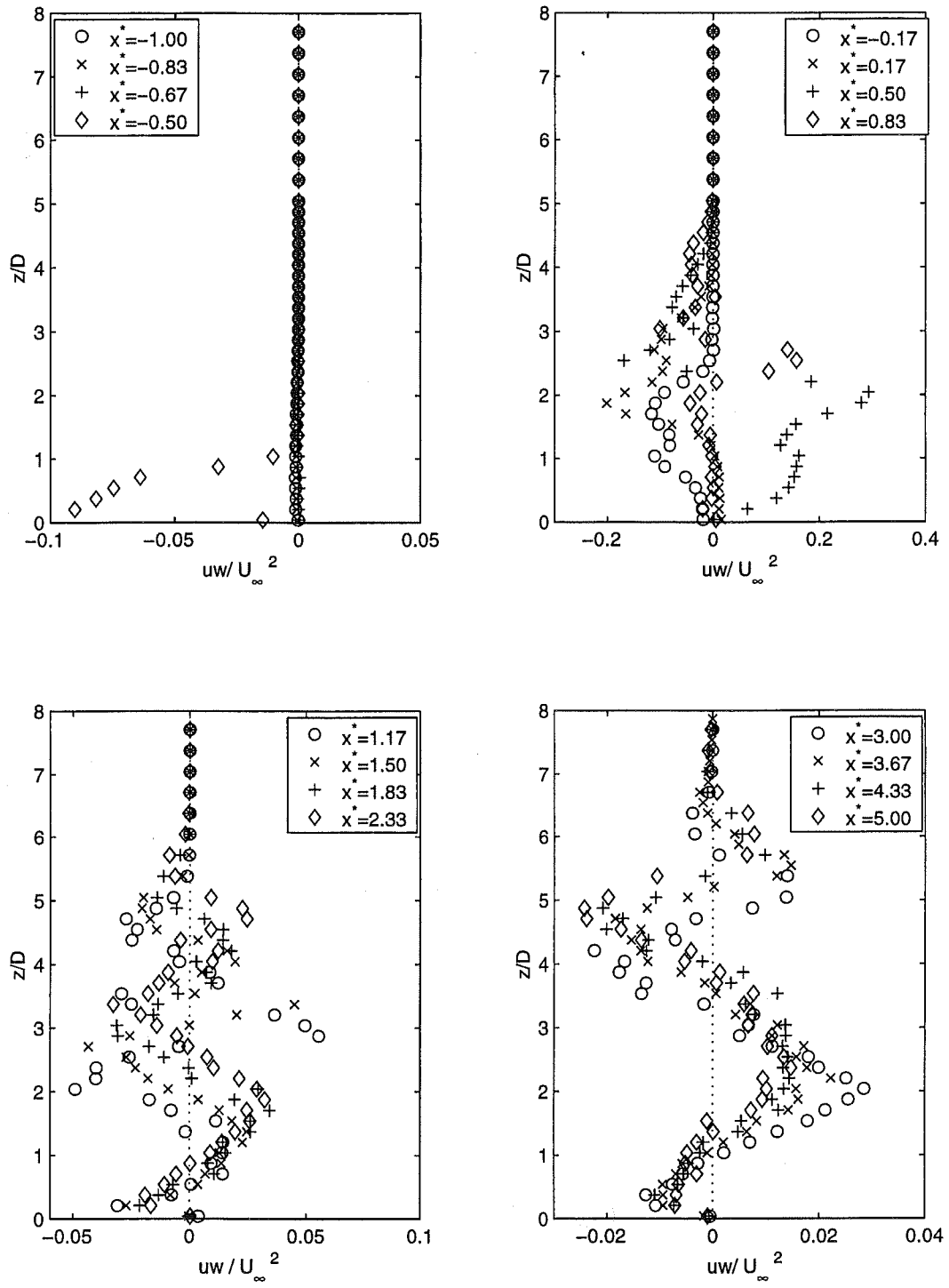

Fig. 4.2.21 Variation of the normalized turbulent shear stress uw^* with z^* at various x^* locations in the y^*=0 plane for R=3.3

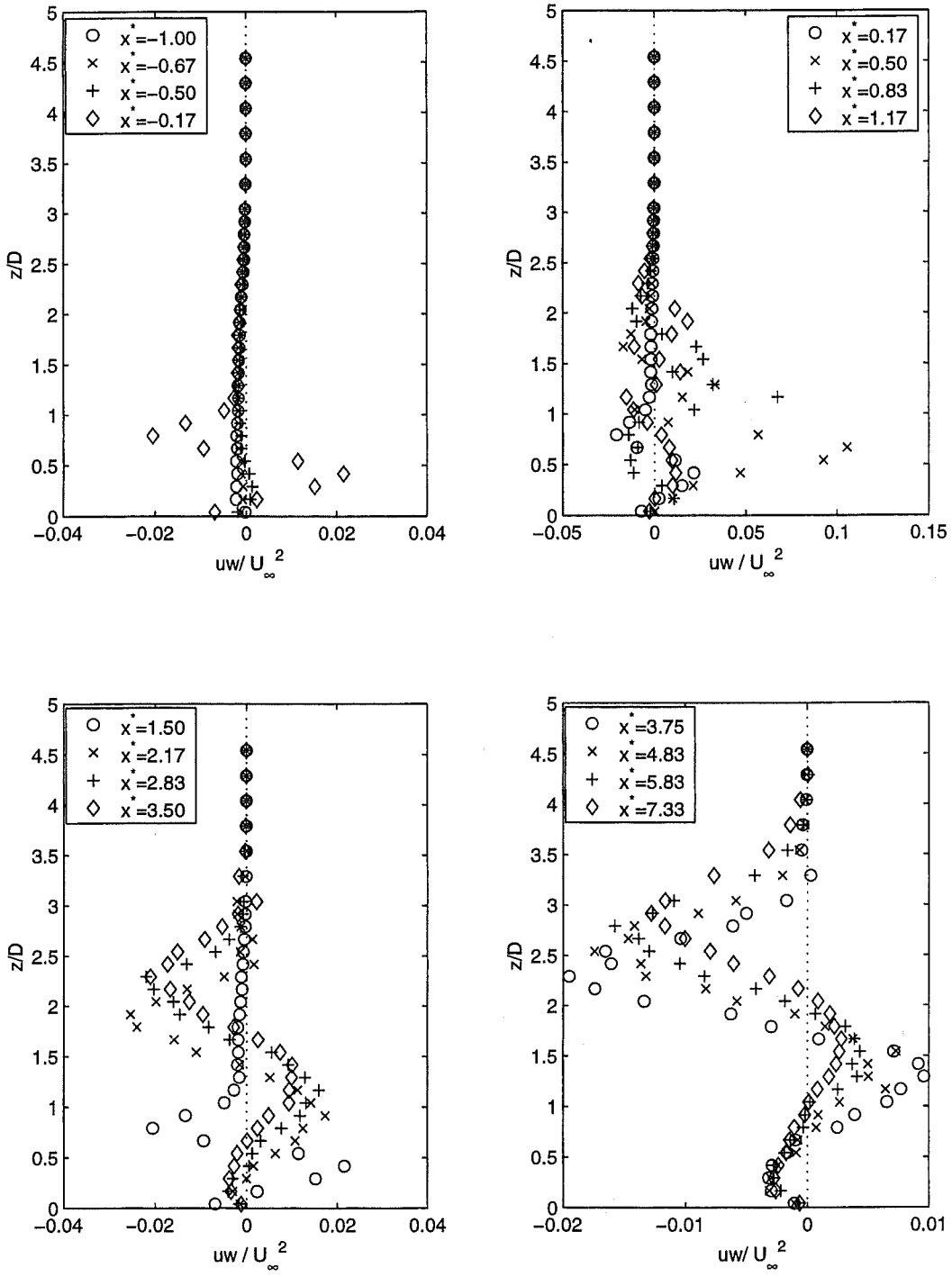

Fig. 4.2.22 Variation of the normalized turbulent shear stress uw^* with z^* at various x^* locations in the y^*=0 plane for R=1.3

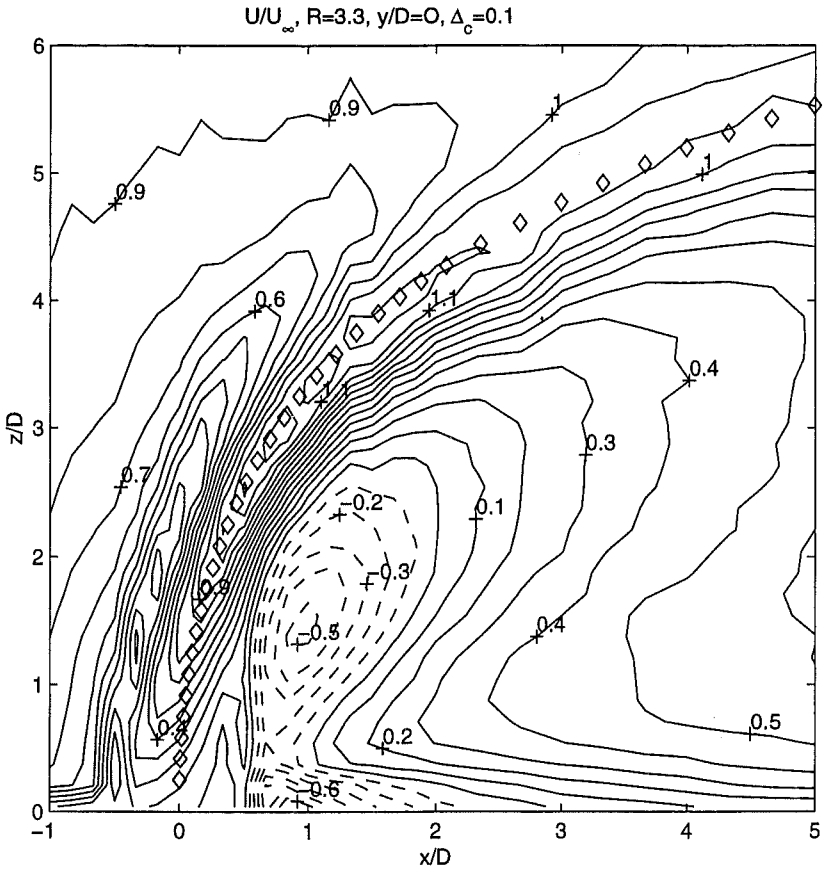

Fig. 4.2.23 Contour plot of the normalized streamwise mean velocity U^* in the y^*=0 plane for R=3.3

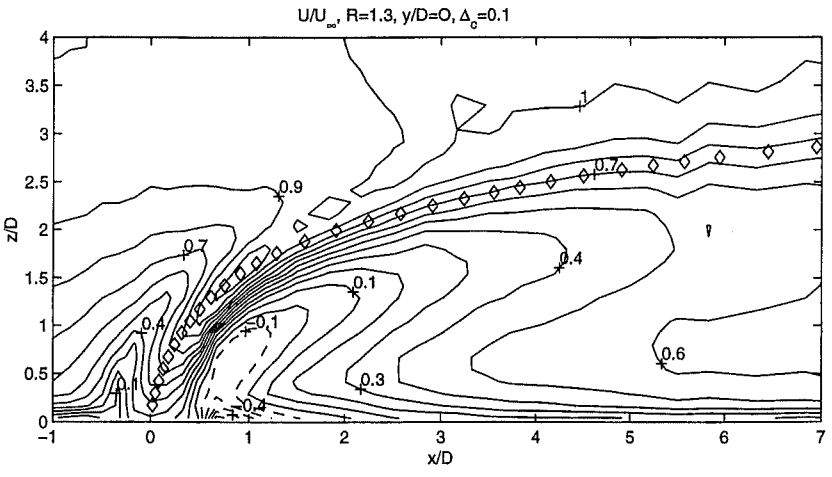

Fig. 4.2.24 Contour plot of the normalized streamwise mean velocity U^* in the y^*=0 plane for R=1.3

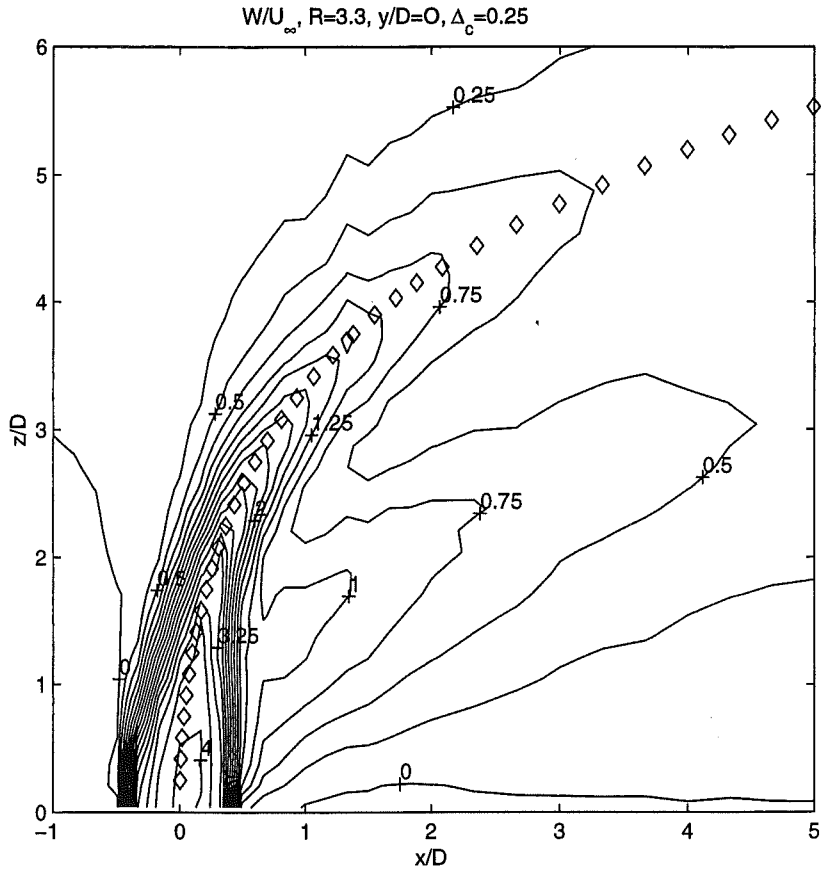

Fig. 4.2.25 Contour plot of the normalized vertical mean velocity W^* in the y^*=0 plane for R=3.3

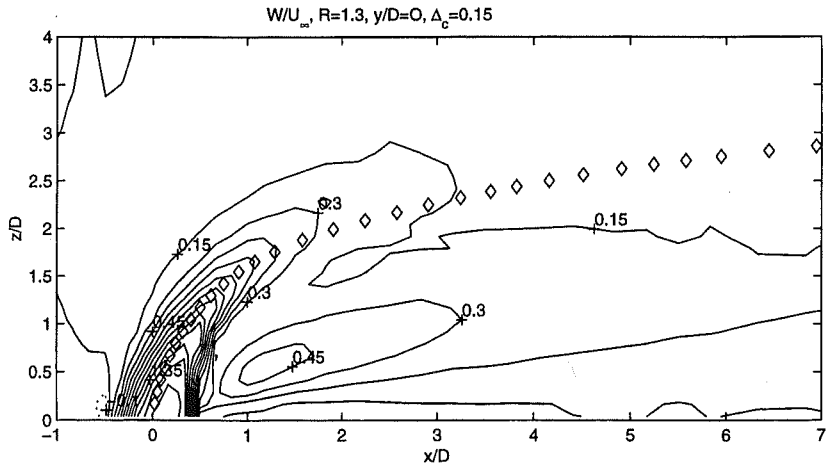

Fig. 4.2.26 Contour plot of the normalized vertical mean velocity W^* in the y^*=0 plane for R=1.3

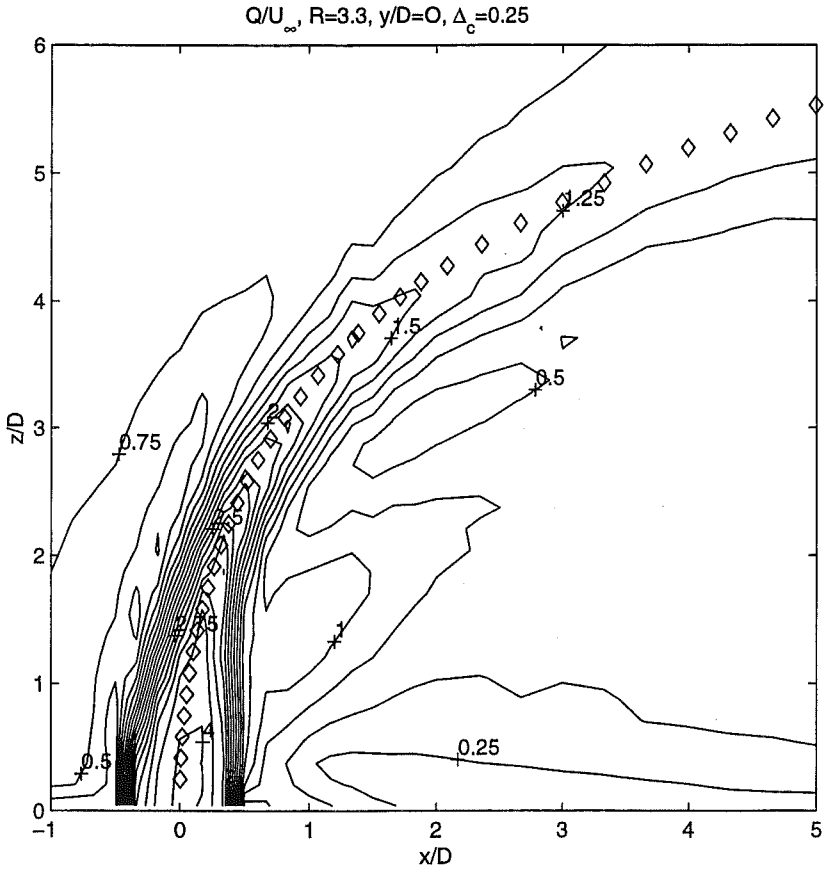

Fig. 4.2.27 Contour plot of the normalized total mean velocity (speed) Q^* in the y^*=0 plane for R=3.3

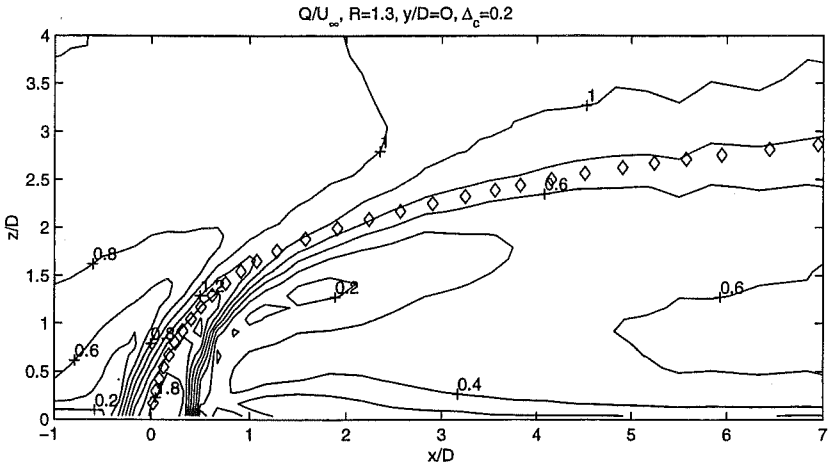

Fig. 4.2.28 Contour plot of the normalized total mean velocity (speed) Q^* in the y^*=0 plane for R=1.3

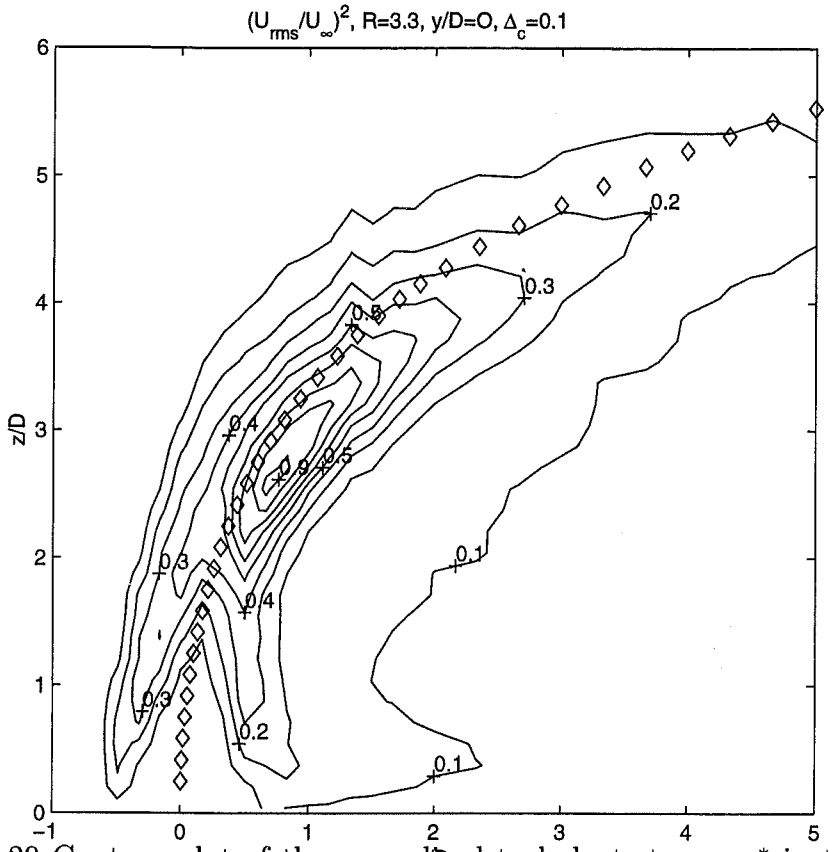

Fig. 4.2.29 Contour plot of the normalized turbulent stress uu^* in the y^*=0 plane for R=3.3

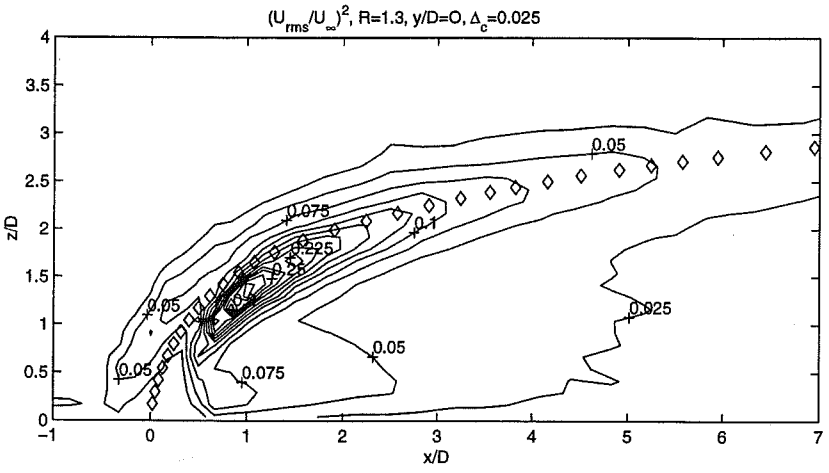

Fig. 4.2.30 Contour plot of the normalized turbulent stress uu^* in the y^*=0 plane for R=1.3

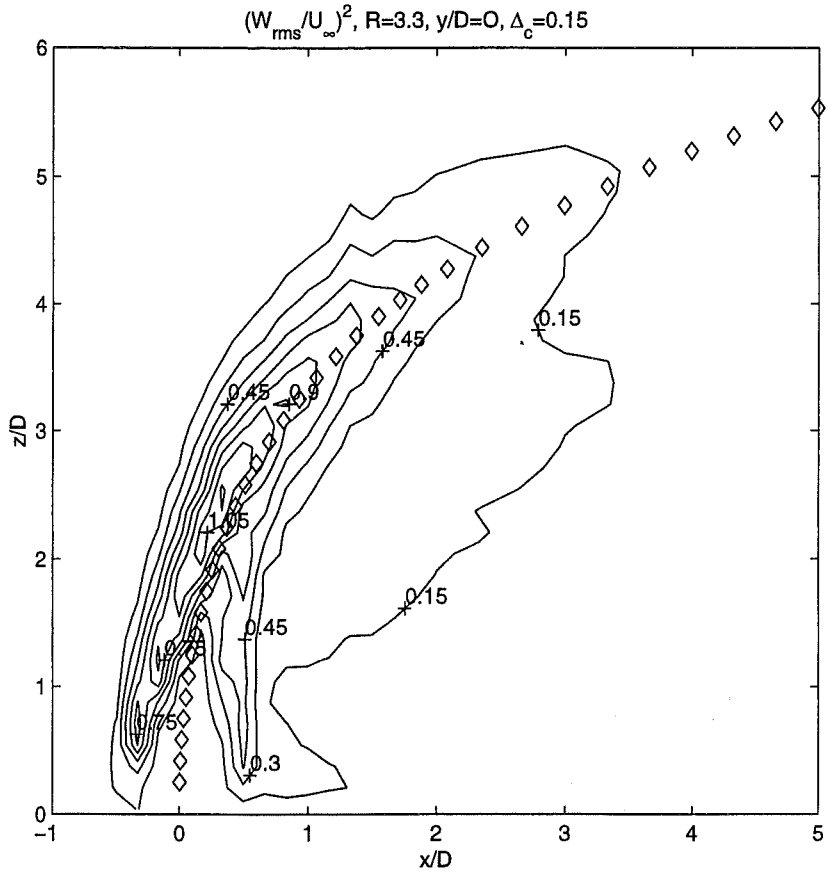

Fig. 4.2.31 Contour plot of the normalized turbulent stress ww^* in the y^*=0 plane for R=3.3

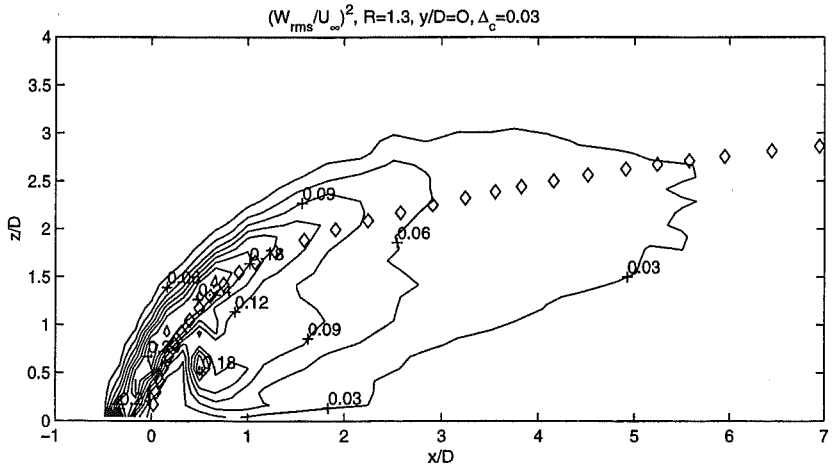

Fig. 4.2.32 Contour plot of the normalized turbulent stress ww^* in the y^*=0 plane for R=1.3

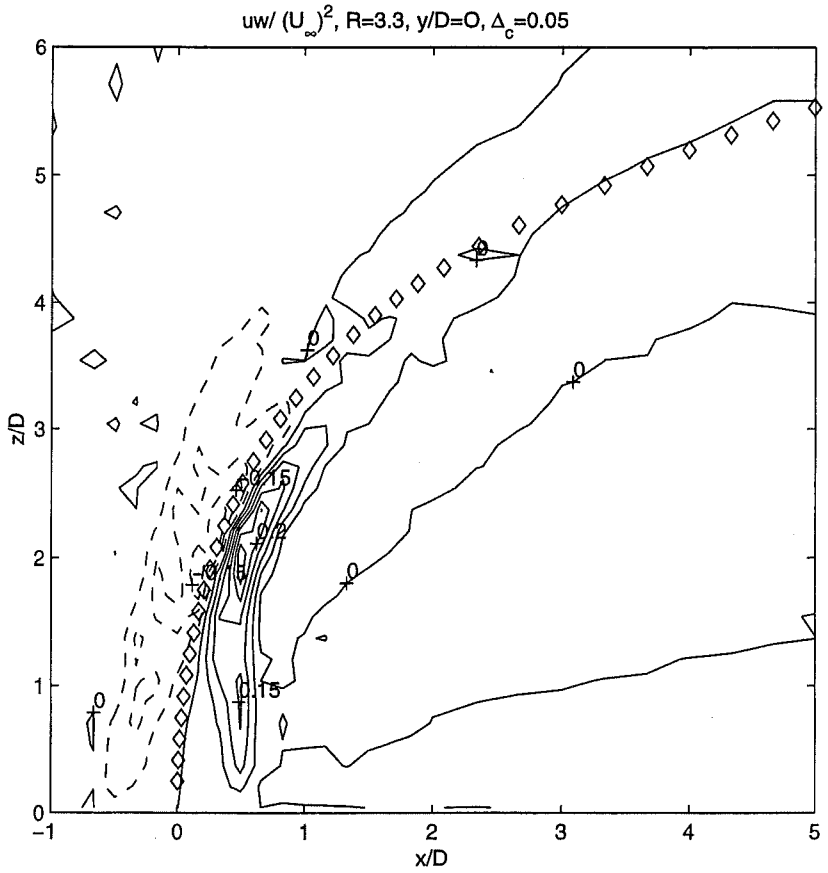

Fig. 4.2.33 Contour plot of the normalized turbulent shear stress uw^* in the y^*=0 plane for R=3.3

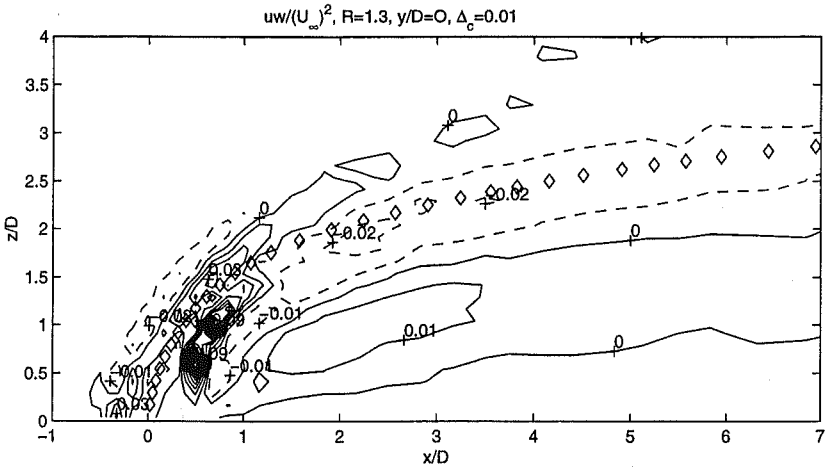

Fig. 4.2.34 Contour plot of the normalized turbulent shear stress uw^* in the y^*=0 plane for R=1.3

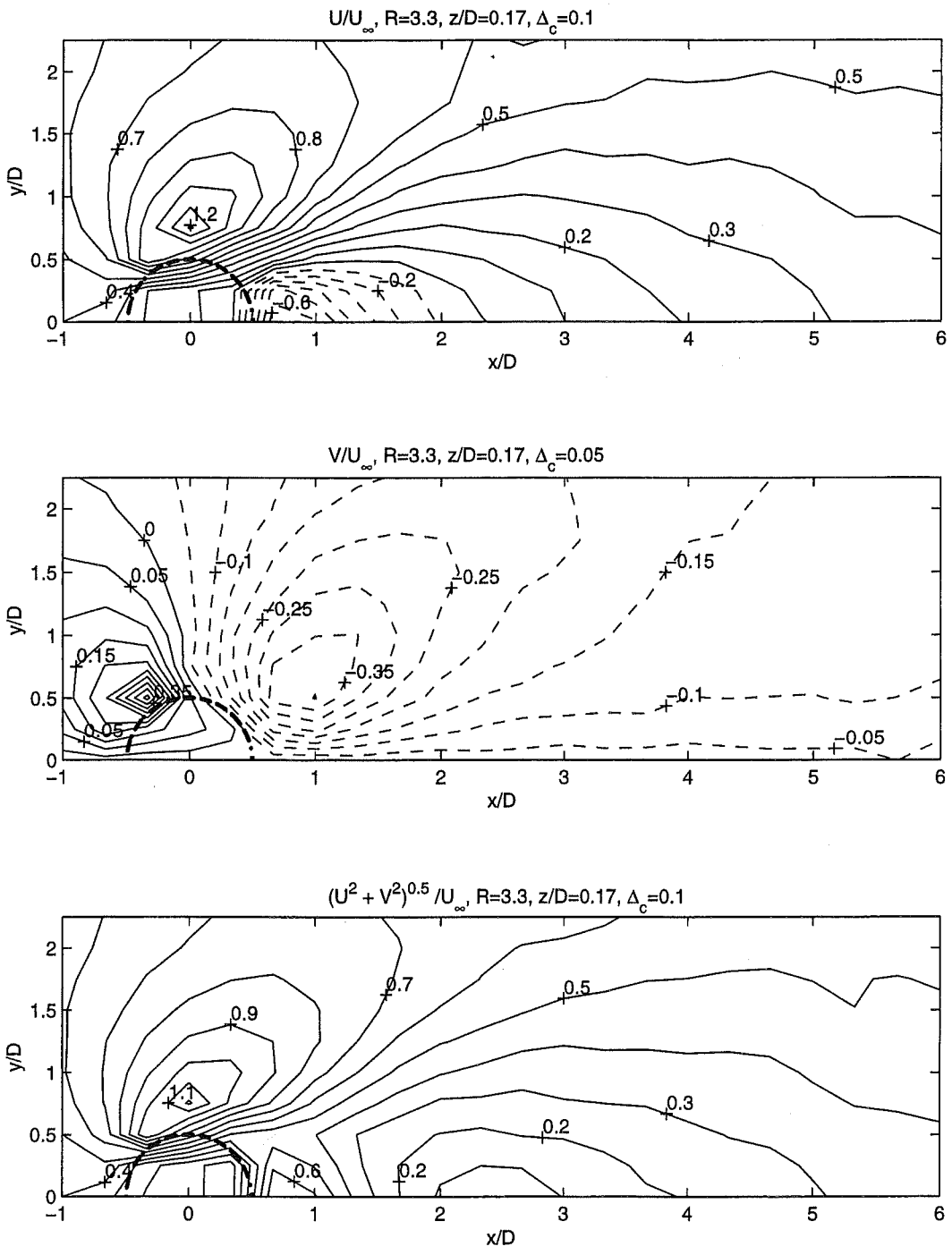

Fig. 4.3.1 Contour plots of the normalized mean velocities U^*, V^* and $Q_z{}^*$ in the z^*=0.17 plane for R=3.3

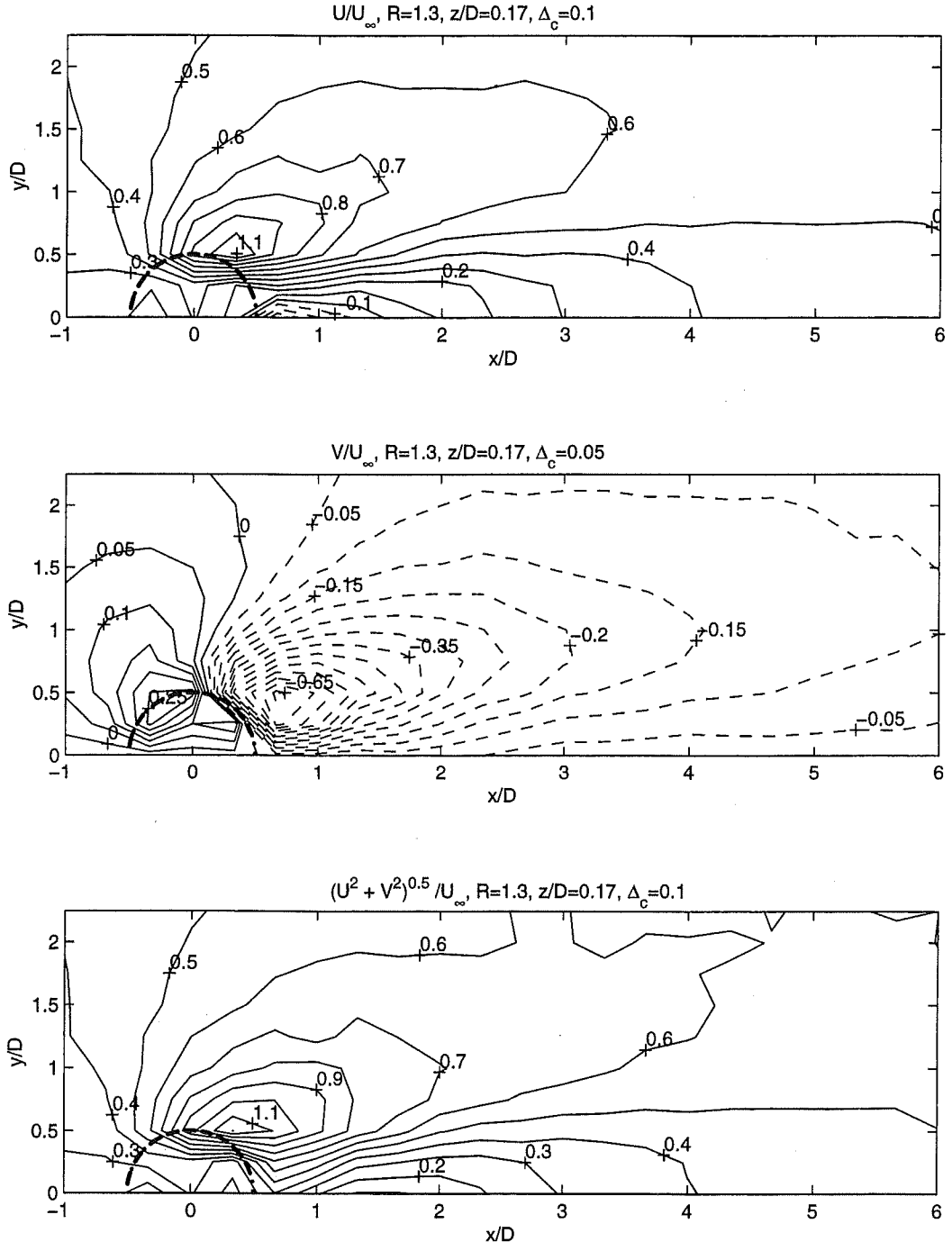

Fig. 4.3.2 Contour plots of the normalized mean velocities U^*, V^* and ${Q_z}^*$ in the z^*=0.17 plane for R=1.3

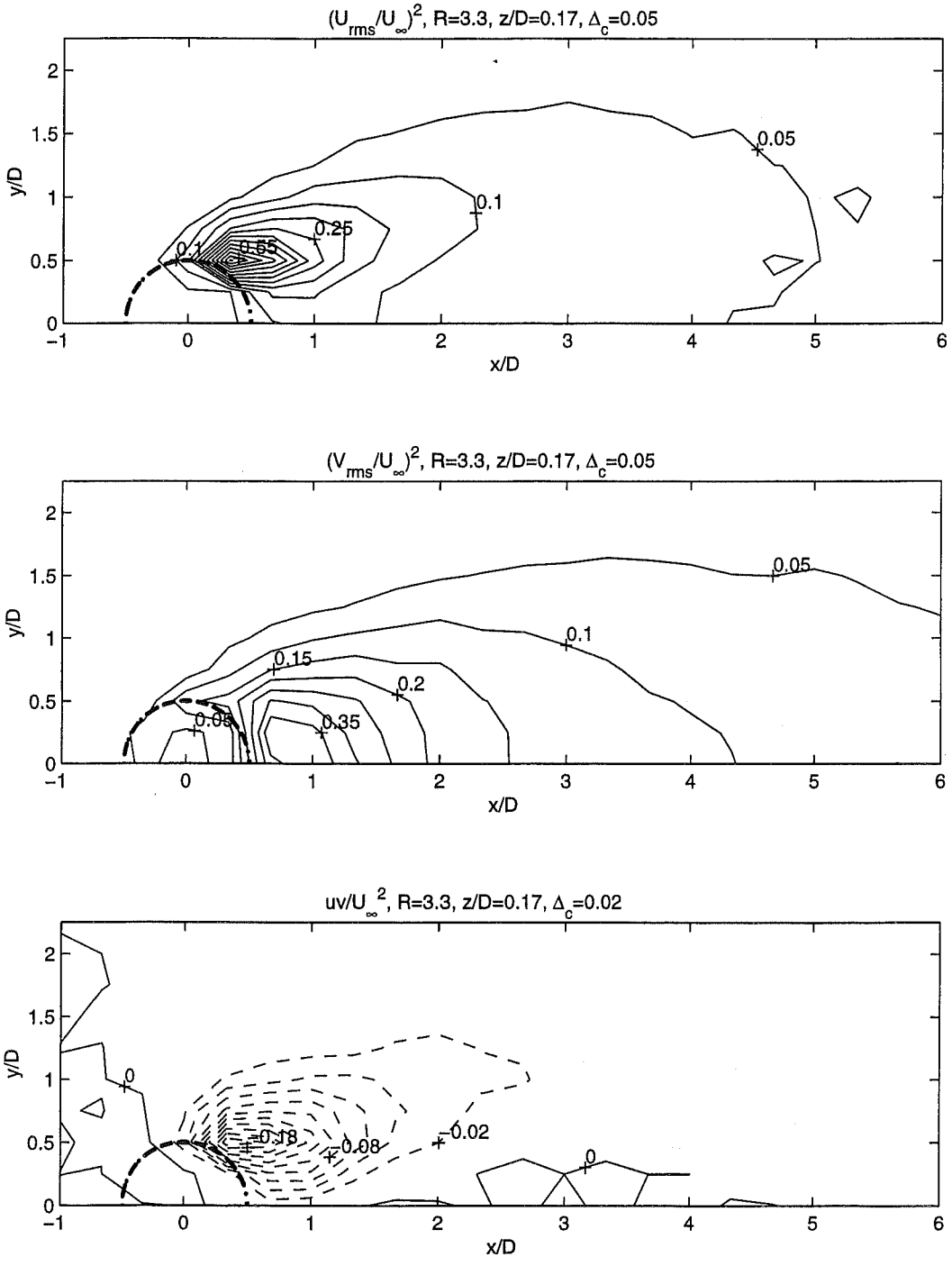

Fig. 4.3.3 Contour plots of the normalized turbulent stresses uu^*, vv^* and uv^* in the z^*=0.17 plane for R=3.3

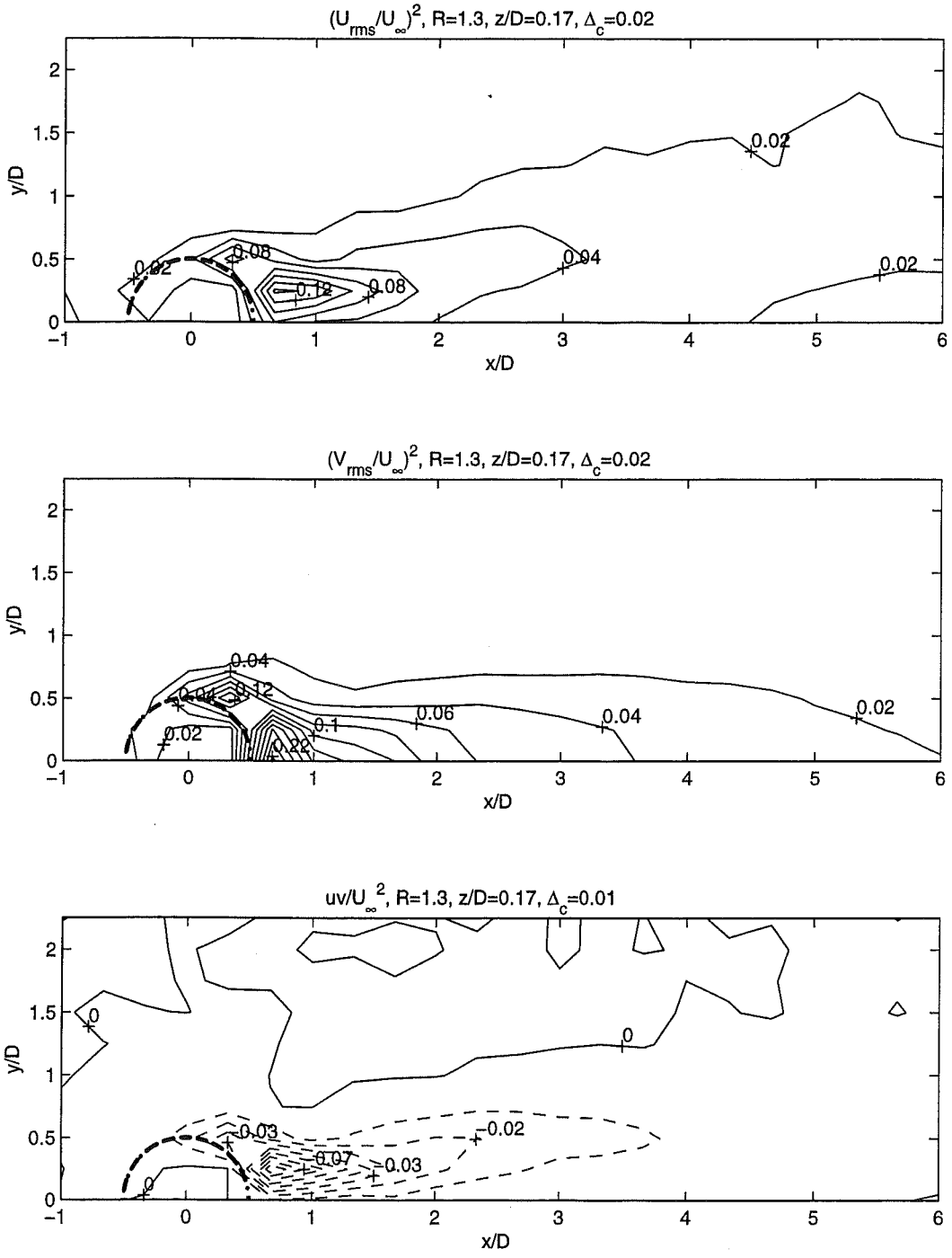

Fig. 4.3.4 Contour plots of the normalized turbulent stresses uu^*, vv^* and uv^* in the z^*=0.17 plane for R=1.3

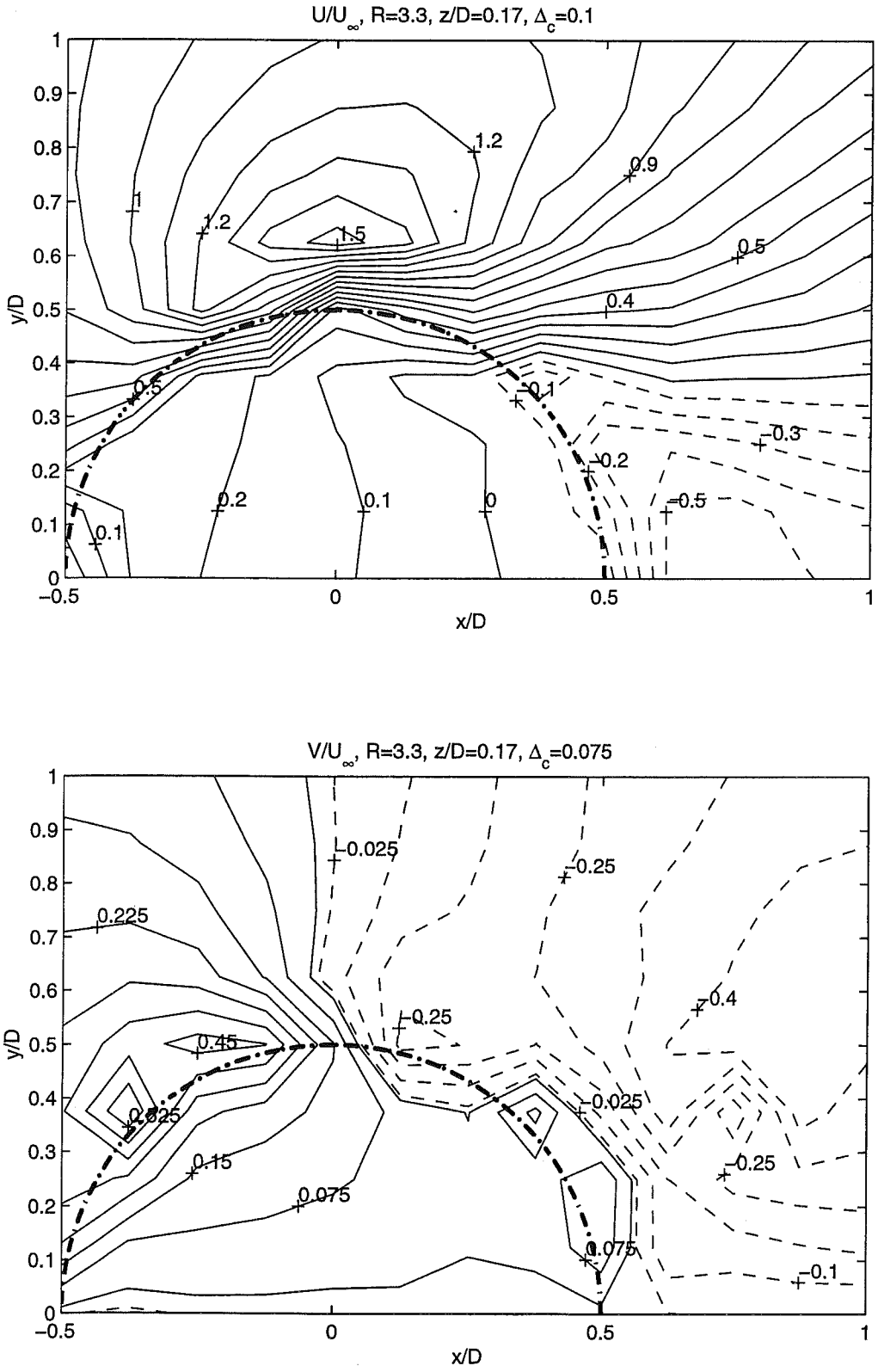

Fig. 4.3.5 Contour plots of the normalized streamwise and spanwise mean velocities U^* and V^* in the z^*=0.17 plane near the jet exit for R=3.3

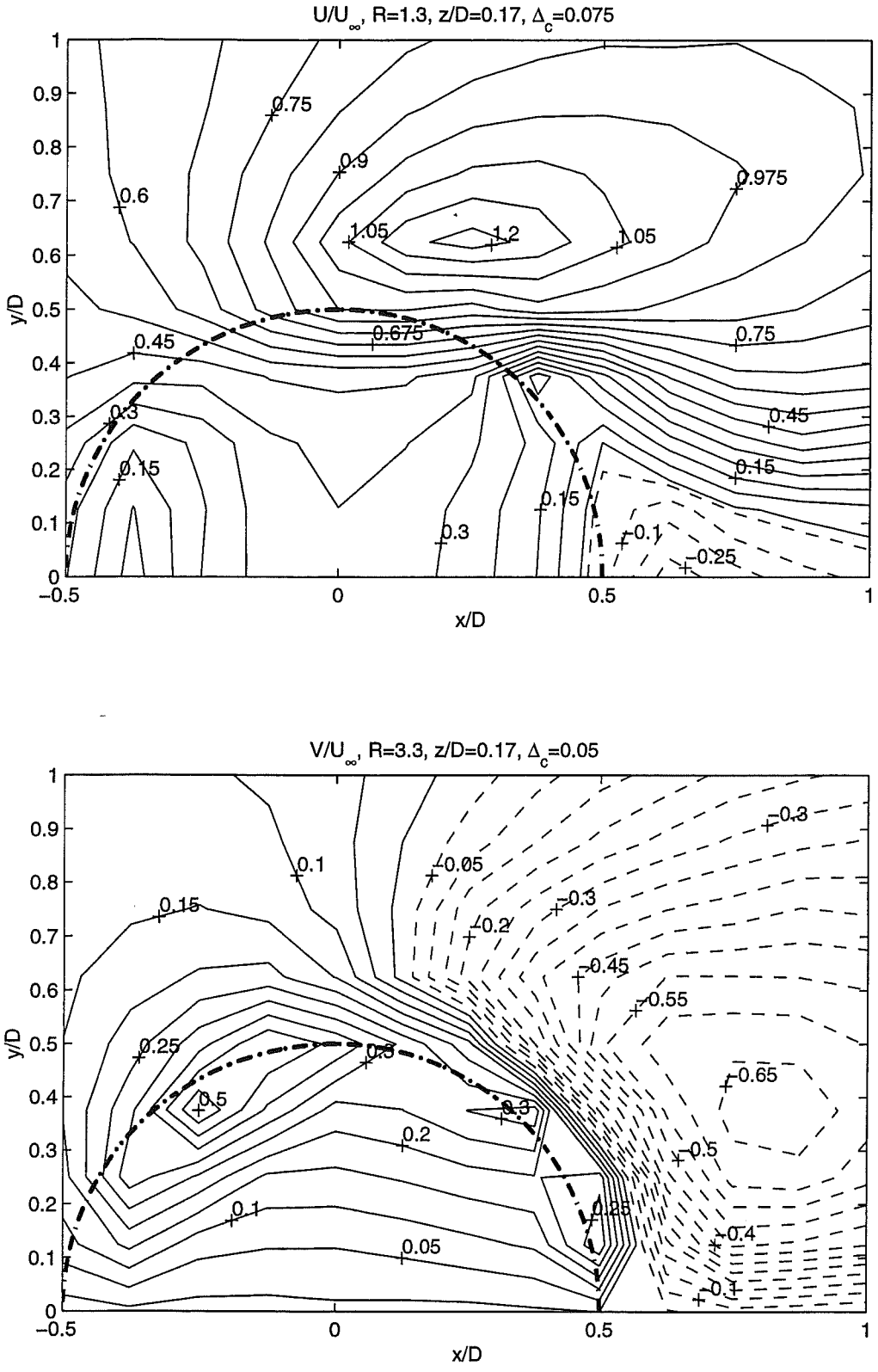

Fig. 4.3.6 Contour plots of the normalized streamwise and spanwise mean velocities U^* and V^* in the z^*=0.17 plane near the jet exit for R=1.3

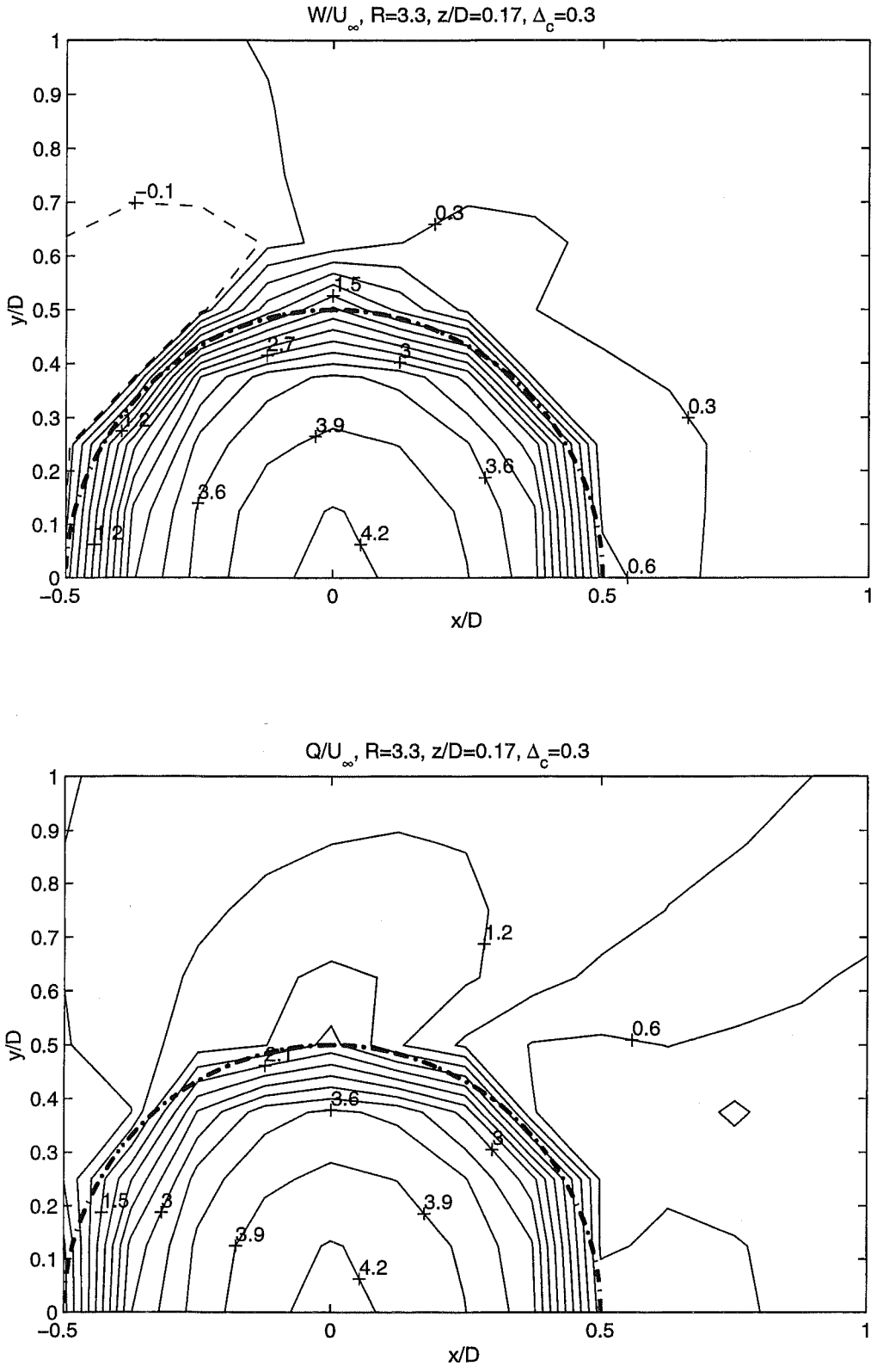

Fig. 4.3.7 Contour plots of the normalized vertical and total mean velocities W^* and Q^* in the z^*=0.17 plane near the jet exit for R=3.3

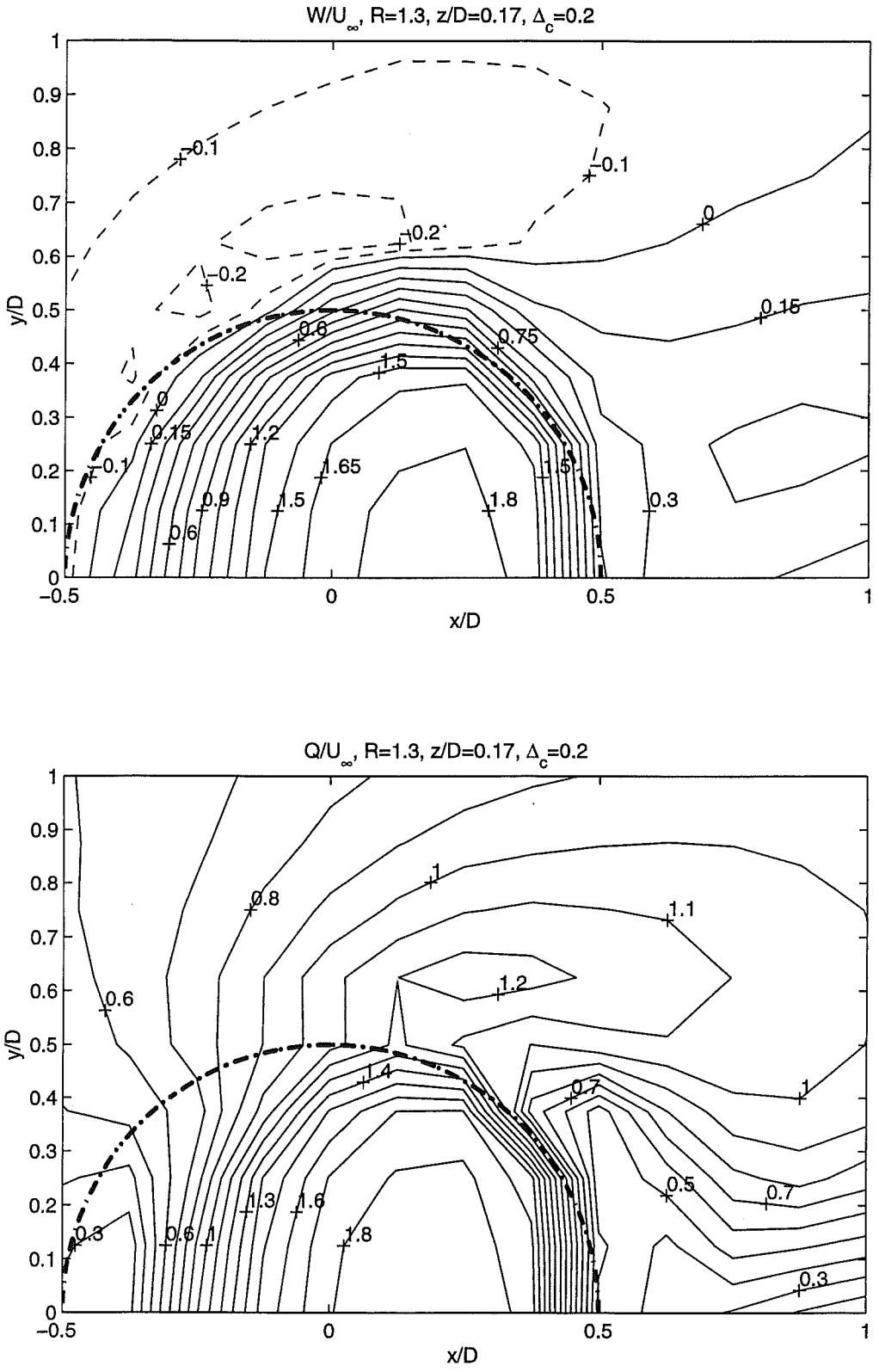

Fig. 4.3.8 Contour plots of the normalized vertical and total mean velocities W^* and Q^* in the z^*=0.17 plane near the jet exit for R=1.3

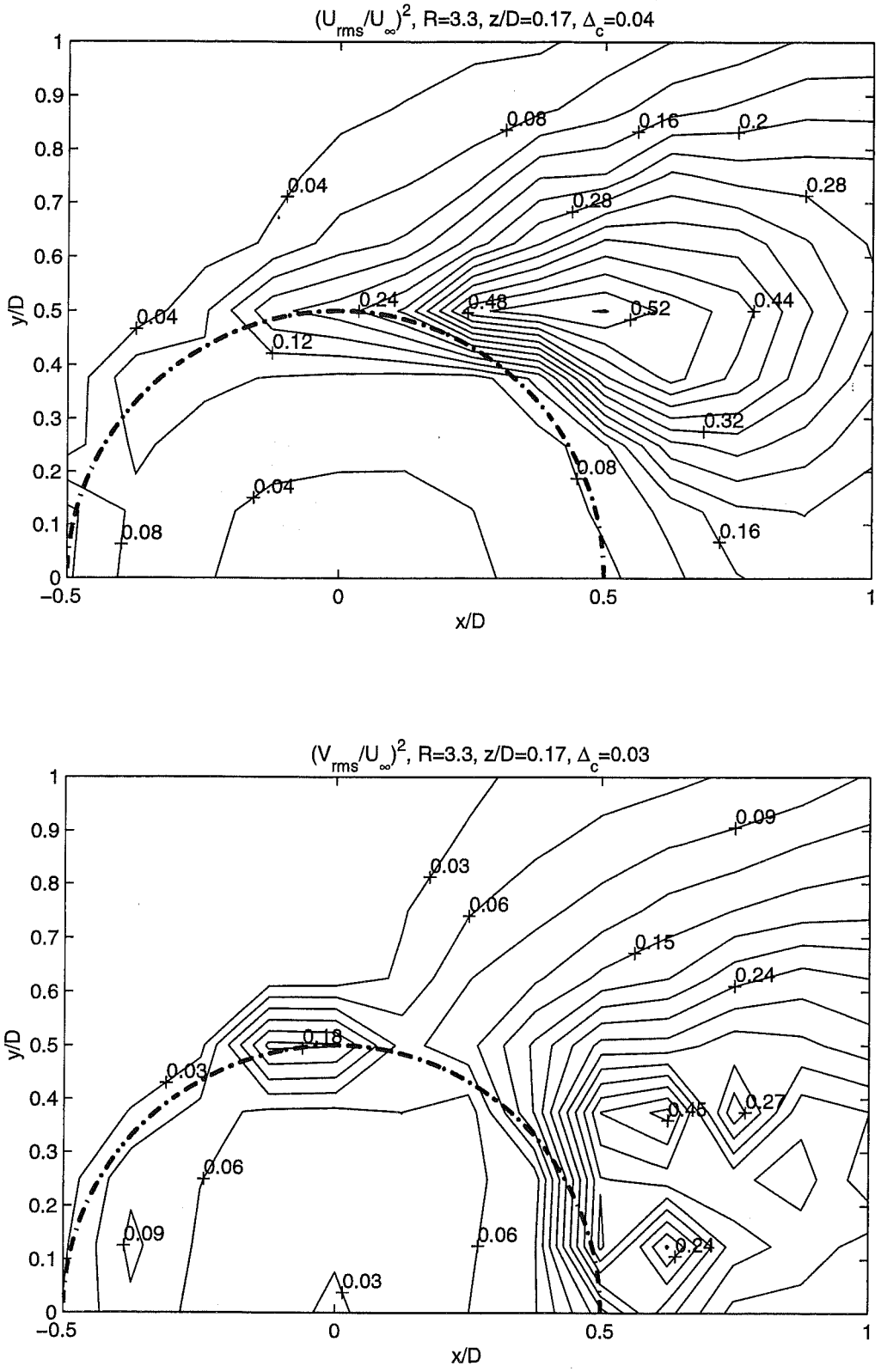

Fig. 4.3.9 Contour plots of the normalized turbulent stresses uu^* and vv^* in the z^*=0.17 plane near the jet exit for R=3.3

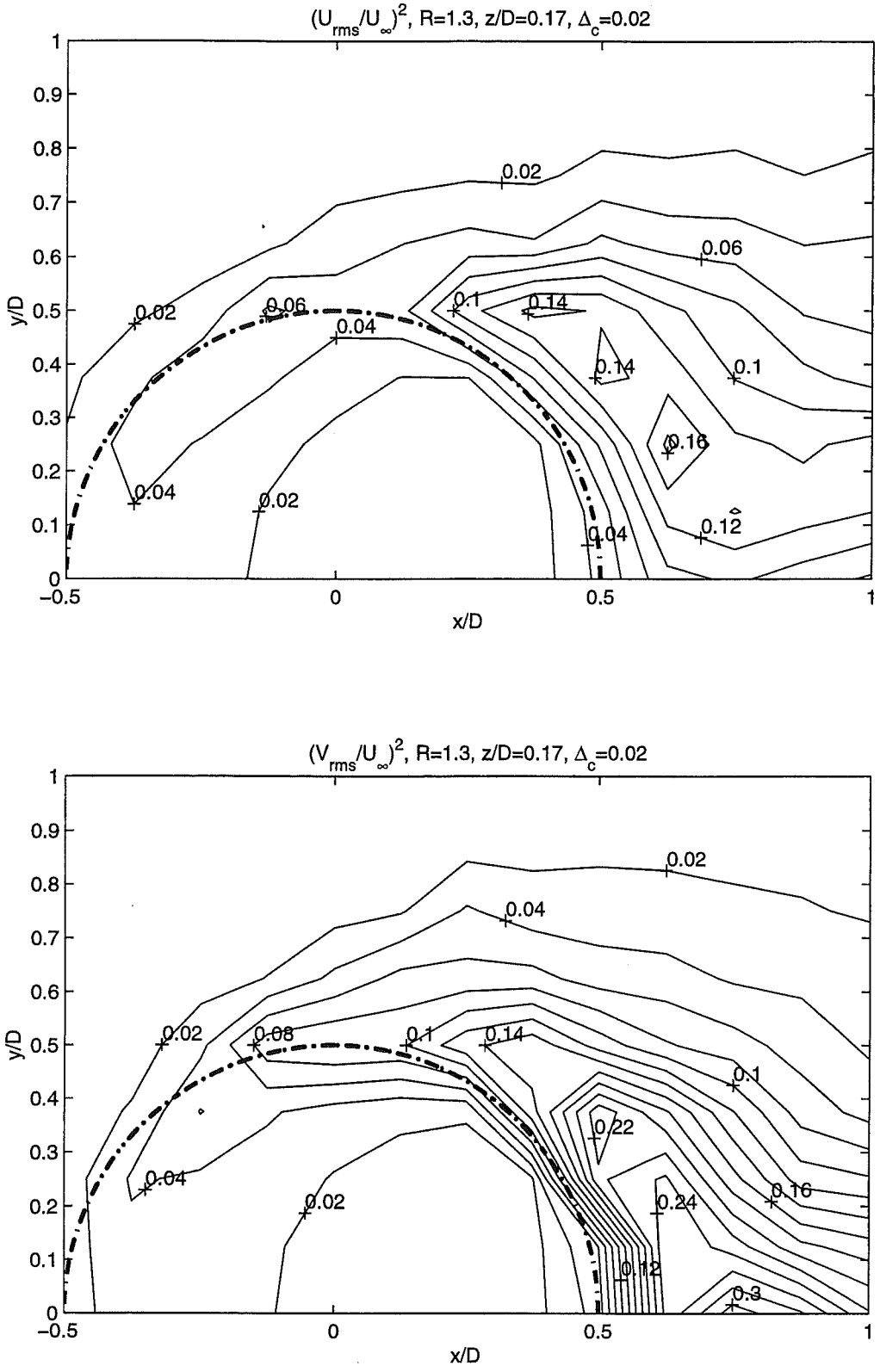

Fig. 4.3.10 Contour plots of the normalized turbulent stresses uu^* and vv^* in the z^*=0.17 plane near the jet exit for R=1.3

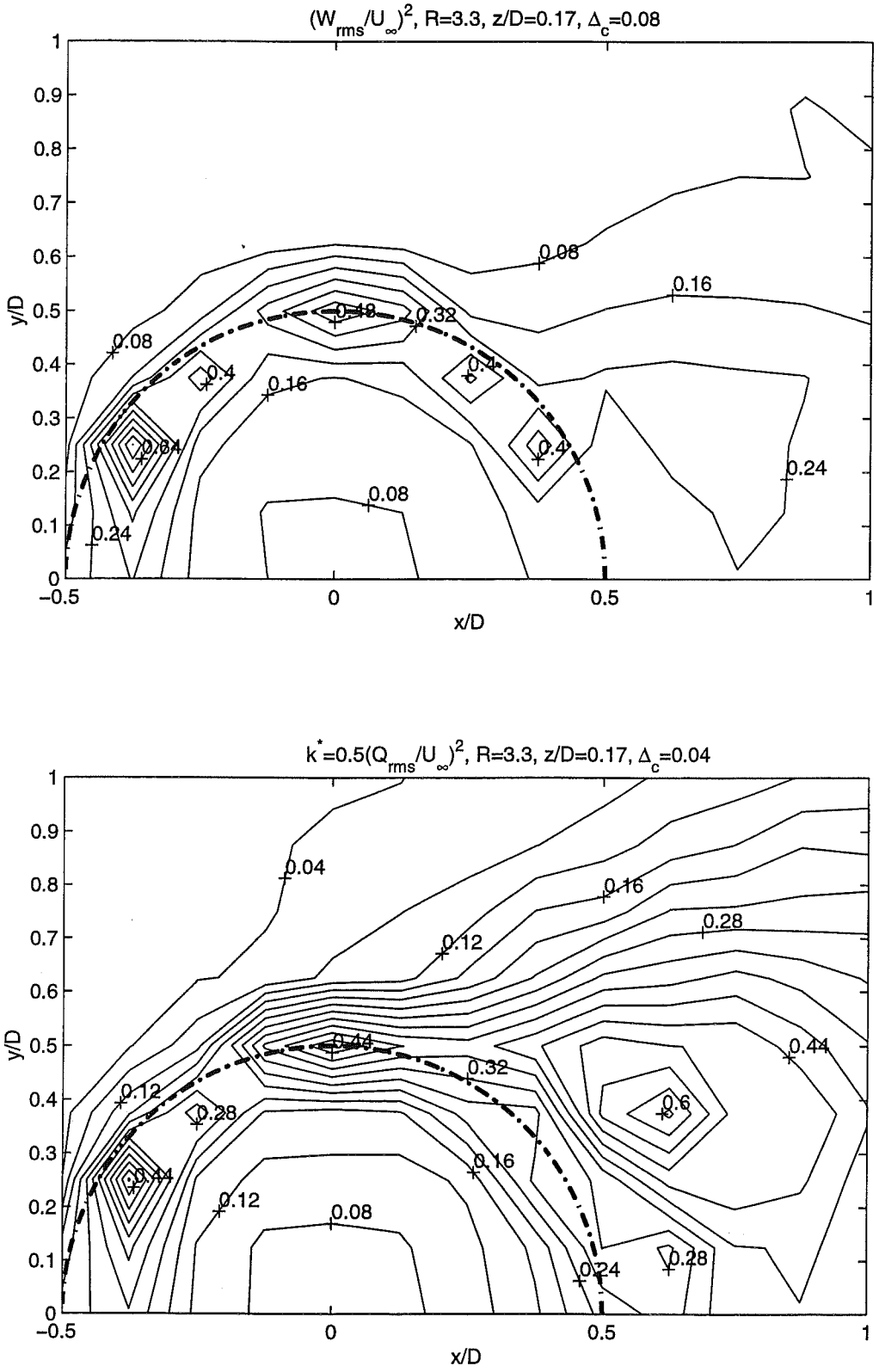

Fig. 4.3.11 Contour plots of the normalized turbulent stress ww^* and the normalized turbulent kinetic energy k^* in the z^*=0.17 plane near the jet exit for R=3.3

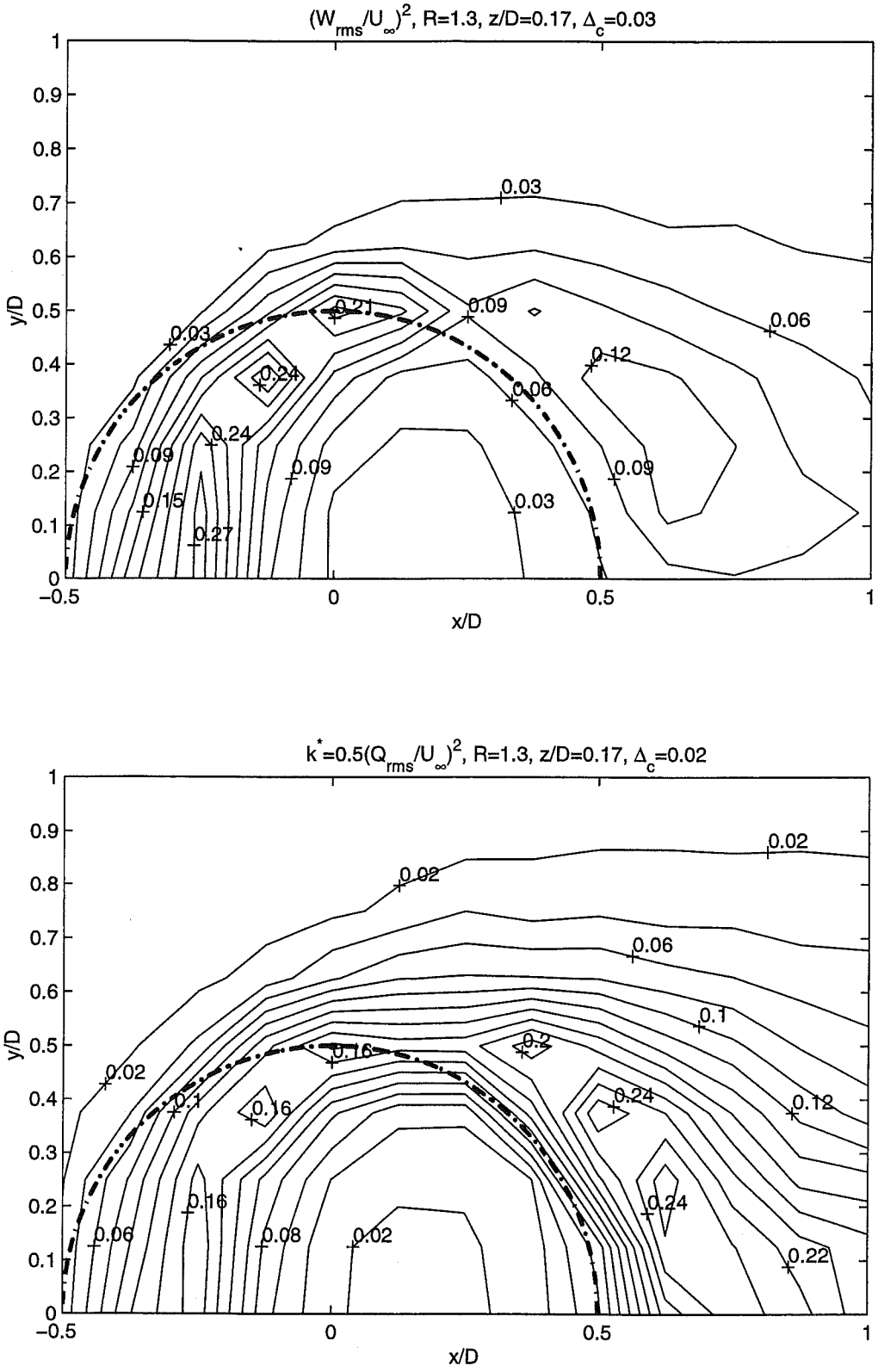

Fig. 4.3.12 Contour plots of the normalized turbulent stress ww^* and the normalized turbulent kinetic energy k^* in the z^*=0.17 plane near the jet exit for R=1.3

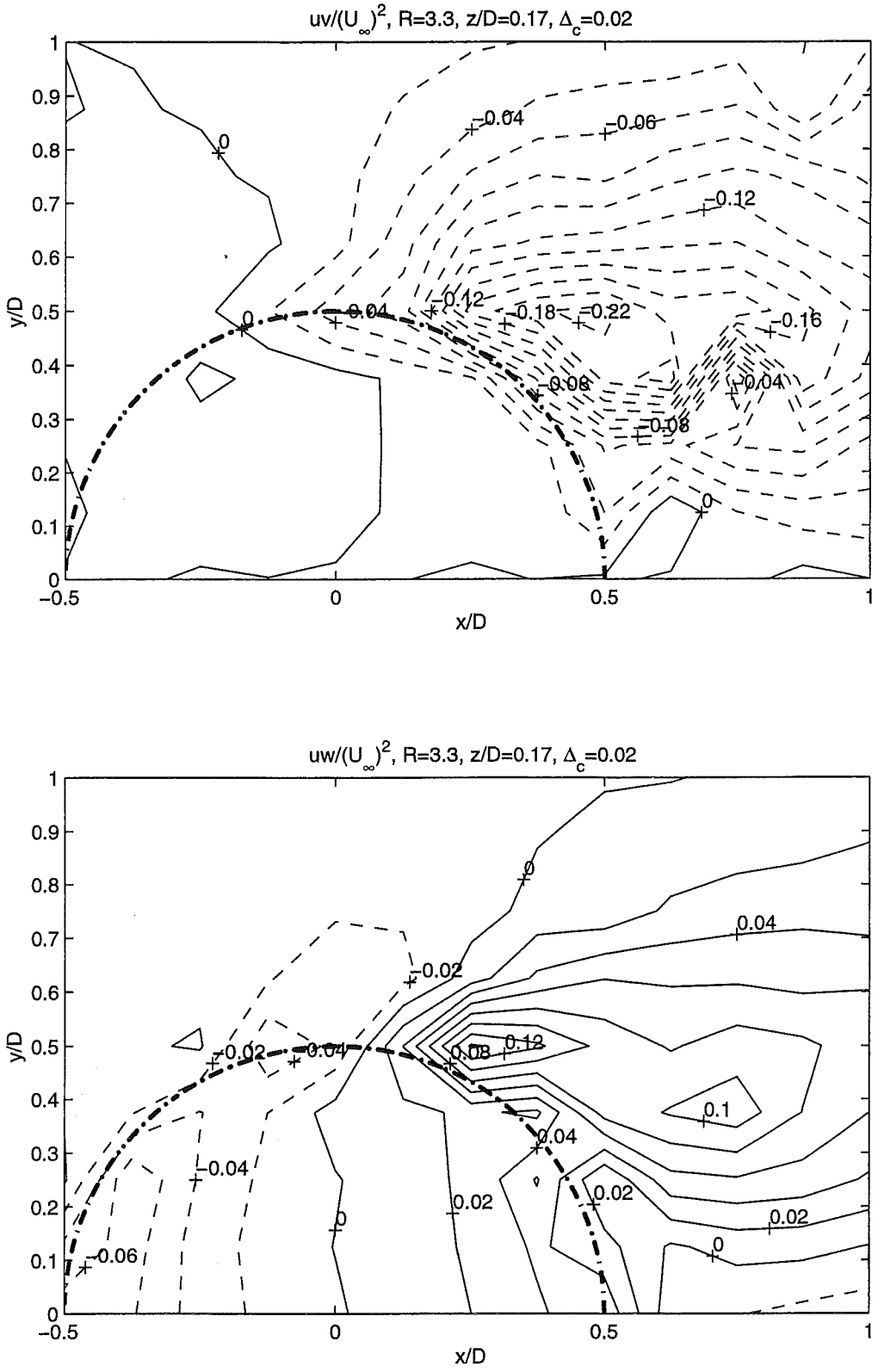

Fig. 4.3.13 Contour plots of the normalized turbulent shear stresses uv^* and uw^* in the z^*=0.17 plane near the jet exit for R=3.3

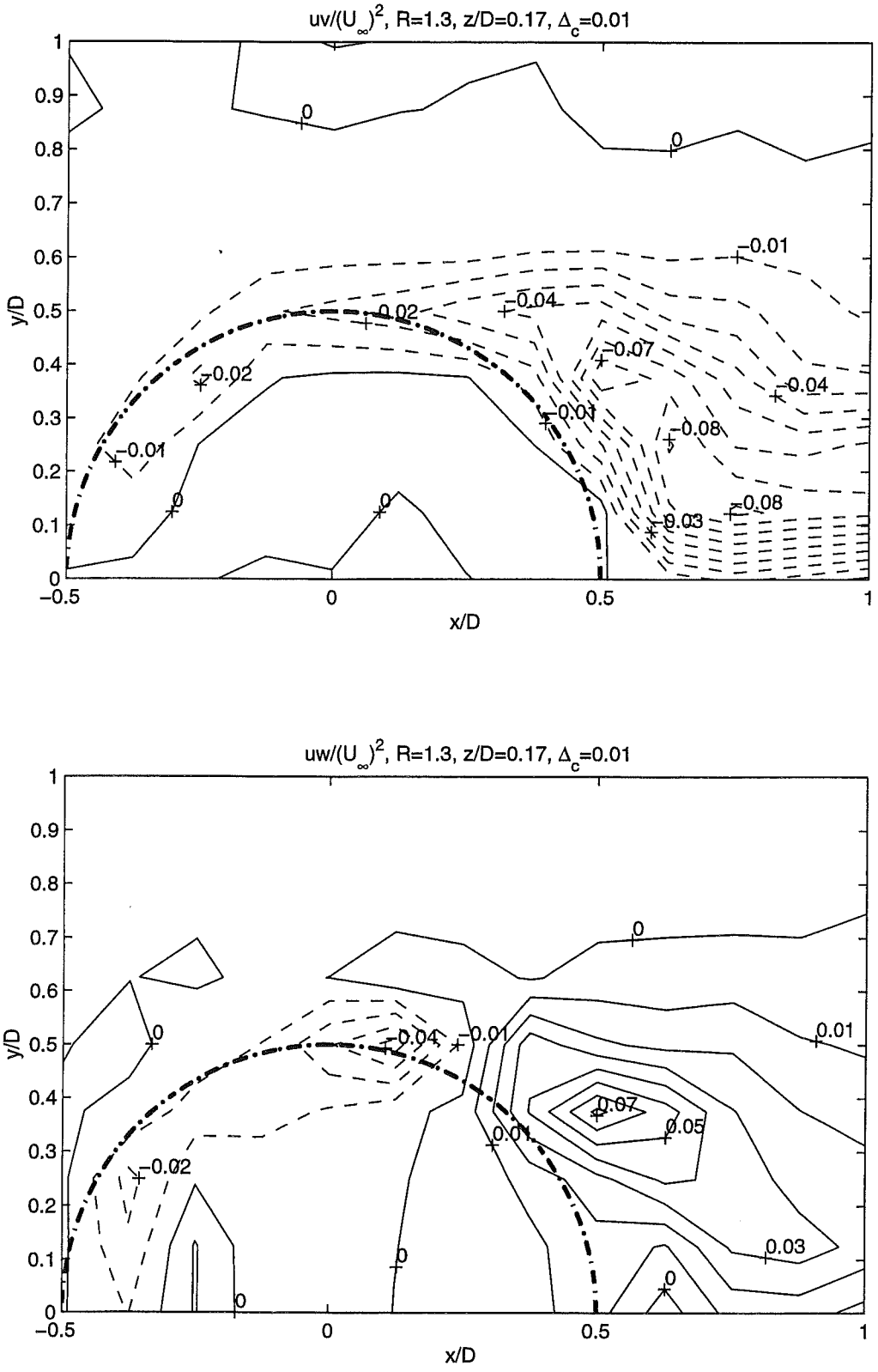

Fig. 4.3.14 Contour plots of the normalized turbulent shear stresses uv^* and uw^* in the z^*=0.17 plane near the jet exit for R=1.3

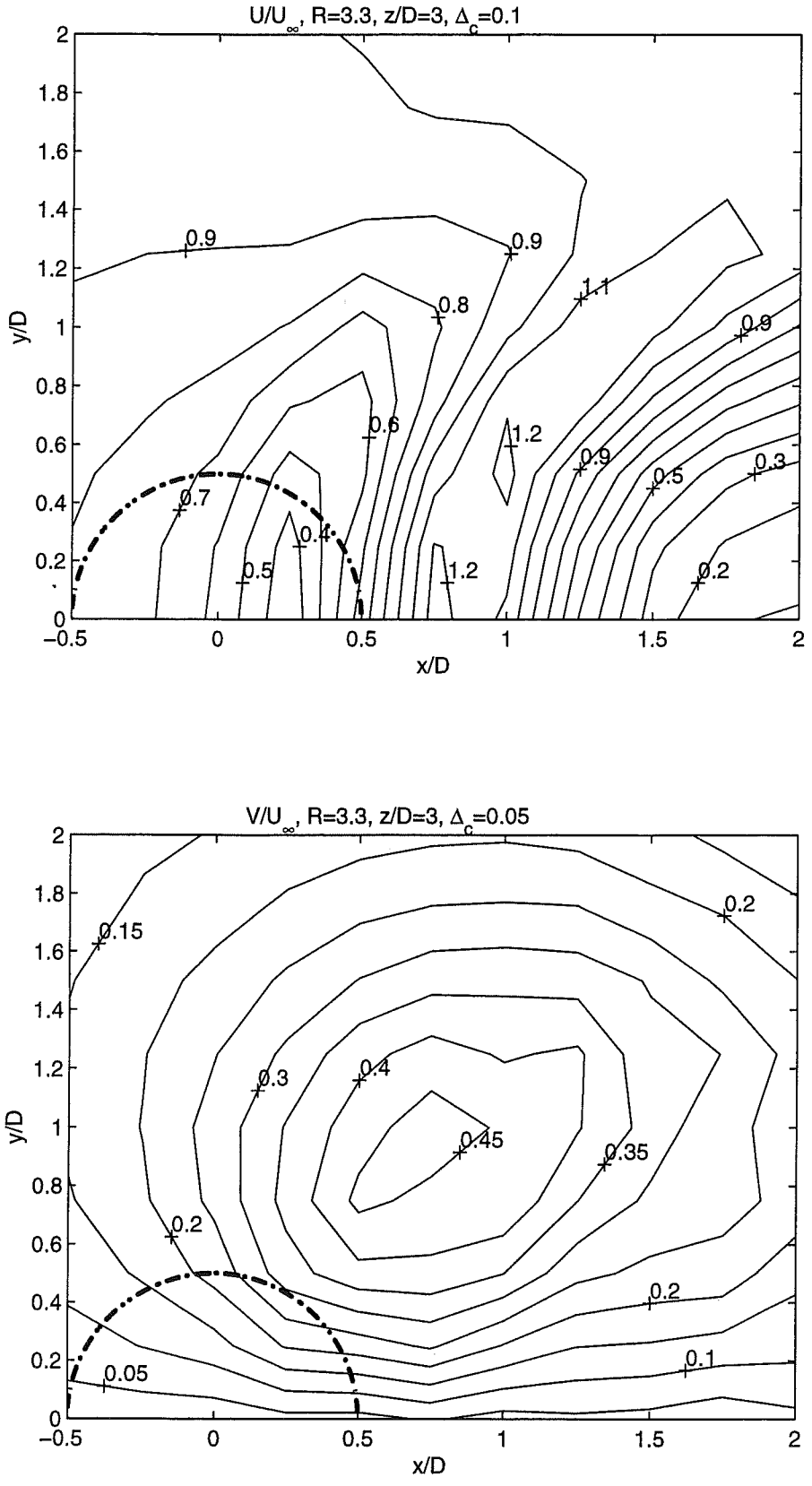

Fig. 4.3.15 Contour plots of the normalized streamwise and spanwise mean velocities U^* and V^* in the z^*=3.00 plane near the jet exit for R=3.3

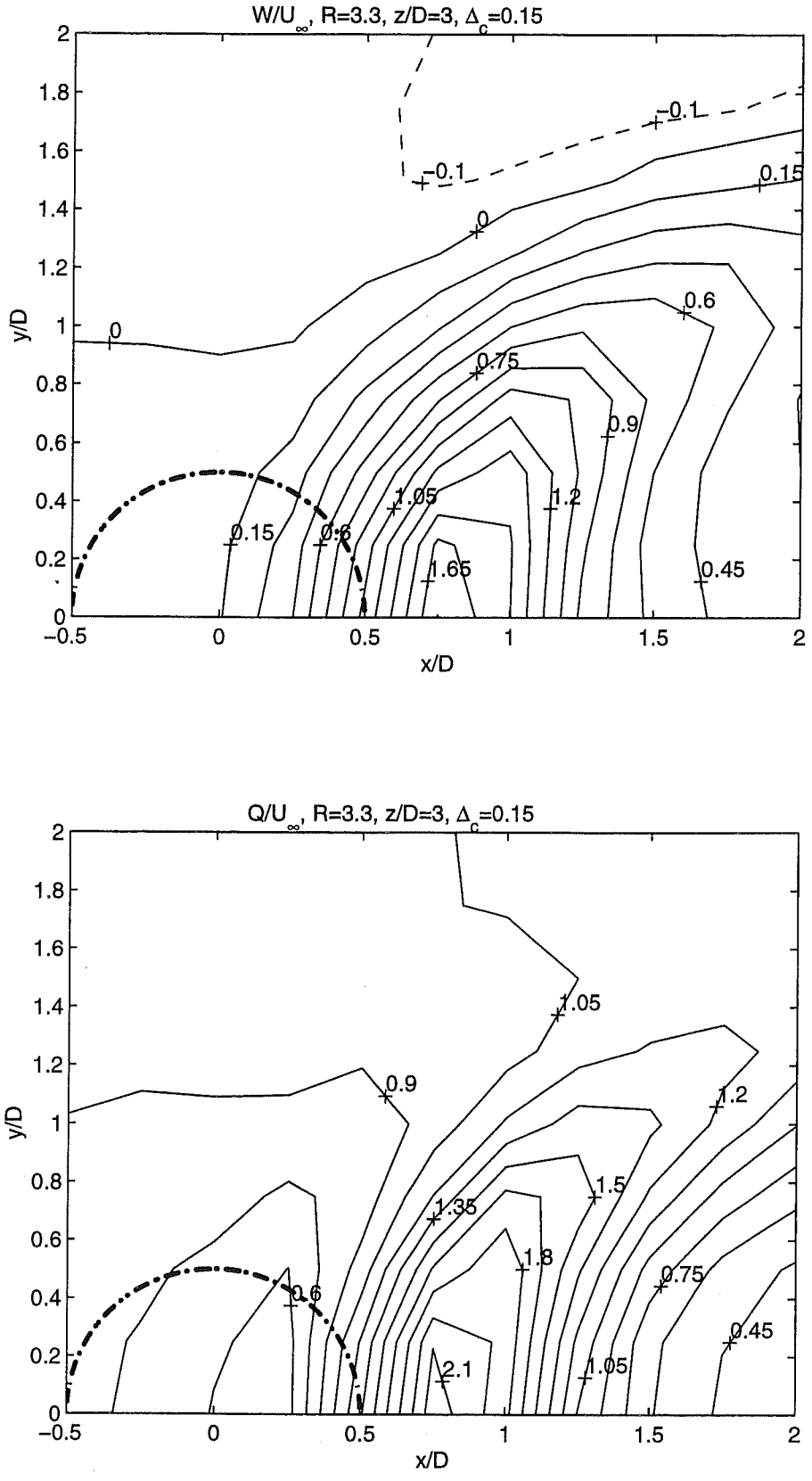

Fig. 4.3.16 Contour plots of the normalized vertical and total mean velocities W^* and Q^* in the z^*=3.00 plane near the jet exit for R=3.3

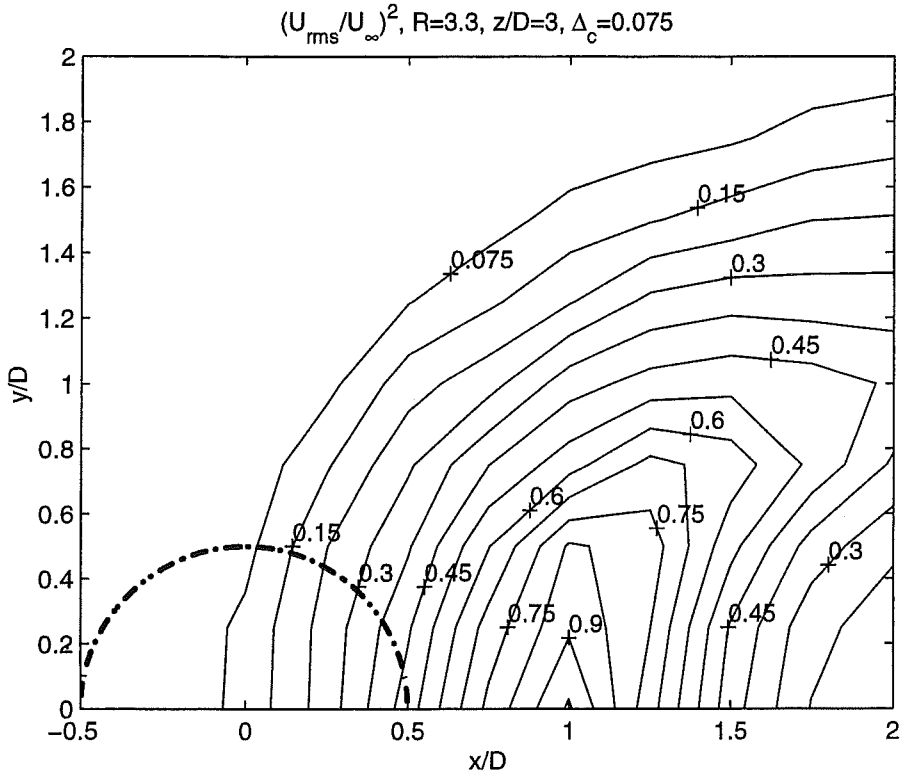

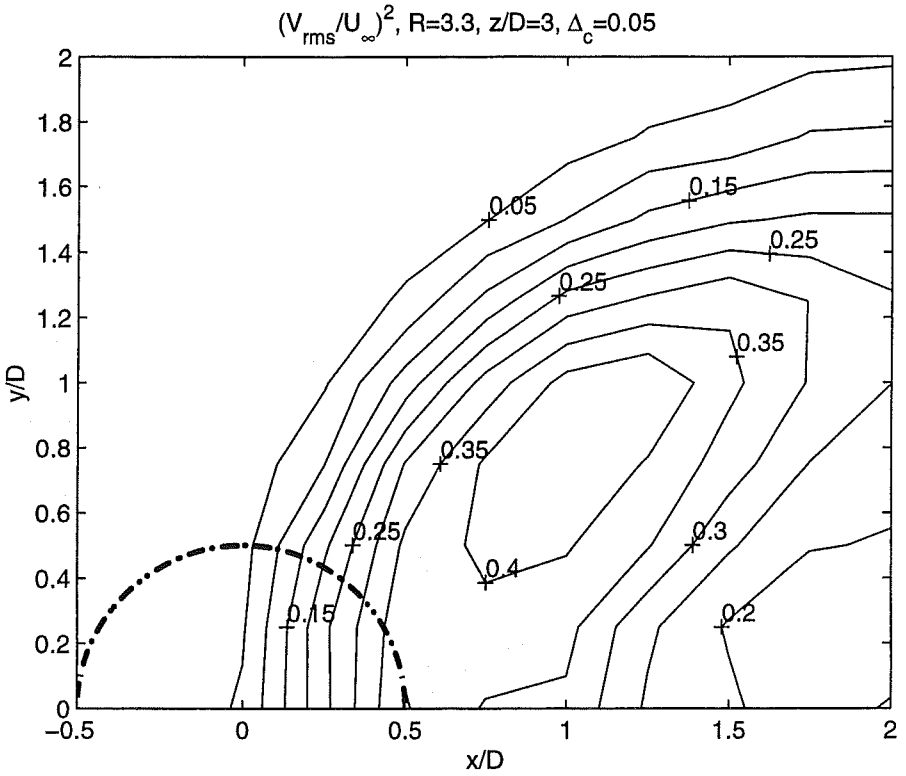

Fig. 4.3.17 Contour plots of the normalized turbulent stresses uu^* and vv^* in the z^*=3.00 plane near the jet exit for R=3.3

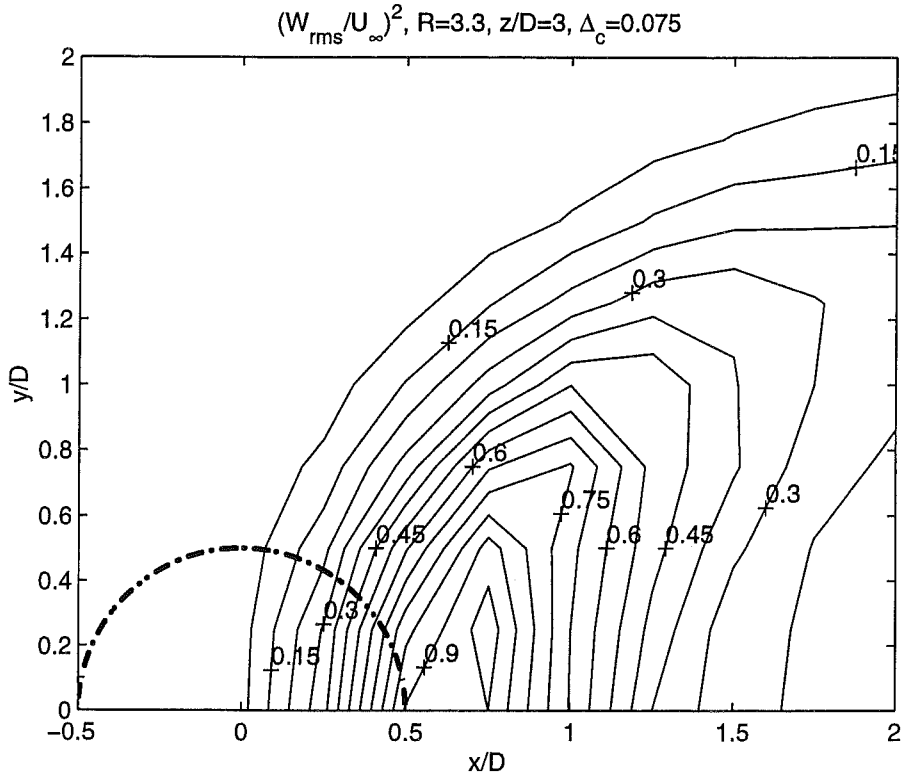

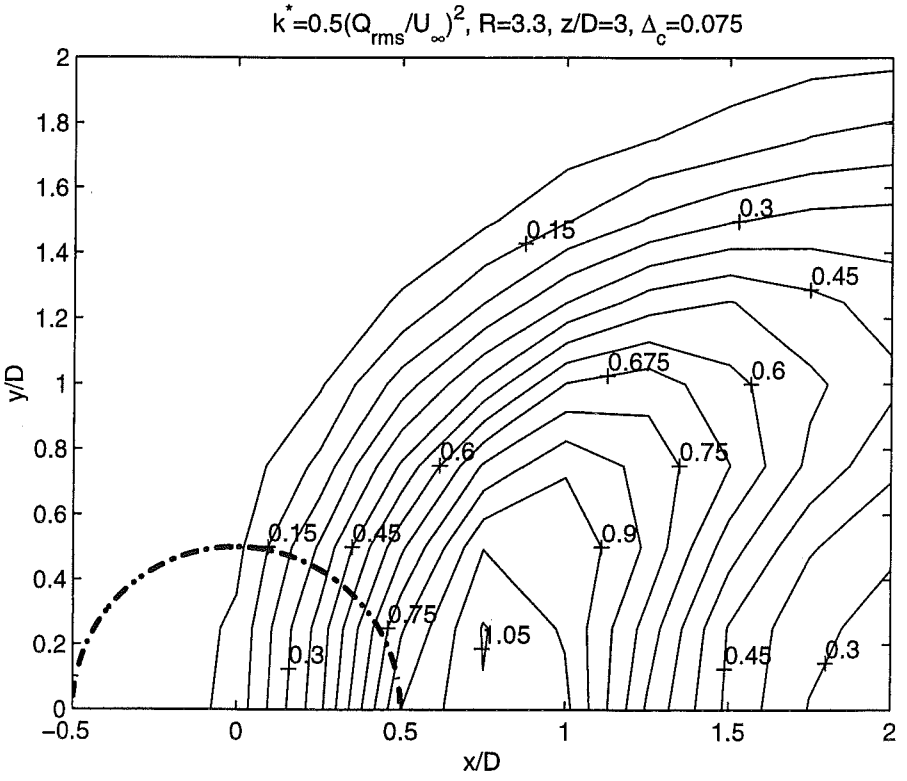

Fig. 4.3.18 Contour plots of the normalized turbulent stress ww^* and the normalized turbulent kinetic energy k^* in the z^*=3.00 plane near the jet exit for R=3.3

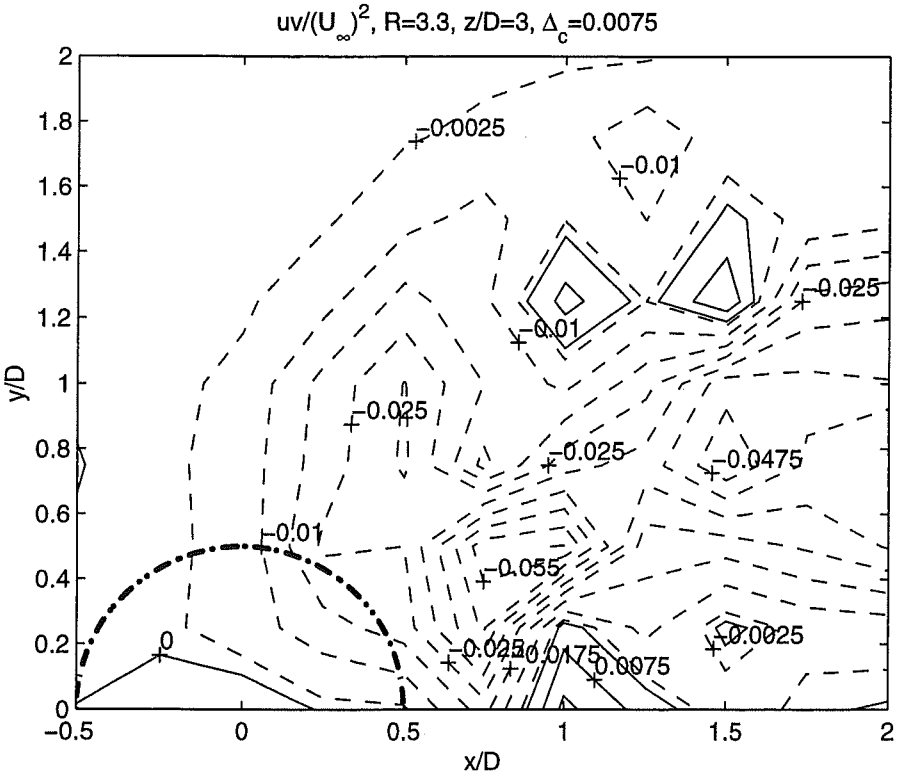

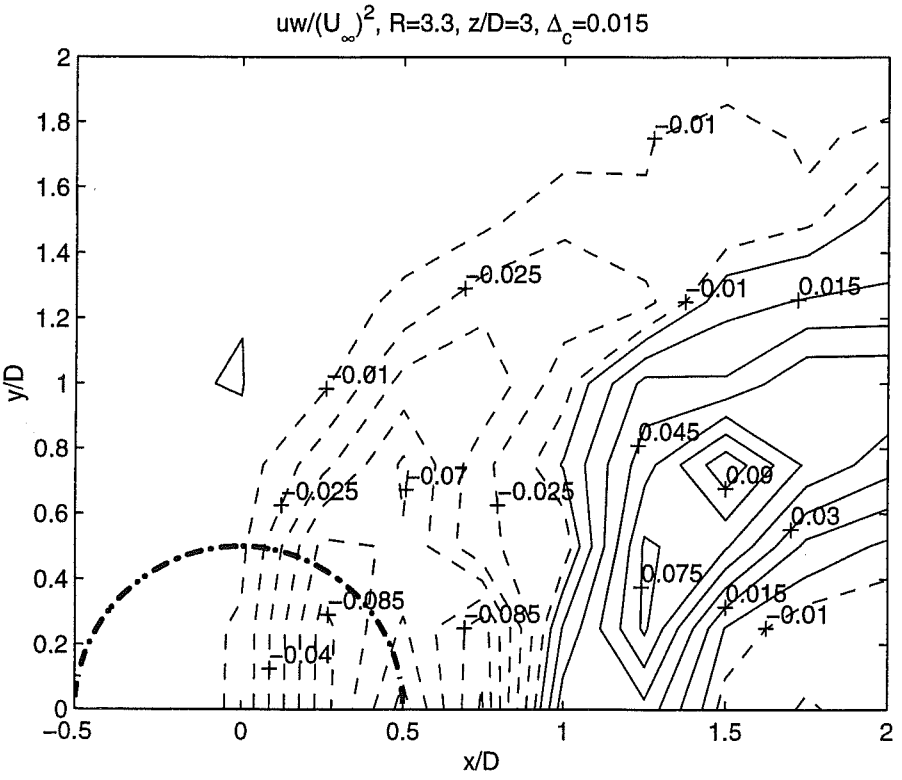

Fig. 4.3.19 Contour plots of the normalized turbulent shear stresses uv^* and uw^* in the z^*=3.00 plane near the jet exit for R=3.3

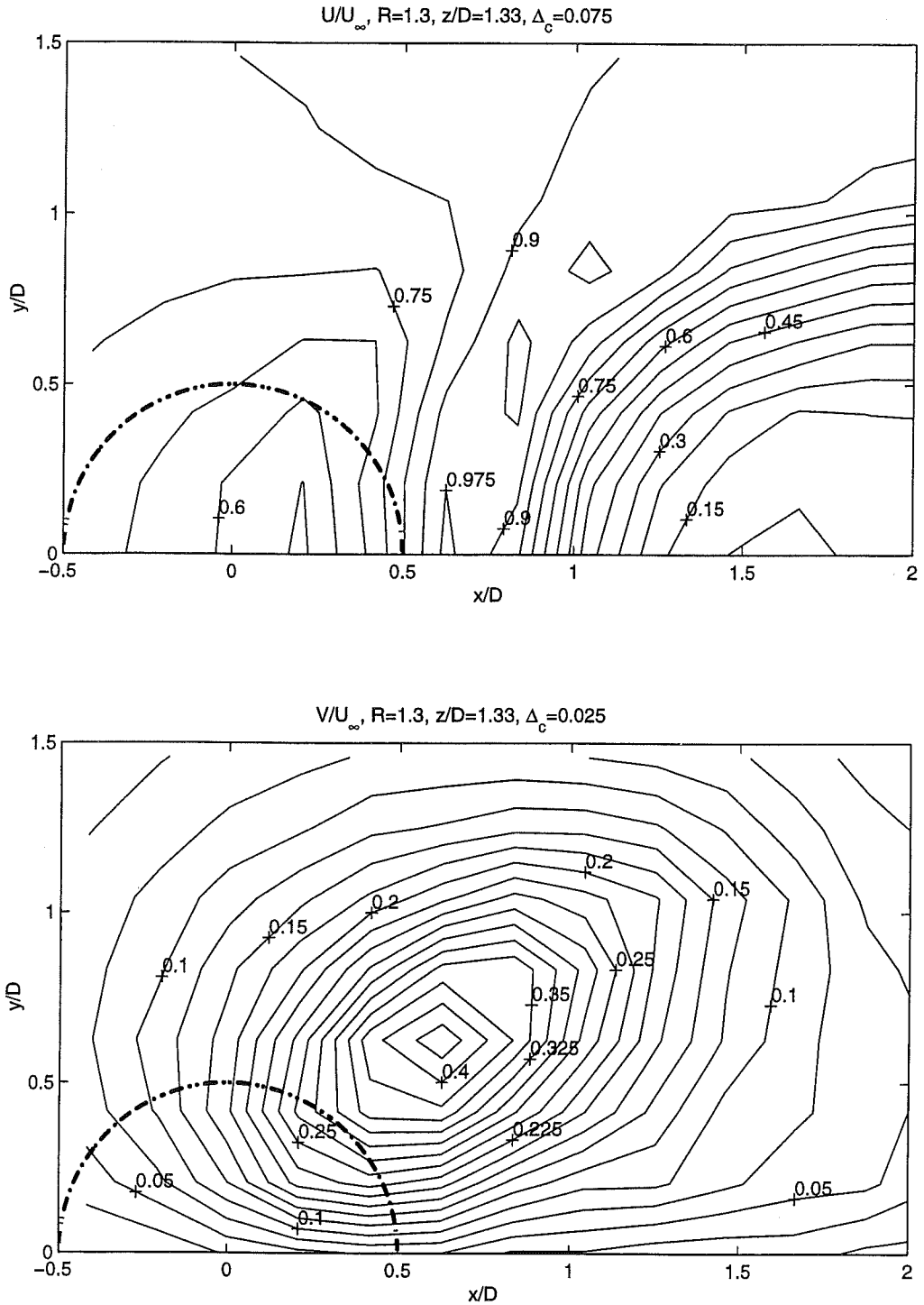

Fig. 4.3.20 Contour plots of the normalized streamwise and spanwise mean velocities U^* and V^* in the z^*=1.3 plane near the jet exit for R=1.3

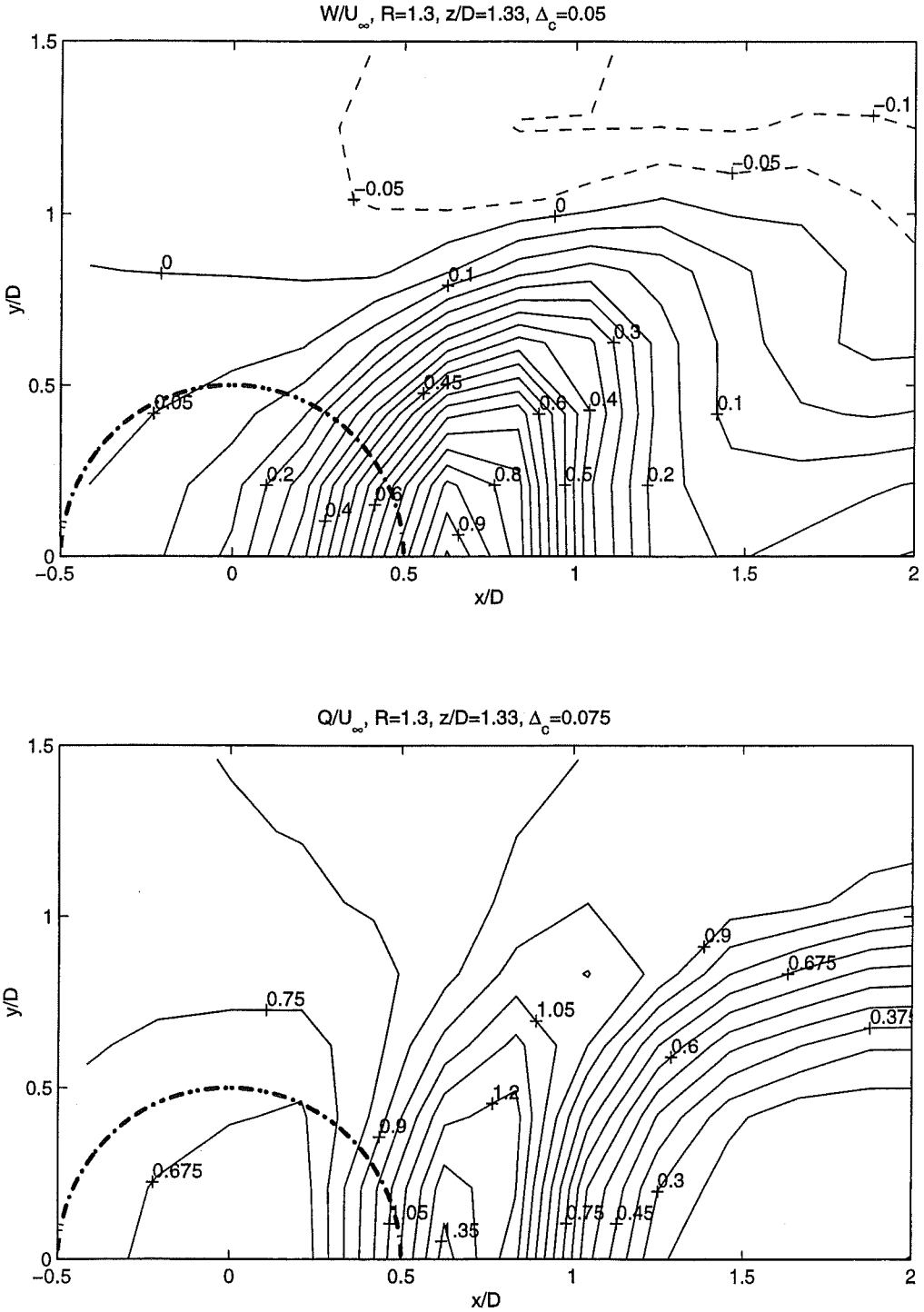

Fig. 4.3.21 Contour plots of the normalized vertical and total mean velocities W^* and Q^* in the z^*=1.3 plane near the jet exit for R=1.3

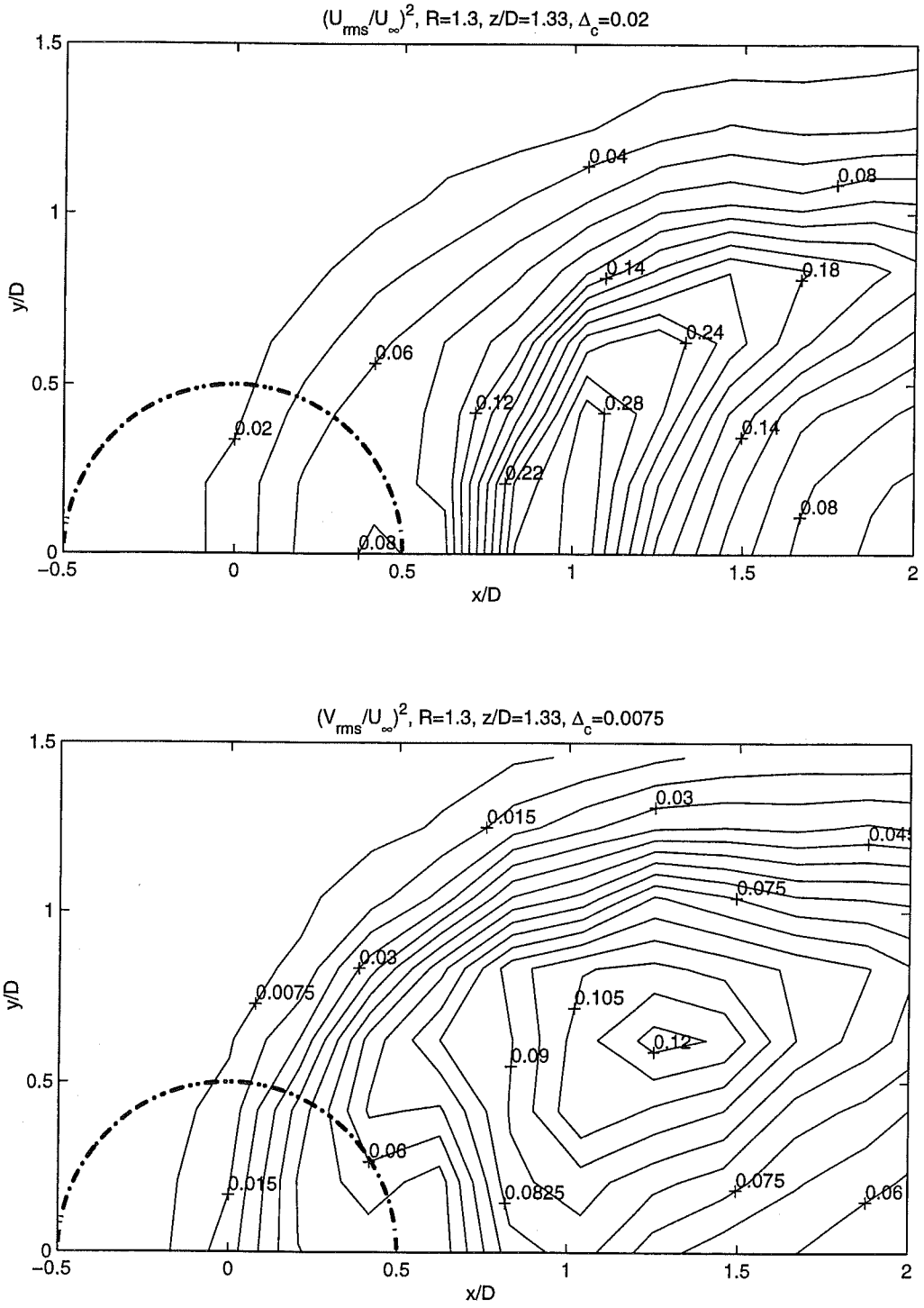

Fig. 4.3.22 Contour plots of the normalized turbulent stresses uu^* and vv^* in the z^*=1.3 plane near the jet exit for R=1.3

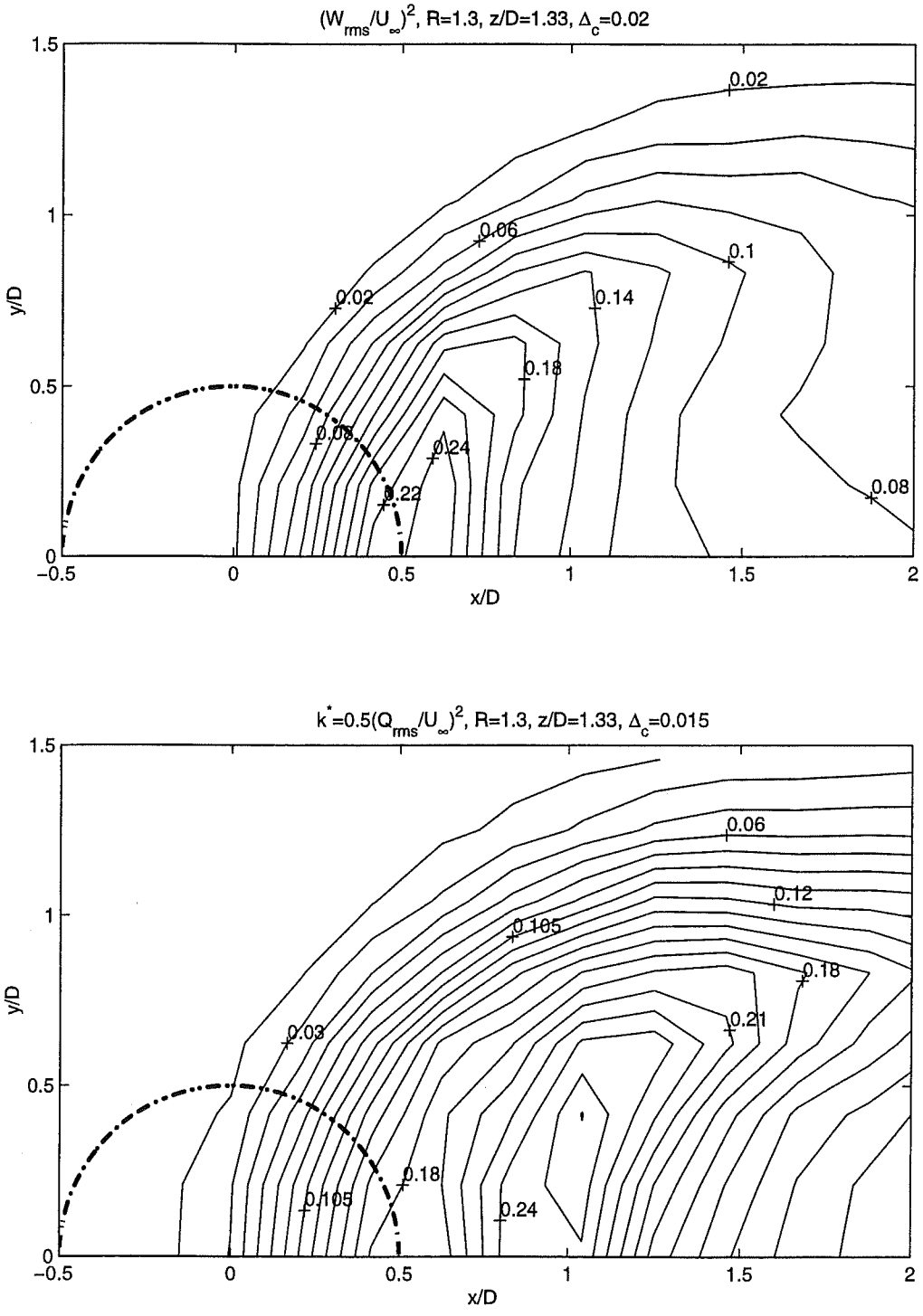

Fig. 4.3.23 Contour plots of the normalized turbulent stress ww^* and the normalized turbulent kinetic energy k^* in the z^*=1.3 plane near the jet exit for R=1.3

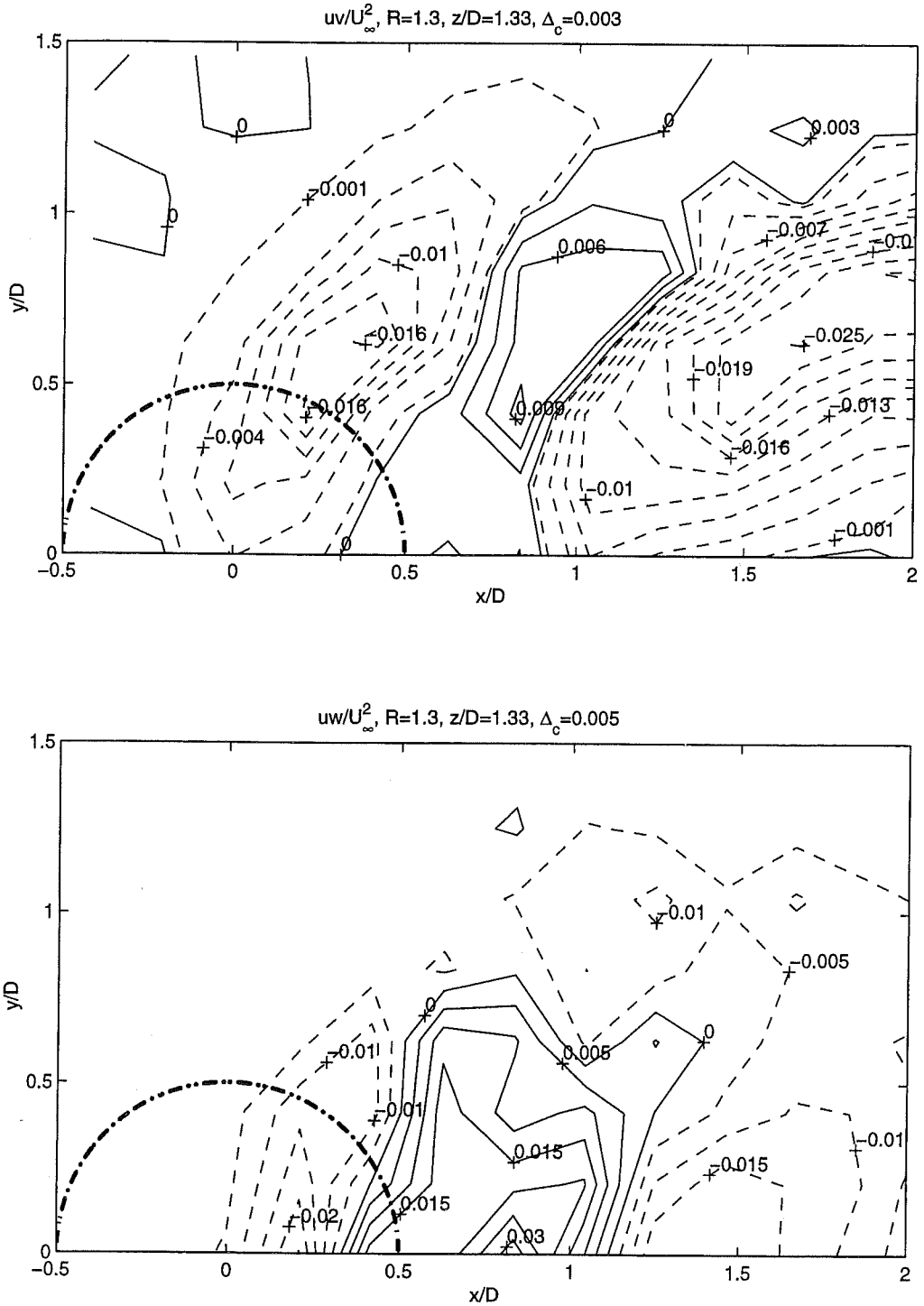

Fig. 4.3.24 Contour plots of the normalized turbulent shear stresses uv^* and uw^* in the z^*=1.3 plane near the jet exit for R=1.3

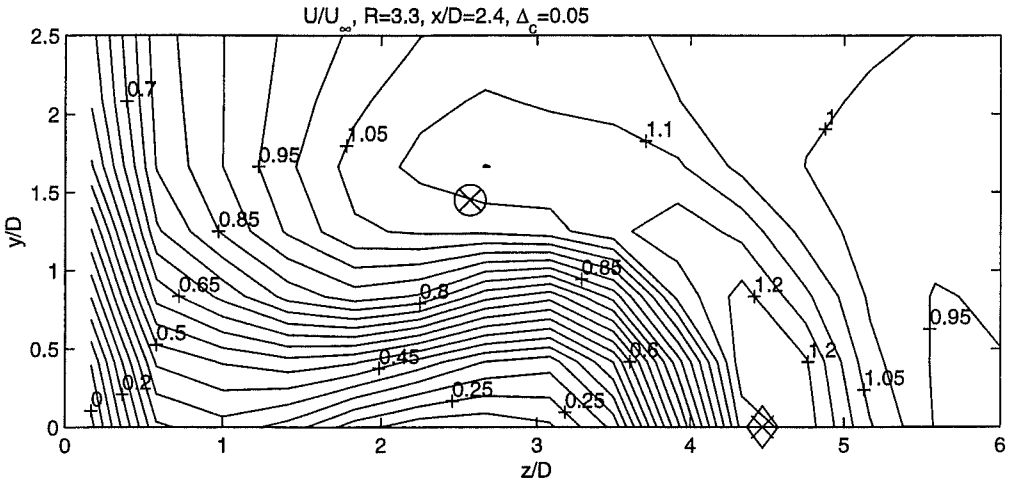

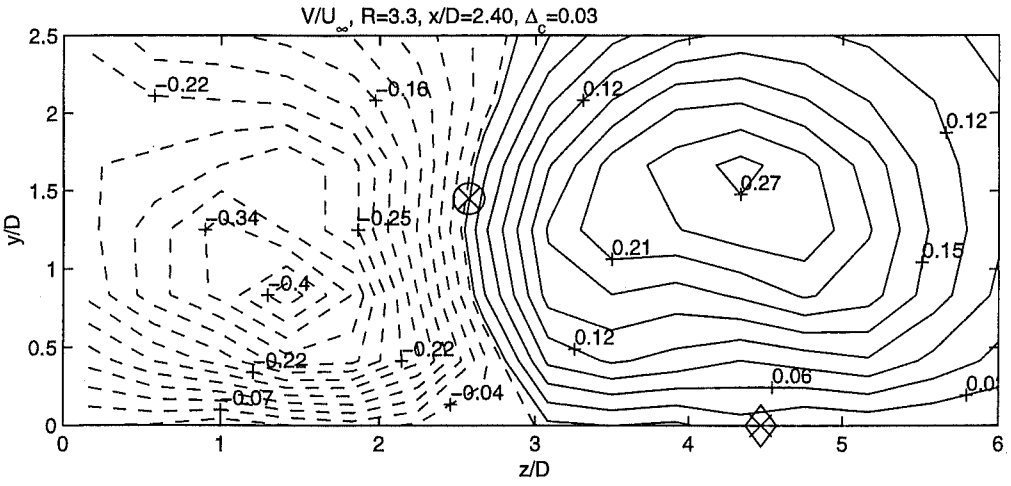

Fig. 4.4.1 Contour plots of the normalized streamwise and spanwise mean velocities U^* and V^* in the x^*=2.40 plane for R=3.3

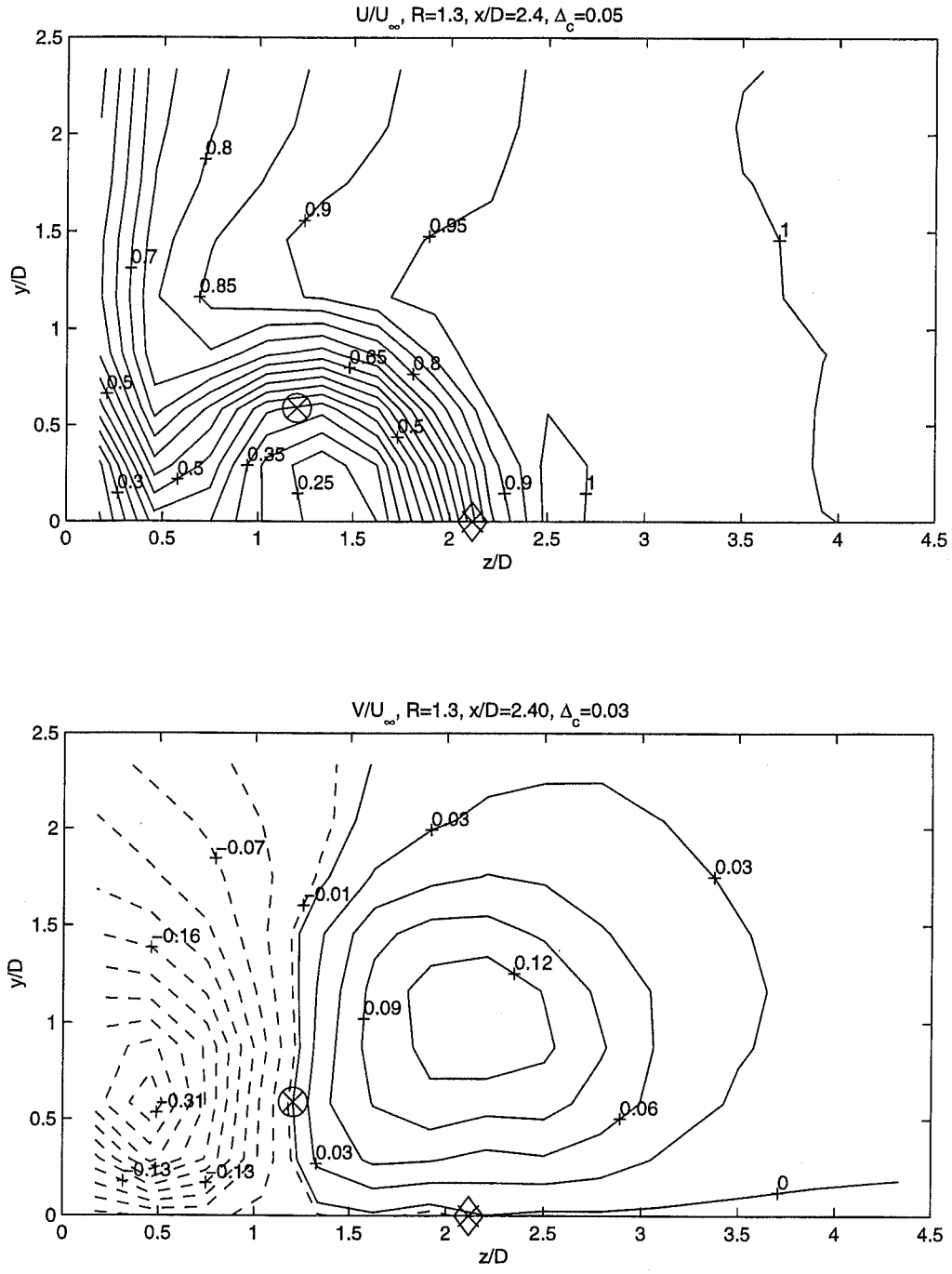

Fig. 4.4.2 Contour plots of the normalized streamwise and spanwise mean velocities U^* and V^* in the x^*=2.40 plane for R=1.3

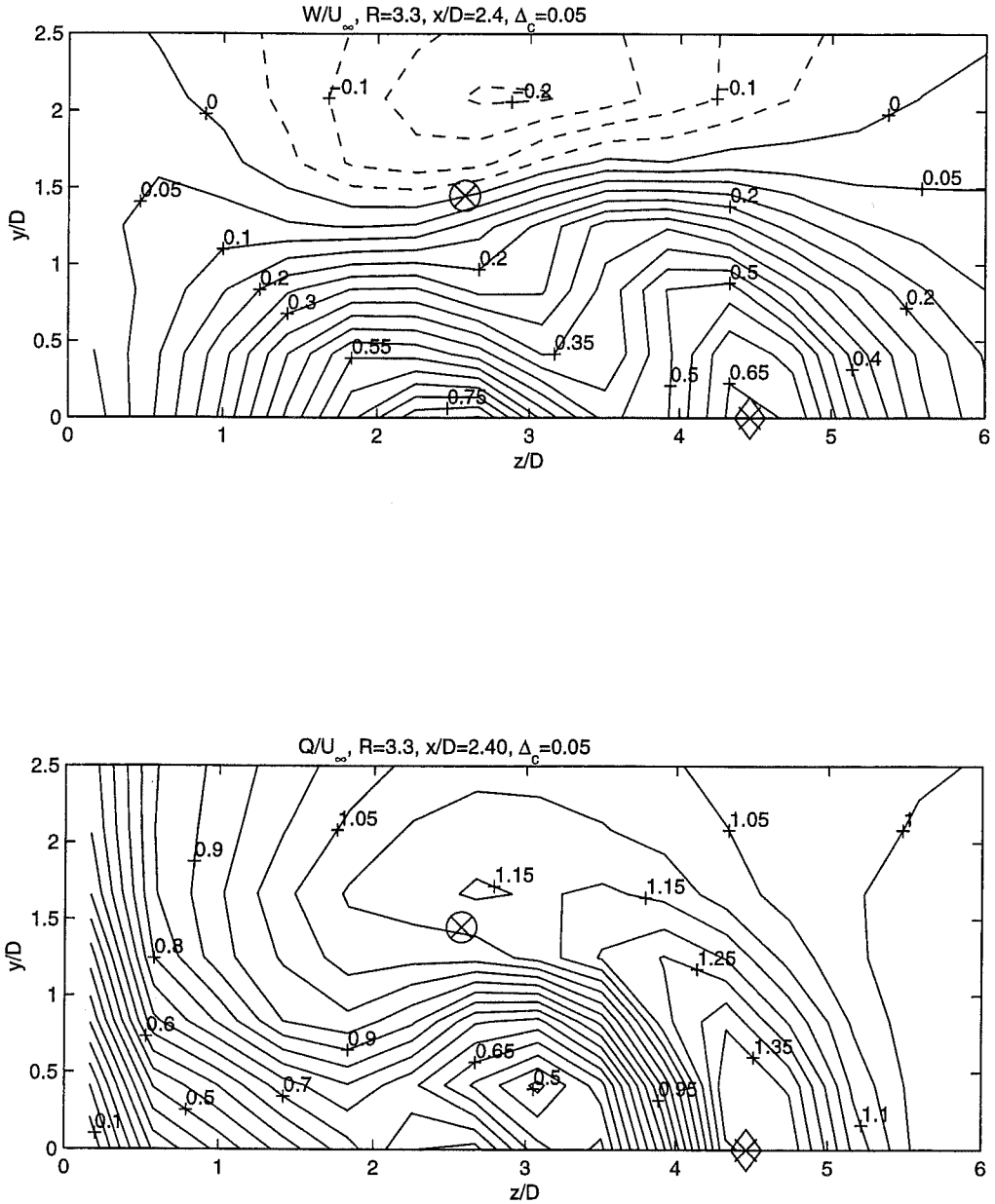

Fig. 4.4.3 Contour plots of the normalized vertical and total mean velocities W^* and Q^* in the x^*=2.40 plane for R=3.3

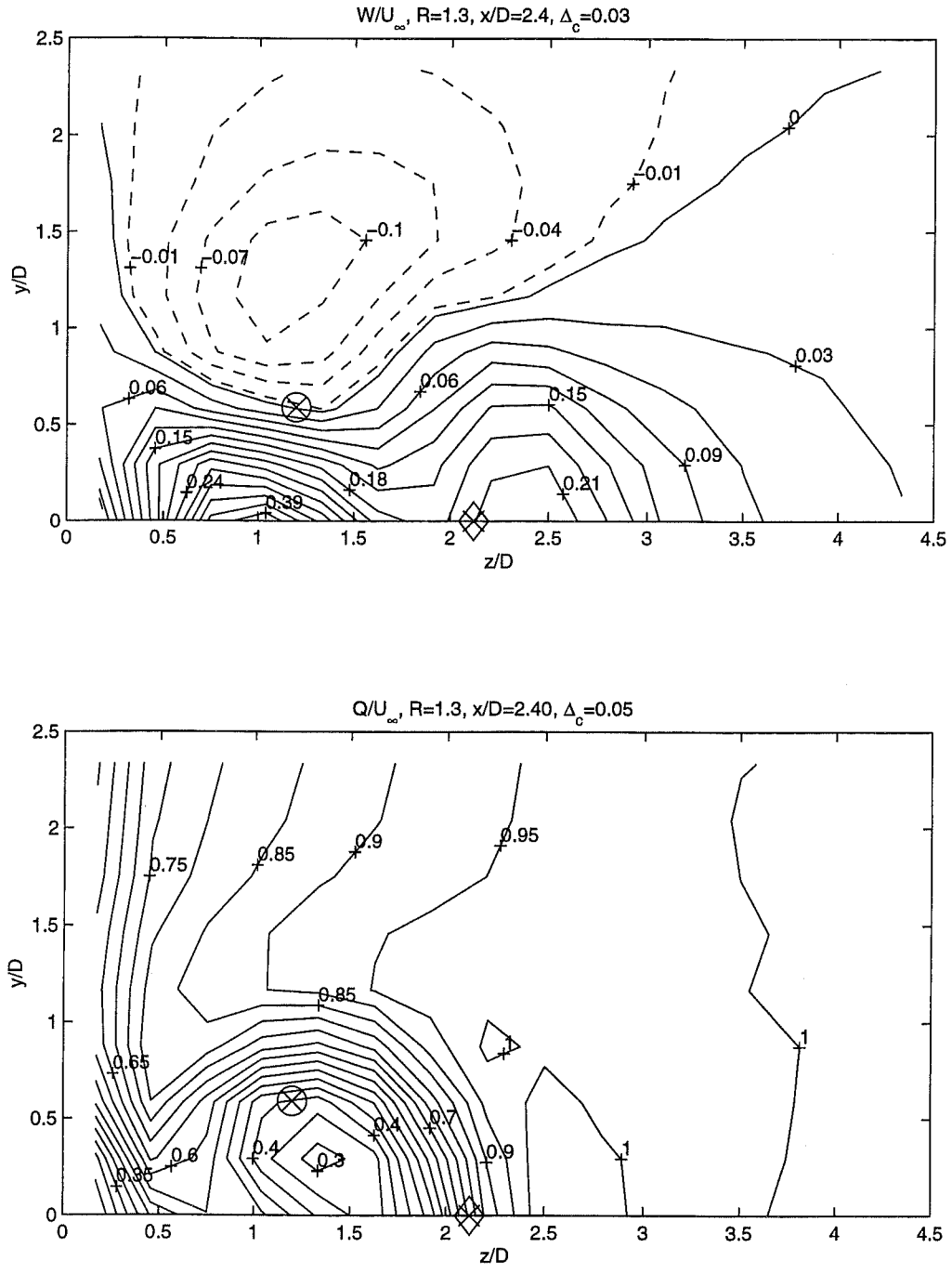

Fig. 4.4.4 Contour plots of the normalized vertical and total mean velocities W^* and Q^* in the x^*=2.40 plane for R=1.3

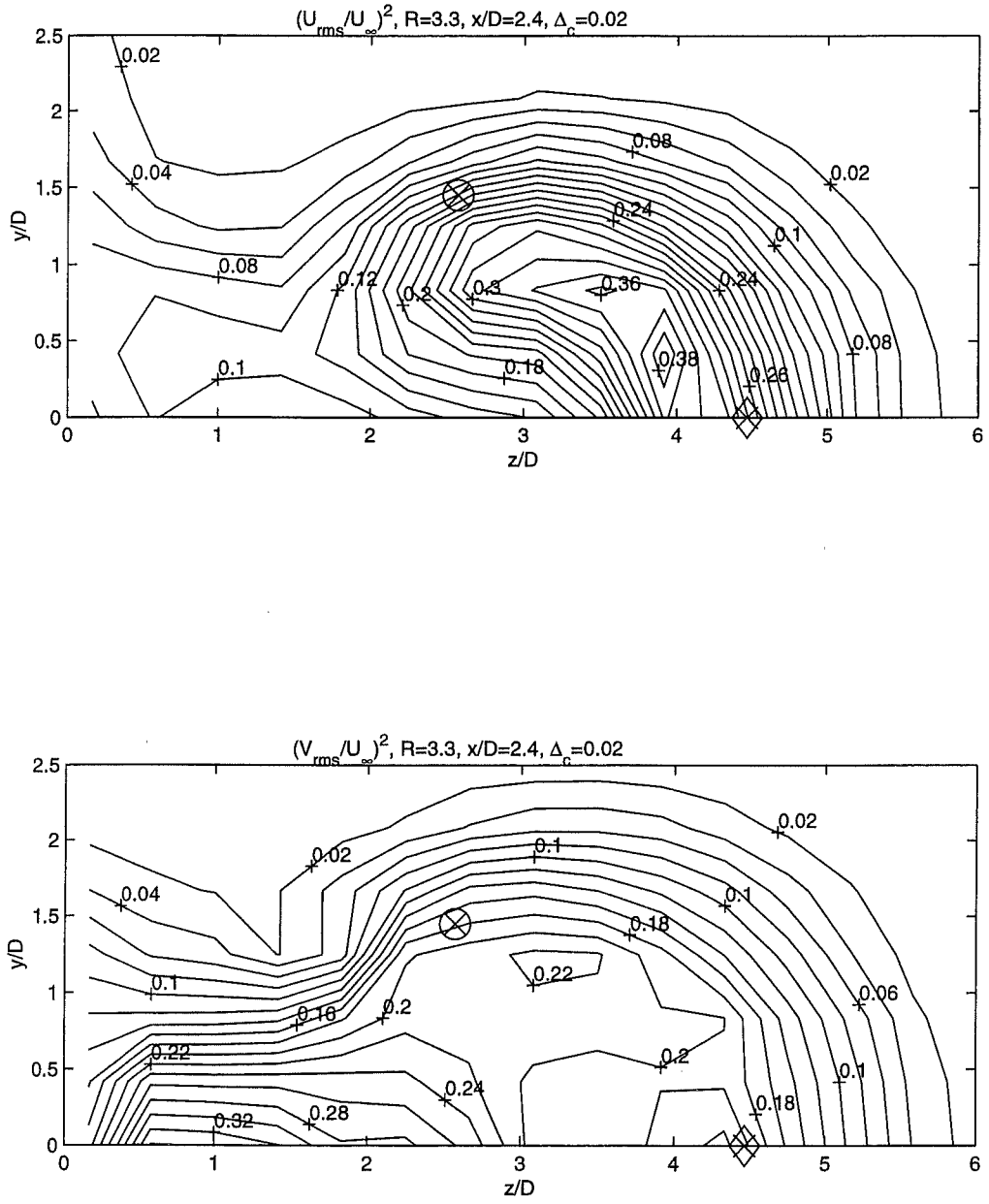

Fig. 4.4.5 Contour plots of the normalized turbulent stresses uu^* and vv^* in the z^*=3.00 plane near the jet exit for R=3.3

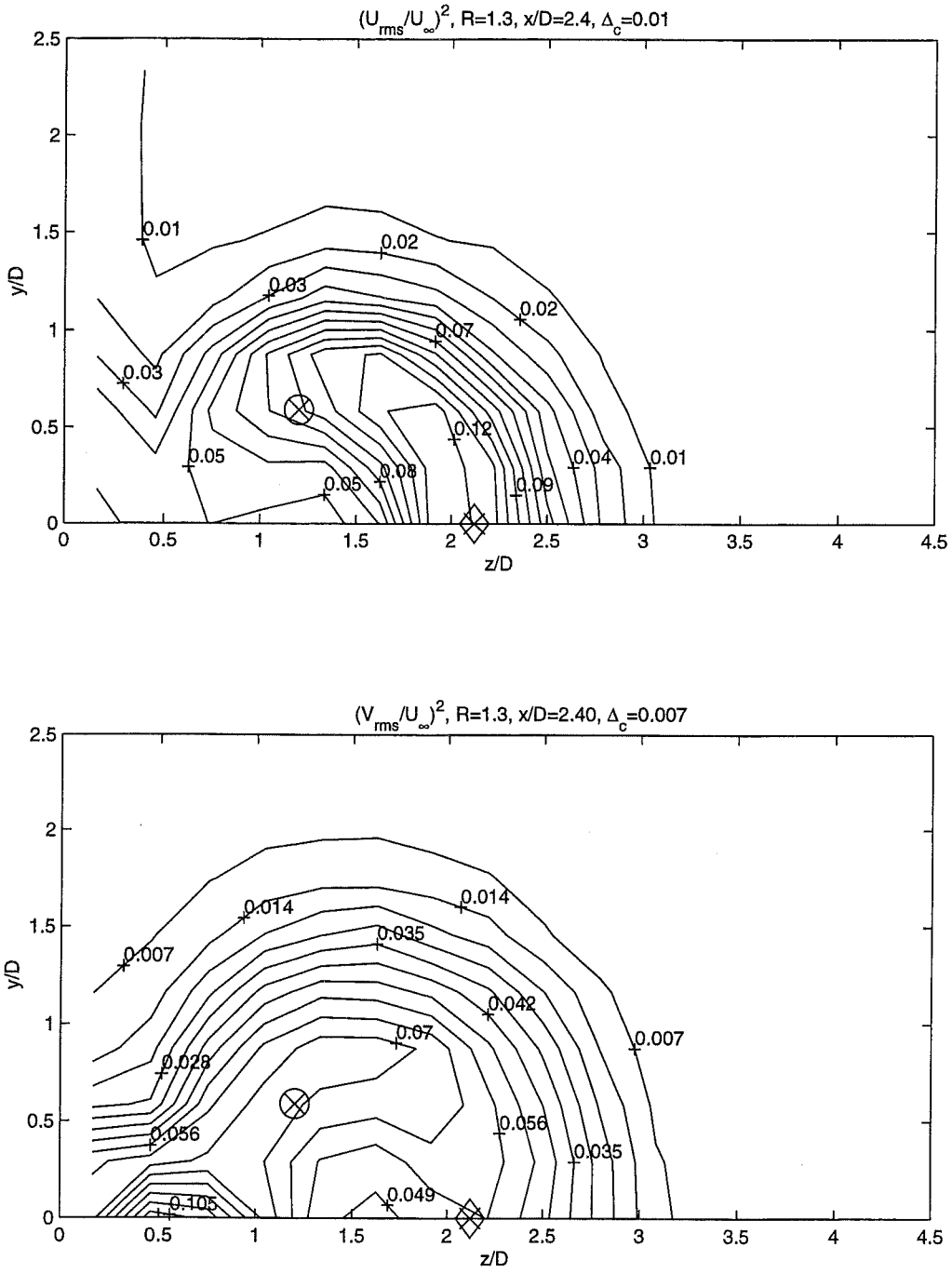

Fig. 4.4.6 Contour plots of the normalized turbulent stresses uu^* and vv^* in the z^*=3.00 plane near the jet exit for R=1.3

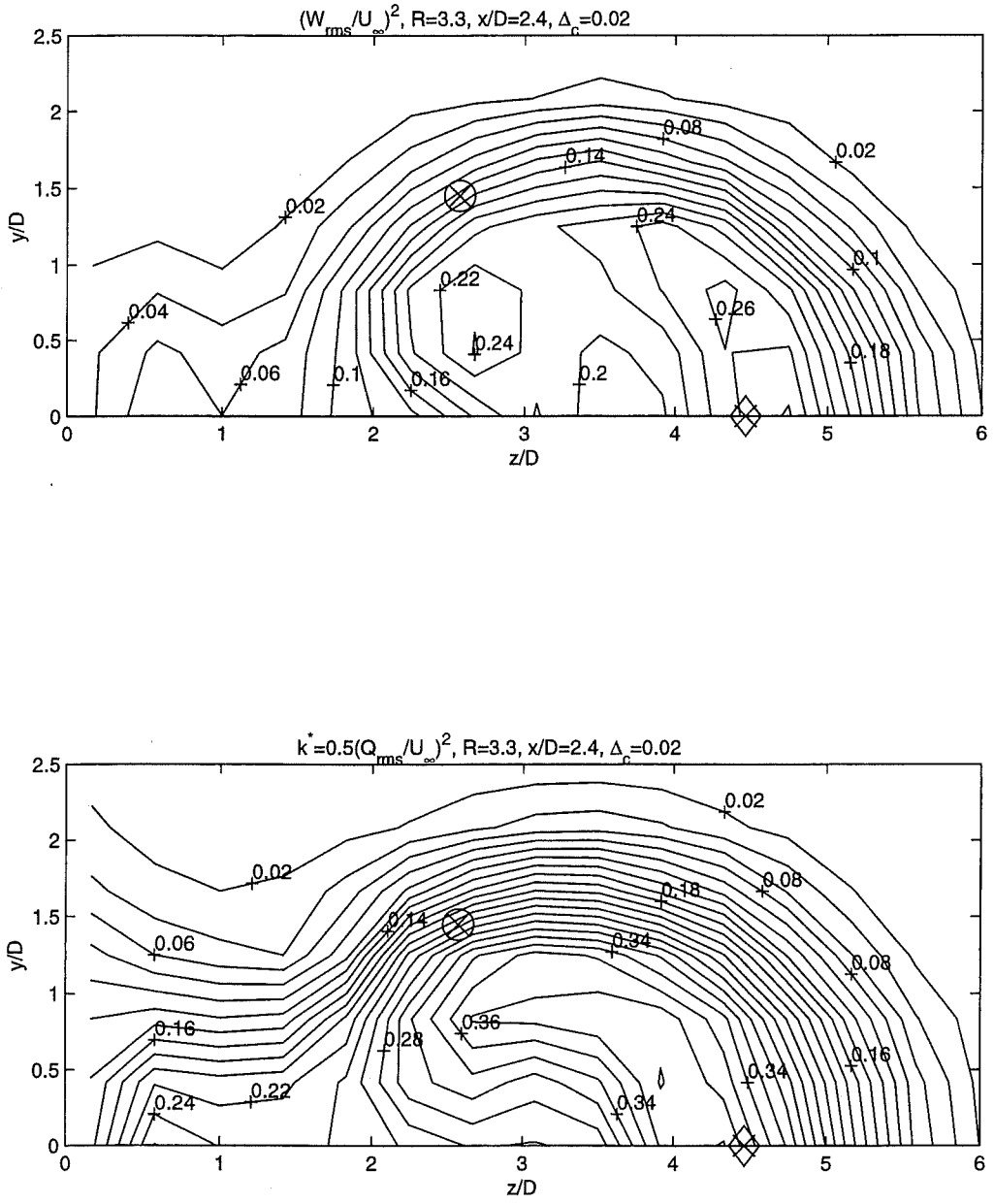

Fig. 4.4.7 Contour plots of the normalized turbulent stress ww^* and the normalized turbulent kinetic energy k^* in the x^*=2.40 plane for R=3.3

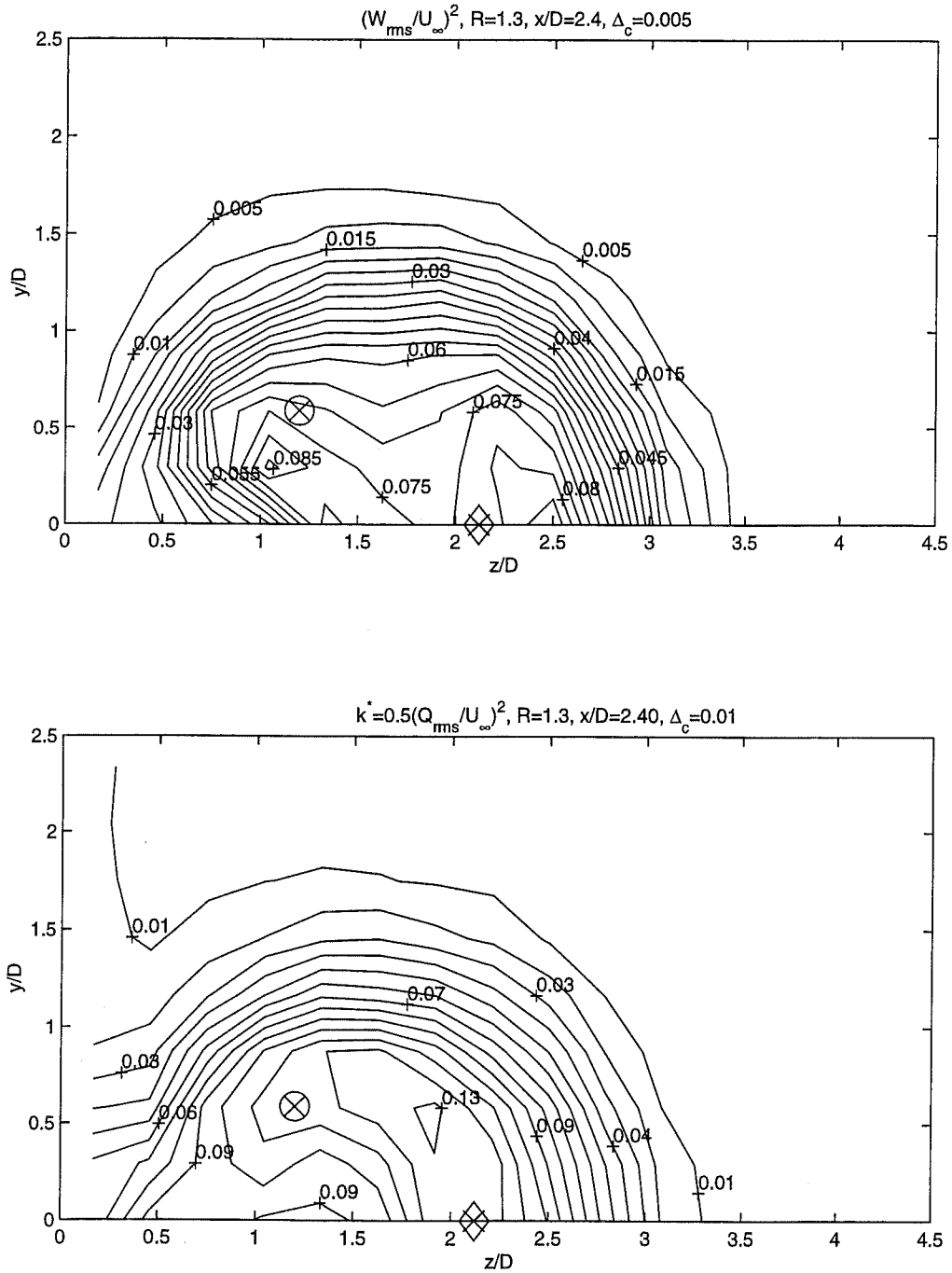

Fig. 4.4.8 Contour plots of the normalized turbulent stress ww^* and the normalized turbulent kinetic energy k^* in the x^*=2.40 plane for R=3.3

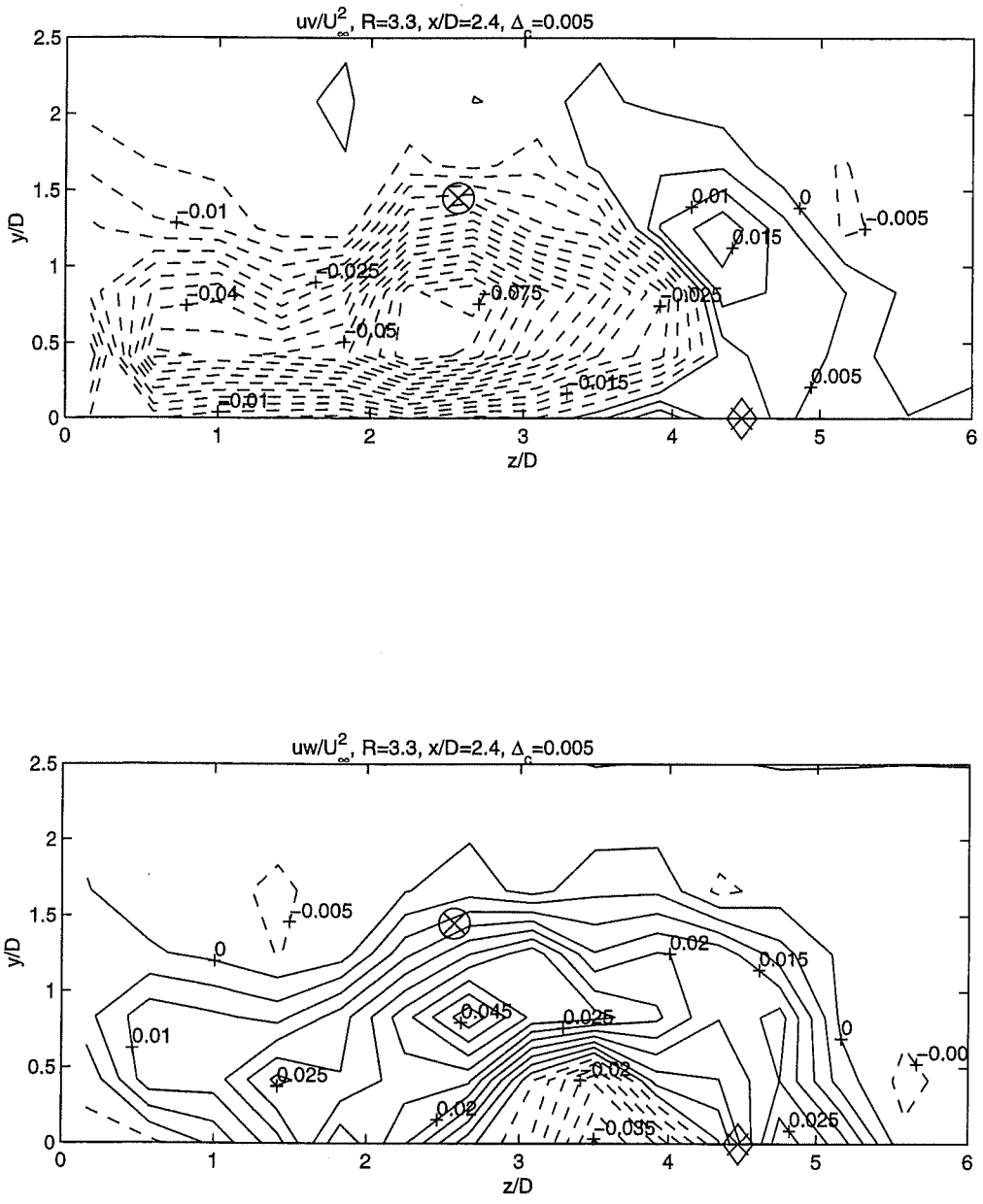

Fig. 4.4.9 Contour plots of the normalized turbulent shear stresses uv^* and uw^* in the x^*=2.40 plane for R=3.3

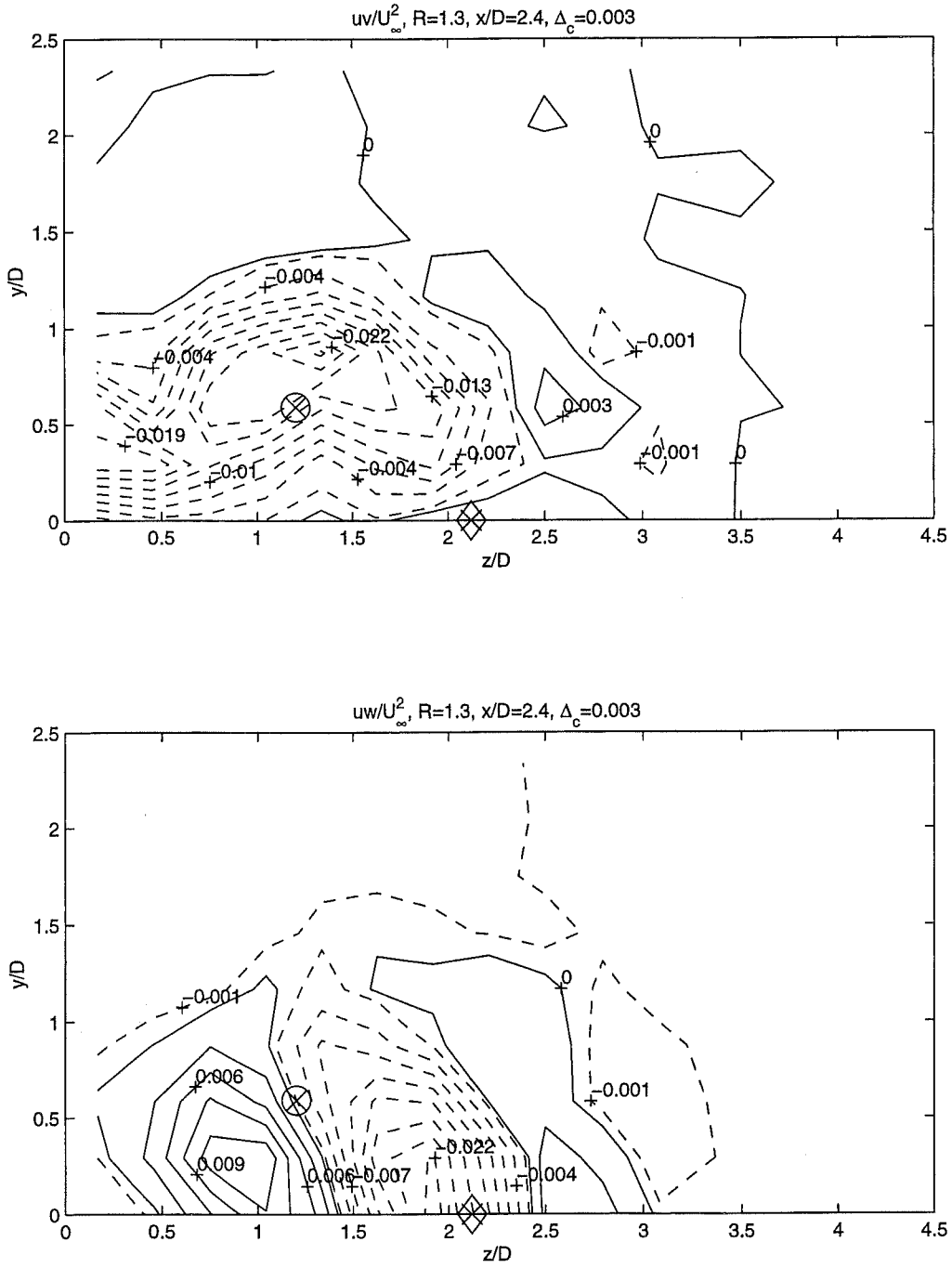

Fig. 4.4.10 Contour plots of the normalized turbulent shear stresses uv^* and uw^* in the x^*=2.40 plane for R=1.3

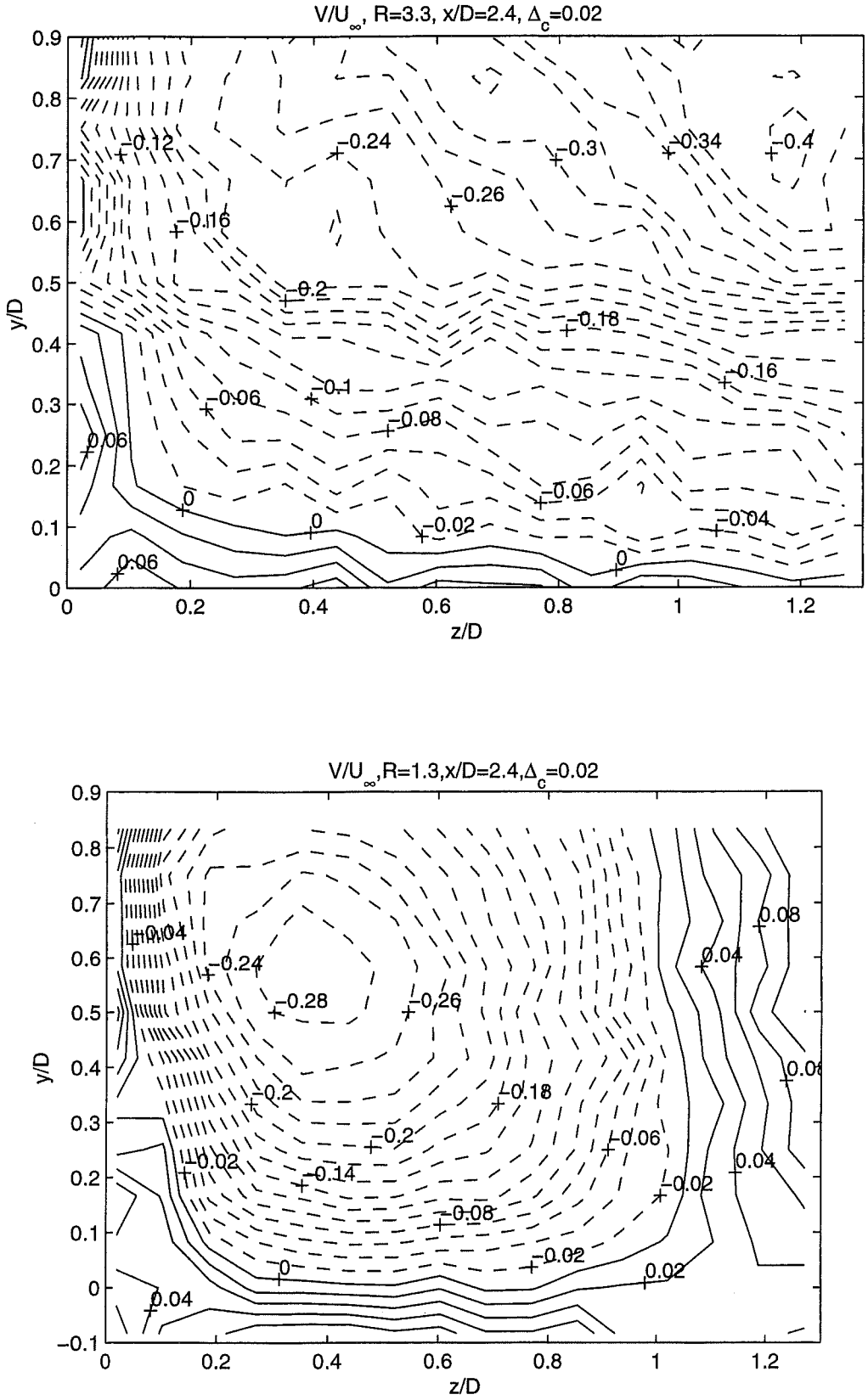

Fig. 4.4.11 Contour plots of the normalized spanwise mean velocity V^* in the x^*=2.40 plane near the flat plate for R=3.3 and 1.3

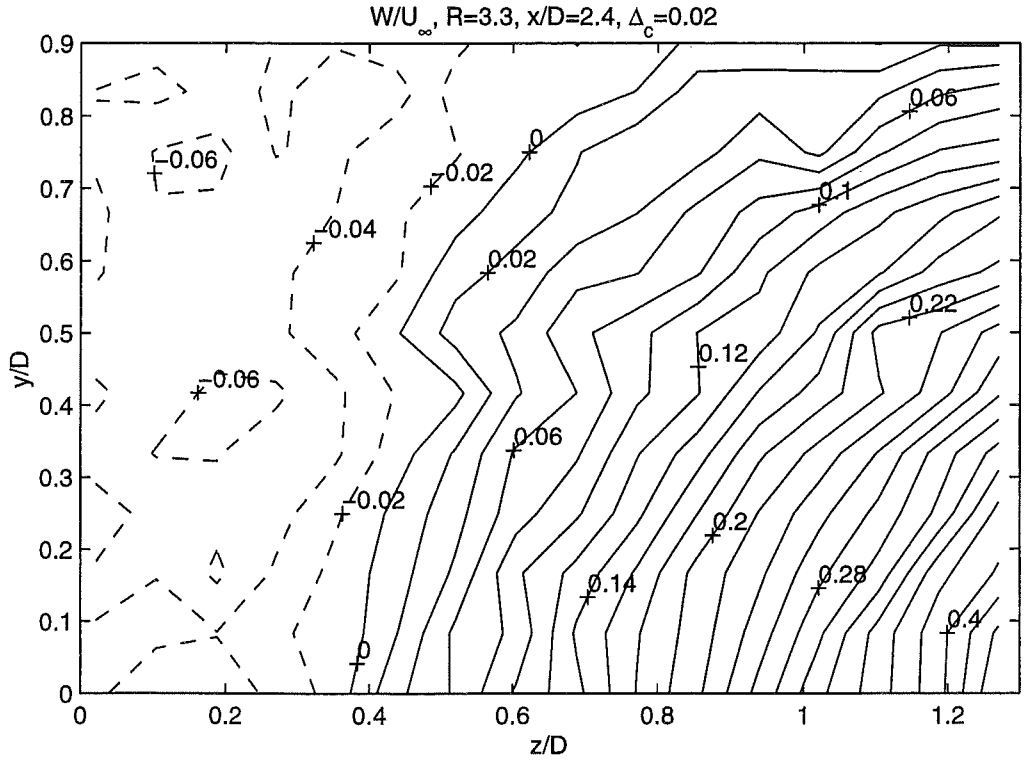

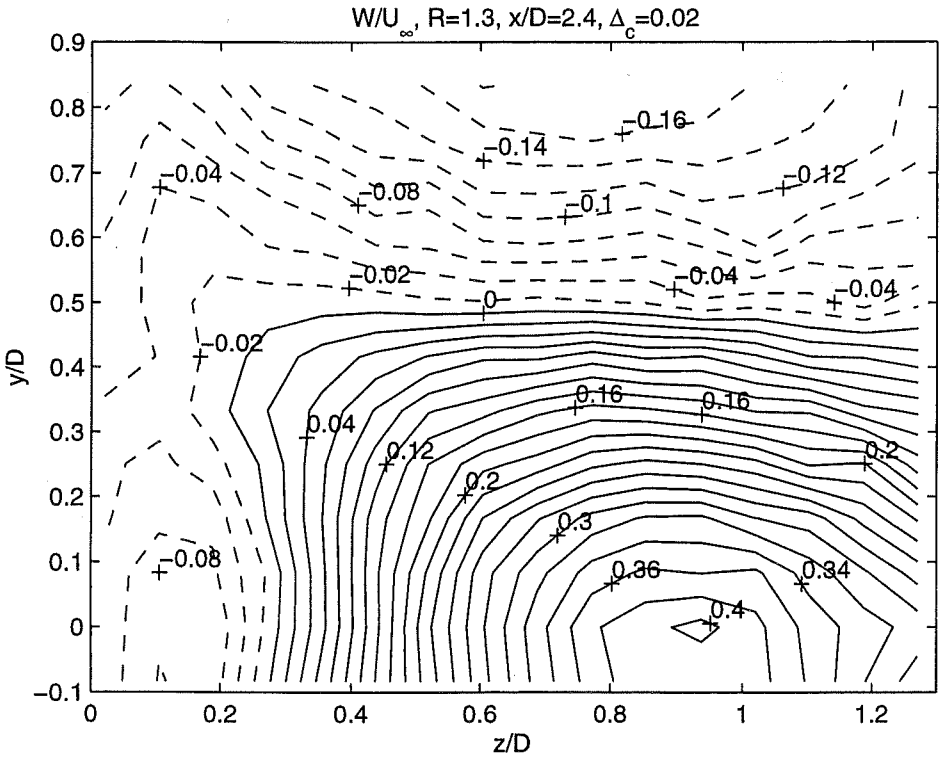

Fig. 4.4.12 Contour plots of the normalized vertical velocity W^* in the x^*=2.40 plane near the flat plate for R=3.3 and 1.3

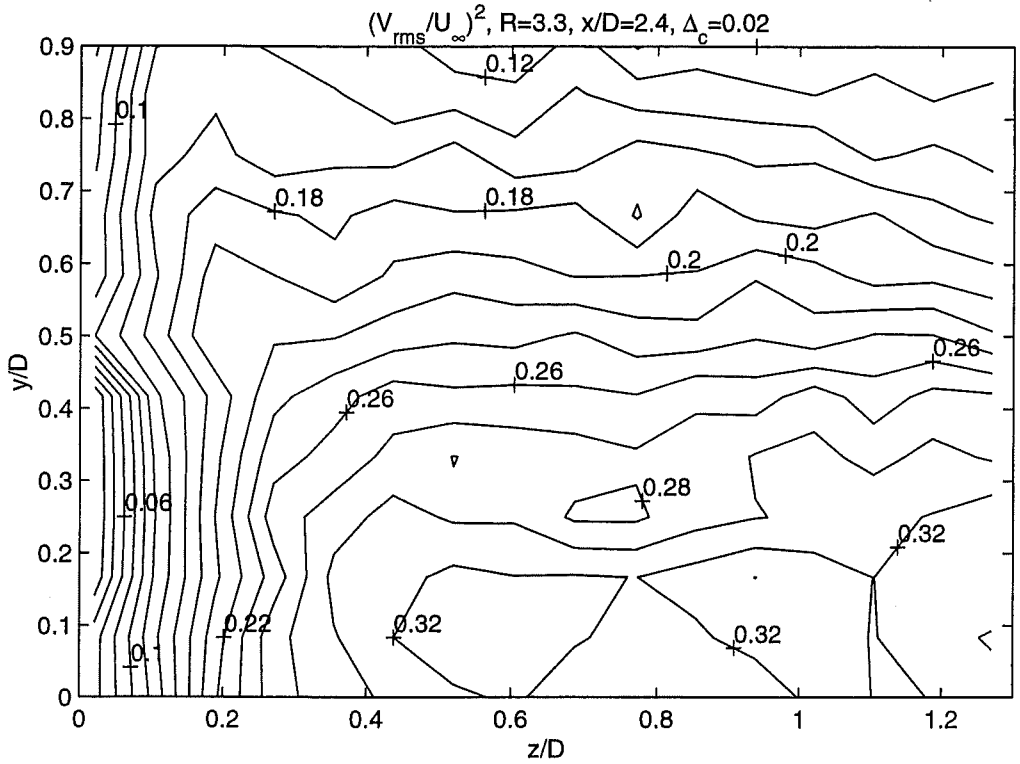

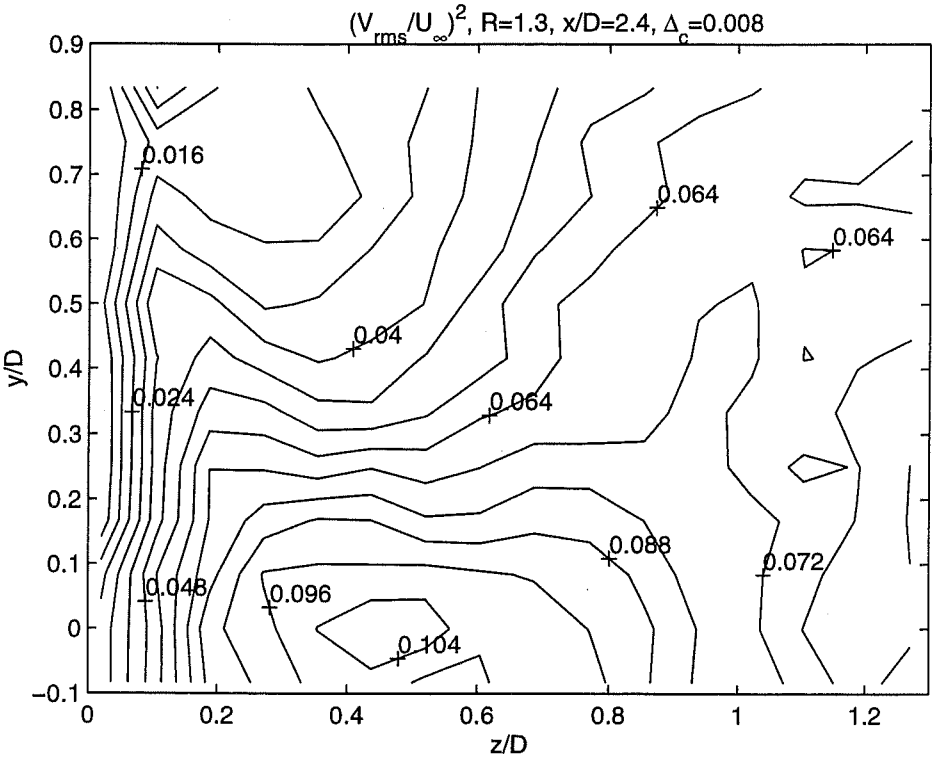

Fig. 4.4.13 Contour plots of the normalized turbulent stress vv^* in the x^*=2.40 plane near the flat plate for R=3.3 and 1.3

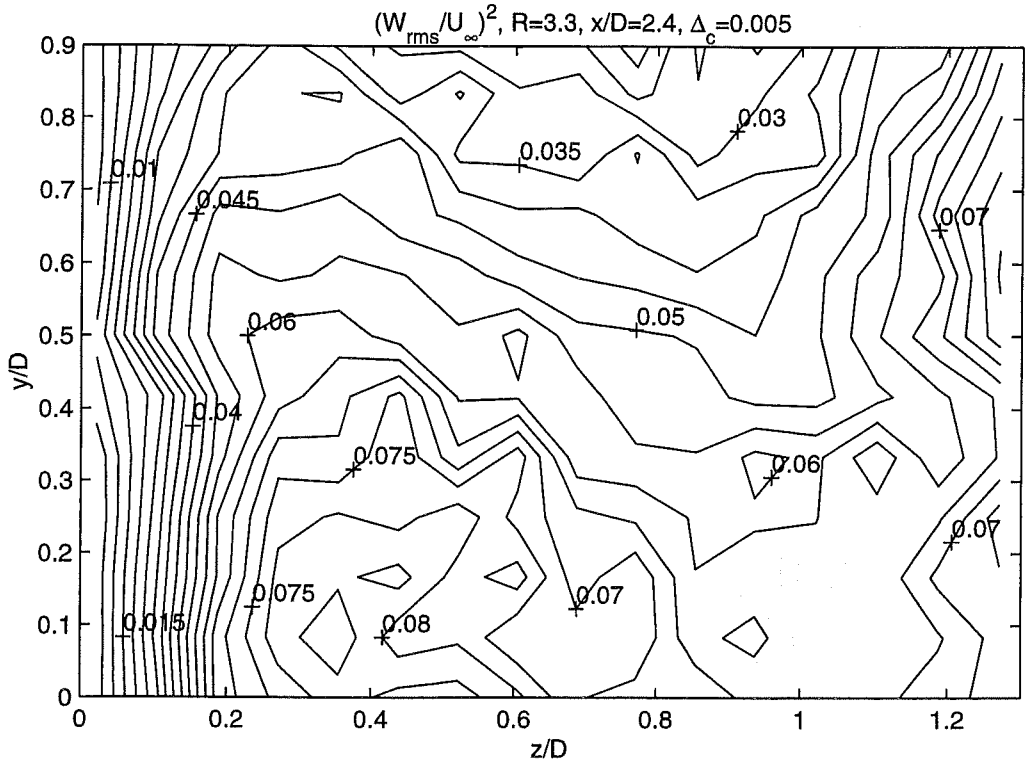

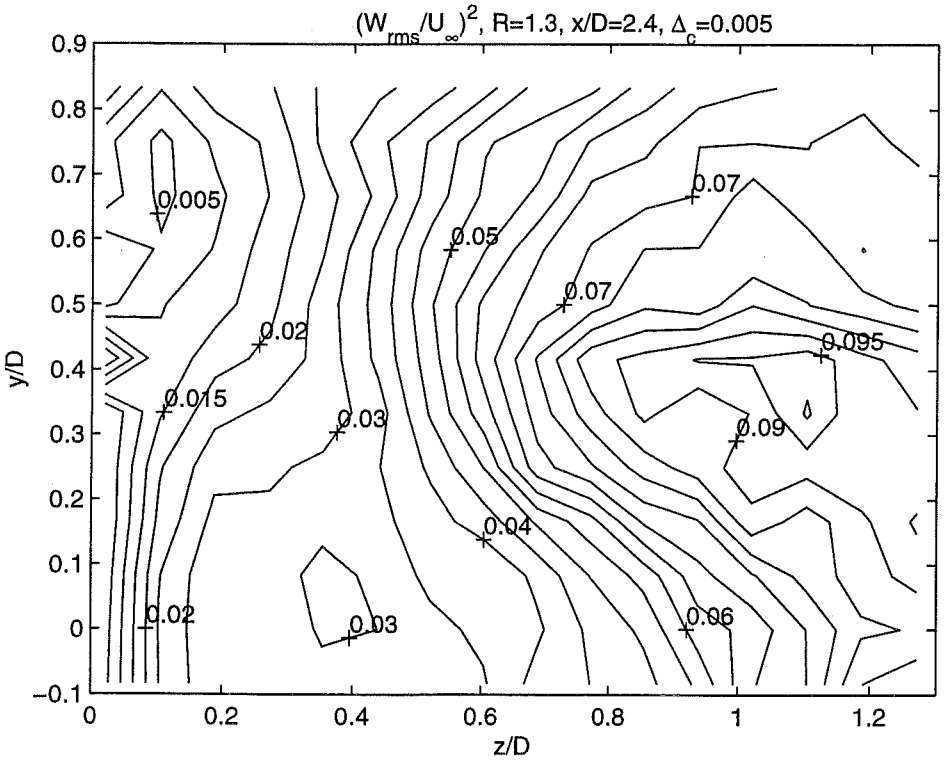

Fig. 4.4.14 Contour plots of the normalized turbulent stress ww^* in the x^*=2.40 plane near the flat plate for R=3.3 and 1.3

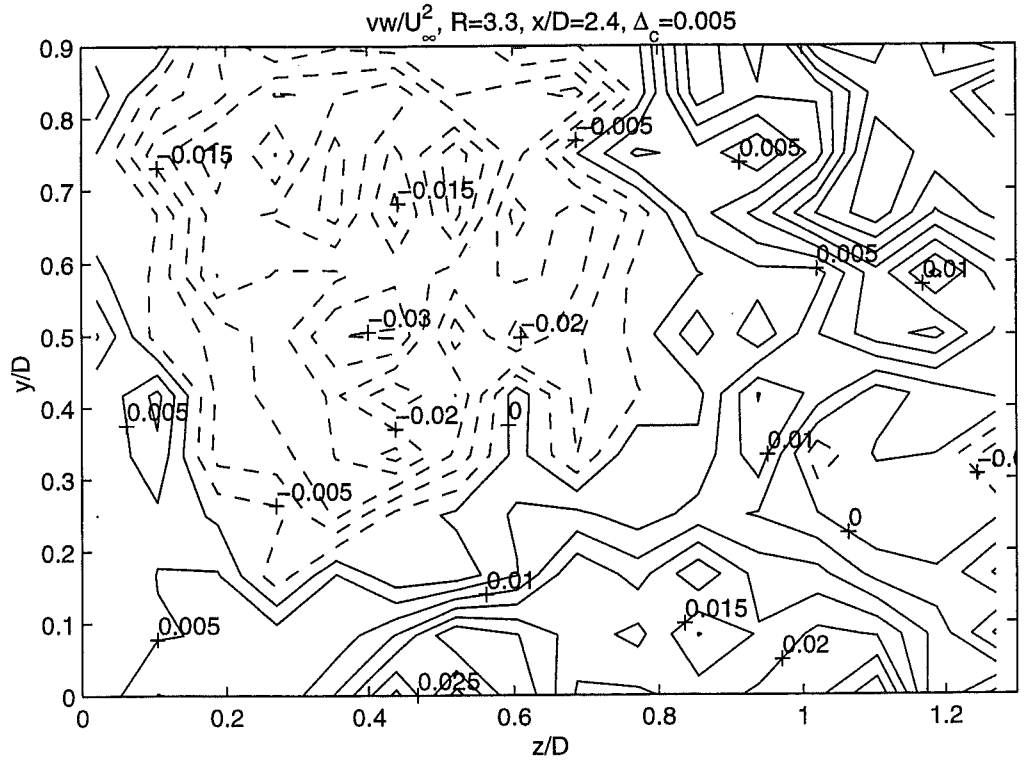

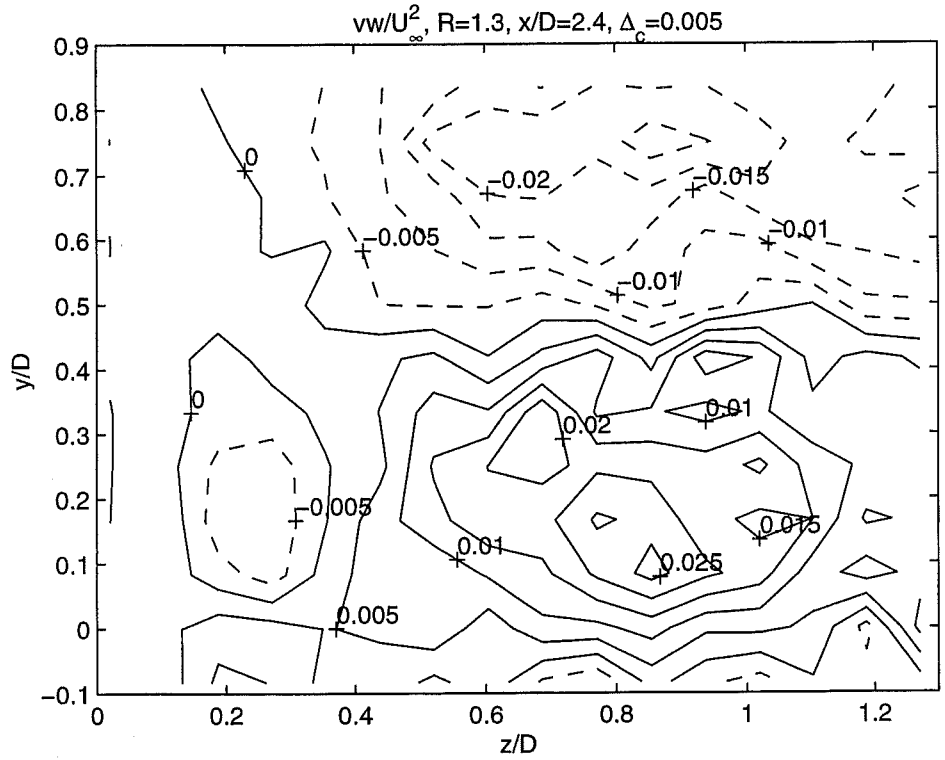

Fig. 4.4.15 Contour plots of the normalized turbulent shear stresses vw^* in the x^*=2.40 plane near the flat plate for R=3.3 and 1.3